
# Control of Voltage Source Converters Connected to Variable Impedance Grids

## PhD Thesis

Mathieu Kervyn de Meerendre

Wind and Marine Energy Systems CDT & PEDEC Group

Electrical and Electronic Engineering Department

University of Strathclyde, Glasgow

9th June 2023

To Beatrice and my family

# Declaration

This thesis is the result of the author's original research. It has been composed by the author and has not been previously submitted for examination which has led to the award of a degree.

# Acknowledgements

A special thank you to my first supervisor, Dr. Agustí Egea-Àlvarez, for his technical support and light-hearted humour. The Saturday cycle rides, pandemic restrictions permitting, were a vital source of fresh air and ideas. Thank you also to my second supervisor, Dr. Khaled Ahmed, for his insight, advice and chartership guidance. The PEDEC group as a whole has provided me with valuable support, and I am especially grateful to Euan Andrew and Dimitrios Vozikis for their assistance and comradeship in the laboratory, and Gabriele Amico for his guidance with some of the maths used in this work.

I am grateful to the Centre for Doctoral Training in Wind and Marine Energy Systems staff, researchers and peers for the invaluable learning opportunities and sense of community that the CDT offered throughout my PhD. Thank you Drew Smith, Prof. Alasdair McDonald, Prof. Bill Leithead, and many others. Thank you also to Prof. Oriol Gomis-Bellmunt and Dr. Eduardo Prieto-Araujo from CITCEA-UPC in Barcelona, with whom I spent three months.

Thank you to my partner, Beatrice, for always being so wonderful, and to my family for their love and support.

Finally, I thankfully acknowledge the funding I received from the Engineering and Physical Sciences Research Council, National Productivity Investment Fund, Grant Number EP/R512205/1.

Data statement: The laboratory data underpinning this research can be accessed at: https://doi.org/10.15129/4441aab4-c15e-4f3c-b3ff-a451ce70794b

# Abstract

The increase in new renewable energy resources is key to achieving carbon reduction targets, however it also introduces new grid integration challenges. The best renewable resource in Scotland is found in remote parts of the country, and as a result new renewable-based generation is increasingly subjected to high and variable levels of impedance. Impedances that cause resonances are also increasingly common, given the higher order characteristics of impedance when transformers, filters, subsea cables, compensators and so on are present in the network. For a better understanding of impedance related stability issues, the estimation of the grid impedance using both Thévenin equivalent and wide-spectrum techniques is studied in this thesis and integrated into the converter's control. These estimations inform the controller of the grid conditions, allowing for controller adaptation.

In instances where weak grid conditions are severe and the local grid impedance is dominant, a disturbance rejection mechanism called the pre-emptive voltage decoupler (PVD) is proposed. The PVD feeds forward the active current reference and measured voltage, and adapts the reactive current reference as a function of the impedance estimation, to pre-emptively compensate the local voltage for changes in active power transfer. This is justified through small signal analysis using linearised state space models and validated in the laboratory using large inductors and a converter. The control is also made more resilient with an instability detector, proposed to prevent instability when significant grid disturbances occur. Through early detection of sudden power angle changes, stability can be maintained. This is achieved by momentarily reducing the power reference and re-establishing grid parameters. The implementation of the proposed changes improves the steady state stability region from -0.75 – 0.55 pu

to -0.85 – 0.75 pu. Further, the nonlinear transient performance is much more resilient, and uninterrupted power flow can be maintained.

When the local grid is not dominant, and higher order grid impedances cause undesired resonances, a detection of the resonant frequency allows for an adaptation of the outer loop gains, thus damping the resonances and improving stability. Such grids are also prone to instability, but a reduction of the power reference does not improve stability, on the contrary the reduction of the power reference shifts eigenvalues into the right hand plane. A better preventative measure is to reduce the outer loop gains, and once the frequency of the problematic resonances is identified, final decisions on outer loop tuning can be taken. With this implementation, the stability of the system is maintained and the power output can be recovered within about 1 second.

# Contents

# List of Figures

# List of Tables

# Chapter 1

# Introduction

## 1.1 Background

To limit the temperature rise caused by climate change to 2 °C as per the Paris Agreement [1], the way energy is produced and consumed must change. For a long time, the focus was on promoting renewable energy sources (RES) via government incentives [2–4]. Such incentives are much less relevant now as RES have become cost-competitive against gas and coal [5, 6]. The unprecedented growth in wind [7, 8] and solar farms [9] the world over is transforming electricity production. On the demand side, the electrification of transport and heating through electric cars and heat pumps [10] is transforming how we consume energy. Even alternative fuel technologies, such as green hydrogen production, require electricity to power the production process [11, 12].

The key technology that is enabling this energy transition is the power converter. All the above-mentioned changes, from RES to electrolysers and electric cars, are connected to the grid via power converters. In wind turbines, the converter interface allows for the variable speed operation of the turbine; maximising power capture, reducing structural loads, and enabling grid code requirements such as fault ride through [13]. Photovoltaic (PV) panels, batteries and hydrogen fuel cells all produce DC power, so these technologies also require an converter for grid integration. In addition, new high voltage direct current (HVDC) transmission lines are increasingly used to connect

offshore wind farms to the grid [14] and to inter-connect different national grids via interconnectors [15].

While the converter is an enabling technology, it also presents new challenges. For example, it is more prone to damage due to short term overcurrents than synchronous machines, coming in at approximately 1.2 pu of the rated current rather than 6 pu [16]. There are also challenges at a network level, such as frequency stability [17], with grid codes increasingly requiring RES to participate in frequency regulation [18]; and energy balancing [19], with ongoing research into batteries [20], hydrogen [21] and ammonia [22] storage solutions, as well as demand-side participation [23]. In this thesis, the research problems being investigated are the integration of converters into grids of low strength and resonant grids.

The local grid strength is determined by dividing the localised short circuit power by the rated power of the RES, resulting in the generalised short circuit ratio (SCR) [24]. This generalisation is acceptable when the local grid impedance is dominant, allowing for a linear representation of the grid impedance. A large offshore wind farm connected to a remote part of the grid with a large local grid impedance will have a relatively low short circuit ratio, otherwise described as a weak grid [25–27]. Low SCR grids are characterised by low voltage stiffness, where fluctuations in local loads and generation output can significantly affect the local bus voltage [28]. This results in poor voltage stability, making the local system less tolerant to disturbances such as faults and other grid events (such as the loss of electrical equipment) [29].

A sudden change in SCR in an already weak network is arguably a contributing factor to the 9 August 2019 GB grid power outage. The technical report [30] describes active and reactive power swings at the Hornsea wind farm prior to the disconnection of 1 million customers. It describes how the local network at the Hornsea wind farm was already weak and experiencing oscillatory behaviour when a transmission line (the Eaton Socon – Wymondley 400 kV circuit) was disconnected due to a lightening stike. It can be inferred that the transmission line loss further reduced Hornsea wind farm's local grid strength, increasing the coupling between active and reactive power. Such conditions could easily result in growing undamped oscillations and the Hornsea wind

farm's protection systems to trip. Seen from this angle, the tripping of the Hornsea wind farm highlights the importance of appropriate controller tuning, a task complicated by the varying grid impedance [31, 32].

Typically, the control action for converters in weak grids is relatively slow, with various reasons given in [33–38]. However, this is in conflict with the growing requirement for primary frequency support from converter-interfaced generation [17]. Thus, not only are converters having to operate comfortably in increasingly weak grids, they must also be able to respond quickly to frequency events without becoming unstable.

A resonant grid is caused by the combination of inductive elements, such as overhead lines and transformers, with capacitive elements, such as reactive power compensators [39], subsea cables [40, 41] and series compensation [42]. The resulting higher order impedance may contain problematic resonances [43] that are unaccounted for by the Thévenin equivalent impedance and, by extension, SCR. Therefore, such networks require more detailed information about the grid impedance across a wide frequency spectrum.

This thesis aims to improve the dynamic performance and resilience of converters that employ vector current control (VCC) algorithms when subjected to grid impedance variations. VCC is studied specifically because it is the most widely used control strategy, making the proposals in this thesis relevant to industry. As for impedance variation, it is studied because it is an under-researched area. It is difficult to tune a converter to have both good dynamic performance and remain stable for different degrees of grid strength. It is even more difficult if the variations in grid impedance are significant and sudden. Similarly, an unexpected grid-induced resonance can cause undesirable converter - grid interactions and may result in instability. These two areas of research, weak grids and resonant grids, are addressed separately in this thesis. However the solutions proposed to each problem are procedurally similar: allow the controller to independently detect changes in grid conditions, determine what the new grid conditions are, and adapt appropriately. This adaptability is advantageous as it overcomes the paradox of prioritising dynamic response over controller robustness, or vice versa.

## 1.2 Summary of work presented in thesis

Chapter 2 introduces the concept of weak grids, resonant grids and VCC. The coupling of active power and PCC voltage in varying grid strengths is studied in detail. Similarly, the problems associated with resonances and the appearance of resonance as a function of grid configuration is also studied. Both the time domain models and the linearised models of VCC are derived, and the linear model is validated against the time domain model. Further, a review of the literature on converter integration in weak grids as well as resonant grids is undertaken.

As grid strength and grid resonances are a function of grid impedance, Chapter 3 reviews impedance estimation techniques from the literature. The most promising techniques are subsequently tested in simulations and laboratory experiments. A study is undertaken to understand why on-demand estimations using passive techniques are not possible.

In Chapter 4, the relationship between active current and reactive current is derived, and a novel technique that decouples the active and reactive components is proposed. By taking into account the measured PCC voltage, estimated grid impedance and active current reference, it is able to pre-emptively decouple the PCC voltage from changes in active power, thus the name Pre-emptive Voltage Decoupler.

Chapter 5 seeks to improve the resilience of VCC when subjected to large grid-induced disturbances, such as a transmission line loss. Therefore, the instability detector is developed as a means of monitoring changes in local voltage angle. The instability detector is combined with a power reference management mechanism, which reduces the active power reference and, by extension, the power angle when instability is detected. This allows for the system to settle and stability to be maintained. An impedance estimator from Chapter 3 and the PVD from Chapter 4 are also included in the proposed resilient VCC, allowing for independent optimisation of the PVD. The local state machine control, which coordinates all the aforementioned additional components to VCC, is presented through state machine notation and a range of simulation and experimental time series plots covering various scenarios with regards to very weak

grid operation and unexpected grid-induced disturbances.

In Chapter 6, a wide-spectrum impedance estimator developed in Chapter 3, as well as the instability detector from Chapter 5, are combined with novel resonance damping techniques. The resulting modified VCC is resilient to changing resonance frequencies through independent detection of instability onset and preventative action, identification of the resonant frequency, and automatic adaptation to the new resonance through outer loop gain modification. The benefits of outer loop gain modification is determined through small signal studies and time domain simulations, and are compared to other techniques in the literature such as the use of notch filters.

The simulation and small signal studies undertaken in this thesis employ parameters based on a 350 MVA wind farm converter, similar to numerous existing literature [44–47]. All hardware results are produced using a 1 kVA experimental setup in the power electronics laboratory, with parameters justified in Section 2.4 based on the available hardware. Both sets of parameters are presented in Appendix A.

## 1.3 Scientific contributions

- The identification of the mathematical constraints that prevent the estimation of grid impedance in stationary and unperturbed grid conditions.

- A novel voltage compensation technique is proposed in the form of the Preemptive Voltage Decoupler, which predicts voltage sensitivity in respect to active power. This is a notable improvement on existing weak grid integration techniques of VCC, which are either reactionary or of reduced bandwidth. This contribution is validated with laboratory experiments.

- A novel instability detector is presented. During the course of the research, it was found that the main indicator of instability is the shift in local voltage angle over short periods of time. Therefore, by monitoring this angle, it is possible to identify instability onset before voltage collapse occurs and triggering preventative action. This implementation is suitable for both weak grid-induced instability and undamped resonance instability. This contribution is validated with laboratory

experiments.

- A local state machine controller is proposed to coordinate all the modifications made to VCC. This ensures that the instability detector triggers the stabilising measures appropriately, that the impedance estimation is undertaken correctly, and that the Pre-emptive Voltage Decoupler is updated with the latest impedance estimation. This contribution is validated with laboratory experiments.

- A novel approach to improve stability in resonant grids is proposed, where problematic resonances are identified and mitigated in real time. The instability detector and local state machine controller previously described are adapted and redeployed as part of this solution, with the instability mitigation undertaken by re-tuning the proportional gains of the controller's outer loop.

## 1.4 List of publications

- *Robustness Testing of Two Impedance Estimation Techniques*, proceeding from the PEMD conference, March 2020.

- *Review of Local Network Impedance Estimation Techniques*, published in IEEE Access in November 2020.

- *Responsive and Resilient Vector Current Control for Variable Grids*, published in Open Journal of Power Electronics in 2023.

# Chapter 2

# Future Grid Challenges and Converter Control Review

The first part of this chapter provides an overview of the problems associated with weak grids and resonant grids. Weak grids are characterised by a large and dominant local grid impedance, which reduces the stiffness of the local voltage. As a result, the local voltage is coupled with the active power, with the voltage collapsing as the active power transfer increases. Resonant grids, on the other hand, experience undamped conditions at the resonance frequencies due to the presence of resonant LC elements into the network – for example, a transmission line with reactive power compensation. Such resonances are only problematic when they match similarly undamped frequencies within the converter control.

The second part of this chapter presents vector current control, complete with time domain and frequency domain derivations and tuning strategies. Subsequently, the existing literature covering weak grid and resonant grid integration of converters is reviewed.

## 2.1 Future grid challenges

### 2.1.1 Weak Grids

In Fig. 2.1, the grid is represented by Thévenin equivalent impedance, comprising of a resistance $R_n$ and an inductance $L_n$. The use of Thévenin equivalent impedance is standard for weak grid studies [28,36,48], where a simplified RL impedance is assumed. It is also appropriate for the studies undertaken in Chapters 4 – 5 due to the timescales of interest. $e_{abc}$, the stiff grid voltage, is an ideal voltage source. $i_{nabc}$ is the grid current. The local PCC voltage is $u_{abc}$.

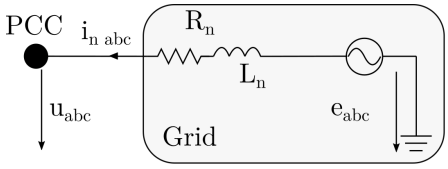


**Figure 2.1:** Representation of the grid.

In steady state conditions, voltages and currents can also be represented as phasors relative to the PCC voltage angle, such that $\overline{U} = U\angle 0$ and $\overline{E} = E\angle\delta$. Or, equivalently in vector form, $\overline{U} = U$ and $\overline{E} = E(jsin(\delta) + cos(\delta))$ The grid impedance can also be represented as a vector $\overline{Z}_n$, where $\overline{Z}_n = R_n + j\omega L_n = R_n + jX_n$, or as a phasor, where $\overline{Z}_n = Z_n\angle\phi$. $\omega$ is the fundamental frequency of the grid.

#### 2.1.1.1 Short circuit ratio

The simplification of the grid impedance into a first order RL impedance (i.e. the Thévenin equivalent impedance) allows for the use of the short circuit ratio (SCR) as a means of assessing grid strength. The generalised SCR equation [24, 49] is as follows

$$SCR = \frac{S_{SC}}{S_{rated}} = \frac{\frac{U_{ll}^2}{Z_n}}{S_{rated}} \tag{2.1}$$

where $S_{SC}$ is the network power when a three-phase balanced short circuit occurs and $S_{rated}$ is the generator rating. Given the high $X_n/R_n$ ratios experienced in transmission circuits, $Z_n$ is often substituted with $X_n$. The value of $U$ is measured when there is

no power transfer at the PCC, thus $U \equiv E$; and the subscript $ll$ represents line-to-line quantities. Commonly, a very weak grid has a SCR below 2 and a weak grid has a SCR between 2 and 3 [50]. A SCR higher than 3 represents a strong grid.

Equation (2.1) helps to establish the relationship between SCR, voltage and impedance at the PCC. In normal conditions, it can be assumed that steady state voltage levels operate within specified limits of ± 5 % of nominal values, as per the UK grid code [51]. Thus, the SCR is the Thévenin equivalent impedance are directly linked [38,52]. Variations in grid impedance can occur daily as loads are connected and disconnected [53]; but also more significantly, for example with the disconnection of a transmission line [49].

The generalised SCR is appropriate when assessing a single converter connected to a grid with a dominant local impedance, such as those undertaken in Chapters 4 – 5. Care should be taken when the local grid hosts multiple converter based generators and loads [54]. Some variants of the SCR, such as the weighted SCR (WSCR), the composite SCR (CSCR), or the SCR with interaction factors (SCRIF), might be better tools for studying specific network configurations and/or grid-wide stability at a power systems level. While these are not employed in this thesis, they are outlined in [54].

#### 2.1.1.2 Power angle limitations in weak grids

The relationship between active power transfer and power angle is crucial to weak grid studies. This is because weak grids, characterised by large grid impedance, requires much larger power angles in order to transfer active power compared to a stronger grid. Consider the steady state apparent power equation

$$S = 3\overline{U}\left(\frac{\overline{E}-\overline{U}}{\overline{Z}_n}\right)^* \tag{2.2}$$

By using the vector form of $\overline{U}$ and $\overline{E}$, and extracting the real components only, the equation of active power as a function of grid impedance is derived.

$$P = \frac{3U(EX_n sin(\delta) + R_n(Ecos(\delta) - U))}{X_n^2 + R_n^2} \tag{2.3}$$

Given (2.1) and assuming a fixed $X_n/R_n$ ratio of 10, Fig. 2.2 shows the relationship between $\delta$ and $P$ for various SCRs.

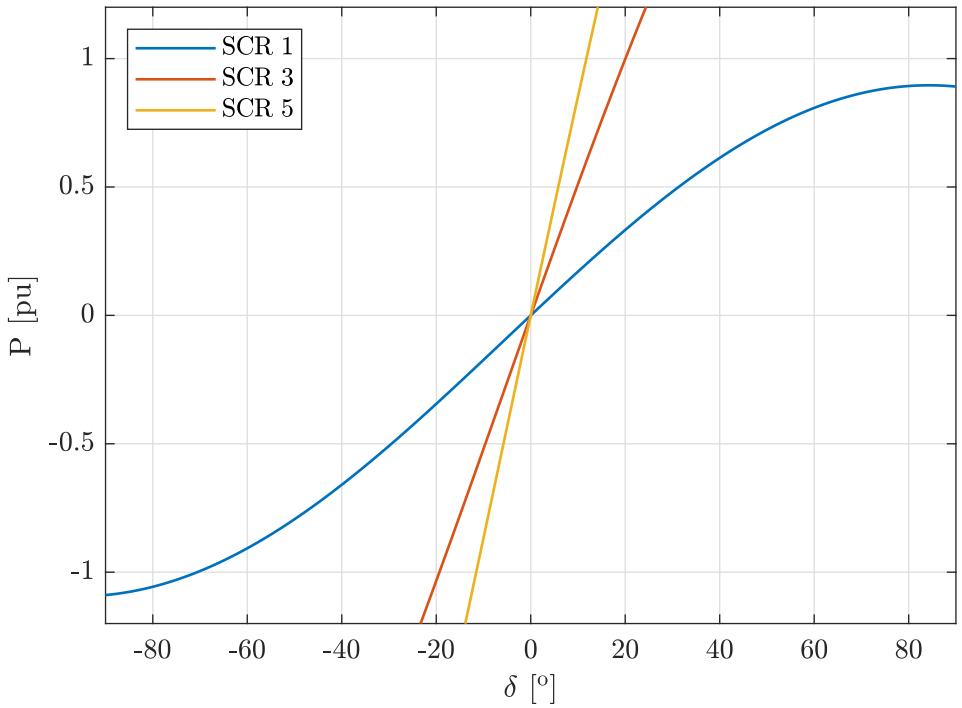


**Figure 2.2:** The characteristics of active power transfer across increasing grid impedances.

Strong grids, represented by the orange and yellow traces, requires very small changes in power angle to produce a transfer of active power. In such conditions, the generator operation is highly linear with a constant relationship between power and angle. Weak grids with a SCR of 1, represented by the blue trace, present very different working conditions for generators. Much larger power angles are required to absorb or inject active power. Further, the relationship between power angle and active power is no longer linear, i.e. the plant is nonlinear.

#### 2.1.1.3 Coupling between active power and PCC voltage

By assuming zero reactive power transfer, the PCC voltage magnitude can be linked to the power angle $\delta$, and thus to active power.

$$U = -\frac{ER_n sin(\delta) - EX_n cos(\delta)}{X_n} \tag{2.4}$$

Plotted against active power, the PCC voltage magnitude for varying SCRs is presented in Fig. 2.3.

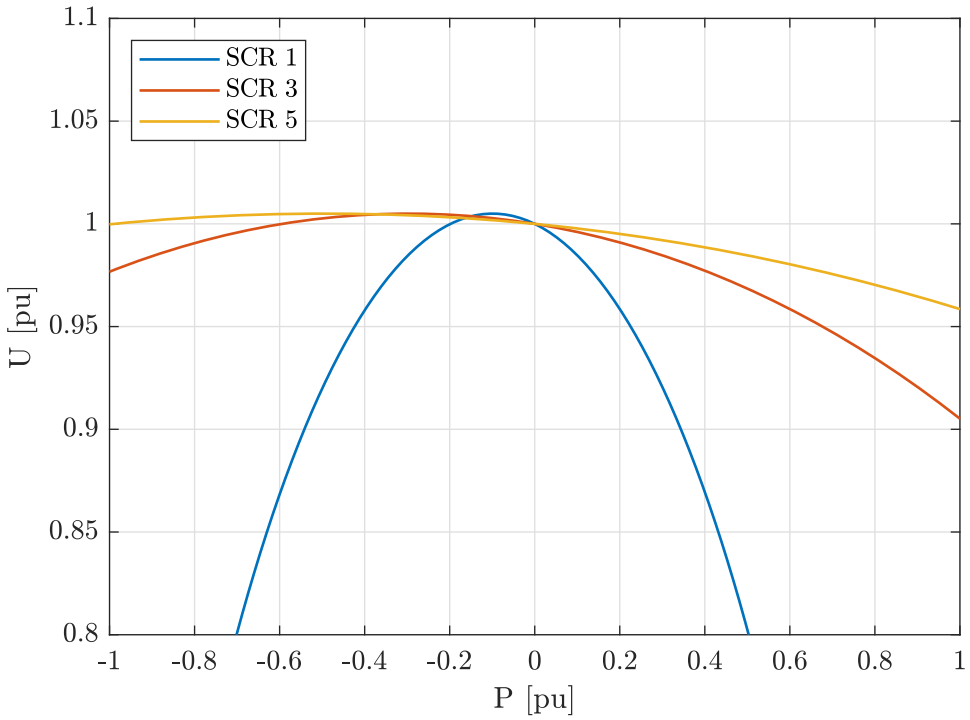


**Figure 2.3:** Coupling between active power and PCC voltage without any reactive power provision.

From Fig. 2.3, the PCC voltage remains relatively constant when the SCR is 5. However, as the grid becomes weaker, the PCC voltage variability is much greater. This coupling between active power and PCC voltage justifies the requirement for reactive power provision by generators in order to support the PCC voltage.

#### 2.1.1.4 Reactive power provision for voltage support

The analytical relationship between reactive power and power angle, for a fixed PCC voltage, is as follows

$$Q = \frac{3ER_nUsin(\delta) - 3EUX_ncos(\delta) + 3U^2X_n}{X_n^2 + R_n^2} \tag{2.5}$$

Using equations (2.3) and (2.5), active and reactive power can be plotted against one another for various SCRs, as per Fig. 2.4.

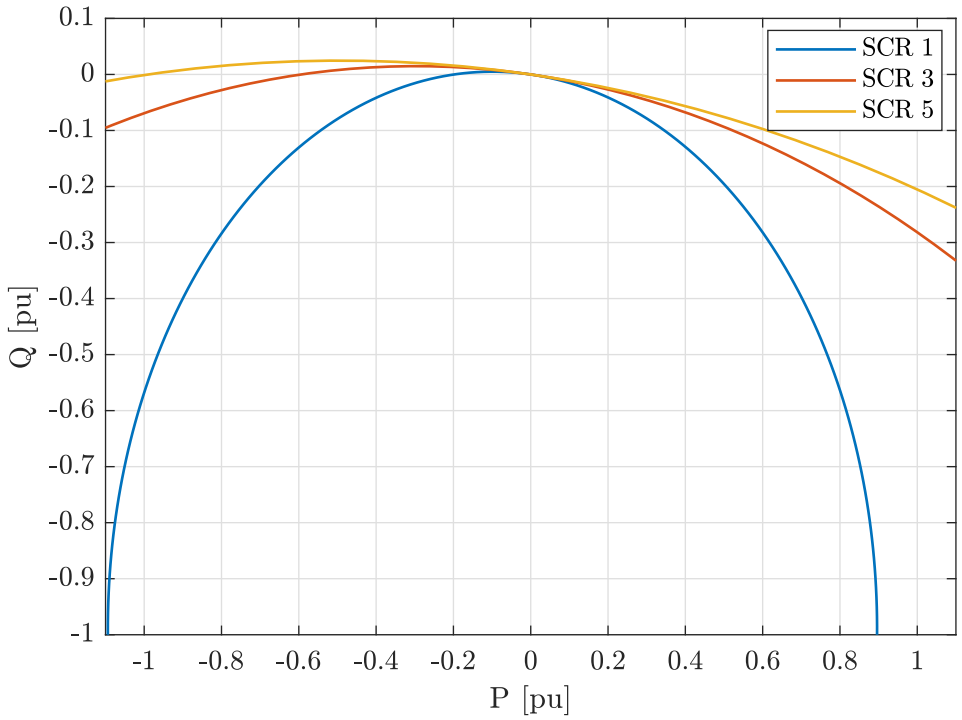


**Figure 2.4:** Relationship between active power and reactive power.

Fig. 2.4 demonstrates the reactive power provision required to support the local voltage at a fixed value. The reactive power requirements are especially high in very weak grids, extending to approximately $-0.6$ pu of the rated power when the SCR is 1.

### 2.1.2 Grids with embedded resonances

Unlike weak grid studies, where Thévenin equivalent impedances are used, grids with resonances must be represented by a wide frequency spectrum impedance, consisting of an arrangement of inductances, resistances and capacitances, and their effect on one another. This produces a higher order aggregated impedance with resonances. For the

purposes of this Section, the converter impedance is not considered.

There are two types of resonances within electrical networks: resonances caused by series configuration of the capacitor relative to the other passive elements, as per Fig. 2.5a; and resonances caused by parallel configuration of the capacitor relative to the other passive elements, as per Fig. 2.5b. Resistive and inductive impedances typically represent power lines and transformers, whereas the capacitive elements represent a range of phenomena and assets, such as cable shunt capacitance, series compensation, VAR compensation, PWM filters, etc. Subscript *cs* represents the converter side elements, and *gs* represents grid side elements.

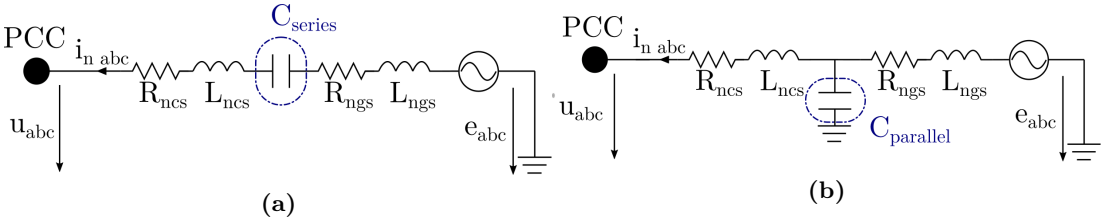


**Figure 2.5:** Electrical system with (a) series capacitance and (b) parallel capacitance.

Series capacitances, as per Fig. 2.5a, occur when series compensation is employed in long power lines. The use of series compensation can result subsynchronous series resonances (SSR) [55], causing the undesirable exchange of electrical energy in the network and, in the case of conventional power stations and some wind turbines, mechanical energy in the generator [42]. One commonly cited such event occurred in 1970 at the Mohave Generating Station (a coal-fired power plant located in southern Nevada), where torque oscillations caused by SSR resulted in catastrophic failure of the turbine generator shafts [55]. Such undesirable exchange in energy can also happen with wind farms comprising of Type-II [42] and Type-III [56] wind turbines as series compensation is added to power lines to cater for the growth in wind turbine generation. The negative slip in such machines, due to the rotor angular speed being higher that the electrical angular rotation of the stator, result in the machines' resistance becoming negative [57]. There is therefore a risk of undamped oscillations when directly coupled to a grid containing SSR [58]. This scenario occurred on 22 October 2009 at the Zorillo-Gulf wind farms, where an oscillation between the capacitor of a series compensated line

resonated against the generators of Type-III wind turbines. Within a couple seconds, the voltage at the wind turbines had reached 195 % of the rated voltage, causing the failure of numerous crowbars at the wind farms [59]. According to [60], it is still unclear if the exact cause of the resonance is due to the "induction generator effect", undesirable control reaction, or both. Type-IV wind turbines appear much more resilient to SSR issues, as the decoupling of the generator from the grid reduces the possibility for series compensation - generator interaction [60]. The literature on VSCs in SSR conditions suggests that if well designed, the controllers should not exhibit any negative resistance [61]. Furthermore, VSCs can be used to dampen SSCs locally [62–64].

Parallel capacitances, as per Fig. 2.5b, occurs with LC and LCL filters, subsea and underground AC cables, overhead AC lines (due to the cable-to-ground capacitance), and power factor correction devices such as Static VAR compensators and reactive power compensators (i.e. shunt capacitor banks) [65, 66]. Impedances containing parallel capacitances are characterised by a large impedance magnitude at the resonant frequency. The task of designing networks and wind power plants to be free problematic resonances is challenging, as outlined in [43]. This is because resonant frequencies can vary significantly as a function of the number of turbines in operation [67], grid configuration [43], and the switching of capacitor banks [68]. Further, the frequency of a parallel resonance can be quite low, with third harmonic resonances reported in [69]. For reference, a 500 kV underground cable is assigned a shunt capacitance value of 0.3072 $\mu$F/km in [40] and in [41], a 220 kV subsea cable has a shunt capacitance value of 0.1283 $\mu$F/km. Reactive power compensation capacitances can be calculated as $C_{shunt} = X_{t-pu}V^2/(\omega S_{t-rating})$ where $X_{t-pu}$ is the transformer per unit impedance and $S_{t-rating}$ is the transformer rating (reactive power compensation is usually stepped down) [39].

The transfer functions for impedances containing series and parallel capacitances as seen from the PCC are presented in equations (2.6) and (2.7) respectively.

$$Z_{n\ series}(s) = R_{ncs} + L_{ncs}s + \frac{1}{C_{series}s} + R_{ngs} + L_{ngs}s \tag{2.6}$$

$$Z_{n\ parallel}(s) = R_{ncs} + L_{ncs}s + \frac{R_{ngs} + L_{ngs}s}{C_{parallel}L_{ngs}s^2 + C_{parallel}R_{ngs}s + 1} \tag{2.7}$$

Note, the series impedance equations is based on the equation for compensation factor (CF), as follows [70]:

$$X_{Cseries} = CF(L_{ncs} + L_{ngs})\omega \tag{2.8}$$

$$C_{series} = \frac{1}{\omega X_{Cseries}} \tag{2.9}$$

Bode plots for equations (2.6) and (2.7) are presented in Fig. 2.6, where $R_{ncs} = 1.81\ \Omega$, $L_{ncs} = 17.3$ mH, $R_{ngs} = 5.432\ \Omega$, $L_{ngs} = 57.6$ mH, $C_{parallel} = 1.86\ \mu$F and $C_{series} = 87.9\ \mu$F. These parameters provide a grid side impedance that is three times larger than the converter side impedance; the parallel capacitor produces a parallel resonance of 290 Hz; and the series resonance provides the transmission line with a CF of 0.5 pu. The base voltage and power parameters are presented in Appendix A.1.

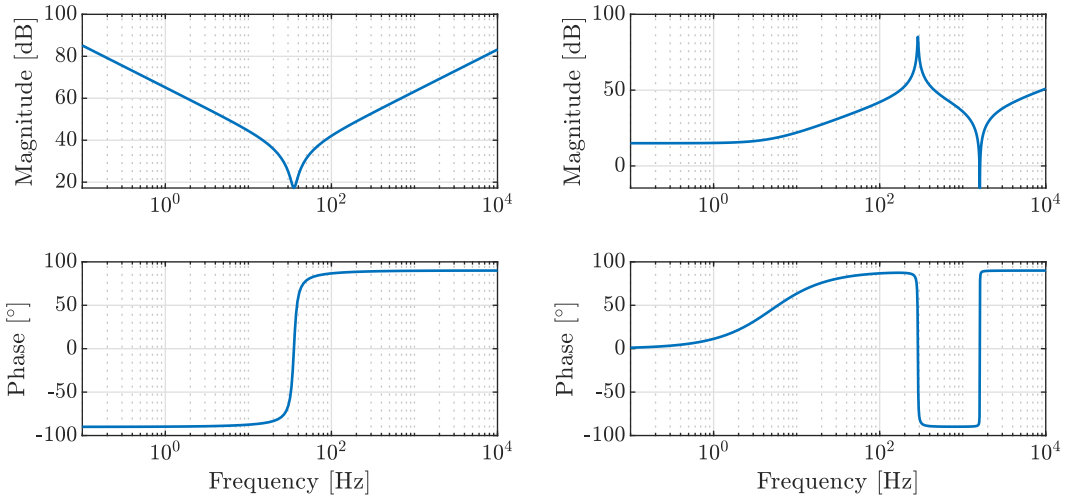


**Figure 2.6:** Typical bode plot shapes for aggregated grid impedances containing (a) a series capacitance and (b) a parallel capacitance.

From Fig. 2.6a, the series capacitance produces a series resonance, represented by a dip in magnitude in the bode plot. Series compensators are common causes of

series resonances, in which case the resonance is also called a subsynchronous resonance (SSR) due to its sub-fundamental frequency characteristics [56,64]. Given the relatively predictable impact of series compensation on SSR, any problems can be mitigated in advance with some careful consideration [56, 71, 72].

The parallel capacitance in Fig. 2.6b produces compound resonances, with a parallel resonance (the peak), and the series resonance (the dip). In this case the resonances are supersynchronous. The relationship between impedances containing parallel capacitances and the resulting resonances is studied in further detail in Section 2.1.2.1.

#### 2.1.2.1 Grids with parallel capacitances

For a given capacitance, the value of converter side and grid side impedances will impact the frequency of the resonances. This is studied in the following subsections.

##### 2.1.2.1.1 Variation in resonances as a function of grid side impedance

Bode plots for (6.1) are presented in Fig. 2.7, where the converter side impedance is assigned a SCR of 6 and the X/R ratio is 10 (i.e. $L_{ncs} = 57.6\,mH$ and $R_{ncs} = 1.81\Omega$), the parallel capacitor has a value of 1.76 $\mu F$ because this results in a parallel resonance in the region of the third harmonic, identified as a problem in [69]. The grid side impedance is a function of the converter side impedance, such that $Z_{ngs}(s) = K_1 Z_{ncs}(s)$. $K_1$ is a variable (with a value of 3, 6 or 12) used to illustrate the impact of the grid side impedance on the resonance frequency.

The bode plots in Fig. 2.7 illustrate that the series resonance occurs at a higher frequency than the parallel resonances, and that unlike the parallel resonance, the frequency of the series resonance is independent of the grid side impedance. On the other hand the greater the grid side impedance, the lower the frequency of the parallel resonance. To take this example further, Fig. 2.8 plots the impedance of the grid, as seen from the PCC. In Fig. 2.8, the axes are linear rather than logarithmic.

The reduction in parallel resonance as a result of grid side impedance increases is concerning, as such impedance changes might cause the resonance to further approach the fundamental frequency. Given the already low resonance issues discussed in [69],

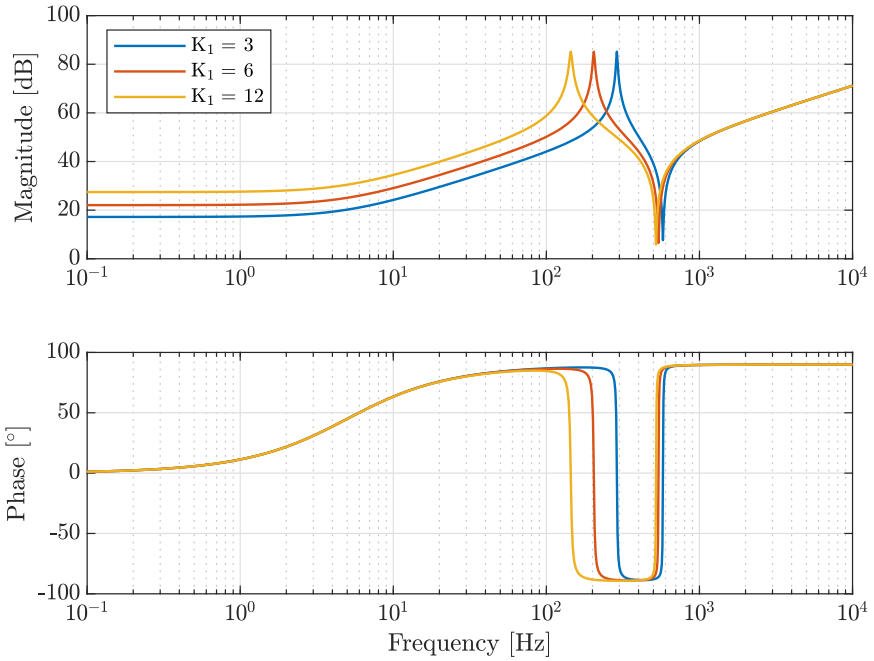


**Figure 2.7:** Bode plots of aggregated grid impedance for varying values of grid side impedance.

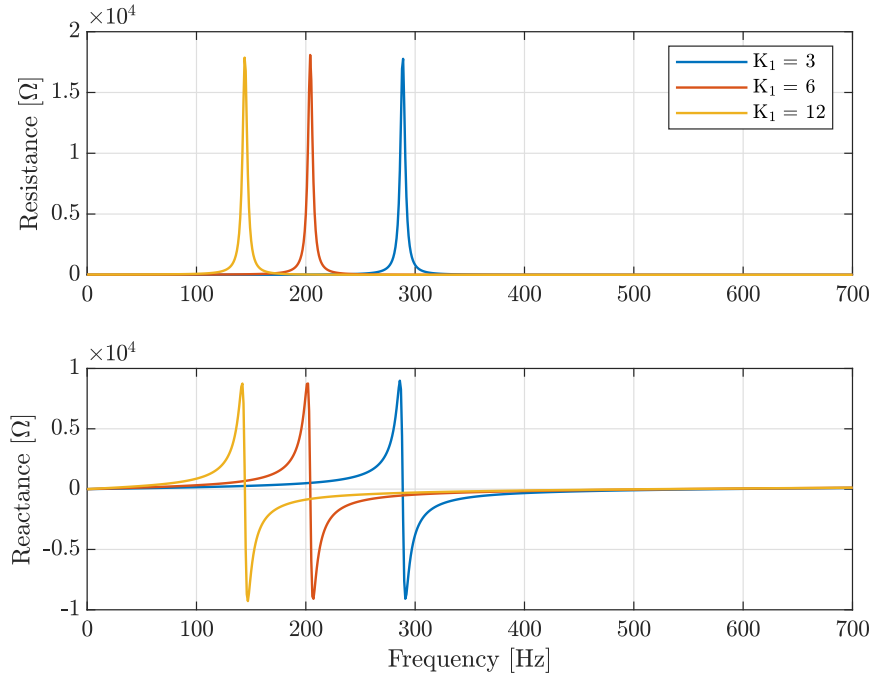


**Figure 2.8:** Linear scaling equivalence impedance plots for varying values of grid side impedance.

where third harmonic resonances are discussed due to the presence of capacitor banks and long transmission systems, the problem of parallel resonance is likely to increase as grids become weaker. The final observation with regards to Fig. 2.8 is that given the linear axes scaling (linear and not logarithmic), the parallel resonances are very obvious (large spikes), but the series resonances are not discernible. This could be resolved by plotting the admittance (see Fig. B.1 in Appendix B).

#### 2.1.2.1.2 Variation in resonances as a function of converter side impedance

Consider an alternative scenario, where the grid side impedance ($Z_{ngs}(s)$), in isolation, is equivalent to a SCR of 6 (i.e. with the values of $Z_{ncs}(s)$ presented in the previous example). The relationship between converter side impedance and grid side impedance is such that $Z_{ncs}(s) = K_2 Z_{ngs}(s)$. In this example $K_2 \leq 1$, as it is assumed that the grid side impedance is higher than the converter side impedance. The value for grid capacitance is the same. This results in the bode plots of Fig. 2.9.

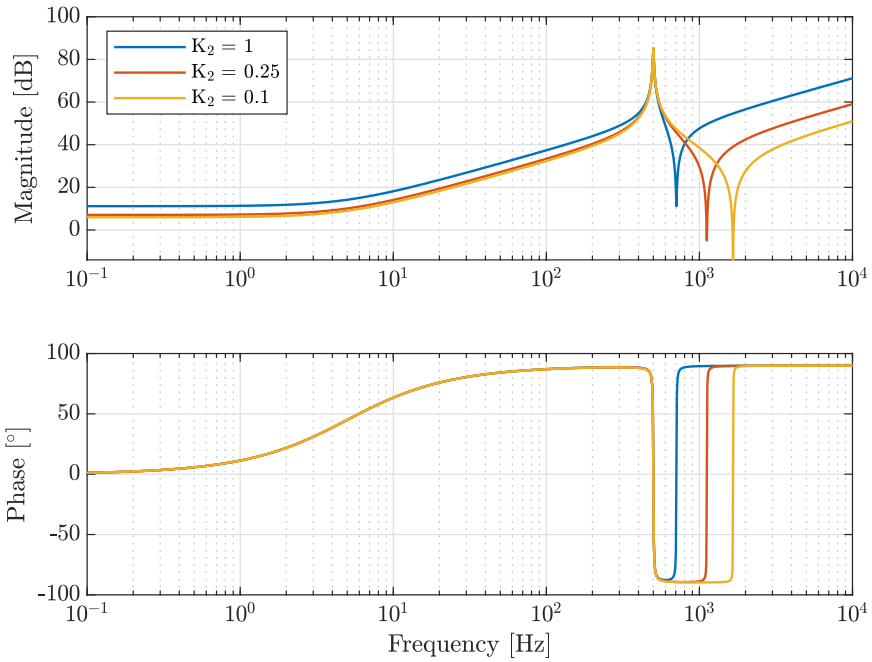


**Figure 2.9:** Bode plots of aggregated grid impedance for varying values of converter side impedance.

From Fig. 2.9, the parallel resonance is stationary for all values of $K_2$, but the

series resonance shifts. Thus, the series resonance is a function of the converter side impedance. The independence of the parallel resonance to changes in converter side impedance is even more pronounced in Fig. 2.10, which plots the impedance as seen from the PCC using linear axes.

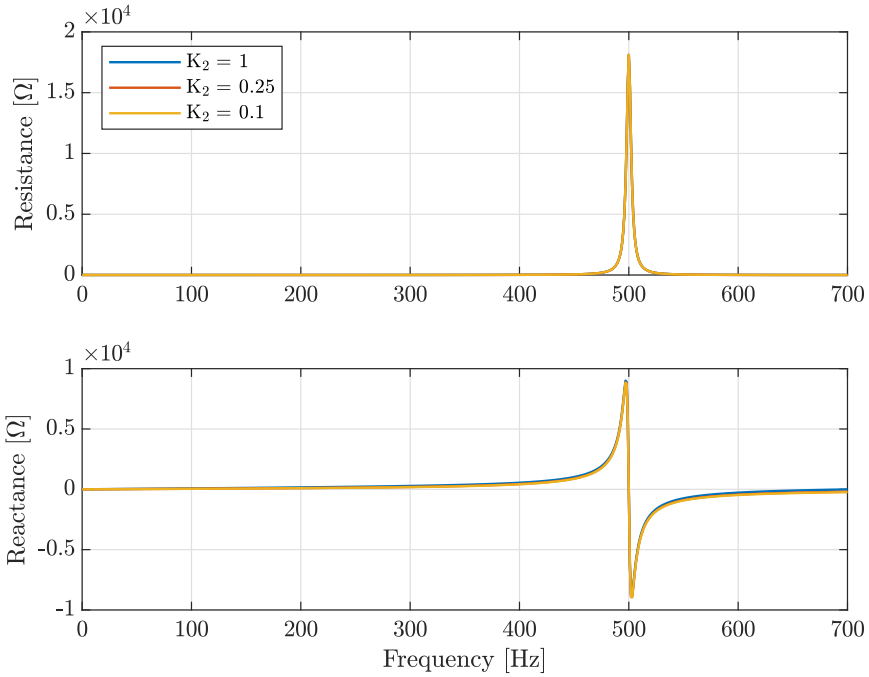


**Figure 2.10:** Linear scaling equivalence plots for varying values of converter side impedance.

In Fig. 2.10, the grid impedance, as seen from the PCC, is exactly the same despite the variations in converter side impedance. The equivalent admittance plot is included in Appendix B as Fig. B.2 for completeness.

#### 2.1.2.1.3 Resonance frequency equations

The frequency of the parallel resonance in a parallel impedance is a function of grid side inductance and the parallel capacitance, such that

$$f_{res\ parallel} = \frac{1}{2\pi\sqrt{L_{ngs}C_{parallel}}} \tag{2.10}$$

This relationship is completely independent of the converter side impedance.

The frequency of the series resonance in a parallel impedance, however, is a bit

more complicated to calculate, as it affected by both the grid side and converter side impedance as well as the capacitor, such that

$$f_{res\ series} = \frac{1}{2\pi\sqrt{\frac{L_{ncs}L_{ngs}}{L_{ncs}+L_{ngs}}C_{parallel}}} \tag{2.11}$$

The resonance frequency equations (2.10) and (2.11) match the frequency of the resonances of the bode plots Fig. 2.7 and 2.9, as per Table 2.1 below.

**Table 2.1:** Plotted and calculated resonances

| Figure | Trace | $f_{res\ parallel}$ (from figure) | $f_{res\ series}$ (from figure) | $f_{res\ parallel}$ (2.10) | $f_{res\ series}$ (2.11) |
|---|---|---|---|---|---|
| Fig. 2.7 | $K_1 = 3$ | 289 Hz | 577 Hz | 289 Hz | 577 Hz |
| Fig. 2.7 | $K_1 = 6$ | 204 Hz | 540 Hz | 204 Hz | 540 Hz |
| Fig. 2.7 | $K_1 = 12$ | 144 Hz | 520 Hz | 144 Hz | 520 Hz |
| Fig. 2.9 | $K_2 = 1$ | 500 Hz | 707 Hz | 500 Hz | 707 Hz |
| Fig. 2.9 | $K_2 = 0.25$ | 500 Hz | 1118 Hz | 500 Hz | 1118 Hz |
| Fig. 2.9 | $K_2 = 0.1$ | 500 Hz | 1658 Hz | 500 Hz | 1658 Hz |

#### 2.1.2.2 Summary and final observations

From Fig. 2.7 – 2.10, the parallel capacitance creates a parallel resonance and a series resonance. The frequency of the parallel resonance is a function of capacitance and grid side impedance only. This is unlike the series resonance which is affected by both the converter side and the grid side impedances. With increasing weak grid concerns, it is likely that problematic parallel resonances will become more common, as the frequency of the resonance interferes with converter controllers (more on that in Chapter 6). Further, grid impedance variability due to the connection and disconnection of loads and lines [49, 53] make it likely that the frequency of resonances will shift. It could, therefore, be advantageous for converters to determine in real-time what the existing parallel resonances are. This would allow converters to independently take mitigating action or perhaps even communicate this problem with nearby reactive power compensators and other network infrastructure. A study on wideband impedance estimation process is presented in Section 3.5.2 as part of the Impedance Estimation chapter, with proposed solutions to parallel resonances pursued in Chapter 6.

## 2.2 Converter control

### 2.2.1 Time domain of vector current control

Vector current control (VCC) was invented in Germany in 1971 to control electrical machines, allowing for the independent control of magnetic flux and torque [73]. This was done by converting the three stator currents of a three-phase AC electric motor into two orthogonal components. These techniques have since been adapted to three phase electrical converters for independent control of active and reactive power [74]. However, as illustrated in Section 2.1.1, the active power transfer and the PCC voltage in weak grids are highly coupled.

The overall layout of VCC is presented in Figure 2.11. The electrical system including voltages, currents and impedances is the same as Fig. 2.1 with the addition of the converter filter where the converter voltage is $v_{abc}$ and the converter current is $i_{cabc}$. The filter impedance $Z_c$ comprises of resistance $R_c$ and inductance $L_c$. The PWM filter capacitor is represented by $C_f$.

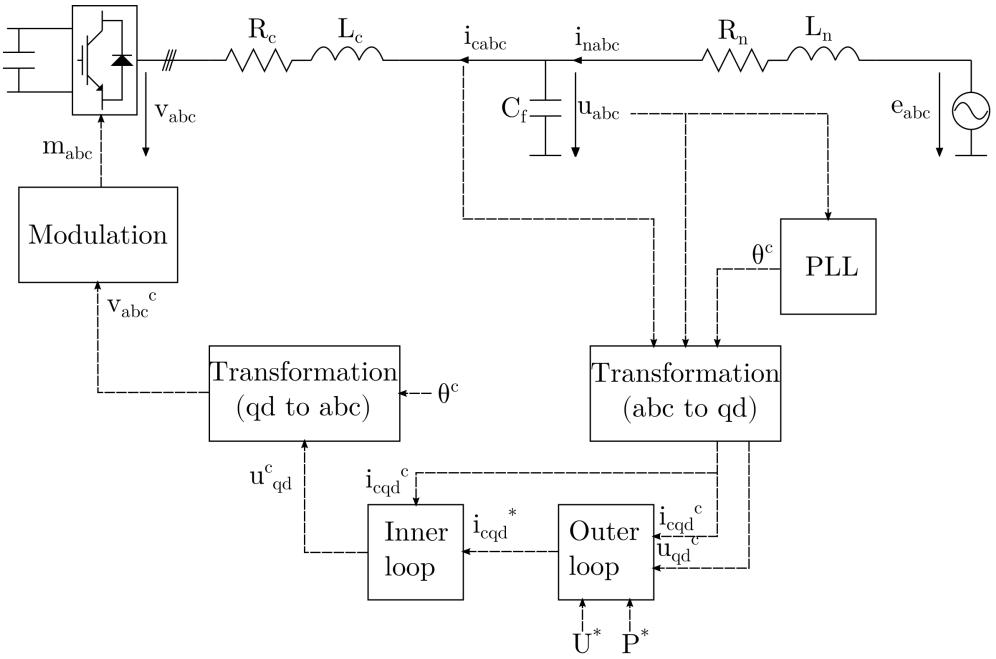


**Figure 2.11:** Basic outline of VCC control structure.

The three phase sinusoidal *abc* voltages and currents are transformed into the *qd-*

frame by the DQZ transforms, using the synchronisation angle produced by the phase locked loop (PLL). The inner current loop is responsible for controlling the current flowing across the RL component of the converter filter, and the outer loop is responsible for controlling active power transfer and supporting the PCC voltage magnitude.

#### 2.2.1.1 qd reference frame

In order to simplify the control of three phase voltages and currents, it is preferable to transform the three phase sinusoidal abc quantities, $f_{abc}$, into two DC quantities, $f^c_{qd}$, where the $q$-sequence is real and leading the imaginary $d$-sequence by 90°. As with the majority of academic literature, no neutral is assumed and the $f^c_0$ component is ignored. This is justified by the common use of delta connections for both Type-IV wind turbines [75] and bipole HVDC connection [76] (i.e. HVDC connected wind farms), with the grounding in the DC-link. The superscript $c$ specifies that the values are in the converter frame rather than the grid frame, a distinction that is particularly important for small signal studies. The DQZ transformation (sometimes referred to as the Park transform) is produced by combining the Clarke transform and a rotation, such that

$$\begin{bmatrix} f^c_q \\ f^c_d \\ f^c_0 \end{bmatrix} = \begin{bmatrix} cos(\theta^c) & cos(\theta^c - \frac{2\pi}{3}) & cos(\theta^c + \frac{2\pi}{3}) \\ sin(\theta^c) & sin(\theta^c - \frac{2\pi}{3}) & sin(\theta^c + \frac{2\pi}{3}) \\ \frac{1}{2} & \frac{1}{2} & \frac{1}{2} \end{bmatrix} \begin{bmatrix} f_a \\ f_b \\ f_c \end{bmatrix} \tag{2.12}$$

And inversely,

$$\begin{bmatrix} f_a \\ f_b \\ f_c \end{bmatrix} = \begin{bmatrix} cos(\theta^c) & sin(\theta^c) & 1 \\ cos(\theta^c - \frac{2\pi}{3}) & sin(\theta^c - \frac{2\pi}{3}) & 1 \\ cos(\theta^c + \frac{2\pi}{3}) & sin(\theta^c + \frac{2\pi}{3}) & 1 \end{bmatrix} \begin{bmatrix} f^c_q \\ f^c_d \\ f^c_0 \end{bmatrix} \tag{2.13}$$

The transformation derivations are presented in Appendices C.1 – C.3.

#### 2.2.1.2 Phase locked loop

The PLL enables the rotation of the $qd$-frame by supplying the DQZ transformations with reference angle $\theta^c$, enabling the controller can work with DC quantities. Given that $u_d^c$ is the imaginary component, alignment by the PLL is achieved once $u_d^c = u_d^* = 0$. Assuming steady state equilibrium (i.e. $\theta^c = 0°$), $u_q^c$ and $u_d^c$ are as follows

$$u_q^c = Ucos(\theta^c) = Ucos(0) = U \tag{2.14}$$

$$u_d^c = Usin(\theta^c) = Usin(0) = 0 \tag{2.15}$$

The time domain implementation of the controller is presented in Fig. 2.12. The error, $\Delta u_d$ (where $\Delta u_d = u_d^* - u_d^c$) is processed by PI gains, outputting the change in frequency $\Delta\omega^c$. By adding $\Delta\omega^c$ to the base grid frequency ($2\pi 50$ rad/s), the instantaneous grid frequency is obtained. Integrating the instantaneous grid frequency results in the rotating angle $\theta^c$ to which the transformations are aligned.

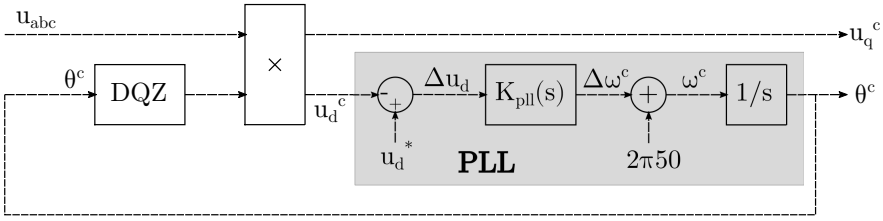


**Figure 2.12:** PLL and the PCC voltage transformation loop.

To obtain the transfer function of the PLL, it is necessary to linearise the PLL. This can be done by representing the input to the PLL as an angle rather than a voltage. Substituting $u_d^*$ with $Usin(\theta^*)$ and $u_d^c$ with $Usin(\theta^c)$, the error going into the PI gains is $\Delta u_d = Usin(\theta^*) - Usin(\theta^c)$. Assuming steady state, $u_d^*$ is very small, so $\theta^*$ is also very small, therefore $sin(\theta^*) \cong \theta^*$. Similarly, the angle $\theta^c$ is very small, thus $sin(\theta^c) \cong \theta^c$. Combining these assumptions and simplifications,

$$\Delta u_d \cong U(\theta^* - \theta^c) \tag{2.16}$$

Resulting in a linearised closed loop PLL system, presented in Fig. 2.13.

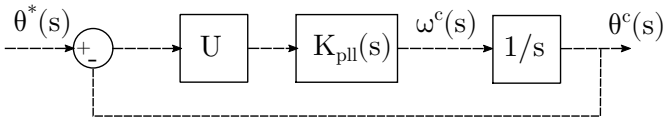


**Figure 2.13:** Simplified PLL representation.

Where

$$K_{pll}(s) = K_{p\,pll} + \frac{K_{i\,pll}}{s} = \frac{K_{p\,pll}s + K_{i\,pll}}{s} \tag{2.17}$$

Therefore, the PLL closed loop transfer function is

$$H_{pll\,CL}(s) = \frac{\theta^c(s)}{\theta^*(s)} = \frac{K_{pll}(s)U}{s + K_{pll}(s)U} = \frac{K_{p\,pll}Us + K_{i\,pll}U}{s^2 + K_{p\,pll}Us + K_{i\,pll}U} \tag{2.18}$$

Equation (2.18) is a second order transfer function [77]. Compared to the second order general form [78] (where $\zeta$ is the damping ratio and $\omega_b$ is the bandwidth)

$$H(s) = \frac{2\zeta\omega_b s + \omega_b^2}{s^2 + 2\zeta\omega_b s + \omega_b^2} \tag{2.19}$$

It can be determined that

$$K_{p\,pll} = \frac{2\zeta\omega_b}{U} \tag{2.20}$$

$$K_{i\,pll} = \frac{\omega_b^2}{U} \tag{2.21}$$

#### 2.2.1.3 Current controller

The objective of the current controller (also referred to as the inner loop) is to determine the converter voltage $v_{qd}^c$ required to obtain a particular current flowing through the RL filter. Consider the RL filter presented in Fig. 2.14, note the positive current direction from grid to converter.

Kirchoff's Voltage Law (KVL) across the filter dictates that

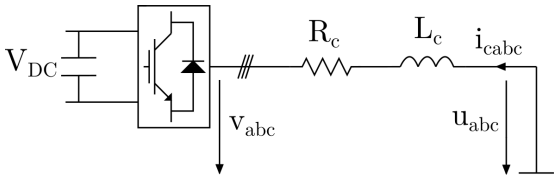


**Figure 2.14:** The converter filter.

$$u_{qd} - v_{qd} = R_c i_{cqd} + \frac{di_{cqd}}{dt} L_c \tag{2.22}$$

Taking the rotating frame into account, $v_{qd} = (v_q - jv_d)e^{j\omega t}$, $u_{qd} = (u_q - ju_d)e^{j\omega t}$ and $i_{cqd} = (i_{cq} - ji_{cd})e^{j\omega t}$

Differentiating $i_{cqd}$ gives:

$$\frac{d}{dt} i_{cqd} = j(i_{cq} - ji_{cd})\omega e^{j\omega t} + (\frac{d}{dt} i_{cq} - j\frac{d}{dt} i_{cd})e^{j\omega t} \tag{2.23}$$

Substituting (2.23) into (2.22) and separating real and imaginary components

$$\mathbb{Re}(u_{qd} - v_{qd}) = u_q - v_q = i_{cq}R_c + i_{cd}\omega L_c + \frac{d}{dt} i_{cq} L_c \tag{2.24}$$

$$\mathbb{Im}(u_{qd} - v_{qd}) = -u_d + v_d = -i_{cd}R_c + i_{cq}\omega L_c - \frac{d}{dt} i_{cd} L_c \tag{2.25}$$

By establishing the transfer functions of the filter, the current controller can be designed and optimised [79, 80]. In the Laplace domain and solved for $v_{qd}$

$$v_q = u_q - i_{cd}\omega L_c - i_{cq}(R_c + L_c s) \tag{2.26}$$

$$v_d = u_d + i_{cq}\omega L_c - i_{cd}(R_c + L_c s) \tag{2.27}$$

Mirroring these equations into the current controller,

$$v_q^c = u_q^c - i_{cd}^c \omega L_c - (i_{cq}^* - i_{cq}^c)\frac{K_{p\,cc}s + K_{i\,cc}}{s} \tag{2.28}$$

$$v_d^c = u_d^c + i_{cq}^c \omega L_c - (i_{cd}^* - i_{cd}^c)\frac{K_{p\,cc}s + K_{i\,cc}}{s} \tag{2.29}$$

it is possible to tune the current controller directly as a function of the filter parameters. Hence, relating the integral to the current controller time constant $\tau_{cc}$, the relationship between filter parameters and controller gains is

$$(K_{i\,cc} + K_{p\,cc}s)\tau_{cc} \propto (R_c + L_c s) \tag{2.30}$$

Thus,

$$K_{p\,cc} = \frac{L_c}{\tau_{cc}} \tag{2.31}$$

$$K_{i\,cc} = \frac{R_c}{\tau_{cc}} \tag{2.32}$$

The resulting current controller, complete with the RL filter dynamics in the form of block diagrams, can be seen in Fig. 2.15. For completeness, the current controller should be much faster than the outer loop in order to maintain separation of dynamics between the inner and outer control loops [81, 82].

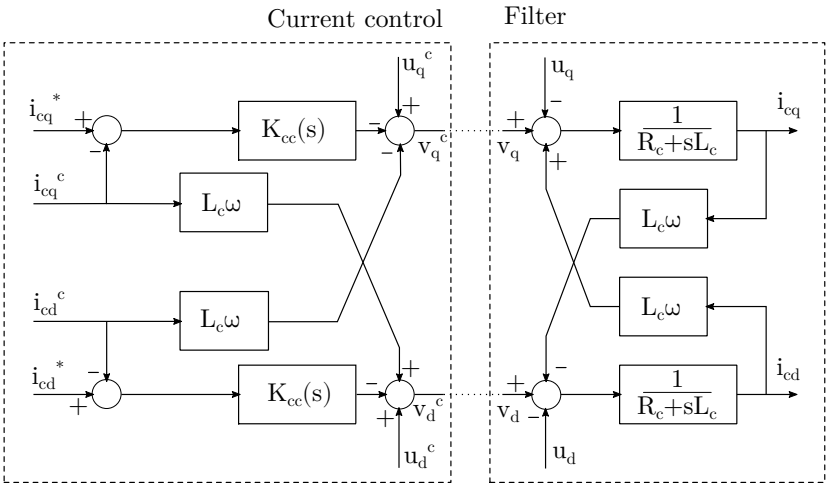


**Figure 2.15:** Control structure of current controller loop.

#### 2.2.1.4 Outer loop control

The outer loop control typically comprises of an active power loop, which determines the active current reference $i^*_{cq}$; and a reactive loop, which determines the reactive current reference $i^*_{cd}$. The active loop can be set to control either active power at the PCC or DC voltage in the DC link. The reactive loop can be used to control either reactive power at the PCC or PCC voltage magnitude. In this thesis, the outer loop is set to P-U control because, as shown in Section 2.1.1, the provision of reactive power to support the local voltage is absolutely necessary for stability. By tracking PCC voltage, the reactive outer loop provides the required reactive power. The controller block diagrams are presented in Fig. 2.16.

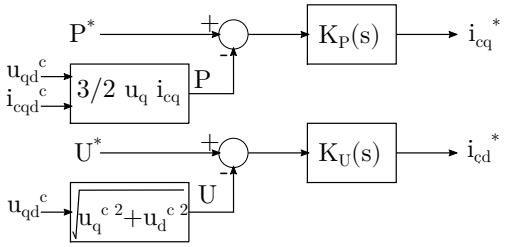


**Figure 2.16:** VCC outer loops.

The tuning of the outer loop is explained in more detail in Section 2.2.2.9, the linearised outer loop section, as small signal models are used for this purpose.

#### 2.2.1.5 Modelling discrete system delays

While real world converters are switched / discrete systems, it is acceptable to use continuous average voltage models to represent them. Continuous models are much faster to run and suffer less from noise. However, for improved accuracy, the average delay of a discrete system must be replicated. In the case of continuous time domain models, this is done with a transport delay block.

The delay represents the lag caused by the periodic sampling, and the discrete pulse width modulation (PWM). This results in a combined delay of 1.5 sampling periods, included at the output of the converter [83, 84] as per Fig. 2.17.

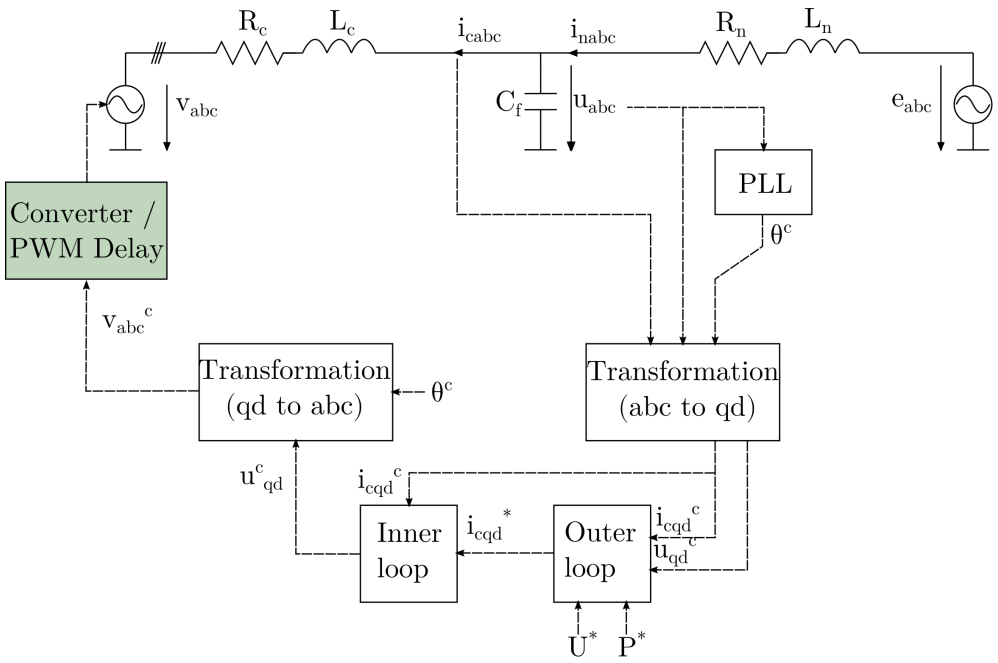


**Figure 2.17:** VCC delays.

### 2.2.2 Linearisation of Power Systems and Vector Current Control

#### 2.2.2.1 Introduction to dynamic systems

Dynamic systems, such as the power systems studied in this thesis, can be described using a set of $n$ ordinary differential equations (ODEs). Thus, the system is of $n^{th}$ order. It is a function of $r$ number of $u$ inputs, and $n$ number of states, $x$. $\dot{x}$ is the state derivative. The number of functions can be represented by subscript $i$, where $i = 1, 2, ..., n$. [85] Thus,

$$\dot{x}_i = f_i(x_1, ..., x_n; u_1, ..., u_r) \tag{2.33}$$

This can be simplified by using vector notation, $\dot{\boldsymbol{x}} = \boldsymbol{f}(\boldsymbol{x}.\boldsymbol{u})$, where $\boldsymbol{f} = [f_1, ..., f_n]^T$, $\boldsymbol{x} = [x_1, ..., x_n]^T$, $\boldsymbol{u} = [u_1, ..., u_r]^T$. Output variables, $y$, can be obtained using functions $g_j$, where $j = 1, ..., m$ such that $\boldsymbol{y} = \boldsymbol{g}(\boldsymbol{x}, \boldsymbol{u})$, where $\boldsymbol{y} = [y_1, ..., y_m]^T$ and $\boldsymbol{g} = [g_1, ..., g_m]^T$. [85]

#### 2.2.2.2 Linearisation of dynamic systems

These dynamic systems can be linearised around equilibrium points, satisfying $\boldsymbol{f}(\boldsymbol{x}_0)$. By linearising complex power systems, stability assessment and optimisation is possible with classical control tools. The system in equilibrium can therefore be represented as $\dot{\boldsymbol{x}}_0 = \boldsymbol{f}(\boldsymbol{x}_0, \boldsymbol{u}_0) = 0$. [85]

Any deviation from the equilibrium assumes that the deviations are sufficiently small that the linear priorities are maintained, therefore the state, input and state derivative vectors become a function of the initial conditions and a small perturbation, $\Delta x$ and $\Delta u$: $\boldsymbol{x} = \boldsymbol{x}_0 + \boldsymbol{\Delta x}$, and $\boldsymbol{u} = \boldsymbol{u}_0 + \boldsymbol{\Delta u}$. [85] Thus,

$$\dot{\boldsymbol{x}} = \dot{\boldsymbol{x}}_0 + \boldsymbol{\Delta}\dot{\boldsymbol{x}} = \boldsymbol{f}[(\boldsymbol{x}_0 + \boldsymbol{\Delta x}), (\boldsymbol{u}_0 + \boldsymbol{\Delta u})] \tag{2.34}$$

Given that $\boldsymbol{\Delta x}$ and $\boldsymbol{\Delta u}$ are small, it is acceptable to simply Taylor's series expansion to a first order system. As such, it can be shown that

$$\boldsymbol{\Delta}\dot{\boldsymbol{x}}_i = \frac{\partial f_i}{\partial x_1}\Delta x_1 + ... + \frac{\partial f_i}{\partial x_n}\Delta x_n + \frac{\partial f_i}{\partial u_1}\Delta u_1 + ... + \frac{\partial f_i}{\partial u_r}\Delta u_r \tag{2.35}$$

and similarly,

$$\boldsymbol{\Delta y}_j = \frac{\partial g_j}{\partial x_1}\Delta x_1 + ... + \frac{\partial g_j}{\partial x_n}\Delta x_n + \frac{\partial g_j}{\partial u_1}\Delta u_1 + ... + \frac{\partial g_j}{\partial u_r}\Delta u_r \tag{2.36}$$

#### 2.2.2.3 Small signal studies

The equations produced by the Taylor series expansion is best described in matrix form, the standard linearised state space representation of power systems [85–87]:

$$\begin{aligned} \boldsymbol{\Delta}\dot{\boldsymbol{x}} &= \boldsymbol{A}\boldsymbol{\Delta x} + \boldsymbol{B}\boldsymbol{\Delta u} \\ \boldsymbol{\Delta y} &= \boldsymbol{C}\boldsymbol{\Delta x} + \boldsymbol{D}\boldsymbol{\Delta u} \end{aligned} \tag{2.37}$$

where $\boldsymbol{x}$ is the state vector; $\boldsymbol{u}$ is the input vector; $\boldsymbol{y}$ is the output vector; $\boldsymbol{A}$ is the state or system matrix; $\boldsymbol{B}$ is the input matrix; $\boldsymbol{C}$ is the output matrix; and $\boldsymbol{D}$ is the

feedforward matrix. The matrices contain the partial derivatives, as per (2.38) – (2.41).

$$\boldsymbol{A} = \begin{bmatrix} \frac{\partial f_1}{\partial x_1} & \dots & \frac{\partial f_1}{\partial x_n} \\ \dots & \dots & \dots \\ \frac{\partial f_n}{\partial x_1} & \dots & \frac{\partial f_n}{\partial x_n} \end{bmatrix} \tag{2.38}$$

$$\boldsymbol{B} = \begin{bmatrix} \frac{\partial f_1}{\partial u_1} & \dots & \frac{\partial f_1}{\partial u_r} \\ \dots & \dots & \dots \\ \frac{\partial f_n}{\partial u_1} & \dots & \frac{\partial f_n}{\partial u_r} \end{bmatrix} \tag{2.39}$$

$$\boldsymbol{C} = \begin{bmatrix} \frac{\partial g_1}{\partial x_1} & \dots & \frac{\partial g_1}{\partial x_n} \\ \dots & \dots & \dots \\ \frac{\partial g_m}{\partial x_1} & \dots & \frac{\partial g_m}{\partial x_n} \end{bmatrix} \tag{2.40}$$

$$\boldsymbol{D} = \begin{bmatrix} \frac{\partial g_1}{\partial u_1} & \dots & \frac{\partial g_1}{\partial u_r} \\ \dots & \dots & \dots \\ \frac{\partial g_m}{\partial u_1} & \dots & \frac{\partial g_m}{\partial u_r} \end{bmatrix} \tag{2.41}$$

The state space equations are graphically represented in Fig. 2.18.

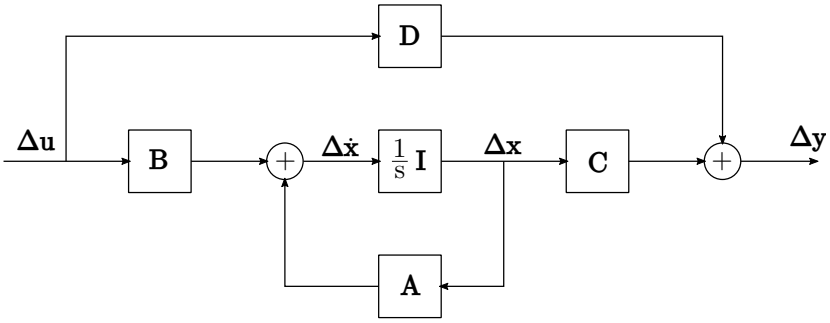


**Figure 2.18:** Graphical representation of the state space equations.

#### 2.2.2.4 Closed loop transfer matrix

The closed loop transfer matrix, Fig. 2.19, is based on [45, 88] and is used extensively in the small signal (state space) studies of this thesis. The matrix includes all the linearised components of the grid and controller, including the PLL, transforms, current controller, outer loop and delays. The inputs are the active power and PCC voltage magnitude references, and the outputs are the measured active power and PCC voltage magnitude. This set of inputs and outputs is chosen because it includes all aspects of this controller, including the outer loop, in the assessment of stability.

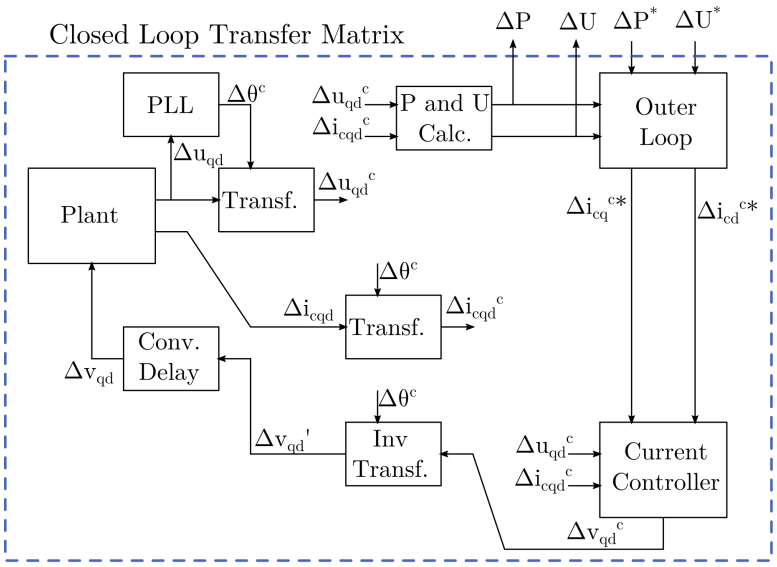


**Figure 2.19:** Closed loop transfer matrix: representation of the combined linearised plant and controller system.

Every block in Fig. 2.19 represents an individual small signal model, as per the format described in (2.18).

In this thesis, the closed loop transfer matrix uses $[\Delta P^* \ \Delta U^*]^T$ as inputs and $[\Delta P \ \Delta U]^T$ as outputs. To represent the open loop system, the inputs are changed to $[\Delta P_{error} \ \Delta U_{error}]^T$ where $[\Delta P_{error} \ \Delta U_{error}]^T = [\Delta P^* \ \Delta U^*]^T - [\Delta P \ \Delta U]^T$.

#### 2.2.2.5 Linearised Electrical System

The plant state space system is obtained by considering Kirchoff's Voltage Law across the converter filter and grid impedances, as well as Kirchoff's Current Law at the PCC

node [44, 45].

KVL across the converter impedance

$$\Delta u_{qd} - \Delta v_{qd} = R_c \Delta i_{cqd} + \frac{d}{dt} \Delta i_{cqd} L_c \tag{2.42}$$

Separating real and imaginary

$$\frac{d}{dt} \Delta i_{cq} = \Delta i_{cq} \frac{R_c}{L_c} - \Delta i_{cd} \omega + \Delta u_q \frac{1}{L_c} - \Delta v_q \frac{1}{L_c} \tag{2.43}$$

$$\frac{d}{dt} \Delta i_{cd} = \Delta i_{cq} \omega + \Delta i_{cd} \frac{R_c}{L_c} + \Delta u_d \frac{1}{L_c} - \Delta v_d \frac{1}{L_c} \tag{2.44}$$

KCL at the PCC node

$$\Delta i_{nqd} - \Delta i_{cqd} = \frac{d}{dt} \Delta u_{qd} C_f \tag{2.45}$$

Resulting in

$$\frac{d}{dt} \Delta u_q = -\Delta i_{cq} \frac{1}{C_f} - \Delta u_d \omega + \Delta i_{nq} \frac{1}{C_f} \tag{2.46}$$

$$\frac{d}{dt} \Delta u_d = -\Delta i_{cd} \frac{1}{C_f} + \Delta u_q \omega + \Delta i_{nd} \frac{1}{C_f} \tag{2.47}$$

KVL across the grid impedance

$$\Delta v_{qd} - \Delta e_{qd} = R_n \Delta i_{nqd} + \frac{d \Delta i_{nqd}}{dt} L_n \tag{2.48}$$

Resulting in

$$\frac{d}{dt} \Delta i_{nq} = -\Delta i_{nq} \frac{R_n}{L_n} - \Delta i_{nd} \omega + \Delta e_q \frac{1}{L_n} - \Delta u_q \frac{1}{L_n} \tag{2.49}$$

$$\frac{d}{dt} \Delta i_{nd} = +\Delta i_{nq} \omega - \Delta i_{nd} \frac{R_n}{L_n} + \Delta e_d \frac{1}{L_n} - \Delta u_d \frac{1}{L_n} \tag{2.50}$$

By combining (2.44) to (2.50), the state space system is

$$\frac{d}{dt}\begin{bmatrix}\Delta i_{cq}\\ \Delta i_{cd}\\ \Delta u_q\\ \Delta u_d\\ \Delta i_{nq}\\ \Delta i_{nd}\end{bmatrix} = \begin{bmatrix} -\frac{R_c}{L_c} & -\omega & \frac{1}{L_c} & 0 & 0 & 0\\ \omega & -\frac{R_c}{L_c} & 0 & \frac{1}{L_c} & 0 & 0\\ -\frac{1}{C_f} & 0 & 0 & -\omega & \frac{1}{C_f} & 0\\ 0 & -\frac{1}{C_f} & \omega & 0 & 0 & \frac{1}{C_f}\\ 0 & 0 & -\frac{1}{L_n} & 0 & -\frac{R_n}{L_n} & -\omega\\ 0 & 0 & 0 & -\frac{1}{L_n} & \omega & -\frac{R_n}{L_n}\end{bmatrix}\begin{bmatrix}\Delta i_{cq}\\ \Delta i_{cd}\\ \Delta u_q\\ \Delta u_d\\ \Delta i_{nq}\\ \Delta i_{nd}\end{bmatrix} + \begin{bmatrix} -\frac{1}{L_c} & 0 & 0 & 0\\ 0 & -\frac{1}{L_c} & 0 & 0\\ 0 & 0 & 0 & 0\\ 0 & 0 & 0 & 0\\ 0 & 0 & \frac{1}{L_n} & 0\\ 0 & 0 & 0 & \frac{1}{L_n}\end{bmatrix}\begin{bmatrix}\Delta v_q\\ \Delta v_d\\ \Delta e_q\\ \Delta e_d\end{bmatrix} \tag{2.51}$$

$$\begin{bmatrix}\Delta i_{cq}\\ \Delta i_{cd}\\ \Delta u_q\\ \Delta u_d\\ \Delta U\\ \Delta P\end{bmatrix} = \begin{bmatrix} 1 & 0 & 0 & 0 & 0 & 0\\ 0 & 1 & 0 & 0 & 0 & 0\\ 0 & 0 & 1 & 0 & 0 & 0\\ 0 & 0 & 0 & 1 & 0 & 0\\ 0 & 0 & \frac{u_{q0}}{U_{LN\ peak}} & \frac{u_{d0}}{U_{LN\ peak}} & 0 & 0\\ \frac{3}{2}u_{q0} & \frac{3}{2}u_{d0} & \frac{3}{2}i_{cq0} & \frac{3}{2}i_{cd0} & 0 & 0\end{bmatrix}\begin{bmatrix}\Delta i_{cq}\\ \Delta i_{cd}\\ \Delta u_q\\ \Delta u_d\\ \Delta i_{nq}\\ \Delta i_{nd}\end{bmatrix} \tag{2.52}$$

The grid frame active power and PCC voltage magnitude, included in the state space system above, are also presented below in (2.53) and (2.54)

$$\Delta U = \frac{d}{dt}\sqrt{u_q^2+u_d^2} = \frac{u_{q0}\Delta u_q}{\sqrt{u_q^2+u_d^2}} + \frac{u_{d0}\Delta u_d}{\sqrt{u_q^2+u_d^2}} = \frac{u_{q0}\Delta u_q}{U} + \frac{u_{d0}\Delta u_d}{U} \tag{2.53}$$

$$\Delta P = \frac{d}{dt}\left(\frac{3}{2}i_{cq}u_q + \frac{3}{2}i_{cd}u_d\right) = \frac{3i_{cq0}\Delta u_q}{2} + \frac{3i_{cd0}\Delta u_d}{2} + \frac{3u_{q0}\Delta i_{cq}}{2}\frac{3u_{d0}\Delta i_{cd}}{2} \tag{2.54}$$

The converter frame power and PCC voltages can also be obtained using a separate state space system, comprising of the same equations but with the converter frame inputs.

#### 2.2.2.6 Linearised Transformations

The linearised transformations capture the lag in angle between the grid $qd$-frame and the controller $qd$-frame for a given PLL angle $\theta^c$. This accounts for the rotation and results in the following for three phase signal $f$

$$\begin{bmatrix} f_q^c \\ f_d^c \end{bmatrix} = \begin{bmatrix} cos(\theta^c) & -sin(\theta^c) \\ sin(\theta^c) & cos(\theta^c) \end{bmatrix} \quad \begin{bmatrix} f_q \\ f_d \end{bmatrix} \tag{2.55}$$

And inversely,

$$\begin{bmatrix} f_q \\ f_d \end{bmatrix} = \begin{bmatrix} cos(\theta^c) & sin(\theta^c) \\ -sin(\theta^c) & cos(\theta^c) \end{bmatrix} \quad \begin{bmatrix} f_q^c \\ f_d^c \end{bmatrix} \tag{2.56}$$

To linearise, the above equations are differentiated

$$\begin{bmatrix} \Delta f_q^c \\ \Delta f_d^c \end{bmatrix} = \begin{bmatrix} cos(\theta_0) & -sin(\theta_0) & [-sin(\theta_0)f_{q0} - cos(\theta_0)f_{d0})] \\ sin(\theta_0) & cos(\theta_0) & [cos(\theta_0)f_{q0} - sin(\theta_0)f_{d0})] \end{bmatrix} \quad \begin{bmatrix} \Delta f_q \\ \Delta f_d \\ \Delta \theta^c \end{bmatrix} \tag{2.57}$$

And inversely,

$$\begin{bmatrix} \Delta f_q \\ \Delta f_d \end{bmatrix} = \begin{bmatrix} cos(\theta_0) & sin(\theta_0) & [-sin(\theta_0)f_{q0} + cos(\theta_0)f_{d0})] \\ -sin(\theta_0) & cos(\theta_0) & [-cos(\theta_0)f_{q0} - sin(\theta_0)f_{d0})] \end{bmatrix} \quad \begin{bmatrix} \Delta f_q^c \\ \Delta f_d^c \\ \Delta \theta^c \end{bmatrix} \tag{2.58}$$

#### 2.2.2.7 Linearised PLL

The purpose of the linearised PLL transfer function [44] is to reproduce the synchronisation angle $\theta^c$ which is also responsible for the transformation lag between the grid frame and the converter frame. Given that

$$\Delta\theta^c = -(K_{p\,pll} + \frac{K_{i\,pll}}{s})\frac{1}{s}[\Delta u_q sin(\theta_0) + \Delta u_d cos(\theta_0) + \Delta\theta^c\{cos(\theta_0)u_{q0} - sin(\theta_0)u_{d0}\}] \tag{2.59}$$

As $u_{d0}$ is zero, $\theta_0$ is zero, and that angle $\Delta\theta^c$ is small such that $cos(\Delta\theta^c) \approx 1$, the above equation reduces to

$$\Delta\theta^c = -(K_{p\,pll} + \frac{K_{i\,pll}}{s})\frac{1}{s}(\Delta u_d + \Delta\theta^c u_{q0}) \tag{2.60}$$

Rearrange into open loop transfer function form

$$G_{PLL}(s) = \frac{\Delta\theta^c}{\Delta u_d} = -\frac{K_{p\,pll}s + K_{i\,pll}}{s^2 + K_{p\,pll}u_{q0}s + K_{i\,pll}u_{q0}} \tag{2.61}$$

With this transfer function, the value $\Delta\theta^c$ can be calculated and provided to all the Park and Inverse Park transformations in the model.

#### 2.2.2.8 Linearised Current Controller

The previously mentioned the inner current control loop equations

$$v_q^c = -(i_{cq}^* - i_{cq}^c)(K_{p\,cc} + \frac{K_{i\,cc}}{s}) - \omega L_c + u_q^c \tag{2.62}$$

$$v_d^c = -(i_{cd}^* - i_{cd}^c)(K_{p\,cc} + \frac{K_{i\,cc}}{s}) + \omega L_c + u_d^c \tag{2.63}$$

can be represented in state space, as follows:

$$\frac{d}{dt}\begin{bmatrix}\Delta v_q^c \\ \Delta v_d^c\end{bmatrix} = \begin{bmatrix}-1 & 0 & 1 & 0 & 0 & 0 \\ 0 & -1 & 0 & 1 & 0 & 0\end{bmatrix}\begin{bmatrix}\Delta i_{cq}^* \\ \Delta i_{cd}^* \\ \Delta i_{cq}^c \\ \Delta i_{cd}^c \\ \Delta u_q^c \\ \Delta u_d^c\end{bmatrix} \tag{2.64}$$

$$\begin{bmatrix} \Delta v_q^c \\ \Delta v_d^c \end{bmatrix} = \begin{bmatrix} K_{i\,cc} & 0 \\ 0 & K_{i\,cc} \end{bmatrix} \begin{bmatrix} \Delta v_q^c \\ \Delta v_d^c \end{bmatrix} + \begin{bmatrix} -K_{p\,cc} & 0 & K_{p\,cc} & -\omega L_c & 1 & 0 \\ 0 & -K_{p\,cc} & \omega L_c & K_{p\,cc} & 0 & 1 \end{bmatrix} \begin{bmatrix} \Delta i_{cq}^* \\ \Delta i_{cd}^* \\ \Delta i_{cq}^c \\ \Delta i_{cd}^c \\ \Delta u_q^c \\ \Delta u_d^c \end{bmatrix} \tag{2.65}$$

#### 2.2.2.9 Linearised Outer Loop

As previously seen in Section 2.2.1.4, the outer loop equations are

$$i_{cq}^* = (P^* - P)K_P(s) \tag{2.66}$$

$$i_{cd}^* = (U^* - U)K_U(s) \tag{2.67}$$

Utilising the general formulation of state space equations to represent the outer loop

$$\frac{d}{dt} \begin{bmatrix} \Delta i_{cq}^* \\ \Delta i_{cd}^* \end{bmatrix} = \begin{bmatrix} K_{i\,p} & 0 \\ 0 & K_{i\,u} \end{bmatrix} \begin{bmatrix} \Delta P^* - \Delta P \\ \Delta U^* - \Delta U \end{bmatrix} \tag{2.68}$$

$$\begin{bmatrix} \Delta i_{cq}^* \\ \Delta i_{cd}^* \end{bmatrix} = \begin{bmatrix} 1 & 0 \\ 0 & 1 \end{bmatrix} \begin{bmatrix} \Delta i_{cq}^* \\ \Delta i_{cd}^* \end{bmatrix} + \begin{bmatrix} K_{p\,p} & 0 \\ 0 & K_{p\,u} \end{bmatrix} \begin{bmatrix} \Delta P^* - \Delta P \\ \Delta U^* - \Delta U \end{bmatrix} \tag{2.69}$$

##### 2.2.2.9.1 Tuning of the outer loop

While the tuning of the PLL and the current controller is determined mathematically via the assignment of a time constant, the tuning of the outer loop is much more complicated due to the multi-input multi-output (MIMO) nature of the control loop. Furthermore, there is an increased coupling between active power and voltage experienced in weak grid networks. As a result, the tuning of the two loops must be done in

tandem, and careful consideration is required. For VCC operating in weak grid conditions, stability is usually obtained by reducing the converter bandwidth [34–36, 38, 89], thus maintaining a stable local voltage (as per Fig. 2.4).

In [88], it is the power loop settling time that is used to assess the controller's dynamic performance, with the target settling time set to $< 750$ ms. For completeness, the settling time is defined as the time required for the error to fall beneath 2 % of the peak value of the error. Similarly, the rise time could also be used as a measure of the controller response, where the rise time is the time taken to rise from 10 % to 90 % of the steady state response.

The outer loop control fixed-structure tuning is undertaken by processing the linearised system with a non-smooth optimization using the Clarke subdifferential of the H-infinity objective [90]. The system is linearised at SCR of 3 and at a power point of -1 pu. -1 pu of power is sensible for wind turbine and wind farm stability analysis because this is the most unstable inversion power point (eigenvalues are furthest to the right); and rectification can be disregarded as RES do not operate as rectifiers for sustained periods. The tuning objectives is for the power loop to have a time constant of 0.02 s and the voltage loop time a constant of 0.06 s. The resulting gains are then verified in EMT simulations to test impact of nonlinearities.

#### 2.2.2.10 Linearised Delays

As previously explained, the delay is of 1.5 sampling periods. The transport delay employed in the time domain model is replaced in the small signal model with a $4^{th}$ order Padé approximation. A $4^{th}$ order is used as it is more similar to the transport delay than lower order approximations.

$$D(s) = \frac{s^4 - 6.67e^5 s^3 + 2e^9 s^2 - 3.11e^{14} s + 2.074e^{18}}{s^4 + 6.67e^5 s^3 + 2e^9 s^2 + 3.11e^{14} s + 2.074e^{18}} \tag{2.70}$$

#### 2.2.2.11 Validation of small signal models

To validate the small signal model, it is directly compared to an equivalent time domain model. This is presented in Fig. 2.20 where the SCR is 3 and the operating point is

$P = -1$ pu. The parameters used are outlined in Appendix A, Sections A.1 and A.1.1.1.

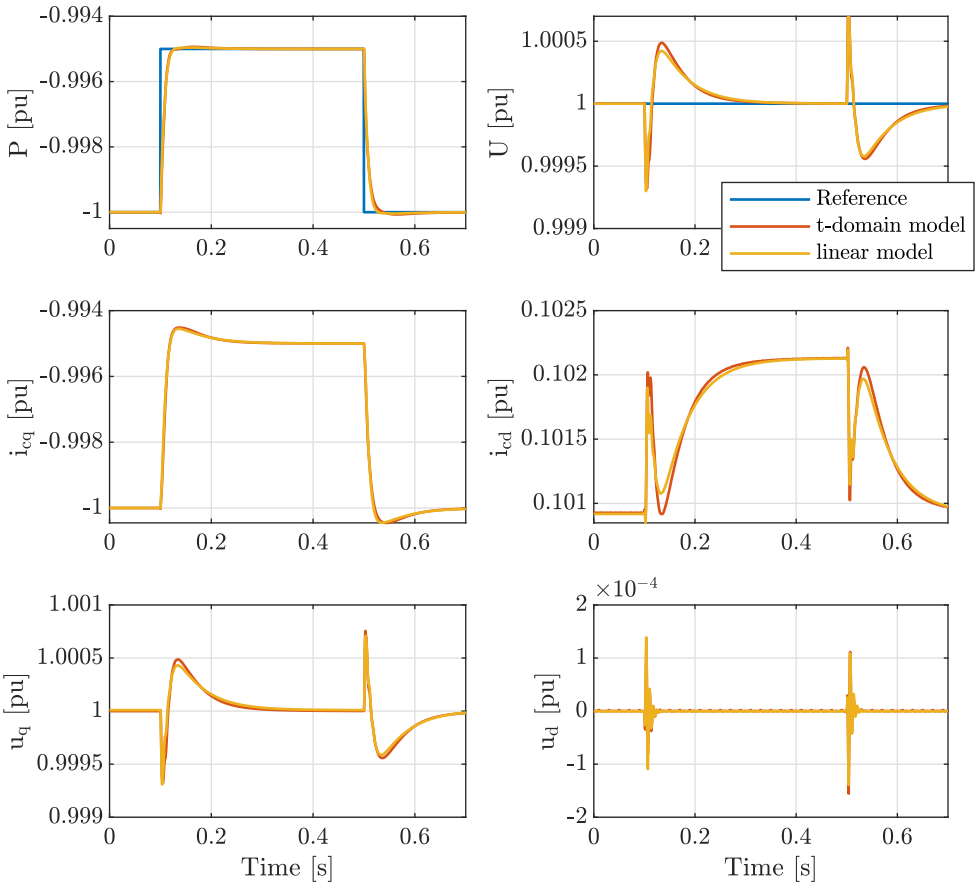


**Figure 2.20:** Validation of linearised model by comparing simulation results to time domain model.

As illustrated in Fig. 2.20, the small signal and time domain models match very well when subjected to the same change in power reference. Thus, the two models are equivalent to one another and further studies using the small signal model can be undertaken.

### 2.2.3 State-of-the-art of converter control in weak grids

The most common form of converter control is classical VCC (VCC without any unusual modifications) [91]. While classical VCC has been the industry standard for many

decades, concern over it's poor performance in weak grids is growing as converters continue to face weak and variable grid conditions. In the literature, proposals to improve converter stability in weak networks can be categorised into three groups: VCC modification, synchonisation mechanism modification, and novel control concepts. These solutions are summarised in Table 2.2.

#### 2.2.3.1 VCC modification

VCC modification involves adapting one or more aspects of the classical VCC structure. Ideally, VCC modification should preserve the inherent current limiting capabilities [38] and fast dynamic response [108] of classical VCC. In the literature, there are two main approaches: modification of the current controller or modification of the outer loop. In [92], the current controller is tuned in real time to the grid conditions by using an impedance estimator, where the current controller proportional and integral gains are re-calculated for every inductance estimation such that the undamped natural frequency and damping ratio of the current controller remains constant. [93] uses a different approach by introducing phase and magnitude compensation branches, making changes to the PLL angle and the modulation reference voltage, respectively, based on the outer loop output. The problem with this idea is that the magnitude compensation branch bypasses the current controller, affecting the controller's overcurrent protection capabilities.

With regards to outer loop modifications, a number of papers propose variations on voltage feedforward, such that the reactive current reference [94–97], and sometimes also the active current reference [96], are amended as a result of voltage measurements. These papers follow a similar pattern: take either the voltage magnitude, the reactive voltage component, the voltage magnitude error or the drop in voltage across the converter filter; process it through a coefficient, a bandpass filter, or a transfer function; and then add it to the reactive current reference [94–97]. In essence, these proposals provide additional voltage support by increasing the reactive current reference as a function of voltage. However, the voltage support is reactionary, as it is dependent on voltage measurements only. Thus, while these proposals may improve the stability

**Table 2.2:** Summary of converter control proposals for weak grid integration

| Ref | Feature | Details | Comments |
|---|---|---|---|
| | | VCC modification | |
| [92] | Current controller mod. | Online tuning via grid inductance estimation | Fundamental change to current controller purpose |
| [93] | Current controller bypass | Bypass of current controller | Loss of current limiting features of VCC |
| [94–97] | Outer loop modification | Voltage feedforward | Reactionary to power and voltage coupling |
| [46] | Outer loop modification | H-infinity controller | Successful decoupling of power and voltage; stationary grid conditions |
| [98] | Outer loop modification | Active power reference feedforward | Sensitive to outer loop tuning and not suited to large impedance variation |
| [99] | PLL and dc-link compensation | Removal of PCC voltage impact on by increasing impedance | Unclear benefit to transient performance |
| [102] | Reshaping impedance | Impedance controller and voltage feedforward | Unclear benefit to transient performance |
| | | Synchronisation mechanism modification | |
| [93] | PLL modification | PLL angle manipulation | Slower PLL |
| [89, 100] | PLL modification | Introduction of virtual impedance | Increases local voltage fluctuations, controller slow |
| [101] | PLL modification | Real-time tuning of PLL gains | PLL bandwidth affected |
| [33] | PLL removal | Power calculation and equation based $\alpha\beta$-$dq$ transformation | Inconsistent use of band-pass filtering |
| [35] | PLL modification | Merging PLL and power controller | Slow power response |
| [103] | FLL | Synchronisation to frequency | Impact to stability unclear from paper |
| | | Novel control concepts | |
| [45] | Power Synchronisation Controller | Swing equation based, no PLL | Slower than VCC, poor response to voltage sags and impedance variation |
| [104] | Synchroverters | High fidelity imitation of synchronous machines | Complex and doesn't consider converter limitations |
| [105–107] | VSM | Swing equation based | Similar comments to PSC |

of the converter, their ability to improve the dynamic performance of VCC is limited because they can only provide voltage support as a response to measured changes in voltage.

The other interesting proposals in the literature involves modification of the outer loop. The H-infinity controller in [46] is academically very interesting given the effective decoupling capabilities the controller.

An improvement on voltage feedforward is presented in [46], which proposes a gain-scheduled multi-variable controller. This technique is promising because it maintains high controller bandwidth in a very weak grid due to its highly optimised tuning. Another article, [98], proposes another alternative with a feedforward branch that amends the reactive current reference based on the active power reference. Both [46, 47] show promise because these are outer loop-based solutions that attempt to integrate some predictive component by considering more than just voltage measurements. However, they also have drawbacks, namely: [46] is highly optimised to (and therefore limited to) a SCR of 1, which is impractical. The tuning is undertaken via small signal optimisation and the gains are gain scheduled for every operating point. An improvement would be to provide a scientific explanation for the assignment of gains in the outer loop cross coupling. [98] is sensitive to the tuning of the active outer loop as the power reference is processed by both the feedforward element and the active power loop simultaneously. Also, it does not address the impact of large SCR variations and does not take advantage of PCC voltage measurements or any other grid parameters. Thus, there is a gap in the literature and potential for new contributions at an outer loop level.

#### 2.2.3.2 Synchonisation mechanism modification

The synchronisation to an artificial voltage via a virtual impedance within the PLL is proposed in [89]. Instead of synchronising to the voltage as per the standard PLL implementation, the current is also taken into account. Using KVL, the virtual voltage is achieved by considering the measured PCC current as well as the virtual impedance, hence resulting in a virtual voltage. While the bandwidth of the power loop in [89]

does not appear to be significantly affected, the figures in the article appear to show a reduction in voltage loop response with increased PCC voltage fluctuations. A very similar article [100] uses a similar voltage and current based PLL, but estimates the equivalent inductance of the grid in order to produce a virtual synchronisation voltage. While stability is improved, the controller is shown to be very slow.

Another PLL adaptation technique is proposed in [101], where the PLL gains are directly modified depending on the results of the grid impedance estimation. Such intervention directly affects the PLL bandwidth. Another paper, [103], suggests synchronising to the voltage frequency instead of the angle. The main motivation in this paper is the loss of synchronisation during large fault scenarios, however it is unclear how the converter's stability and dynamic capabilities are affected in low and variable SCR conditions.

From the above described articles, modifications to the PLL generally affect the controller bandwidth. The PLL determines the synchronisation angle employed by the entire controller, thus any reduction in PLL dynamic capabilities affects the entire controller. While this may be effective at avoiding instability, it compromises the controller's responsiveness.

#### 2.2.3.3 Novel control concepts

Many novel controllers are inspired by conventional synchronous generators and replicate their grid forming capabilities. The level of fidelity to synchronous generator mechanics varies with different grid forming implementations. For example, power synchronous controller (PSC) [45] synchronises to the power instead of voltage assuming a simplified swing equation. On the other hand, the synchoverters [104] mimics synchronous generators to a much higher level of fidelity. In-between these extremes, there are various implementations of virtual synchronous machines (VSMs) which are swing equation-based [105–107]. Collectively, these can be described as grid forming converters, mimicking voltage swing. The challenges facing grid forming control includes the loss of inherent overcurrent protection capabilities [109] and difficulty with fault handling [110]. In addition, multiple grid-forming converters in weak networks

may introduce other unintended stability problems, such as swing-equation induced inter-converter interactions [111, 112]. Grid forming converters are still in early stages of development but they are beginning to gain some industrial interest, as presented in this paper [106] from Siemens Gamesa, which have undertaken field experiments on a Scottish wind farm. Drawbacks from these types of controllers are outlined in [113], for instance slower responses in normal operating conditions, reduced robustness to voltage sags and impedance variability.

#### 2.2.3.4 Gaps in the existing literature

The stability of classical VCC can be improved in weak grids with appropriate tuning, but usually as a trade-off with of dynamic performance. Considering that the grid side converter of a wind turbine controls the DC-bus voltage, a reduced bandwidth will affect the management of the DC link voltage. However, stiff DC voltage is necessary for good generator side stability, which in turn prevents insulation deterioration [28]. Therefore, slow grid side converters negatively impact the lifespan of the generation asset. In addition, wind farms are increasingly required to provide frequency response [114], which requires a fast response from the grid side converter.

Reducing VCC bandwidth, as applied in the above mentioned literature, is an attempt to resolve a symptom of weak grid integration of VCC, namely voltage instability. Indeed, by reducing the response of the active power loop, the reactive voltage loop is more able to stabilise PCC voltage. However, limited research seeks to determine the root cause of VCC instability in weak grids. It is shown in [46] that targeted changes in the control algorithm can result in both fast response and stability in very weak grid conditions. Despite being unsuitable for real-world implementation due to its assumption of stationary grid conditions, it does suggest that alternative approaches to VCC integration in weak grids is possible. Thus, this thesis aims to fill the gap and propose a mechanism to compensate for the increased coupling between active power and PCC voltage in weak grids, as per Chapter 4.

This leads to the next gap in the existing literature – few papers studying the integration of VCC in weak grids consider employing an impedance estimator in order

to optimise the controller despite the impact of grid impedance on converter stability. Existing examples are: [92], which tunes the current controller to the grid inductance; [100, 101], which tune the PLL to the grid impedance; and [101], which looks at feedforwarding voltage past the current controller as a function of grid inductance. Other papers mention adaptive control in passing, but do not provide detail on how the controller performance and/or stability is improved; rather, the focus is on the estimation technique [115–119]. Thus, further work is required to combine impedance estimation and VCC improvements to allow for real-time optimisation to the evolving grid conditions.

Furthermore, while few articles study modest variations in grid conditions, fewer still consider large step changes in grid strength, for instance due to the loss of a critical transmission line. The exception is [89,97]. This thesis proposes a suite of VCC modifications to improve the resilience of VCC in such conditions, as per Chapter 5.

### 2.2.4 State-of-the-art of converter control in resonant grids

The issue of resonances within the grid is usually discussed in the context of electrical networks and physical hardware rather than individual converters or control strategies. For example, [69,120] discuss the analysis techniques used to identify and study resonances, and [66, 121–123] study the design and selection of hardware components such as shunt capacitances and harmonic filtering.

Most articles that do discuss resonances in grids assume Thévenin equivalent impedance grids, often studying LCL and LC filter resonances in weak grids [82,124–126]. However, as the resonances are a function of filter design rather than unforeseen capacitance within the grid, it is not relevant in this case. Nonetheless, there is a small selection of papers that do discuss how converter control can help mitigate problematic resonances caused by the presence of capacitance within the grid. Specifically, [127] discusses how resonances within a high voltage transmission system in China can be reduced or eliminated thanks to a range of measures, including both hardware considerations and improved control strategy of the VSC HVDC terminals. On a smaller scale, resonances caused by the shunt capacitance of cables within a wind farm can

be mitigated when appropriate notch filters are introduced in the current control of individual wind turbines [67].

Given the increasing variability of grid impedances as seen from the PCC of RES, compounded by increases in grid infrastructure that contains capacitive elements, it is likely that resonances caused by a high order grid impedance will become increasingly problematic. As almost all RES are converter interfaced, it is reasonable to expect converters to participate in the damping of these resonances.

## 2.3 Study of VCC in weak grids

### 2.3.1 Steady state stability

In this section, both steady state stability and transient stability of classical VCC are studied. Steady state stability is assessed using incremental steps in the time domain or using linearised state space models in the frequency domain. Transient stability are most easily studied in the time domain, where the system is subjected to large changes in operating points or parameters.

#### 2.3.1.1 Steady state stability

To test steady state stability, the system is made to settle at various power levels. While the steps are themselves not steady state, they are sufficiently incremental to allow fast settling. This them an acceptable proxy for steady state stability, as previously demonstrated in [46, 96]. This is replicated in Fig. 2.21a and 2.21b for a strong grid and a weak grid, respectively.

The plots presented in Fig. 2.21 illustrate how increasing the active power injected into the network further increases oscillatory response, as the small steps in power only introduce small transient instability. The figures also illustrate the relationship between power angle and stability, as small steps in power in a weak grid demand much larger steps in power angle than the equivalent strong grid model.

Using the linearised model outlined in Section 2.2.2.4 (see the closed loop transfer matrix, Fig. 2.19, for an outline of the system), eigenvalue analysis can be undertaken.

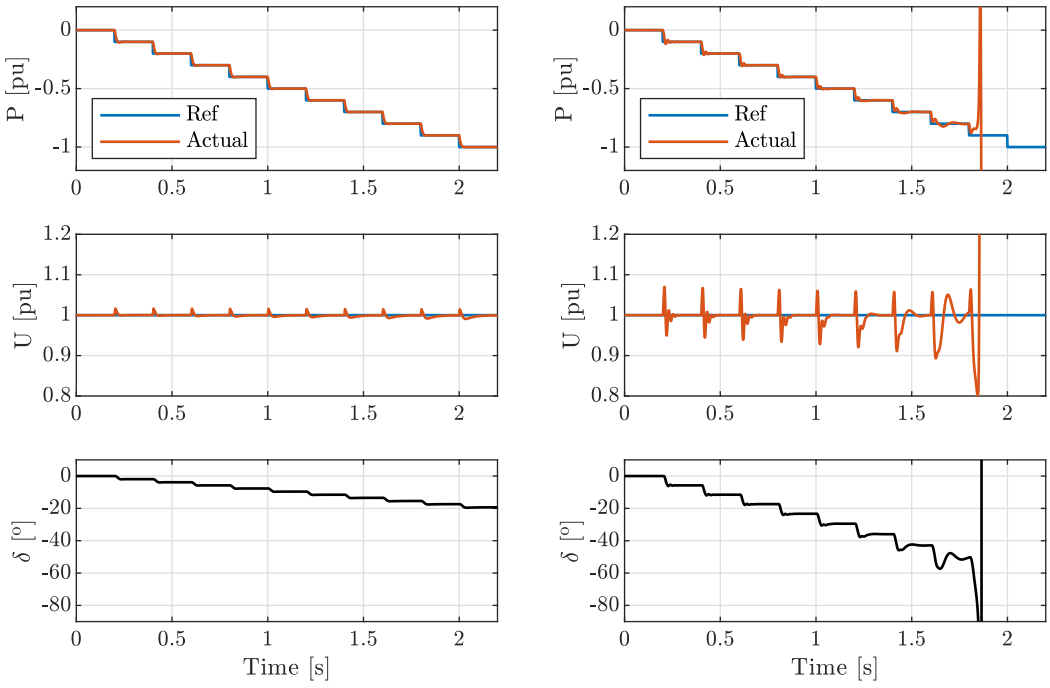


**(a)** SCR = 3. **(b)** SCR = 1.

**Figure 2.21:** Time domain analysis of the relationship between active power, voltage magnitude and power angle.

Fig. 2.22 is plotted below showing the eigenvalues of classical VCC for SCRs of 3 and 1. Inversion is plotted in black and rectification is plotted in red, and the axes are selected to provide detail on key eigenvalues.

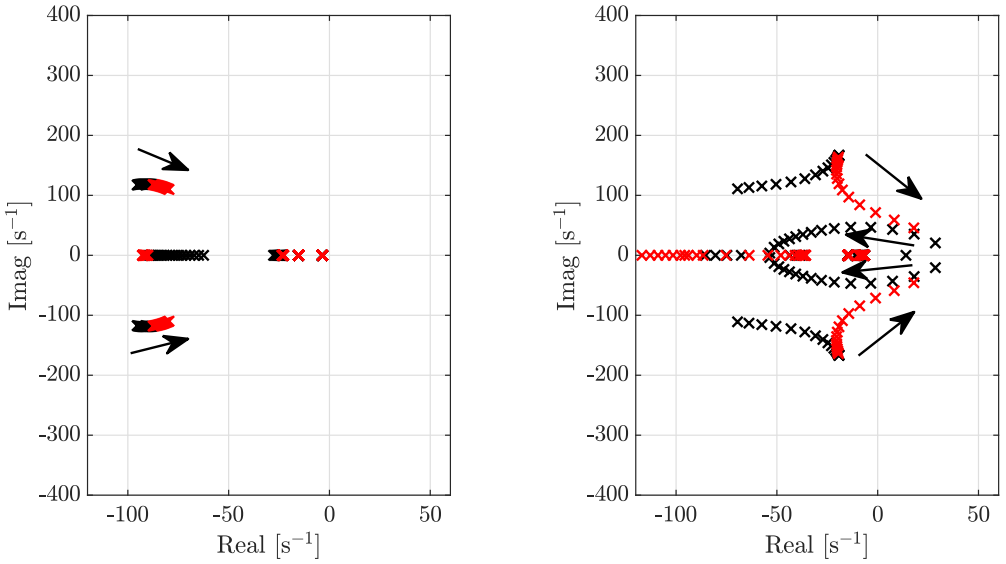


**(a)** SCR = 3. **(b)** SCR = 1.

**Figure 2.22:** Eigenvalues of the closed loop transfer matrix, the arrow indicates increases in power from $-1$ pu to 0.75 pu in increments of 0.05.

In Fig. 2.22a, there are no right hand side poles, hence steady state stability is maintained at a SCR of 3 for all operating points. In Fig. 2.22b, however, high levels of both rectification ($P \geq 0.6$ pu) and inversion ($P \leq -0.85$ pu) lead to instability. There is good matching between the small signal model in Fig. 2.22 and the time domain model in Fig. 2.21, with instability initiating at the same power.

The small signal stability of the converter can also be tested by applying a small step of 0.01 pu of the base values of active power and voltage magnitude references onto the closed loop system transfer function, as per Fig. 2.23 and 2.24. In these plots, the top left subplot illustrates the impact of a change in power reference on power; top right subplot illustrates a change in voltage reference on power; and similarly on the two bottom plots where the output is voltage.

This process is repeated for operating points $P = -0.9$, $-0.85$ and $-0.8$ pu. These set-points a chosen because they best illustrate the variation in performance for these

conditions and set a base case for other examples later on.

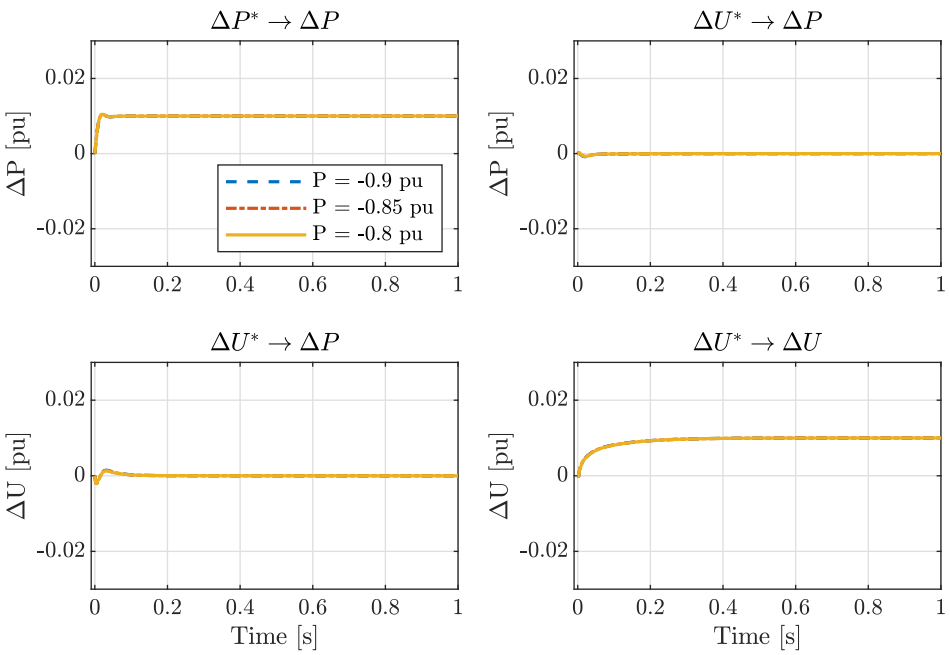


**Figure 2.23:** Step response of the closed loop system for SCRs of 3.

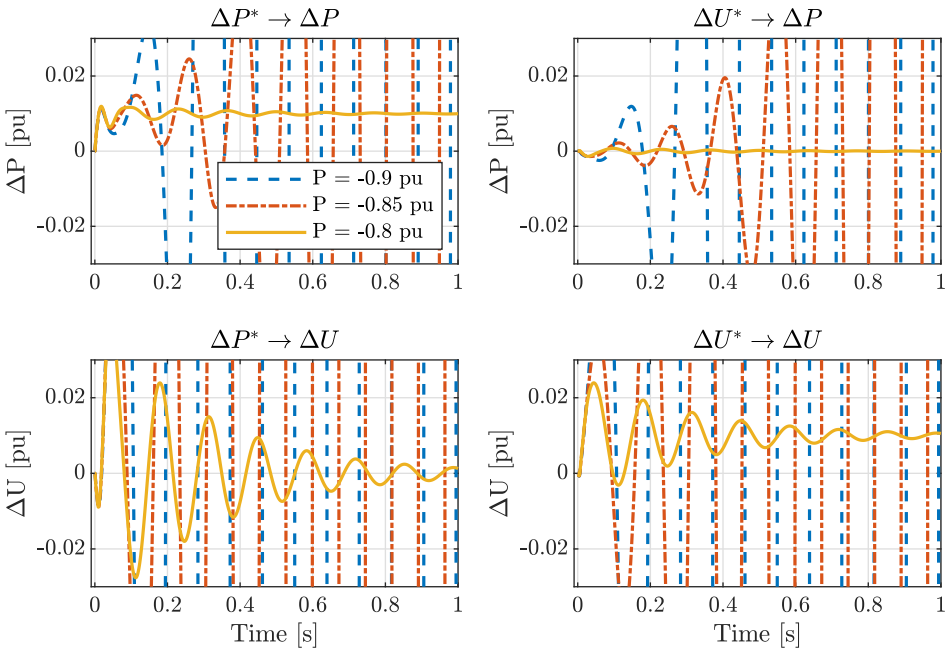


**Figure 2.24:** Step response of the closed loop system for SCRs of 1.

With a grid SCR of 3, Fig. 2.23 shows excellent response to changes in reference. There is also limited coupling between $P^*$ and $U$ as well as $U^*$ and $P$. However, in Fig. 2.24 where the SCR is 1, the increased outer loop coupling radically alters the results. Setpoints $P = -0.9$ and $-0.85$ pu are unstable, and while $P = -0.8$ pu is stable, the increased cross coupling is noticeable in the off-diagonal plots. The undesirable cross coupling is apparent in the increased oscillations and settling time – and this is only taking steady state stability into account.

#### 2.3.1.2 Transient stability

Transient stability is the term used to describe the stability of a system across a large variation of operating points, either because the system is subjected to large power reference changes or because the system state changes significantly. Transient stability studies are therefore complimentary to small signal studies, allowing for a more detailed understanding of nonlinear converter-grid interactions.

The two types of transient events of interest in this thesis are:

- Large ramps in power reference.
- Sudden changes in SCR.

As for large ramps in power reference, consider the example set out in [46], replicated for SCRs of 3 and 1 in Fig. 2.25.

Fig. 2.25 shows the power reference ramping from $-0.2$ pu to $-0.9$ pu in a short period of time, followed by another ramp from $-0.9$ pu to 0.7 pu. The transient stability in Fig. 2.25a is as expected – in a strong grid with a stiff voltage, tracking the power reference is straightforward, and there is no need to prioritise voltage control. However, as illustrated in Fig. 2.25b, it is much harder to track the power reference when the voltage is not stiff. In this figure, two variations of the outer loop tuning are employed, one fulfilling the objectives set out in Section 2.2.2.9.1, and the other optimised for classical VCC steady state stability (with a slower active power loop and a faster voltage loop), with both tuning outlined in Appendix A. In this example, the control effort undertaken by the fast power controller undermines the stability of the

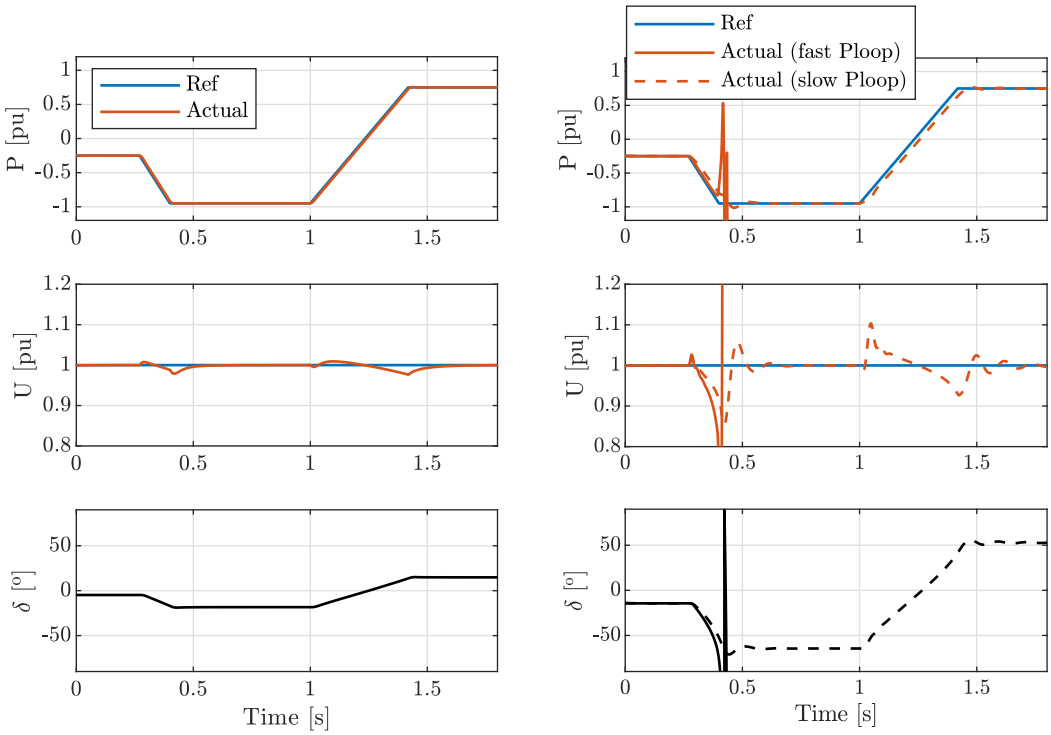


**(a)** SCR = 3. **(b)** SCR = 1.

**Figure 2.25:** Ramps in active power reference.

grid voltage, resulting in voltage collapse. However, in the alternative slower power controller, the voltage controller just about manages to support the PCC voltage and avoid a collapse. The coupling between the active and reactive components is very obvious given the slowly decaying oscillations in the voltage plot in Fig. 2.27b.

Sudden changes in SCR can be emulated by triggering the contactor – presented in the electrical system diagram, Fig. 2.26.

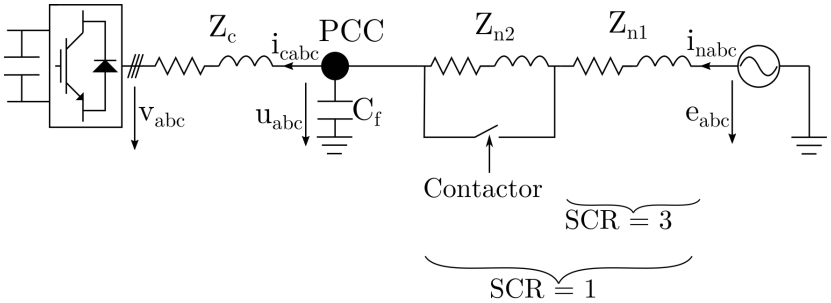


**Figure 2.26:** Electrical system subjected to sudden changes in SCR.

The triggering of the contactor is undertaken in Fig. 2.27, a time domain simulation where the SCR changes from 3 to 1 at 0.4 s.

As previously seen, the converter has steady state stability at $P = -0.75$ pu for both SCRs of 3 and 1. But, according to the simulation presented in Fig. 2.27, it is unstable when transitioning from one stable operating point to another. This is true for both versions of the active power loop, where the controller is tuned to have either fast or slow power response. This presents an additional consideration when analysing the results from linearised converter stability studies, as real life systems cannot be expected to remain stationary.

### 2.3.2 Testing of existing proposals in the literature

Time domain simulations of the virtual voltage PLL and an outer loop modification are undertaken in this section as a means of trialling and assessing some of the most promising proposals in the literature.

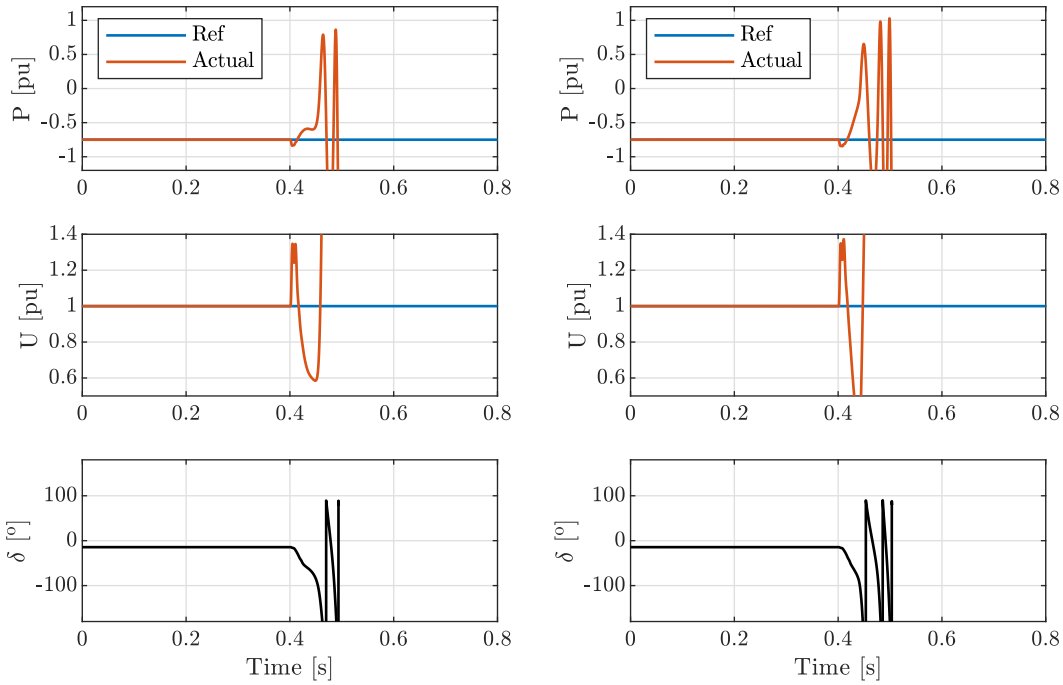


**(a)** Fast power loop. **(b)** Slow power loop.

**Figure 2.27:** SCR step change from 3 to 1.

#### 2.3.2.1 Virtual voltage PLL

To improve weak grid performance, some literature suggest modifying the PLL such that synchonisation is done to a virtual voltage [89, 100]. This idea is tested below, where a simple modification based on [89,100] is implemented to the PLL. The voltage fed to the PLL $u_d$ is replaced by $u_{d\,virtual}$, where

$$u_{d\,virtual} \;=\; u_d \;+\; i_{nq}R_{virtual} \;-\; i_{nd}\omega L_{virtual} \tag{2.71}$$

This implementation is integrated into the control as per Fig. 2.28.

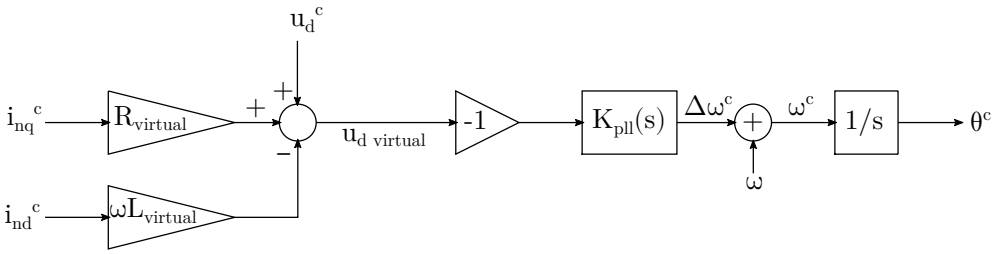


**Figure 2.28:** Block diagram for virtual voltage PLL.

Two variations of this are tested: in the first instance the virtual impedance is a third that of the real grid impedance, i.e. $Z_{virtual} = \frac{1}{3}Z_n$ ($L_{virtual} = \frac{1}{3}L_n$ and $R_{virtual} = \frac{1}{3}R_n$). In the second variation, the virtual impedance is equal to the real grid impedance, i.e. $Z_{virtual} = Z_n$. Both variations are tested in simulation and presented in Fig. 2.29, in a grid SCR of 1. Fig. 2.29a illustrates the stability during small steps in power and Fig. 2.29b the stability during power ramps.

In Fig. 2.29a, both versions of virtual impedance become unstable at $P = -1$ pu. The initial voltage response immediately after the power reference change is also the same for both versions. However, this is where the similarities end. The smaller virtual impedance of $Z_{virtual} = \frac{1}{3}Z_n$ produces smoother power transitions than the larger virtual impedance of $Z_{virtual} = Z_n$, which is much more oscillatory. These oscillations are particularly obvious in the voltage plot. This is due to the voltage controller action being compromised by the virtual voltage PLL, and the difficulty in tracking the reference.

In Fig. 2.29b, the larger virtual impedance is stable throughout despite its oscillat-

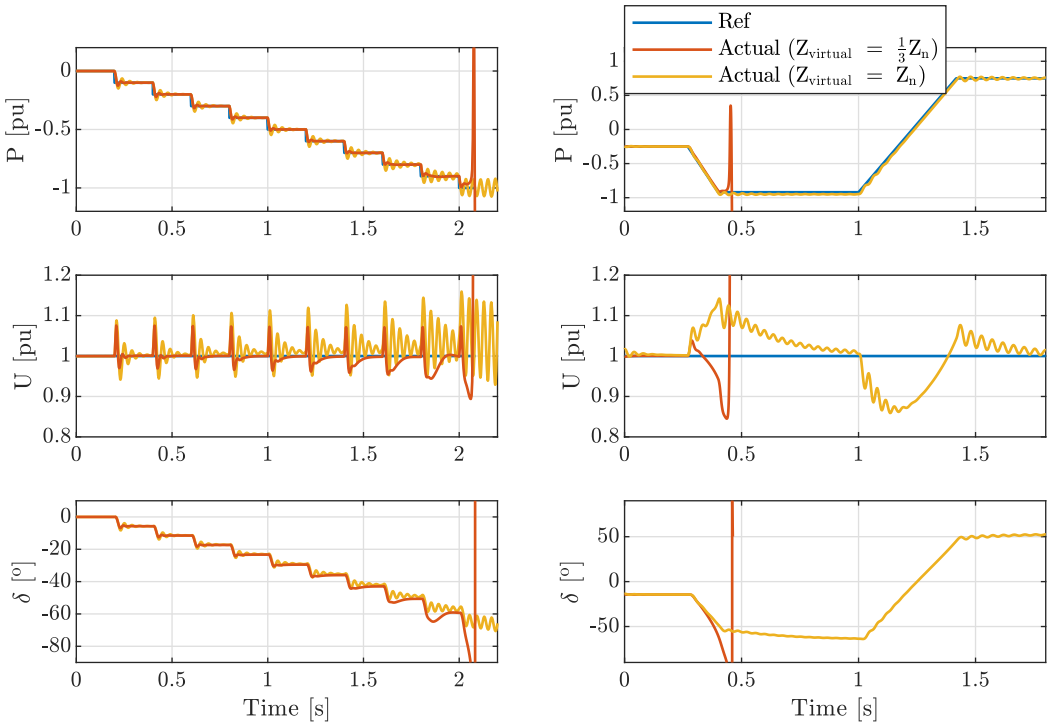


**(a)** Small power steps. **(b)** Power ramps.

**Figure 2.29:** Using a virtual voltage PLL where $Z_{virtual} = \frac{1}{3}Z_n$ and $Z_{virtual} = Z_n$.

ory behaviour and a significant drop in voltage magnitude in the upwards ramp. The smaller virtual impedance, despite being less oscillatory, becomes unstable in this test in the downwards ramp. This is due to insufficient reactive power support provided by the virtual impedance in the PLL.

To further assess the robustness of this proposal against large transient disturbances, Fig. 2.30 assesses the converter's ability to maintain stability in sudden step changes in SCR, from 3 to 1 to 3.

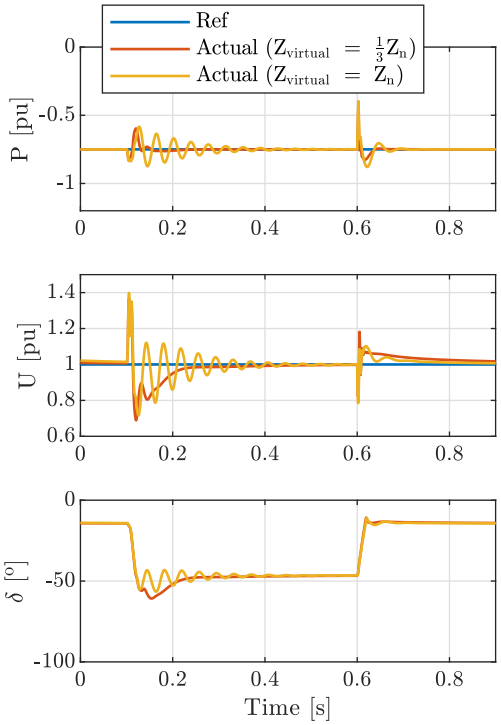


**Figure 2.30:** Step change in SCR from 3 to 1 to 3.

In this instance, both variations of virtual impedance maintain stability. However, the voltage oscillations observed for $Z_{virtual} = Z_n$ are significant.

From Fig. 2.29 – 2.30, the virtual voltage PLL can appear to improve the stability of the converter compared to the classical implementation plotted in Fig. 2.21, 2.25 and 2.27. It does this mainly by slowing down the controller, thus preventing large disruptions from having a sudden and destabilising impact on the converter. However, the virtual voltage PLL does not improve the provision of reactive power. Mainly,

by changing the synchronisation frame and no longer being synchonised to the PCC voltage, the converter behaves in an unpredictable way, slowing down the system and even introducing an undesirable feedback when the virtual impedance is high. While the smaller virtual impedance produces improved results in Fig. 2.29a, it is still unable to track a power reference ramp, as per Fig. 2.29b. Thus, this technique does not introduce any $P-U$ decoupling and certainly does not produce reliable improvements in stability, let alone dynamic performance.

#### 2.3.2.2 Feedforward branch

Another interesting proposal involves modification to the outer loop, proposed by Wu *et al* [98], and presented in Fig. 2.31.

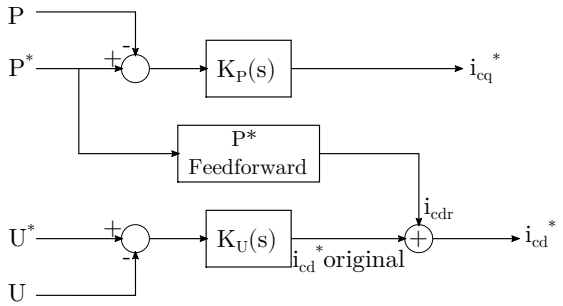


**Figure 2.31:** Block diagram for Wu *et al*'s feedforward branch.

In this instance, changes in power reference directly feeds into the reactive loop and modifies the reactive current reference, such that

$$i^*_{cd} = i_{cdr} + i^*_{cd\ original} \tag{2.72}$$

The equation for the feedforward current $i_{cdr}$ is as follows, amended to reflect a different frame orientation, and complete with all associated equations. It is assumed that the grid impedance is known by the controller. The subscript $ll$ defines line-to-line quantities.

$$i_{cdr} = \frac{Q}{1.5u_q} \tag{2.73}$$

where

$$Q = \frac{-2X_n U_{ll}^2 + \sqrt{\Delta}}{2(X_n^2 + R_n^2)} \tag{2.74}$$

$$\Delta = (2X_n U_{ll}^2)^2 - 4(X_n^2 + R_n^2)(U_{ll}^4 + (2P^* R_n - E_{ll}^2)U_{ll}^2 + P^{*2}(X_n^2 + R_n^2)) \geq 0 \tag{2.75}$$

The implementation of this feedforward branch in the outer loop results in the Fig. 2.32.

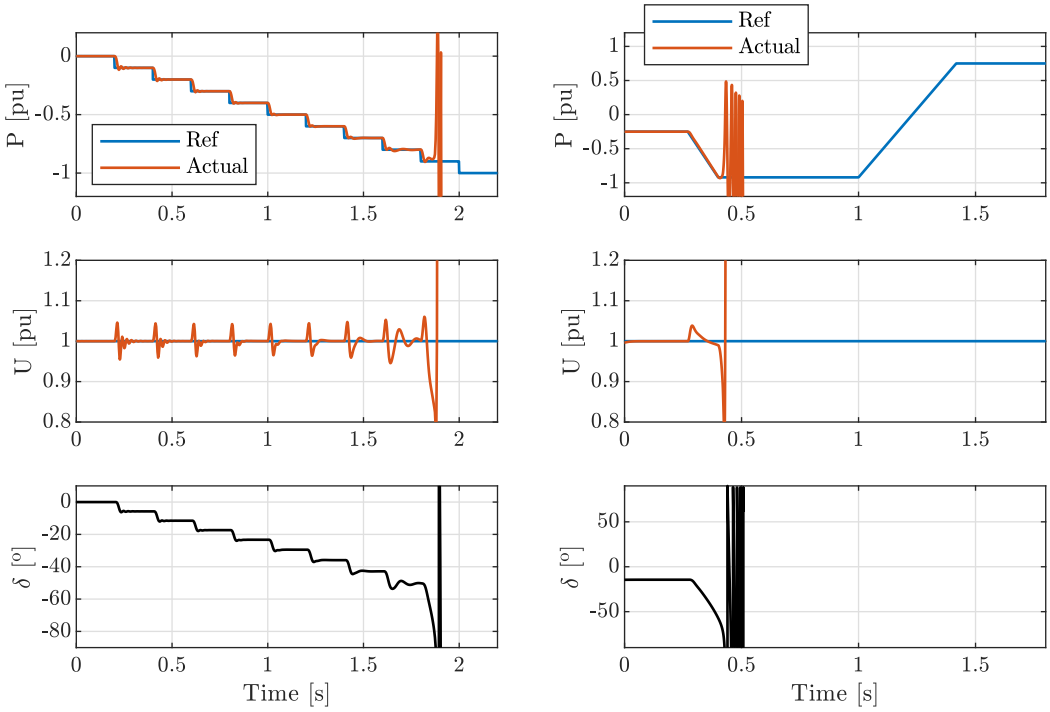


**(a)** Steady state stability. **(b)** Stability in large reference changes.

**Figure 2.32:** Using a feedforward branch from the power to the reactive current reference.

The feedforward branch implementation does appear to reduce the coupling of active and reactive power. The voltage oscillations are shallower and the system stabilises quickly. However, in Fig. 2.32a, instability is reached at the same point as it is without any modifications. Similarly, the large power ramps in Fig. 2.32b are also sufficiently disruptive as to cause instability. Thus, while this implementation of a feedforward branch is promising, it does not sufficiently reduce the active and reactive

power coupling.

#### 2.3.2.3 Discussion on the virtual voltage PLL and the feedforward branch testing

The use of a virtual voltage for PLL synchronisation produced mixed results, depending on the nature of the power reference change and the size of the virtual impedance. With the virtual voltage PLL no longer synchronised to the PCC voltage, the virtual voltage PLL introduces a current cross coupling. This impacts all aspects of the controller, including the active power loop, the current controller and the PLL in question. Also, the voltage support is irregular and unpredictable, as per the large voltage swings in Fig. 2.29b.

The feedforward branch suggested in [98], also produced mixed results. With the outer loop tuned according to the objectives, the steady state performance was marginally improved but the ability to respond to large active power reference ramps was unsuccessful. The philosophy of amending the outer loop will be further investigated in Section 4.2.

## 2.4 Experimental set-up

In order to validate the control adaptations proposed in this thesis, a scaled experimental set-up is produced. In this section, the experimental parameters are derived for the given equipment constraints. The laboratory set-up is also described.

### 2.4.1 Determination of laboratory parameters

The PEDEC laboratory at the University of Strathclyde has a range of inductances available, ranging from the small inductor of dual values 6.5 mH and 13 mH to the large inductor of dual values 10.5 mH and 21 mH. 13 mH inductances are employed for converter filtering at each phase to keep ripple at under 5 %. This leaves the grid impedance, where connecting impedances in series produced 4 possible impedances per phase: 10.5 mH, 21 mH, 31.5 mH or 42 mH. With this arrangement, very weak grid

conditions must be achieved with a maximum inductance of 42 mH.

The other constraints in the laboratory are the DC voltage (400 V max) and the DC current (6 A max).

The next consideration is the base power and the grid voltage. The allowable voltage from the Cinergia voltage emulator (operating as an open loop voltage source) is far higher than the DC power supply limits, so the DC power supply is the limiting factor. The converter is designed to cope with 2 kVA.

The grid strength, as explained in Section 2.1.1, can be represented by a SCR. The SCR usually employs the line-to-line voltage, as per (2.1), but to simplify the presentation of the following tables, the phase voltage is used instead. The main advantage of using SCR to establish the base voltage values is that it indicates how close the system is to the maximum power angle of 90° across the combined grid impedances, or filter+grid impedance. Thus, two versions of SCR are used: the grid SCR and the total SCR.

$$SCR_{grid} = \frac{\frac{(\sqrt{3}U_{ph})^2}{X_n}}{S_{rated}} \tag{2.76}$$

$$SCR_{total} = \frac{\frac{(\sqrt{3}U_{ph})^2}{X_c+X_n}}{S_{rated}} \tag{2.77}$$

Further to SCR, the other constrained variables are

$$V_{DC} > 2\sqrt{2}U_{ph} \tag{2.78}$$

$$I_{DC} = \frac{S_{base}}{V_{DC}} \tag{2.79}$$

where

$$Z_{base} = \frac{U_{ll}^2}{S_{rated}} \tag{2.80}$$

With the base equations established, the two remaining free variables are the grid

voltage and the base power. With the original 2 kVA rating, the following table provides a range of weakest possible SCRs for a range of rms phase voltages.

**Table 2.3:** Parameters of system for $S_{base}$ = 2 kVA.

| $E_{ph}$ | $V_{DC}(min)$ | $I_{DC}$ | $SCR_{grid}$ | $SCR_{total}$ |
|---|---|---|---|---|
| 80 V | 226 V | 8.8 A | 0.73 | 0.57 |
| 100 V | 283 V | 7.1 A | 1.13 | 0.89 |
| 120 V | 339 V | 5.9 A | 1.63 | 1.27 |
| 140 V | 396 V | 5.1 A | 2.23 | 1.73 |
| 160 V | 453 V | 4.4 A | 2.91 | 2.27 |

The ideal grid conditions are met in the second and third rows, where the weakest achievable SCR is less than 2. Unfortunately, the current drawn in these conditions is too high for the DC power supply.

Therefore, this exercise is repeated for a lower $S_{base}$ of 1 kVA.

**Table 2.4:** Parameters of system for $S_{base}$ = 1 kVA.

| $E_{ph}$ | $V_{DC}(min)$ | $I_{DC}$ | $SCR_{grid}$ | $SCR_{total}$ |
|---|---|---|---|---|
| 40 V | 113 V | 8.8 A | 0.36 | 0.28 |
| 60 V | 170 V | 5.9 A | 0.82 | 0.64 |
| 80 V | 226 V | 4.4 A | 1.46 | 1.14 |
| 100 V | 283 V | 3.5 A | 2.27 | 1.78 |
| 120 V | 339 V | 2.9 A | 3.27 | 2.56 |

These values are much more practical given the existing equipment constraints. Given that the converter is required to provide voltage support, the additional 1 kVar allows for some redundancy. With regards to the grid voltage, 78 V is used. This results in a grid SCR of 1.38, 2.77 and 5.53 depending on whether the grid inductance is 42 mH, 21 mH or 10.5 mH, as per the simplified schematic of the hardware presented in Fig. 2.33. The PWM filter is represented by a capacitor ($C_f$). The complete parameters are presented in Appendix A.2.

### 2.4.2 Complete setup

The complete setup is presented in Fig. 2.34.

The proposed controller is implemented into an Texas Instruments F28379D ControlCard attached to a SiC MOSFET two-level converter downgraded to 1 kW. The

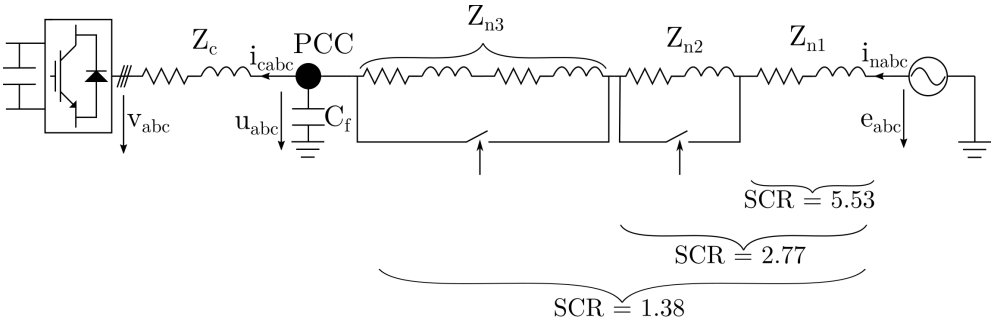


**Figure 2.33:** Schematic of test rig.

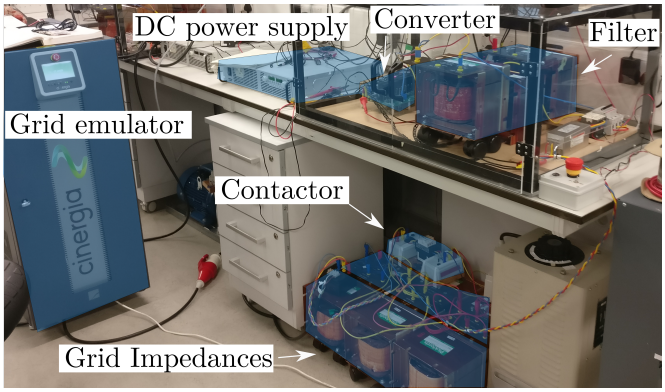


**Figure 2.34:** Photograph of test rig.

grid voltage is produced by the Cinergia grid emulator. For safety purposes, the exposed electrical wiring is all contained within a perspex box, and an external contactor switch allows for immediate disconnection of the converter from the grid. A circuit breaker is also included at the PCC in case of overcurrent. A 4 channel Picoscope is used, allowing for simultaneous data collection during the experimental phase.

# Chapter 3

# Local Impedance Estimation

Estimation of the Thévenin equivalent impedance is useful for understanding local grid conditions; it infers information about the local voltage stiffness and it's impact on active power transfer limitations. Furthermore, the identification of the grid resonances is also studied, as resonances may impact the stability of converters and other generators.

In this chapter, a background on impedance estimation is provided for both Thévenin equivalent and wide-band impedance. For completeness, the Thévenin equivalent impedance assumes that the impedance is linear, and as such a single value for inductance and resistance represent the impedance for all frequencies. On the other hand, the wide-band impedance is nonlinear, i.e. resistance and reactance is frequency dependent.

This is followed by a classification of the various techniques, and a detailed description of each one. A comparison table is produced, allowing for side-by-side assessment of the existing impedance estimators. The non-convergence of the impedance estimation is studied for stationary grids through first principles. Subsequently, the most suitable Thévenin equivalent impedance estimators for the purposes of this thesis (non-harmonic injection and P/Q variation) are tested in simulation and the nonharmonic injection estimator is further tested in the laboratory. A wide spectrum impedance estimator, which introduces a perturbation via a step change in power, is also tested in simulation. This estimator determines grid-induced resonances.

## 3.1 Historical context for impedance estimation

Early impedance estimation literature focused on harmonic content due to power quality concerns [128, 129]. A guide for network harmonic impedance assessment was written by a CIGRE/CIRED Working Group CC02 [130]. The main motivation behind the early literature including the CIGRE/CIRED report was to improve the understanding of the harmonic current caused by power equipment in the network. The identification of resonant frequencies through wide frequency spectrum impedance estimation allowed for the design of harmonic filters and capacitor banks, reducing the resonances and improving power quality [131]. Some of the proposed techniques utilised harmonic excitation (frequency sweeping) with dedicated hardware [128, 132]. Others generated an impulse by close-trip operations of a shunt capacitor bank, causing a large inrush of current and rich spectral excitation [129,130]. Alternatively, [68,133,134] utilise thyristor switches, creating a short circuit and subsequent large current pulse injection, with the intention of monitoring in real-time the evolution of network impedance. [135, 136] exploit the resonances of LCL-filters to excite the system.

With the advancement of microcontroller computational capabilities, online impedance estimators became increasingly common in the literature. Anti-islanding is a common motivation for impedance estimation literature [137–142], with the draft European standard EN50330-1 (or equivalent German standard VDE0126) usually cited as a justification. For completeness, EN50330-1 is now cancelled, and the current standard regarding islanding prevention is EN62116, *Utility-interconnected photo-voltaic inverters – Test procedure of islanding prevention measures* [143]. The estimation techniques employed in [138–140] are based on the injection of a nonharmonic current, followed by fast Fourier transform (FFT) of the nonharmonic frequency current and voltage response. [141, 144] collected information about the system by varying the outer loop active power and reactive power references.

The motivations of recent literature is more relevant to this thesis, as it is interested in offline or online controller tuning for improved stability [92, 100, 117–119, 145, 146]. This is due to the increased network impedance variability and resulting voltage sta-

bility issues [25], consequently increasing the importance of appropriate control tuning [147]. The causes of weak grids and impedance variability more broadly is already covered in Section 2.1.1.

## 3.2 Literature review of local impedance estimation techniques

A high level classification of the estimation techniques is presented in Fig. 3.1. Passive methods are discussed in more detail in Section 3.2.1; active techniques in Section 3.2.2; and quasi-passive techniques in Section 3.2.3.

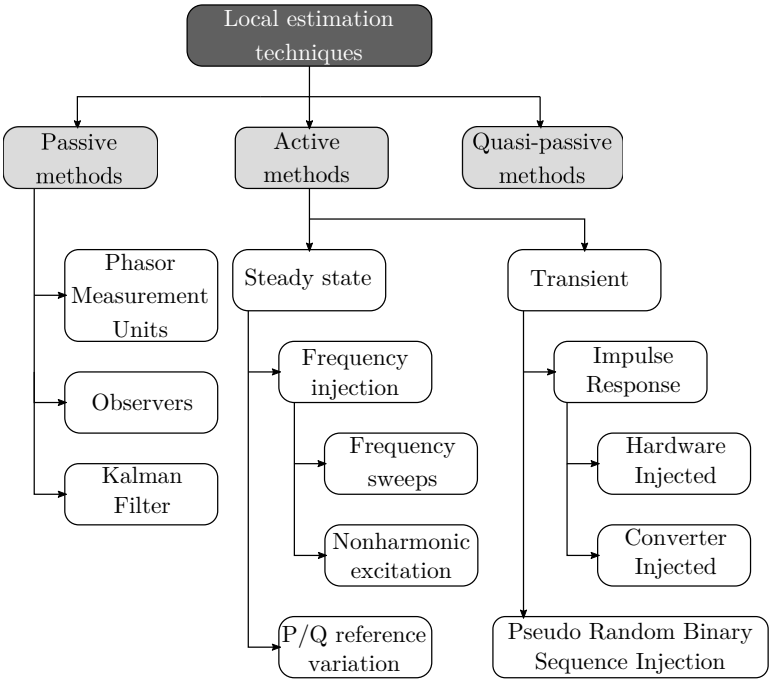


**Figure 3.1:** Classification of local impedance estimation techniques and relevant section.

Estimation techniques can be subdivided into active, passive or quasi-passive techniques, depending on whether the perturbation is intentionally introduced periodically, is dependent on other sources of perturbation in the grid, or is intentionally introduced only when pre-determined conditions are met, respectively.

### 3.2.1 Passive techniques

Passive techniques utilise existing transients, caused by sufficiently large grid events, to undertake impedance estimations. Passive techniques can be loosely categorised as local PMU derived observers, PCC observers and Kalman Filters.

#### 3.2.1.1 Local PMU derived observers

PMUs are used to produce synchrophasor measurements – fundamental frequency voltage and current measurements that are time synchronised [148]. Normally, synchophasors are communicated to a central computer, and this information can be used to undertake state estimation, fault detection/location and wide area monitoring, including protection [149–151]. While the use of synchrophasors from multiple PMUs can be used to measure line impedance [152–154], the focus of this chapter is on the local techniques which utilise local measurements only. A single PMU, benefiting from the accurate time stamping of phasors, can be used to estimate the Thévenin equivalent properties of the network. The high level procedure is summarised in Fig. 3.2, where the adaptive technique is based on [155], the recursive least squares (RLS) solver is derived from [31, 32, 156, 157], and the algebraic technique is derived from [118, 158].

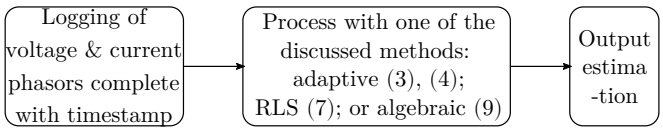


**Figure 3.2:** Flow chart typical of most local PMU derived observers.

Firstly, regarding the adaptive solver [155], the PCC voltage phasor $\overline{U}$ can be described as

$$\overline{U} = \overline{E} - \overline{Z}_n \overline{I_n} \tag{3.1}$$

In this example, the notation is slightly different to the rest of the thesis. The reference angle is that of the current, such that $\overline{I_n} = I_n \angle 0°$. Thus, $\overline{U}$ is the PCC voltage phasor ($\overline{U} = U\angle\kappa$), $\overline{E}$ is the equivalent grid voltage phasor ($\overline{E} = E\angle\beta$), and $\overline{Z}_n$ is the grid impedance ($\overline{Z}_n = R_n + jX_n$). The phasor relation of $\overline{U}$, $\overline{E}$ and $\overline{I_n}$ is

graphically represented in the Fig. 3.3 phasor diagram.

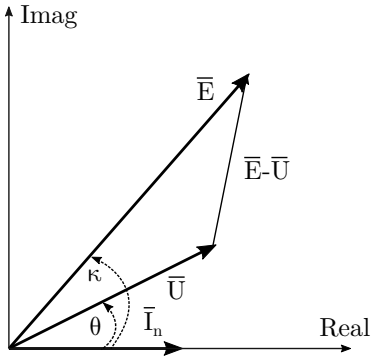


**Figure 3.3:** Phasor diagrams for local PMU-based estimation techniques.

Given that $\overline{Z}_n = R_n + jX_n$, (3.1) can be rearranged and separated into real and imaginary components, as follows

$$E\cos(\beta) = R_n I_n + U\ \cos(\kappa) \tag{3.2}$$

$$E\sin(\beta) = X_n I_n + U\ \sin(\kappa) \tag{3.3}$$

In the two above equations, there are four unknowns: $E$, $\beta$, $R_n$ and $X_n$. However, if the network is known to be much more inductive than resistive ($X_n >> R_n$), then it is acceptable to assume $R_n = 0\ \Omega$ [155]. This assumption allows the decoupling of $X_n$ from $\overline{E}$ by rearranging (3.2)

$$\beta = \cos^{-1}\left(\frac{U\cos(\kappa)}{E}\right) \tag{3.4}$$

In [155], an initial $E$ estimate is made by taking the mean value of the expected voltage region, and updating for a new value with every consecutive timestep using (3.3) and (3.4). Every updated value of $E$ corresponds to a unique value of $X_n$. The direction of the error for $E$ is dependent on the variations of the load impedance (analogous to the converter output impedance which includes both the filter and the converter) called $Z_l$. When $X_n$ and $Z_l$ vary in the same direction, estimates of $E$ reduce; otherwise $E$ increases.

Alternatively to the adaptive solver is the RLS solver [31, 32, 156, 157]. The RLS solver allows an under-determined system to generate a unique set of estimations by allowing the use of many measurement points without making the equations over-determined. RLS is usually undertaken using rectangular notation instead of phasor notation. Using the same notation as Fig. 2.1, the implementation is as follows:

$$\boldsymbol{Y} = \boldsymbol{A}\hat{\boldsymbol{X}} - \boldsymbol{Q} \tag{3.5}$$

Expanded in full matrix form

$$\begin{bmatrix} \overline{U}_1 \\ \overline{U}_2 \\ \vdots \\ \overline{U}_k \end{bmatrix} = \begin{bmatrix} \overline{I_{n1}} & 1 \\ \overline{I_{n2}} & 1 \\ \vdots & \vdots \\ \overline{I_{nk}} & 1 \end{bmatrix} \cdot \begin{bmatrix} \hat{\overline{Z_n}} \\ \hat{\overline{E}} \end{bmatrix} - \begin{bmatrix} q_1 \\ q_2 \\ \vdots \\ q_k \end{bmatrix} \tag{3.6}$$

Where $\hat{\boldsymbol{X}}$ is the estimate of $\boldsymbol{X}$ and $\boldsymbol{Q}$ is the error between $\boldsymbol{X}$ and $\hat{\boldsymbol{X}}$. The use of the bar for voltages and current denote rectangular notation, where $\overline{U} = u_{real} + ju_{imag}$, $\overline{E} = e_{real} + je_{imag}$, and $\overline{I_n} = i_{real} + ji_{imag}$. The RLS technique requires some manipulation [159] which results in (3.7). This form allows a simple closed-form solution which minimises the error.

$$\hat{\boldsymbol{X}} = (\boldsymbol{A}^T\boldsymbol{A})^{-1}(\boldsymbol{A}^T\boldsymbol{Y}) \tag{3.7}$$

To conclude the PMU derived observers is the algebraic solvers, described in [118, 158]. In this instance, only two measurement sets are used and solved algebraically, resulting in the following equation. The initial measurement set has the subscript 0, and the following measurement set has the subscript 1.

$$\overline{Z_n} = \frac{\overline{U_1} - \overline{U_0}}{\overline{I_{ncs}} - \overline{I_{n0}}} \tag{3.8}$$

Both above mentioned papers [118, 158] proceed to enhancing the equation, compensating for measurement drift caused by the deviation from fundamental frequency experienced by the signals, as follows

$$\overline{Z_n} = \frac{\overline{U_1}e^{j\Delta\theta} - \overline{U_0}}{\overline{I_{ncs}}e^{j\Delta\theta} - \overline{I_{n0}}} \tag{3.9}$$

Where in this context $\Delta\theta$ is the shift in phase due to the deviation from fundamental frequency.

#### 3.2.1.2 PCC Observers

This subcategory is relevant to devices with measurement capabilities that do not utilise GPS synchronisation. This is the case for most converters and buses with current and voltage sensors. Observers generally follows the flow chart depicted in Fig. 3.4 of recognising a grid event, storing the information, and mathematically extracting an impedance estimation, normally in the frequency domain.

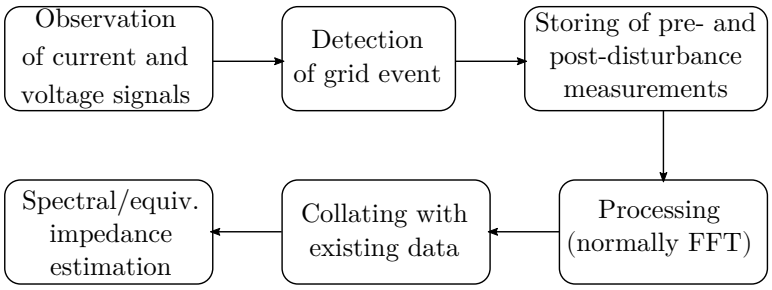


**Figure 3.4:** Flow chart typical of most observers.

Reference [160] identifies that a sufficiently large grid event has occurred when a 3% change in RMS voltage is registered. The transients caused by such an event can provide information about the system across a wide range of frequencies. Triggered by the transient, the estimation procedure requires the storage of voltage and current measurements for five fundamental periods immediately before and after the event is detected. FFT is then used to convert pre- and post-disturbance voltage and current from the time domain to the frequency domain up to the 50th harmonic, and (3.10) is used to estimate the impedance, where $\omega$ represents the frequency being analysed.

$$\overline{Z_n}(\omega) = \frac{\overline{U}(\omega)_{pre} - \overline{U}(\omega)_{post}}{\overline{I_n}(\omega)_{pre} - \overline{I_n}(\omega)_{post}} = \frac{\Delta\overline{U}(\omega)}{\Delta\overline{I_n}(\omega)} \tag{3.10}$$

Notice that (3.10) is similar to (3.8), with the difference being that (3.8) is valid for the fundamental frequency impedance only (the Thévenin equivalent), whereas (3.10)

can determine the impedance at a range of frequencies, subject to the FFT implementation.

With the observer implementation described in [160], good estimations require data accumulated by 70 grid events over 15 days – the accuracy of the estimates are not explicitly stated, but this is can be inferred from the paper's figures. In [161], the same authors presented the same data with the addition of the reference impedance value.

If the impedance estimator is part of a converter controller, the noise induced naturally by the switching of the converter can be used as the basis of disturbances. This is the case in [162] where the switching frequency of 10 kHz introduces voltage and current harmonics into the system. Assuming there is no pre-existing high frequency harmonics in the grid voltage it is demonstrated that results can be obtained within 20 ms. [92] uses a similar process and assumptions, but with more focus on the timing of the samples relative to the space vector pulse width modulation (SV-PWM) switching. An estimation time of 50 ms is achieved. Another paper, [163], also utilises PWM induced noise but this time uses the Recursive Least Squares technique as a means of mathematically extracting the impedance information. With a switching frequency of 2.8 kHz, the impedance estimation time is 1.2 s.

An alternative implementation of the observer monitors the variations in active power. A sufficiently large disturbance within the system, such as a step change in network impedance, will excite the system and cause the active power injection to vary [164]. In [164], FFT is used to extract the Thévenin equivalent impedance when a disturbance is detected using (3.10). This technique can be classified as passive because the change in power set-point is not undertaken specifically to disturb the system.

#### 3.2.1.3 Kalman Filter

Some researchers have recently suggested using nonlinear variations of the Kalman Filter in order to estimate the impedance. Whilst this technique is a type of observer, the computation and implementation is very different to the above mentioned observers – therefore the Kalman Filter is considered separately. The Kalman Filter flow chart is presented in Fig. 3.5 [165]. It begins with the initialization, and then continually loops

around as long as the Kalman Filter continues to receive new system measurements.

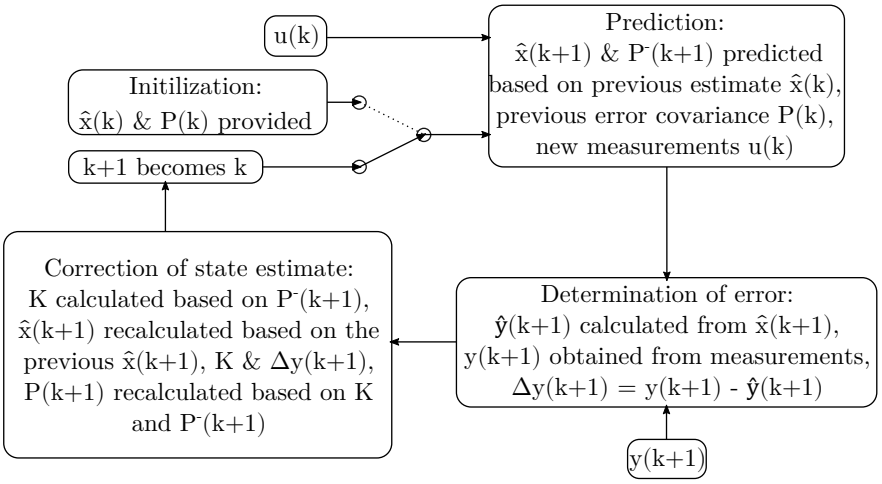


**Figure 3.5:** Flow chart typical of the extended Kalman Filters.

The Kalman Filter works in roughly three main steps:

The first is the *prediction* step which involves estimating the system states $\hat{\boldsymbol{x}}$ and the error covariance of the states $\boldsymbol{P}^{-}$, as per (3.11) (3.12).

$$\hat{\boldsymbol{x}}(k+1|k) = \boldsymbol{A}\hat{\boldsymbol{x}}(k) + \boldsymbol{B}\boldsymbol{u}(k) \tag{3.11}$$

$$\boldsymbol{P}^{-}(k+1) = \boldsymbol{A}\boldsymbol{P}(k)\boldsymbol{A}^{T} + \boldsymbol{V}\boldsymbol{M}\boldsymbol{V}^{T} \tag{3.12}$$

Where $\boldsymbol{A}$ is the state matrix, $\boldsymbol{B}$ is the input matrix, $\boldsymbol{V}$ is the predicted estimation error and $\boldsymbol{M}$ is the expected white noise of the estimation process.

The second step is to use the state estimations to determine the corresponding outputs $\hat{\boldsymbol{y}}$ (3.13), and *determine the error* by comparing the measured and estimated output values (3.14). $\boldsymbol{C}$ is the output matrix.

$$\hat{\boldsymbol{y}}(k+1) = \boldsymbol{C}\hat{\boldsymbol{x}}(k+1|k) \tag{3.13}$$

$$\boldsymbol{\Delta y}(k+1) = \boldsymbol{y}(k+1) - \hat{\boldsymbol{y}}(k+1) \tag{3.14}$$

The final step is to *correct the state estimate*. This is done by calculating the new Kalman Gain from the prediction error covariance and the expected measurement noise

($\boldsymbol{N}$) (3.15), and using the Kalman Gain to undertake a final state estimation (3.16). The prediction covariance is also subsequently updated (3.17).

$$\boldsymbol{K}(k+1) = \boldsymbol{P}^{-}(k+1)\boldsymbol{C}^{T}\left(\boldsymbol{C}\boldsymbol{P}^{-}(k+1)\boldsymbol{C}^{T} + \boldsymbol{N}(k+1)\right)^{-1} \tag{3.15}$$

$$\hat{\boldsymbol{x}}(k+1|k+1) = \hat{\boldsymbol{x}}(k+1|k) + \boldsymbol{K}(k+1)\boldsymbol{\Delta y}(k+1) \tag{3.16}$$

$$\boldsymbol{P}(k+1) = (\boldsymbol{I} - \boldsymbol{K}(k+1)\boldsymbol{C})\boldsymbol{P}^{-}(k+1) \tag{3.17}$$

The “extended" Kalman Filter (EKF) is an augmentation of the Kalman Filter intended for nonlinear systems. The EKF is implemented in [166, 167] where a Jacobian matrix is used instead of the state matrix to account for the nonlinearities, demonstrating good results for the assumed Thévenin equivalent system. The authors of [166] do concede, however, that system tuning is complex, requiring EKF optimisation through trial and error for the various grid conditions and operating points.

### 3.2.2 Active techniques

Active techniques, unlike passive techniques, do not rely on existing grid events. Instead, these techniques intentionally introduce a controlled perturbation or change in operating point, increasing the information available about the network. Active techniques can be further subcategorised into steady state and transient techniques.

#### 3.2.2.1 Steady state

Steady state techniques require the network response to a perturbation to settle prior to the collection of any measurement. All steady state techniques assume stationary network conditions for the duration of the testing.

#### 3.2.2.1.1 Frequency sweeps

Frequency sweeps remain the most common grid characterisation technique, normally employed for network studies at a PCC [128]. Typical implementation is presented in Fig. 3.6.

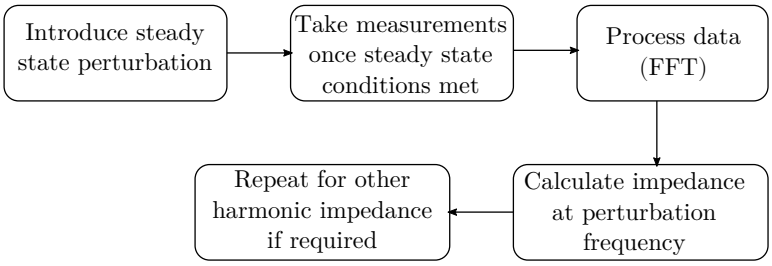


**Figure 3.6:** Flow chart for frequency sweeping.

Frequency sweeps are usually undertaken by attaching specialised hardware at the point of interest [168], injecting small steady state sinusoidal perturbations at a wide range of frequencies, and employing Fourier analysis to calculate the network impedance in the frequency domain, as per (3.18) where $\omega$ represents the perturbation frequency [132, 169]. Note that the perturbation frequency must be different to the fundamental frequency. Assuming that the network is stationary for the duration of the test, the wide spectrum impedance analysis can provide detailed grid characterisation complete with nonlinearities (such as resonances) at the cost of lengthy testing duration [130]. Frequency sweeping can be undertaken with specialised equipment installed temporarily in a node of the system or via standard grid-connected power converters. [170] focuses on line impedance estimation.

$$\overline{Z_n}(\omega) = \frac{\overline{U}(\omega)}{\overline{I_n}(\omega)} \tag{3.18}$$

This type of analysis has been further developed, with [168] using inexpensive hardware to estimate impedance from 20 Hz to 24 kHz, [171] using high resolution equipment to estimate the the impedance from 2 to 150 kHz, and [172] undertaking frequency sweeps of multiple frequencies simultaneously, increasing the data captured with each sweep. Frequency sweeps are not used only in utility grids but also in contained systems, such as on aircraft and ships [173, 174].

Wide spectrum frequency sweeps are occasionally implemented in converters as a means of validating the laboratory results of alternative impedance estimators – such as [175] (impulse-response) and [116] (pseudo random binary sequence injection).

#### 3.2.2.1.2 Nonharmonic excitation

A number of publications choose to assume simplified RL impedance and only excite a single noncharacteristic frequency. This is known as nonharmonic excitation. For example, [137, 139, 140] inject a noncharacteristic harmonic current of 75 Hz periodically. The settled values of current and voltage are recorded and converted into the frequency domain with Fourier transform analysis (or wavelet transform as per [137]). The voltage and current values at 75 Hz are extracted and the impedance is calculated with $\overline{Z_n}(\omega_h) = R_n + j\omega_h L_n$ (where $\omega_h$ is the nonharmonic frequency). It is assumed that the impedance at 75 Hz and 50 Hz is the same. [138] provides a very similar methodology, except that the period in between disturbances is 5 seconds. [115, 176] excites at 400 and 600 Hz, except that in [115] voltage is excited instead of the current. Interestingly, [177] excites a frequency of 10 Hz. Of the implementations discussed in this section, only [115, 176, 177] calculated both resistance and reactance as separate parameters – all other implementations only calculated the impedance magnitude. Nonharmonic perturbations can be injected in the *qd*-frame as per Fig. 3.7.

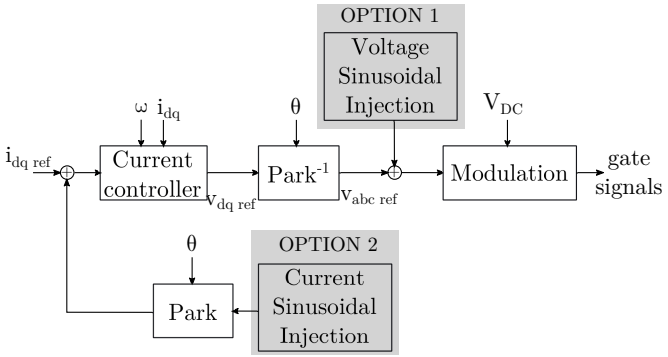


**Figure 3.7:** Examples of current and voltage sinusoidal injection within vector control.

More recently, some researchers have explored using the Wavelet Transform (WT) as an alternative to FFT [137, 178]. The perturbations are the same as previously explained, with nonharmonic frequencies of 75 and 630 Hz utilised in these papers, and

with both inductance and resistance estimated. The WT is explained in more detail at the end of Section 3.2.2.2.1 as it is generally more appropriate to transient methods.

As an aside, the WT is not limited to impulse-response. [178] utilises the WT combined with a steady state nonharmonic current injection.

#### 3.2.2.1.3 P/Q reference variation

The final steady state technique is the P/Q reference variation technique. In this technique, the active power and reactive power references are intentionally varied in order to allow the detection of both the resistive and inductive parts of the network Thévenin equivalent impedance [179]. With variations in outer loop references, the P/Q reference variation technique causes a very small amount of noise and disruption in the network [179]. This is described in Fig. 3.8.

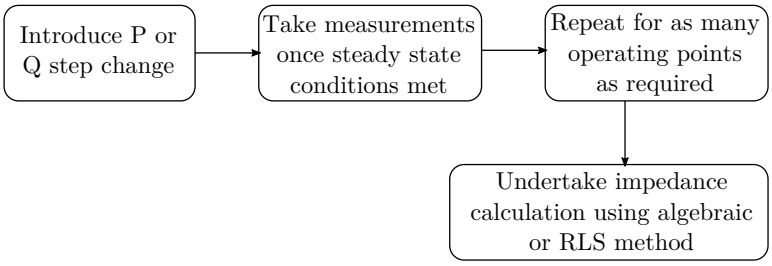


**Figure 3.8:** Flow chart of P/Q reference variation.

The techniques described in [100, 179–181] require two sets of measurements, where P and Q deviations can be either positive or negative. The impedance is subsequently calculated algebraically as per (3.19) and (3.20), or similar. The Park transformation values for PCC voltage and grid current are used, such that $\overline{U} = u_q - ju_d$ and $\overline{I_n} = i_{nq} - ji_{nd}$. Subscripts 1 and 2 represent the two sets of measurements.

$$R_n = \frac{(u_{q1} - u_{q2})(i_{nq1} - i_{nq2}) + (u_{d1} - u_{d2})(i_{nd1} - i_{nd2})}{(i_{nq1} - i_{nq2})^2 + (i_{nd1} - i_{nd2})^2} \tag{3.19}$$

$$L_n = \frac{1}{\omega_0} \frac{(u_{d1} - u_{d2})(i_{nq1} - i_{nq2}) - (u_{q1} - u_{q2})(i_{nd1} - i_{nd2})}{(i_{nq1} - i_{nq2})^2 + (i_{nd1} - i_{nd2})^2} \tag{3.20}$$

The P/Q variation technique is further expanded in [141, 182] to use a RLS solver. The RLS solver is already described earlier in (3.5), (3.6) and (3.7) and the analysis

techniques are the same. However, when implemented in a converter, the active and reactive power can be controlled to ensure variability in operating points. This is illustrated in Fig. 3.9, where three different measurement sets are used.

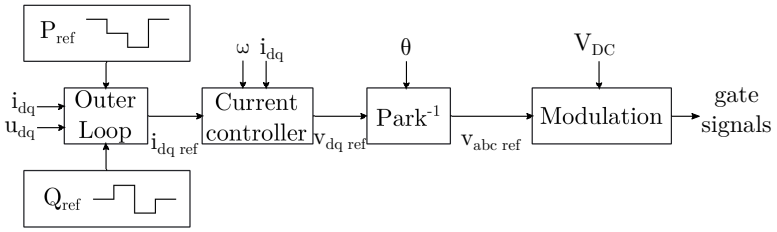


**Figure 3.9:** PQ variation with 3 different measurement points.

Recent publications have seen principles of the P/Q variation technique applied to relatively new concepts. [183] has adapted the P/Q variation technique to grid forming converter control and [184] has implemented the method to a system with no direct voltage measurements and only active power variation.

#### 3.2.2.2 Transient techniques

Unlike active techniques, transient techniques utilise the immediate transient response to a perturbation in order to extract information about the network. The most common form of transient technique is the impulse-response technique, but a number of papers also use the pseudo random binary sequence injection technique.

Irrespective of the nature of the perturbation, the impedance calculation is as follows – taking into account both the pre-disturbance and post-disturbance measurements [185] [68]. Notice that this is the same equation as (3.10) – the calculation is the same, the difference is simply in whether the disturbance is detected or intentionally injected.

$$\overline{Z_n}(\omega) = \frac{\Delta\overline{U}(\omega)}{\Delta\overline{I_n}(\omega)} \tag{3.21}$$

##### 3.2.2.2.1 Impulse-response

The impulse-response technique involves injecting a current or voltage perturbation pulse into the network in order to obtain a response for a wide range of frequencies [186], with the flow chart presented in Fig. 3.10. Given the short duration of the impulse,

the size of the frequency spectrum of interest and the possibility of high signal to noise ratio (SNR), the impulse must be large [130,185]. This allows for full spectral excitation in a very short period of time, making this technique particularly attractive in highly variable networks [134]. As such, additional hardware is often used to generate the impulse (such as the 5 pu of current injected in [68]). The use of additional hardware also allows for the disturbance to be injected directly in the PCC of interest, making the estimation of both the converter output impedance and grid impedance possible. Examples of hardware for impulse generation are shunt capacitor banks [129, 130, 185], the use of thyristor switches to create a short circuit [68, 187], or even switching the DC link voltage across an L filter inductor [186]. [175] use a dedicated power converter for increased control over the disturbance, as does [188], where the injected rectangular impulse is designed to extract impedance information at frequencies 2 kHz to 150 kHz.

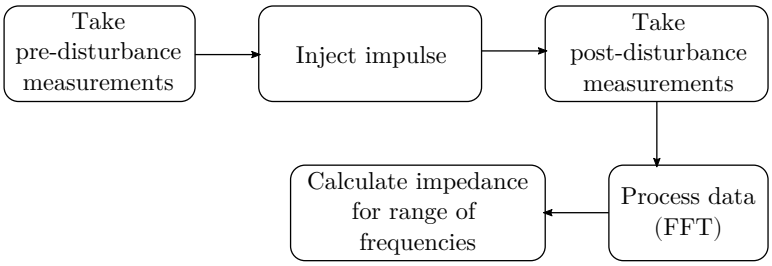


**Figure 3.10:** Flow chart for the impulse technique.

Not all papers using the impulse-response technique rely on additional hardware. Some have implemented the impulse-response technique directly into a converter. Unlike the aforementioned techniques that use dedicated impulse generating hardware, converter based injections are limited by the rating of the converter. Motivation for the impedance estimation vary from the identification of stability margins [189] to online PLL bandwidth adaptive control [101]. Due to the wide number of varying features described in impulse-response literature, Table 3.1 has been produced to simplify the comparison process.

Table 3.1 identifies whether the impulse is a voltage or a current; the type of filter used (L or LCL-filter); the type of grid that is being assessed (sometimes the grid is assumed to be a simple inductor with no resistance, but other times it is more complex with parallel branches and multiple resonances); the properties of the injection,

including the per unit value if it is provided or calculable; the injection width in micro or milliseconds, the number of measurements taken, the frequency range processed by the FFT, and a note on how the technique is validated. Note that only [175, 189–191] are online, with complete microcontroller integration of the estimation technique.

From Table 3.1, it can be deduced that even converter-implemented impulse-response techniques inject a significant disturbance into the network, with the majority of implementations injecting at least 0.5 pu of base current or voltage. However, this allows for a very short measurement period and an impedance estimation covering a large range of frequencies (almost all variations measure up to 2 kHz). In general, measurement periods are even shorter if the impulse is larger (i.e. 1.5 pu impulse). The types of grids varies greatly, from simple inductors to complex networks with parallel capacitors, therefore introducing resonant behaviour and replicating certain grid behaviours.

With regards to the converter controller, there are two main implementations of the converter induced impulse. Either it is injected as a current in the d-component of the current reference [189], or as a voltage in the q-component of the voltage reference during the zero crossing [190]. These are represented graphically in Fig. 3.11.

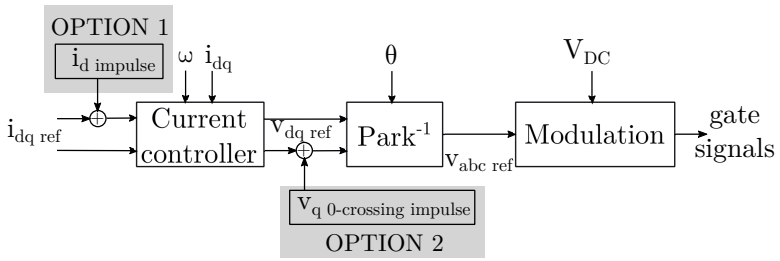


**Figure 3.11:** Typical locations of converter induced impulses. pseudo random binary sequence injection location would be similar.

As an alternative to the FFT, the impulse-response technique could utilise the Wavelet Transform (WT) as a means of analysing measurement results, as per [193]. The difference between FFT and WT is that FFT compares a given signal to sinusoidal signals in order to decompose the signal into individual frequencies; whereas WT compares a given signal to wavelets [194]. There are multiple advantages to this: the WT is more suited to analysing a transient signal; and the WT is capable of identifying when a specific frequency appears in a signal and when it ends [195]. This is because

**Table 3.1:** Various implementations of the converter injected impulse-response technique

| Ref | Dist. type | Filter | Type of grid | Injection properties | Injection width | Measurements | Target freq. range | How is it validated? |
|---|---|---|---|---|---|---|---|---|
| [175] | V | L | Circuit 1: L only Circuit 2: L parallel with C | Triangular | 500 $\mu$s | 8 transient cycles and 8 steady state cycles | $<1$ kHz | Freq sweeps |
| [192] | V | L | Circuit 1: RL Circuit 2: RL parallel with RC Circuit 3: Multiple resonances | Stepped injection with a maximum amplitude of $\sim 0.5$ pu | $\sim 80$ ms | 8 transient cycles and 8 steady state cycles | $<1$ kHz | Ideal trace calculated |
| [189] | I | L | Circuit with L parallel to CR | 1.5 pu | $\sim 1$ ms | 1 transient cycle and 1 steady state cycle | $<2$ kHz | Freq sweeps |
| [186] | I | L | Circuit with multiple resonances | 60 - 100 A (Base values not specified) | 650 $\mu$s | 8 transient cycles and 8 steady state cycles | $<2$ kHz | Ideal trace calculated |
| [191] | I (x2) | LCL | Simple RL | $\sim 0.5$ pu | 2 pulses: 0.5 ms and 0.7 ms | 1 transient cycle and 1 steady state cycle | 120 Hz - 2 kHz | Ideal trace calculated |
| [190] | V | LCL | Simple RL | 0.1 pu | 1 or 2 ms | Not specified | 150 Hz - 1.65 kHz | Known RL |

the wavelet can be both compressed and expanded to accommodate for the various frequencies, but it can also be shifted, to undertake wavelet estimations at different time instances. This is different to FFT as the exact location of a frequency in the time domain cannot be determined. With regards to the application of post-disturbance voltage and current analysis, as per [193, 196], the use of the WT has significantly reduced the number of periods required for pre- and post- disturbance analysis (from 8 periods to one period).

#### 3.2.2.2.2 Pseudo random binary sequence

The pseudo random binary sequence (PRBS) injection is a pre-determined sequence of wide-band excitation without the high total harmonic distortion (THD) of the impulse-response technique [117, 197, 198], with the flow chart presented in Fig. 3.12. These signals are in effect ones and zeros [199]. The length of the sequence, its magnitude and the switching frequency determines the achievable spectral resolution [200]. Compared to the impulse-response technique, this technique can work in much higher SNR conditions with significantly lower injection amplitude [116]. The spectral energy content of the injection can also be controlled in order to minimise interference with normal grid control and maximise the response of the desired frequencies [201]. Similarly to the impulse-response technique, FFT is applied to the measurements in order to estimate the spectral impedance [202], with the main advantage of improved immunity against the effect of nonlinear distortions.

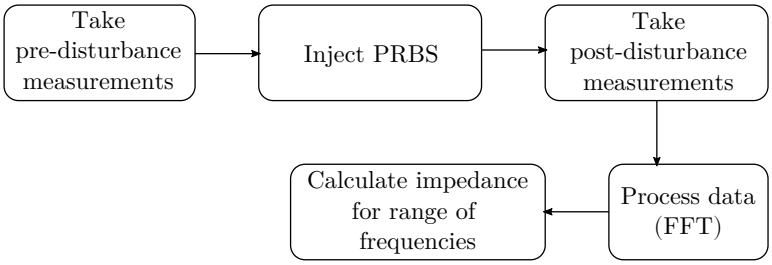


**Figure 3.12:** Flow chart for the PRBS technique.

### 3.2.3 Quasi-passive techniques

Quasi-passive techniques combine an observer with an active technique. The observer is employed to identify *when* the network impedance may have changed. If it is determined that a change has occurred, the active technique is triggered. This a compromise between maximising quality of estimation and reducing the occurrence of a disturbance injection: by tracking changes to the grid, a pre-determined criterion can initiate the active technique, introducing a disturbance on the system only when necessary [141, 190].

In [141], the trigger is a “quality threshold" ($\Gamma$). The quality threshold is the “voltage error", squared, divided by the current, averaged over a sampling window (3.22). It requires the latest grid impedance and grid voltage estimations as well as voltage and current measurements. The window is $k$ samples long. When the estimation values are correct, $\Gamma$ should be close to zero.

$$\Gamma_k = \frac{1}{2k} \sum_{i=k-n}^{k+n} \frac{||V_i - I_{n\,i}\hat{Z}_{n\,i} - \hat{E}_i||^2}{|I_{n\,i}|} \tag{3.22}$$

Should a grid event affect the grid impedance, the estimation becomes outdated and $\Gamma$ will increase. Once $\Gamma$ goes past a pre-determined threshold, it triggers the estimation process [141].

Ref. [190] proposes a Luenberger observer in order to trigger the active technique. The Luenberger observer is very similar to the Kalman Filter except that there is no change in "correction" gain and a linear state matrix is employed. The active technique is initiated when the difference between the estimated PCC voltage ($\hat{U} = f(I_n, \hat{E}, \hat{Z}_n)$ ) and the measured PCC voltage ($U$) exceeds a pre-determined magnitude ($\Delta U = U - \hat{U}$).

Quasi-passive techniques, however, introduce new delays due to the time required for the observer to detect an impedance change [141].

## 3.3 Comparison table of local impedance estimation techniques

Table 3.2 presents a summary of the local impedance estimation techniques found in the literature. The column are as follows

- Target frequencies: the frequencies for which the impedance is estimated.
- Disturbance amplitude: Some techniques require large disturbances, and some techniques don't require any disturbance.
- Disturbance duration: The duration of the disturbance per impedance estimation routine.
- Considered SCR networks: This column aims to identify if the various papers for each technique cover a range of network strengths, identifying whether some techniques are more popular for specific network strengths.
- Considered X/R ratios: This column aims to identify if various impedance to resistance ratios are covered by the literature.
- Typical error: The estimations are sometimes compared to the name plate values, mathematical models of the experimental set-up or frequency sweep results, indicating how accurate the estimations are. Techniques that yield an error of $< 2\%$ are considered to have low error. Between 2% and 5%, the error is medium. Any error larger than 5% is considered large.
- Comments: This column aims to highlight an important aspect of the technique which is not necessarily covered by the other columns.
- Data analysis techniques: Various analysis techniques are used such as FFT, WT, algebraic or RLS.

**Table 3.2:** Comparison of Local Impedance Estimation Techniques

| Technique | References | Target frequencies | Disturbance amplitude | Duration of disturbance | Are various SCR networks discussed? | Are various X/R ratios discussed? | Typical error | Comments | Data analysis technique |
|---|---|---|---|---|---|---|---|---|---|
| PMU (Adaptive) | [155] | $\omega_1$ | —— | —— | Yes | No, only $X_n >> R_n$ | Inconclusive | Only relevant for transmission level | Adaptive |
| PMU (RLS) | [31, 32, 156, 157] | $\omega_1$ | —— | —— | Yes | Yes | Low / Med | Stable estimations but not fast | RLS |
| PMU (Algebraic) | [118, 158] | $\omega_1$ | —— | —— | Yes | No, only $X_n/R_n = 0.2$ | Inconclusive | Limited research undertaken | Algebraic |
| Observers | [92, 160–164, 203] | $\omega_1$ to $\omega_{50}$ | —— | —— | Yes | Yes | Dependent on grid conditions | Dependent on grid event occurrence | FFT |
| Kalman Filter | [166, 167] | $\omega_1$ only $\omega_1$ to $\omega_{13}$ | —— | —— | Yes | No, only X/R ratios of $<$ 1.2 tested | Low / Variable | Very complex | KF |
| Frequency sweeping | [128, 130, 132, 168–171, 173, 174] | As required | $\sim$ 0.01 pu | 32 $\times$ $T_{fund}$ to $\sim$ 1 min per harmonic | Yes | Yes | Low | Invasive and time consuming | FFT |
| Nonharmonic excitation (FFT) | [115, 138–140, 176, 177] | $\omega_1$ | 0.05 to 0.077 pu | 0.02 to 0.04 s | Yes | No, only X/R ratios of $<$ 0.3 tested | Low / Med | Assumes equiv. impedance | FFT |
| Nonharmonic excitation (WT) | [137, 178] | $\omega_1$ | 3 A (base unit not specified) | 0.025 s | No | No | Low / Med | Assumes equiv. impedance | WT |
| Simultaneous frequency sweeping | [172] | As required | $\sim$ 0.02 pu per freq | 0.01 to 1 s | No | No | Low | Invasive | FFT |
| P/Q reference variation | [100, 141, 144, 179–184] | $\omega_1$ | Setpoint step change 0.1% to 10% | $\sim$ 0.1 to 1 s | No | No, only X/R ratios of $<$ 0.75 tested | Low / Med | Rate of estimation restricted by settling time | RLS or Algebraic |
| Hardware injected impulse-response | [68, 129, 130, 134, 175, 185–187] | $\omega_1$ to 10 kHz | $\sim$ 1.5 to 5 pu | 500 $\mu$s to 1.6 ms | Yes | Yes | Medium | High THD | FFT |
| Converter injected impulse-response (FFT) | [101, 189–192] | $\omega_1$ to 2 kHz | 0.1 to 1.5 pu | 500 $\mu$s to 80 ms | Yes | Yes | Medium | High THD | FFT |
| Converter injected impulse-response (WT) | [193, 196] | $\omega_1$ to 2 kHz | 20 A (base units not specified) | 1 ms | No | No | Inconclusive | High THD but lower processing time | WT |
| Pseudo random binary sequence injection | [116, 117, 145, 197, 198, 200–202, 204] | $\omega_1$ to 3 kHz | 0.1 to 0.2 pu | 5 $\times$ $T_{fund}$ to 1 s | Yes | Yes | Low / Med | Complex | FFT |

## 3.4 Estimation non-convergence

Non-convergence of the impedance estimation occurs when there are insufficient constraints, and an infinite set of solutions satisfy the equations. In the case of impedance

estimation, this occurs when the converter power output and the grid conditions are stationary, and only one set of measurements is obtained. To illustrate this, the PCC voltage and grid current for a single steady state operating point ($P = -1$ pu and SCR $= 1$) is used to estimate reactance and stiff grid voltage in the $qd$-frame (all unknown parameters) with the aide of four equations: two derived from Kirchoff's Voltage Law and two derived from power transfer equations.

First, KVL across the grid impedance is as follows.

$$e_{qd} - u_{qd} = R_n i_{nqd} + \frac{di_{nqd}}{dt} L_n \tag{3.23}$$

By separating the complex planes

$$\frac{1}{\omega}\frac{d}{dt} i_{nq} = -i_{nq}\frac{R_n}{X_n} - i_{nd} + \frac{e_q}{X_n} - \frac{u_q}{X_n} \tag{3.24}$$

$$\frac{1}{\omega}\frac{d}{dt} i_{nd} = +i_{nq} - i_{nd}\frac{R_n}{X_n} + \frac{e_d}{X_n} - \frac{u_d}{X_n} \tag{3.25}$$

These can be rearranged as

$$X_n = \frac{e_q i_{nd} - u_q i_{nd} - e_d i_{nq}}{i_{nq}^2 + i_{nd}^2} \tag{3.26}$$

$$R_n = \frac{e_q i_{nq} - u_q i_{nq} + e_d i_{nd}}{i_{nq}^2 + i_{nd}^2} \tag{3.27}$$

Consider also the PCC power equations (3.28) and (3.29) below, which are the vector equivalent of equations (2.3) and (2.5).

$$P = \frac{3}{2}\frac{u_q(R_n(e_q - u_q) - X_n e_d)}{X_n^2 + R_n^2} \tag{3.28}$$

$$Q = \frac{3}{2}\frac{u_q(X_n(e_q - u_q) + R_n e_d)}{X_n^2 + R_n^2} \tag{3.29}$$

With equations (3.26) to (3.29), there are four equations and four unknowns, $X_n$, $R_n$, $e_q$ and $e_d$. Usually, equal numbers of equations and unknowns results in a single

set of correct values. However, this is not the case here. Assuming a constant X/R ratio, hence reducing the problem into a three dimensional problem, the four equations above can be plotted, as per Fig. 3.13.

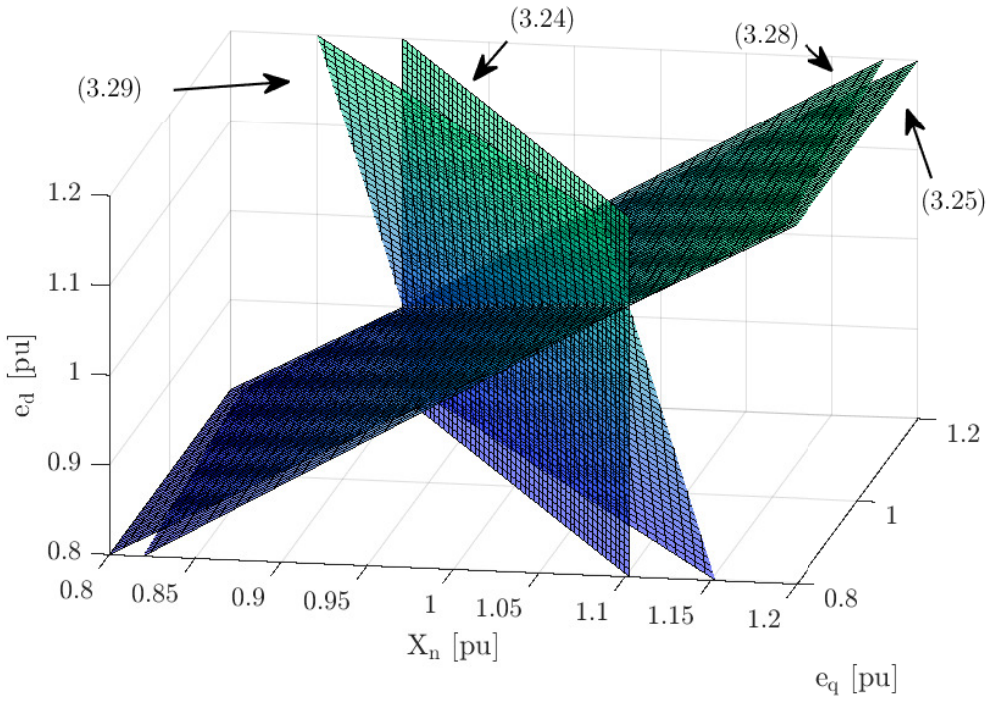


**Figure 3.13:** Plotting the four system equations, 3D view.

Although it is not clear from Fig. 3.13, there is a line of possible solutions that satisfy all equations. This is clearer in Fig. 3.14 which presents a different view of the same plot.

These figures visually explain why the iterative and algorithmic methods described in Section 3.2 always require some form of disturbance or change in operating point in order to allow for convergence. Consider Fig. 3.15 where equations (3.26) and (3.27) are plotted for two different operating points ($P = -1$ and $-0.95$ pu). In this instance, the two sets of equations at two different operating points intersect clearly and produce a singular answer.

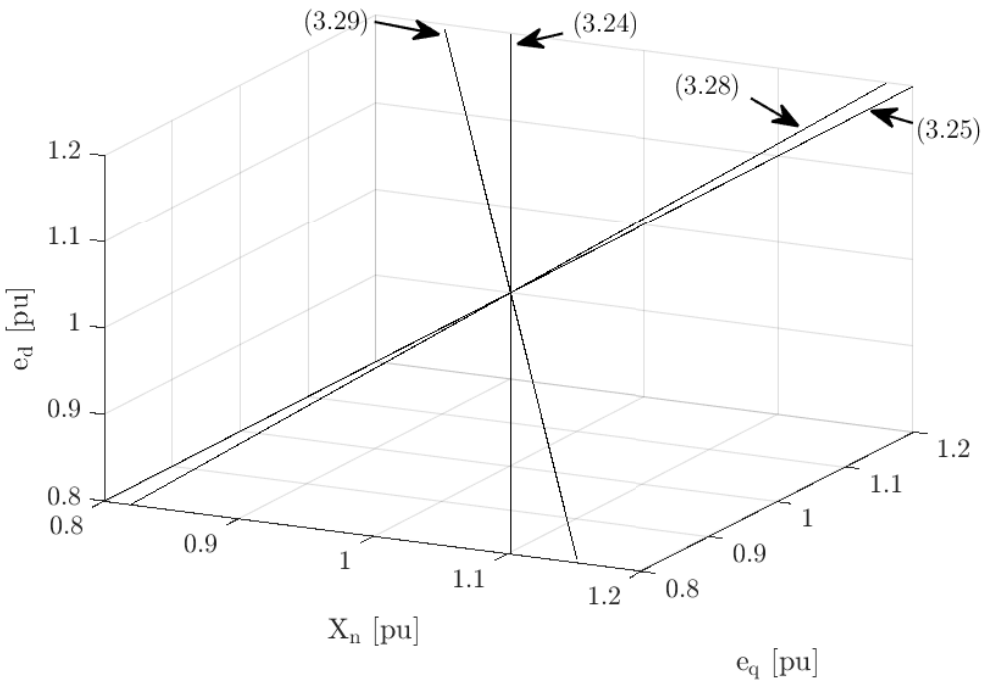


**Figure 3.14:** Plotting the four system equations, alternative view.

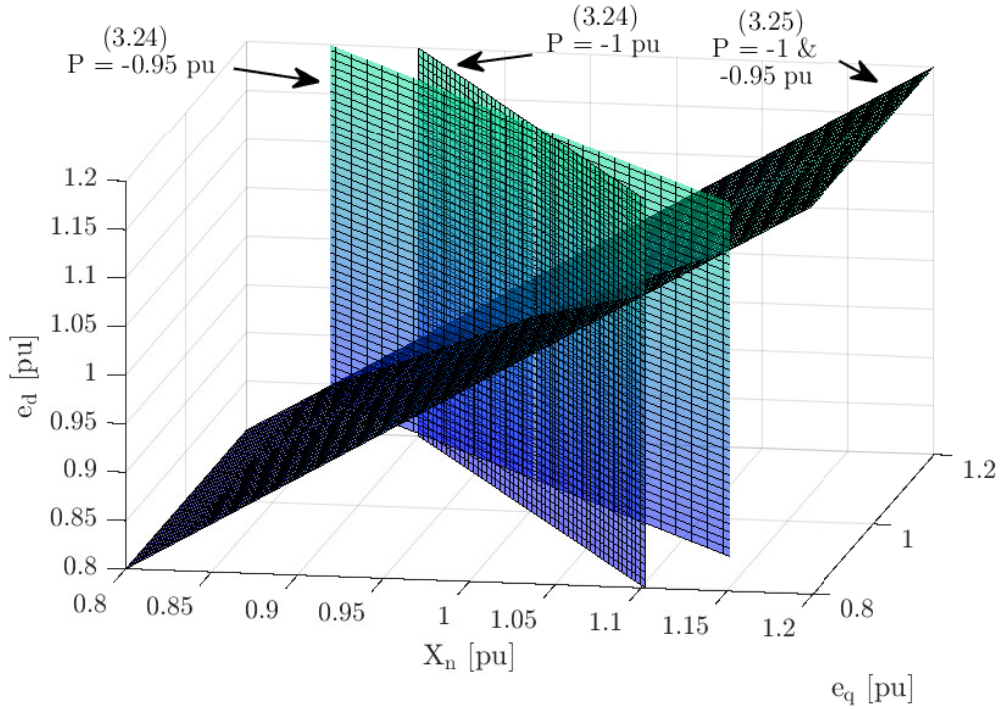


**Figure 3.15:** Plotting two sets of equations (for two different operating points).

## 3.5 Testing various impedance estimation techniques

The ideal impedance estimator produces accurate and on demand results without injecting any disturbances into the network. Unfortunately, this is not possible because passive techniques are by definition disturbance free, and are therefore reliant on external grid events. The two most suitable estimators for the purposes of real-time adaptable control are the nonharmonic excitation technique combined with FFT and the P/Q variation technique combined with RLS. These techniques are chosen due to the accuracy, as outlined in Table 3.2. They are also on demand, and unlike transient techniques like the impulse injection, produce a small amount of noise. This is especially true for the P/Q variation technique as small variations in active and reactive power are common in normal operation. Observers are deemed inappropriate as they are dependent on disturbances within the system.

### 3.5.1 Thévenin equivalent estimation

The impedance estimation techniques that only target the Thévenin equivalent impedance are simpler to integrate into controllers and produce estimation results much more quickly than the wide spectrum alternatives. In this section, the nonharmonic injection and the P/Q variation techniques are tested in simulation. They are subjected to the same test, where they are integrated into a converter controller which operates at varying active power levels. This is repeated for two different SCRs. As the nonharmonic injection technique produced better results in simulation, it is subsequently integrated and tested in hardware.

#### 3.5.1.1 Simulation of the nonharmonic injection technique

The nonharmonic injection technique applied to simulation models injects a perturbation voltage of 60 Hz and 0.02 % of the peak phase voltage. Hence, the disturbance is very small. The disturbance is maintained for 9 periods, and only the final three are sampled at a sampling rate of 20 samples per period. Hence, the estimation is based on 60 samples of phase A current and phase A voltage and the total length of disturbance

is 150 ms.

The estimator is tested as per Fig. 3.16, where the estimator is subjected to various power levels (0,−0.4,−0.7,−0.9) and two different SCRs (1 and 3). The estimation is extracted at the end of each power output, immediately before the change in power reference. For convenience, the estimation update occurs at the dotted lines.

The purpose for this test is to assess the estimator's capabilities in various conditions. The error of the estimation for both resistance and reactance is within 5 %.

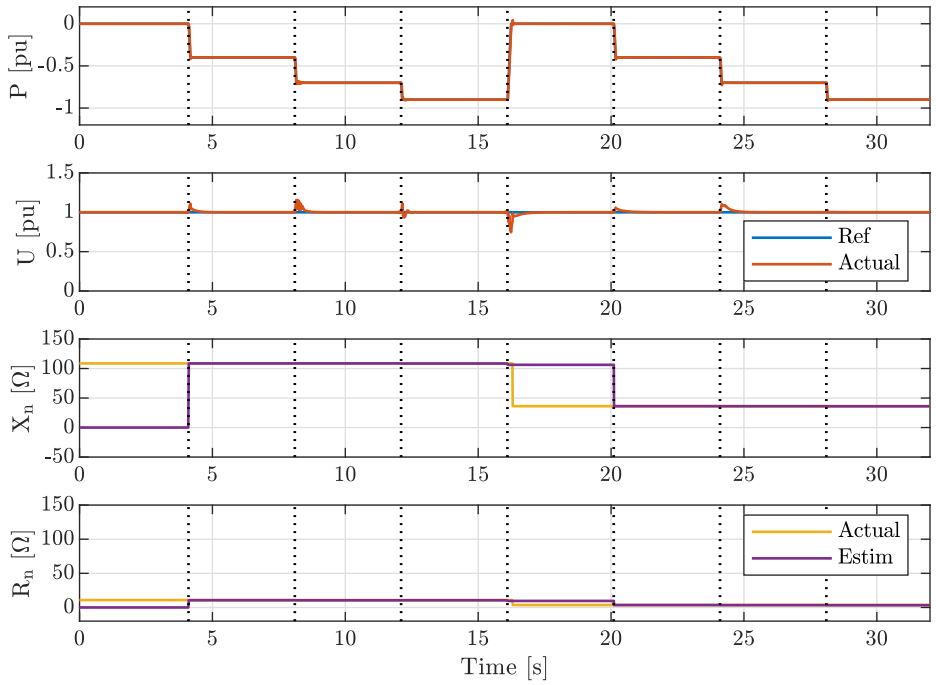


**Figure 3.16:** Testing of the online nonharmonic impedance estimator for varying power levels and grid conditions.

### 3.5.1.2 Simulation of the P/Q variation technique

The P/Q variation technique is submitted to the same test as the nonharmonic injection technique. The implementation of the P/Q variation impedance estimator uses 5 different combinations of $P^*$ and $U^*$ values. Each combination is given 0.4 s to settle, hence the estimation process requires 2 s and produces 5 sets of measurements of $u^c_{qd}$ and $i^c_{nqd}$. The power variation sequence is [0.0004 0.0008 0.0006 0.0002] pu and the

voltage variation sequence is [0.0025 0.0037 0.0013 0.005] pu. This was determined by trial and error across different conditions. The results are presented in Fig. 3.17. The error of the estimation for both resistance and reactance is much more variable: in the strong grid the error is within 20 % for reactance but over 50 % error for resistance. In a weak grid, especially at high power outputs, the estimation is completely wrong for both. Error occurs when steady state conditions are not completely achieved, a problem more common in the weak grids given the increased settling time.

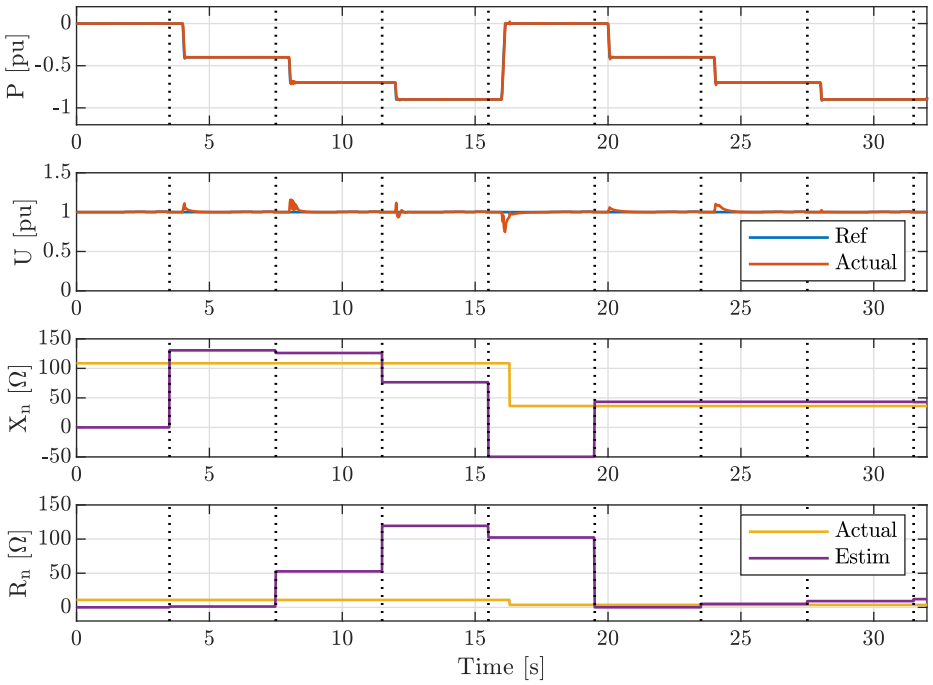


**Figure 3.17:** Testing of the online P/Q variation impedance estimator for varying power levels and grid conditions.

#### 3.5.1.3 Comparison between nonharmonic injection and P/Q variation techniques

In terms of consistency and accuracy, the nonharmonic injection is much more consistent. The problem with the P/Q variation technique is that it requires absolute steady state values, and even small amounts of noise can disrupt the estimations.

Some amendments could be made to improve the estimations, such as increasing the

measurement set or using a moving average filter to remove some of the noise. However, this would significantly increase the duration of the estimation process, something that is undesirable in a variable grid. Thus, the nonharmonic injection technique is to be implemented into the controller going forward.

#### 3.5.1.4 Hardware testing of the nonharmonic injection technique

The nonharmonic injection technique is tested at two SCRs for various levels of power, as per Fig. 3.18. In this instance, the perturbation frequency is 75 Hz, and the magnitude of the perturbation is 6 mV. Further, a moving average filter of four samples is used to smooth the current and voltage values used for the estimation.

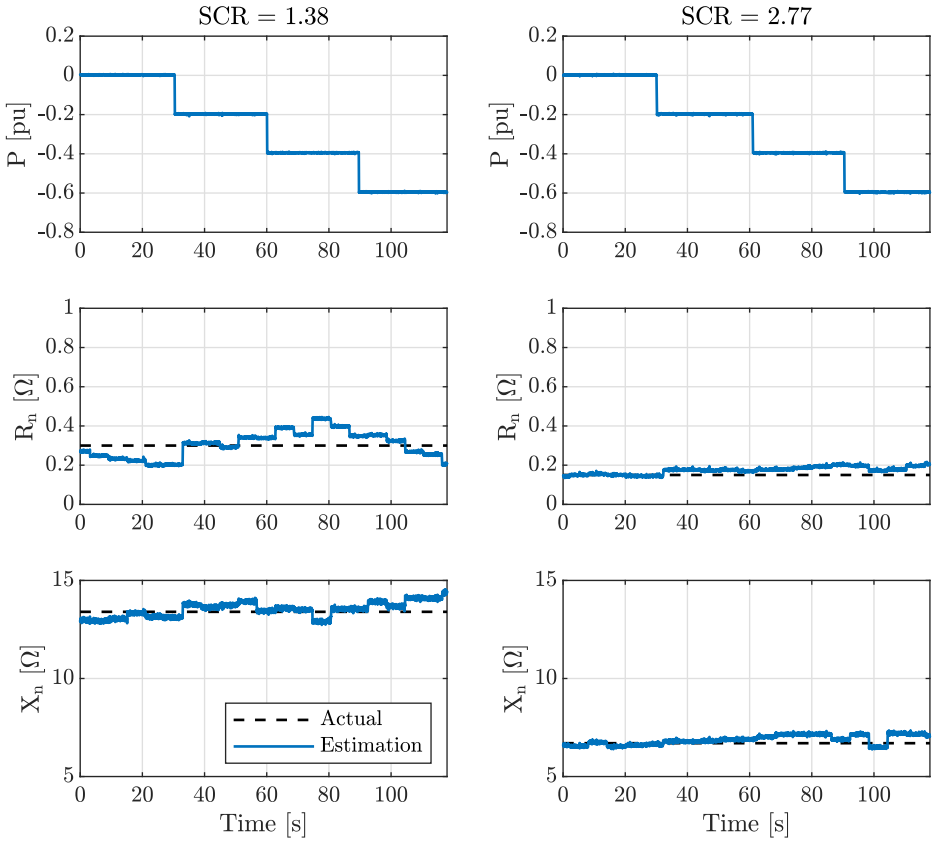


**Figure 3.18:** Output of impedance estimator for various power levels.

In Fig. 3.18, the top plot represents the various power levels at which the impedance

estimator is tested to ensure the estimations are power agnostic. The middle plot displays the resistance estimation and the bottom plot displays the reactance estimation. The reactance is dominant and thus the crucial parameter in the network given the high $X_n/R_n$ ratio ($>$ 40). The reactance estimation error is consistently less than 10 % at all power levels and both SCRs. The resistance is a bit less accurate, with the error at approximately 35 % in the worst conditions. However, as a function of impedance magnitude, the error of the resistance is acceptable. Therefore, for the purposes of this thesis, the nonharmonic impedance estimator is determined to be reliable and able to produce acceptable estimations irrespective of the grid stiffness and the active power.

### 3.5.2 Wideband frequency impedance estimation

Estimating the impedance across a wide frequency spectrum allows for a more detailed analysis of higher order grid impedance. As explained in Section 2.1.2, this thesis is particularly interested in the identification of problematic resonances. As resonances can vary with changing loads [53], grid configuration [43], reactive power provision via capacitor banks [66], and varying grid impedance [53], it is difficult to mitigate for resonances universally. The wideband frequency impedance estimation techniques tested in this section are based on the transient techniques presented in Section 3.2.2.2 and allow for real-time identification of problematic resonances.

Chapter 6 follows on from this section, proposing automatic controller response to the identification of problematic resonances.

#### 3.5.2.1 Electrical system transfer functions

Consider the grid in Fig. 3.19.

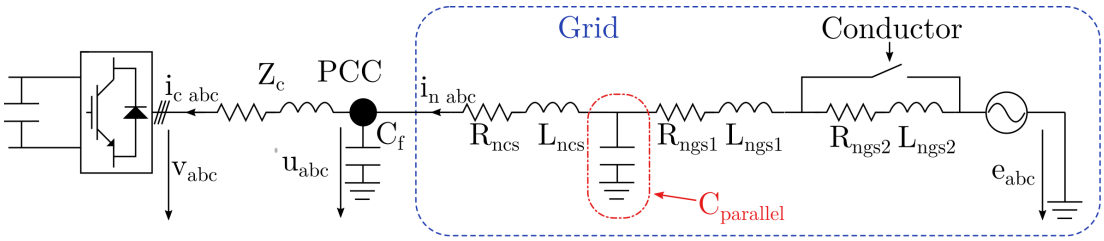


**Figure 3.19:** System under study with parallel resonance.

Where Fig. 3.19 is an expansion of Fig. 2.1 which assumes Thévenin equivalent impedance. The purpose for the contactor is to introduce a step change in resonance frequency, given that [43, 69]

$$f_{res} = \frac{1}{2\pi\sqrt{(L_{ngs1} + L_{ngs2})C_p}} \tag{3.30}$$

From (3.30), it can be inferred that the impedances on the grid side of the parallel capacitor ($Z_{ngs1}(s)$ and $Z_{ngs2}(s)$), as well as the parallel capacitor itself, are the key parameters establishing the frequency of the resonance. The converter side impedance of the grid ($Z_{ncs}(s)$) does not impact the frequency of the resonance, but rather dampens it.

The grid impedance can be calculated as follows

$$Z_n(s) = \frac{U(s)}{I_n(s)} = Z_{ncs}(s) + \frac{(Z_{ngs1}(s) + Z_{ngs2}(s))Z_{parallel}(s)}{Z_{ngs1}(s) + Z_{ngs2}(s) + Z_{parallel}(s)} \tag{3.31}$$

As $Z_{ncs}(s) = R_{ncs} + sL_{ncs}$, $Z_{ngs1}(s) = R_{ngs1} + sL_{ngs1}$, $Z_{ngs2}(s) = R_{ngs2} + sL_{ngs2}$ and $Z_{parallel}(s) = 1/(sC_p)$, (3.31) can be extended to the following transfer function

$$Z_n(s) = R_{ncs} + L_{ncs}s + \frac{R_{ngs1} + R_{ngs2} + (L_{ngs1} + L_{ngs2})s}{C_p(R_{ngs1} + R_{ngs2} + (L_{ngs1} + L_{ngs2})s)} \tag{3.32}$$

Also worth considering is how the capacitor of the PWM filter will interact and affect the perceived impedance at the PCC, should the converter current be used instead of the grid current. For completeness, $Z_{cf}(s) = 1/(sC_f)$. To differentiate this version of the grid impedance from the standard definition, a dash is applied, i.e. $Z'_n(s)$.

$$Z'_n(s) = \frac{U(s)}{I_c(s)} = \frac{Z_{cf}(s)Z_n(s)}{Z_{cf}(s) + Z_n(s)} \tag{3.33}$$

#### 3.5.2.2 Implementation of the wideband impedance estimator

To test the wideband impedance estimator, two sets of parameters are used. Within each set of parameters, the connection and disconnection of $Z_{ngs2}(s)$ with the contactor, as seen in Fig. 3.19, affects the resonance frequency. Thus, the four resulting

resonances, and the impedance composition of each resonance, is described in Table 3.3.

**Table 3.3:** Grid side parameters for specific parallel resonances

| | $f_{res}$ = 155 Hz ($Z_{ngs2}$ bypassed) | $f_{res}$ = 110 Hz ($Z_{ngs2}$ included) | $f_{res}$ = 170 Hz ($Z_{ngs2}$ bypassed) | $f_{res}$ = 139 Hz ($Z_{ngs2}$ included) |
|---|---|---|---|---|
| $R_{ncs}$ | 1.81 Ω | 1.81 Ω | 1.81 Ω | 1.81 Ω |
| $L_{ncs}$ | 57.6 mH | 57.6 mH | 57.6 mH | 57.6 mH |
| $C_p$ | 18.3 mF | 18.3 mF | 15.2 mF | 15.2 mF |
| $R_{ngs1}$ | 1.81 Ω | 1.81 Ω | 1.81 Ω | 1.81 Ω |
| $L_{ngs1}$ | 57.6 mH | 57.6 mH | 57.6 mH | 57.6 mH |
| $R_{ngs2}$ | N/A | 1.78 Ω | N/A | 0.905 Ω |
| $L_{ngs2}$ | N/A | 56.7 mH | N/A | 28.8 mH |

Where a step change in resonance occurs from $f_{res}$ = 155 Hz to 110 Hz by connecting $Z_{ngs2}(s)$, and vice versa by disconnecting the impedance. It is the same case for $f_{res}$ = 170 Hz and 139 Hz.

The tuning used for the outer loop is different in this Section (and in Chapter 6) than it is from the rest of the thesis. For completeness, the outer loop tuning for this section is included in Appendix A.1.2 – it is different from the rest of the thesis because of instability introduced by the resonances. Two sets of tuning were used, with the faster gains used to plot the impedance estimations where $f_{res}$ = 170 Hz and 139 Hz, and a slow tuning, obtained for $f_{res}$ = 155 Hz and 110 Hz. No control changes are made to the PLL or the current controller.

#### 3.5.2.3 Results

The industry standard for wide spectrum impedance estimation is the frequency sweep technique. However, this is a lengthy process as it is repeated for every frequency of interest. According to Table 3.2, the main alternative is the impulse-response technique, which is highly disruptive. It is also well covered by the literature. Thus, two alternative perturbations are studied: one stems from a grid event (i.e. as a result of a connection or disconnection of the impedance $Z_{ngs2}(s)$), and the other from a step change in power reference.

Fig. 3.20 and 3.21 below plot the values for $Z_n(s)$ and $Z'_n(s)$, respectively, for

a grid perturbed by a step change in impedance. The solid lines are the theoretical impedances, and the dotted lines with crosses are the estimated impedance. The value of the currents and voltages used for the estimation are collected immediately after the grid event. The equivalent impedances (i.e. $Z_n(s)$ and $Z'_n(s)$ at $f_{res} = 170$ Hz) are determined using the same voltage measurement but different current measurements, as per (3.31) and (3.33).

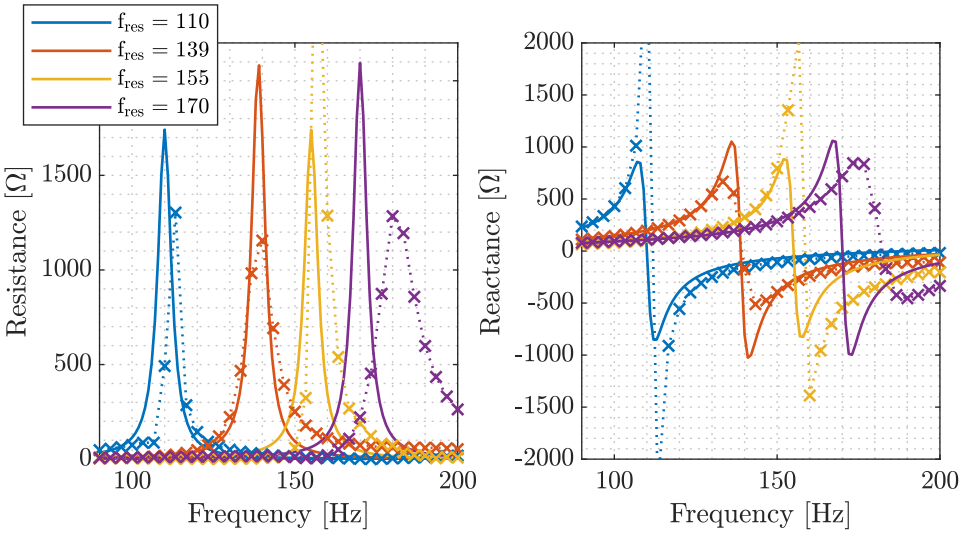


**Figure 3.20:** Estimation of $Z_n(s)$ when subjected to grid event perturbation.

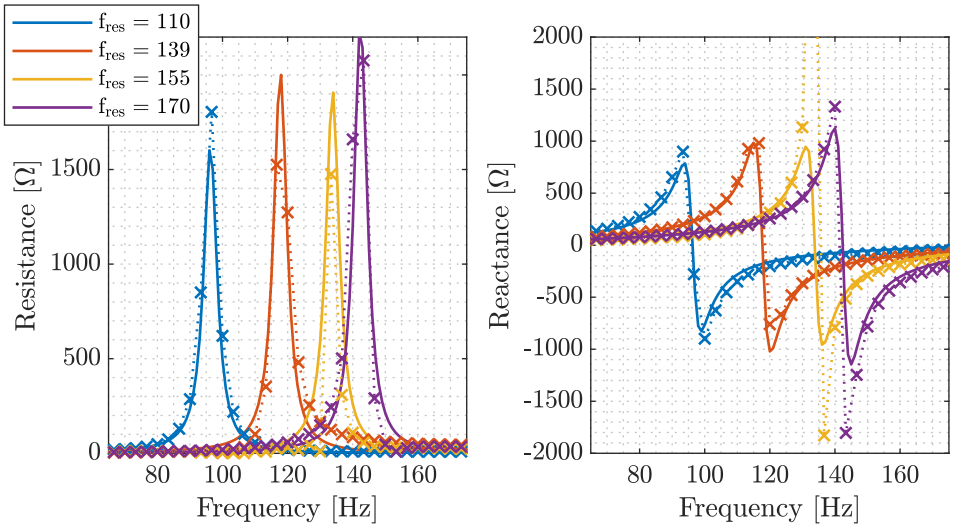


**Figure 3.21:** Estimation of $Z'_n(s)$ when subjected to grid event perturbation.

Comparing Fig. 3.20 and 3.21, it can be determined that $Z'_n(s)$ estimations are

more consistent and accurate than $Z_n(s)$.

Similarly, Fig. 3.22 and 3.23 below plots the impedance estimation when subjected to a power reference step change perturbation.

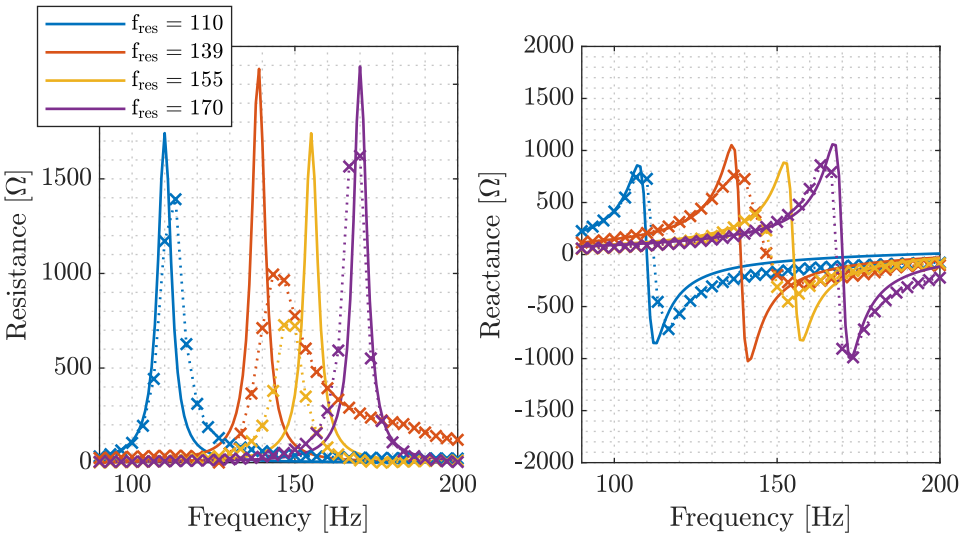


**Figure 3.22:** Estimation of $Z_n(s)$ when subjected to grid event perturbation.

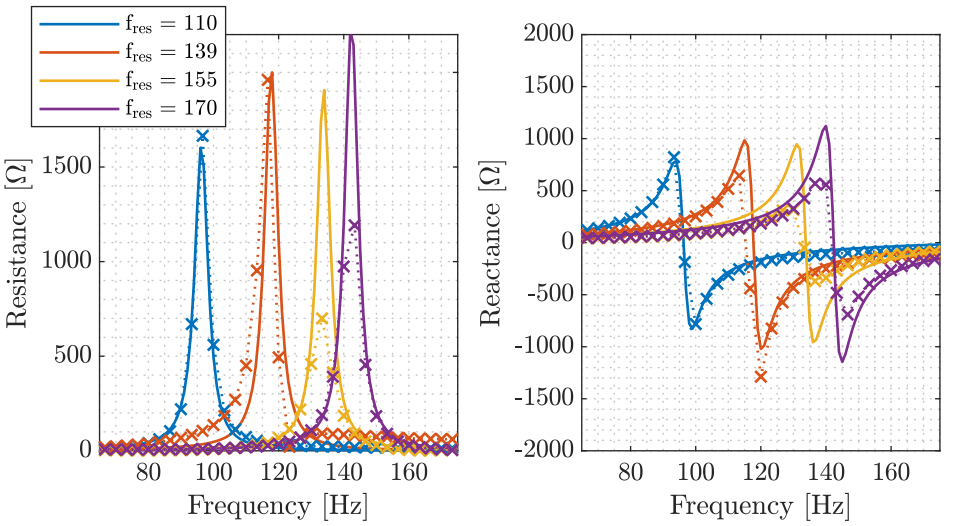


**Figure 3.23:** Estimation of $Z'_n(s)$ when subjected to grid event perturbation.

Again, the estimations for $Z'_n(s)$ are better than for $Z_n(s)$. Thus, the impedance estimation results presented in Fig. 3.20 – 3.23 present superior repeatability and accuracy of the $Z'_n(s)$ estimation process, where the converter current is used instead of the grid current, irrespective of the source of the perturbation.

The main advantage of $Z_n(s)$ over $Z'_n(s)$ is that it produces the true location of the grid resonance as a function of grid impedance. However, depending on the purpose of the impedance estimation, this might not matter. If adaptation measures can be taken with knowledge of $Z'_n(s)$ rather than $Z_n(s)$, then this makes no difference.

It is also observed that when implemented in a converter, the accuracy of any wide-band impedance estimation diminishes rapidly a frequencies higher than approx. 300 Hz. This is due to the increased impact of the converter filtering at those frequencies. This is deemed acceptable, as there is no benefit in determining resonances at frequencies that are sufficiently dampened by filters.

# Chapter 4

# Decoupling Vector Current Control Power and Voltage Loops in Weak Grids

As seen in Section 2.1.1, there is an undesirable coupling between active power and PCC voltage in weak grids. The PCC voltage is affected by changes in active power transfer, and as a result there is a risk that any change in active power reference can cause the outer loops to oscillate against one another, especially if the power loop is responsive. The risk increases as SCR reduces and active power flow increases. This chapter seeks to understand the mathematical relationship of this undesirable coupling and provide a solution that can be retrofitted into existing converter controllers.

This chapter is arranged as follows. First, the objectives are set out. Then, the coupling between active power and PCC voltage is derived and the pre-emptive voltage decoupler is presented. It is studied using small signal techniques, simulations and laboratory experiments.

## 4.1 Objectives

The objectives for an improved VCC, capable of adapting to varying grid strengths, as follows.

1. The proposed controller must be based on classical VCC, preserving the functions of the PLL, current controller and outer loops. These considerations will facilitate the retrofitting existing VCC-based converters while maintaining desirable attributes such as current limiting capabilities.

2. Demonstrate small signal stability at high power outputs for variable SCR values.

3. Maintain VCC dynamic capabilities independently of SCR. This is assessed against a power controller rise time target of $<$ 40 ms and a settling time target of $<$ 400 ms.

4. Demonstrate resiliency to grid events that cause sudden SCR changes.

### 4.1.1 Coupling between active power and PCC voltage

Ideally, the active power controller affects the active current in a linear and predicable way whilst having no impact on the PCC voltage, independently of SCR. Thus, by extension, active current and reactive current should be completely decoupled. This relationship is tested in Fig. 4.1, with Fig. 4.1a plotting active power versus active and reactive current for SCRs of 1, 3 and 5. Further, active current is plotted against reactive current in Fig. 4.1b. All the values are obtained from steady state operating points.

In Fig. 4.1a, the linear relationship between active power and active current is indeed maintained independently of SCR. However, if the controller is configured to control voltage at the PCC, a coupling between active power and reactive current exists, and increases in weak grids due to the increased voltage support requirements through the provision of reactive power. This coupling within the grid is reflected in the active current to reactive current plot of Fig. 4.1b. Decoupling active power and PCC voltage should be at the core of improving the integration of VCC in weak grids.

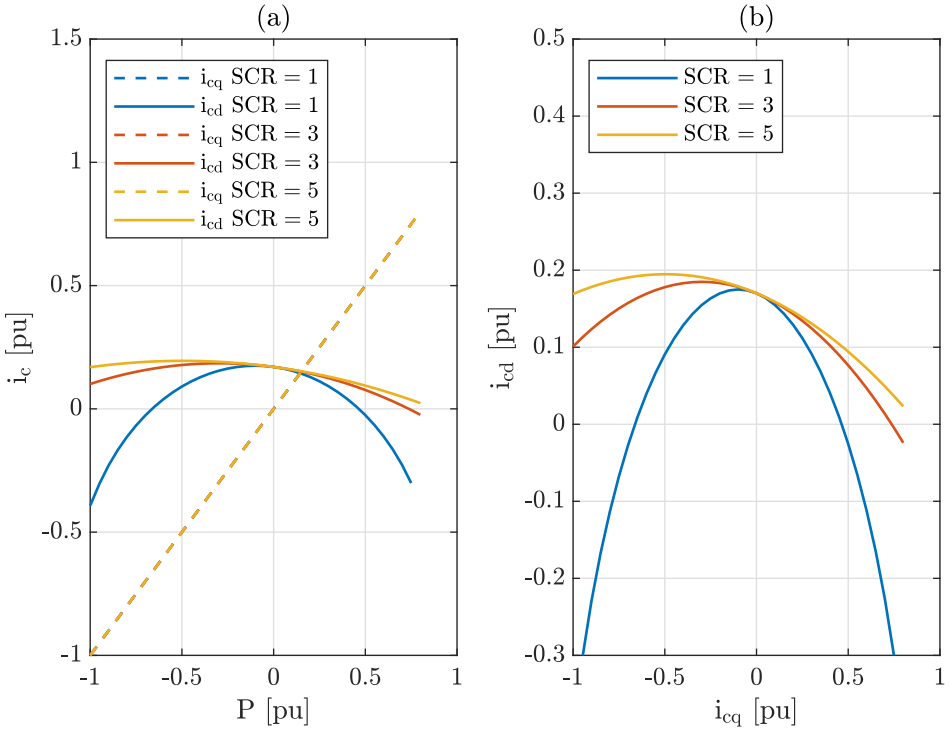


**Figure 4.1:** In steady state conditions: (a) Relationship between active power and current; and (b) relationship between active and reactive current.

## 4.2 Mathematical derivation of the weak grid coupling

Understanding the mathematical relationship of the coupling that exists in weak grids is key to compensating for this coupling through controller action. Such a relationship was attempted in [98], but that proposal came short of properly decoupling active power and PCC voltage in practice. Thus, from first principles, consider equations (4.1) and (4.2) that describe the relationship between active power and reactive power to the grid impedance, voltage and current, using phasor representation (first introduced in Chapter 2).

$$P = \frac{3U(EX_n sin(\delta) + R_n(Ecos(\delta) - U))}{X_n^2 + R_n^2} \tag{4.1}$$

$$Q = \frac{-3ER_nUsin(\delta) - 3EUX_ncos(\delta) + 3U^2X_n}{X_n^2 + R_n^2} \tag{4.2}$$

Given that $\mathbb{R}\text{e}(\overline{I}_n) = i_{nq} = P/3U$ and that $\mathbb{I}\text{m}(\overline{I}_n) = i_{nd} = Q/3U$ in instantaneous representation, and assuming that the grid and PCC voltage magnitudes are the same

$$i_{nq} = \frac{UX_n sin(\delta) + R_n(Ucos(\delta) - U)}{X_n^2 + R_n^2} \tag{4.3}$$

$$i_{nd} = \frac{X_n(Ucos(\delta) - U) - R_nUsin(\delta)}{X_n^2 + R_n^2} \tag{4.4}$$

Rearranging (4.3) and (4.4)

$$U(X_n sin(\delta) + R_n cos(\delta)) = R_nU + i_{nq}(X_n^2 + R_n^2) \tag{4.5}$$

$$U(X_n cos(\delta) - R_n sin(\delta)) = X_nU + i_{nd}(X_n^2 + R_n^2) \tag{4.6}$$

Given trigonometric function,

$$Asin(x) + Bcos(x) = \sqrt{A^2 + B^2}\, sin(x + atan(\frac{B}{A})) \tag{4.7}$$

(4.5) and (4.6) become

$$U(Z_n sin(\delta + atan(\frac{R_n}{X_n}))) = R_n U + i_{nq}(X_n^2 + R_n^2) \tag{4.8}$$

$$U(Z_n sin(\delta + atan(\frac{X_n}{-R_n}))) = X_n U + i_{nd}(X_n^2 + R_n^2) \tag{4.9}$$

Given that $tan(\theta_{Zn}) = X_n/R_n$,

$$U(Z_n cos(\delta - \theta_{Zn}) = R_n U + i_{nq}(X_n^2 + R_n^2) \tag{4.10}$$

$$U(Z_n sin(\delta - \theta_{Zn}) = X_n U + i_{nd}(X_n^2 + R_n^2) \tag{4.11}$$

combining (4.10) and (4.11), solving for $i_{nd}$, and taking the filter capacitor current into account with KCL ($\overline{I_c} = \overline{I_n} + \overline{I_{cap}}$)

$$i_{cd} = \frac{-UX_n \pm UZ_n\sqrt{1 - \frac{(R_n U + i_{cq}(X_n^2+R_n^2))^2}{U^2 Z_n^2}}}{R_n^2 + X_n^2} + \frac{U}{X_c} \tag{4.12}$$

where $X_c$ is the PWM capacitive filter reactance.

This equation is verified in Fig. 4.2 below, by superimposing the output of the equation (labelled "calculated" in legend) to the steady state values obtained from a simulation (labelled "simulated" in legend). The simulated values are obtained with the controller operating in PCC voltage control and active power mode.

As per Fig. 4.2, (4.12) produces and exact overlap. Therefore, it is possible to predict how the reactive current in the grid is impacted by the active current.

### 4.2.1 Implementation

Should the active current on the left hand side of (4.12) be added to the active current reference, the controller becomes pre-emptive. Thus, the integration of this branch in the controller can be described as a pre-emptive voltage decoupler (PVD), where the reactive current (and thus the PCC voltage) is decoupled from the active current (and

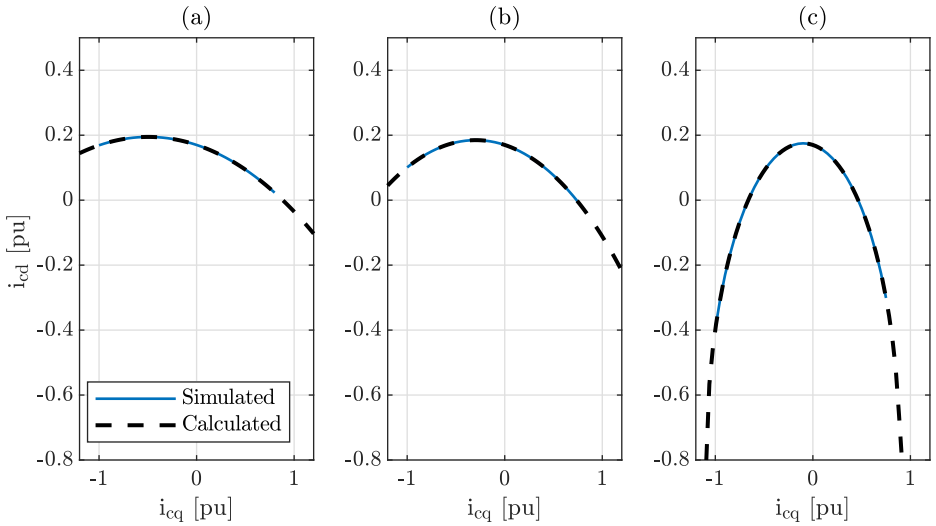


**Figure 4.2:** Relationship between active current and reactive current, comparing the reactive current obtained both from simulation and the equation (4.12) for (a) SCR = 5, (b) SCR = 3, and (c) SCR = 1 (conditionally to constant PCC voltage).

thus the active power). By adapting (4.12) in such a way, the output of the equation can be described as the feedforward current, or $i_{ff}$, as per (4.13).

$$i_{ff} = \frac{-UX_n \pm UZ_n\sqrt{1 - \frac{(R_nU + i^*_{cq}(X_n^2+R_n^2))^2}{U^2Z_n^2}}}{R_n^2 + X_n^2} + \frac{U}{X_c} \tag{4.13}$$

Equation (4.13) can be integrated into the control as per the block diagram presented in Fig. 4.3.

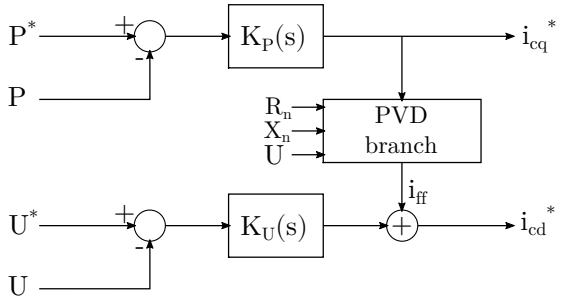


**Figure 4.3:** Implementation of the proposed PVD.

With equation (4.13), the PVD can compensate the reactive current for changes in active current, moving the burden of stabilising the PCC voltage for changes in active power reference from the voltage loop to the PVD branch. As changes in $i^*_{cq}$ are mapped

onto $i^*_{cd}$, the controller can anticipate and counteract the impact of power reference changes on the PCC voltage. The advantages of the PVD are (1) the avoidance of gain scheduling of the outer loop PI gains, and (2) the maintenance of standard outer loop implementation, whereby the active power loop is focused on the active power transfer, and the PCC voltage loop is focused on supporting the PCC voltage. No changes to the PLL or the current controller are required. The main disadvantage, however, is the PVD's dependency on knowledge of the grid impedance. The grid impedance determines the the values of $i_{ff}$, which affects $i^*_{cq}$ and by extension the PCC voltage. Thus, the effectiveness of this relationship is dependent on the implementation of a grid impedance estimator, otherwise the PVD runs the risk of under-compensating or over-compensating the decoupling of the PCC voltage from the active power.

## 4.3 Steady state stability

### 4.3.1 Time domain stability

In line with the testing done in Section 2.3.1.1, Fig. 4.4 plots the stability of VCC with PVD for a SCR of 3 and 1 using time domain simulations. Fig. 4.4b shows much improved VCC performance for weak grids compared to Fig. 2.21b – both the active power and the voltage settle more quickly. The stability region is also increased from all previous implementations, with stability achieved at $-0.9$ pu.

### 4.3.2 Small signal stability

To further study the steady state stability, small signal tools are used. The equivalent linearised equation of (4.13) is achieved by determining the derivative, resulting in (4.14).

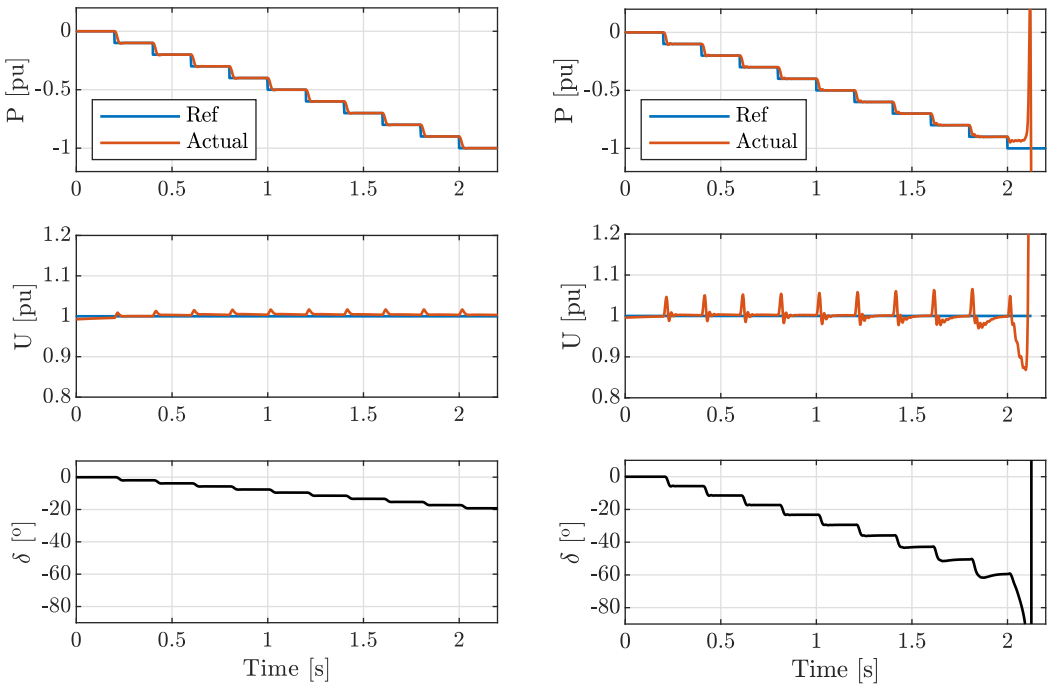


**(a)** SCR = 3. **(b)** SCR = 1.

**Figure 4.4:** Steady state performance of the proposed PVD in the time domain.

$$\Delta i_{ff} = -\frac{(X_n^2+R_n^2)i_{cq0}+R_nU_0}{Z_n\sqrt{U_0^2-\frac{((X_n^2+R_n^2)i_{cq0}+R_nU_0)^2}{Z_n^2}}}\Delta i_{cq}^* + \frac{Z_n\left(2U_0-\frac{2R_n((X_n^2+R_n^2)i_{cq0}+R_nU_0)}{Z_n^2}\right)}{2\sqrt{U_0^2\frac{((X_n^2+R_n^2)i_{cq0}+R_nU_0)^2}{Z_n^2}}}+\frac{X_n^2+R_n^2}{X_c}-X_n + \frac{}{X_n^2+R_n^2}\Delta U \tag{4.14}$$

This can be integrated into the closed loop transfer matrix as per Fig. 4.5.

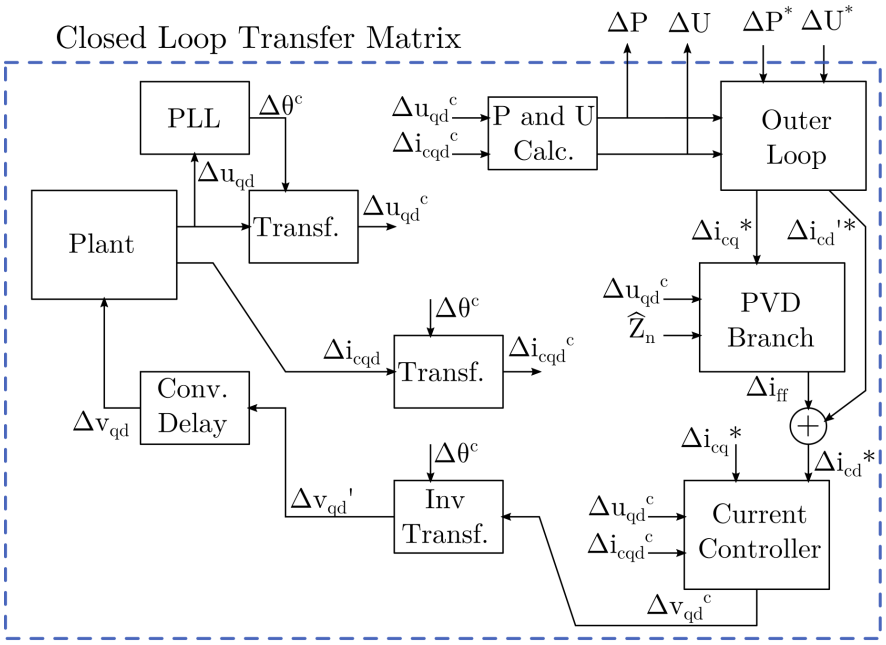


**Figure 4.5:** Closed loop transfer matrix: representation of the combined linearised plant and controller system with PVD.

The eigenvalues of the closed loop transfer matrix are presented in Fig. 4.6, presenting the small signal stability of the system when the PVD is in place. As before, inversion is plotted in black and rectification is plotted in red, and the axes are selected to provide detail on key eigenvalues.

From Fig. 4.6, the system stability is maintained for all active power values for a SCR of 3 and for $P \geq -0.9$ pu for a SCR of 1. Thus, compared to classical VCC (Fig. 2.22), the stability of the converter in a weak grid is significantly improved without having to reduce the power loop gains.

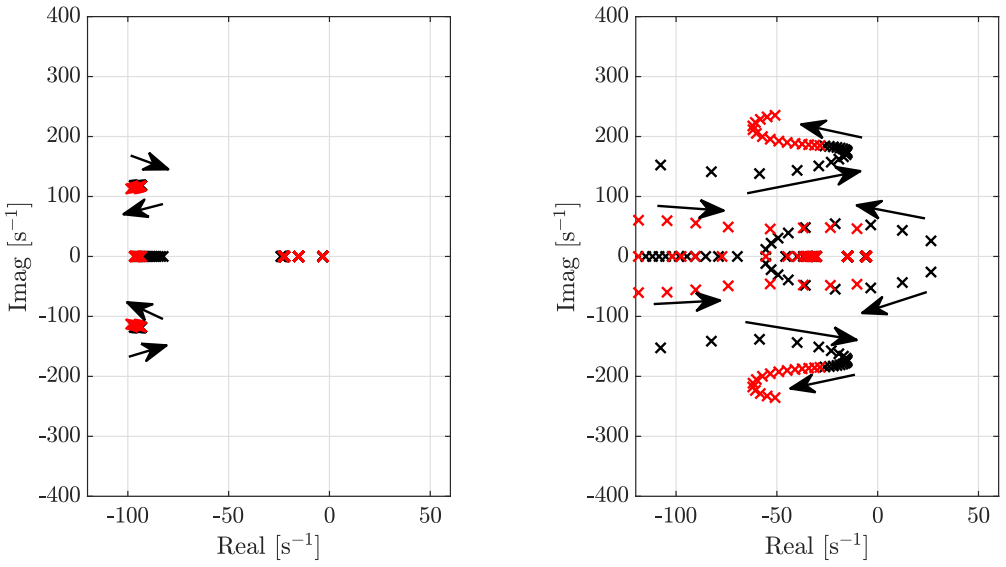


**(a)** SCR = 3. **(b)** SCR = 1.

**Figure 4.6:** Eigenvalues of the closed loop transfer matrix with PVD, the arrow indicates increases in power from −1 pu to 0.75 pu in increments of 0.05.

The improved performance of VCC with PVD can also be illustrated in Fig. 4.7 and 4.8 below by assessing the small signal response to a step in 0.01 pu of the base values of power or voltage magnitude references ($\Delta P^*$ or $\Delta U^*$) onto the closed loop system outputs of $\Delta P$ or $\Delta U$, similar to Fig. 2.23 and 2.24.

Fig. 4.7 produces the same results as Fig. 2.23 when the SCR is 3, demonstrating that the small signal stability of the system is not affected by the PVD in stronger grids. However, the results in Fig. 4.8 are markedly better than Fig. 2.24 with improved stability and reduced settling time. Thus, steady state performance of the PVD PCC is unaffected in strong grids and the stability is much improved in very weak grids, as long as the impedance estimation is correct.

### 4.3.3 Parametric sensitivity

To test the sensitivity of the proposal when incorrect estimations are used, an error is intentionally introduced to impact grid impedance estimations. Fig. 4.9 presents the step response of the small signal model, linearised at $P = -0.8$ pu for a range of estimation errors. The impedance estimation is a function of an error constant $C_{error}$,

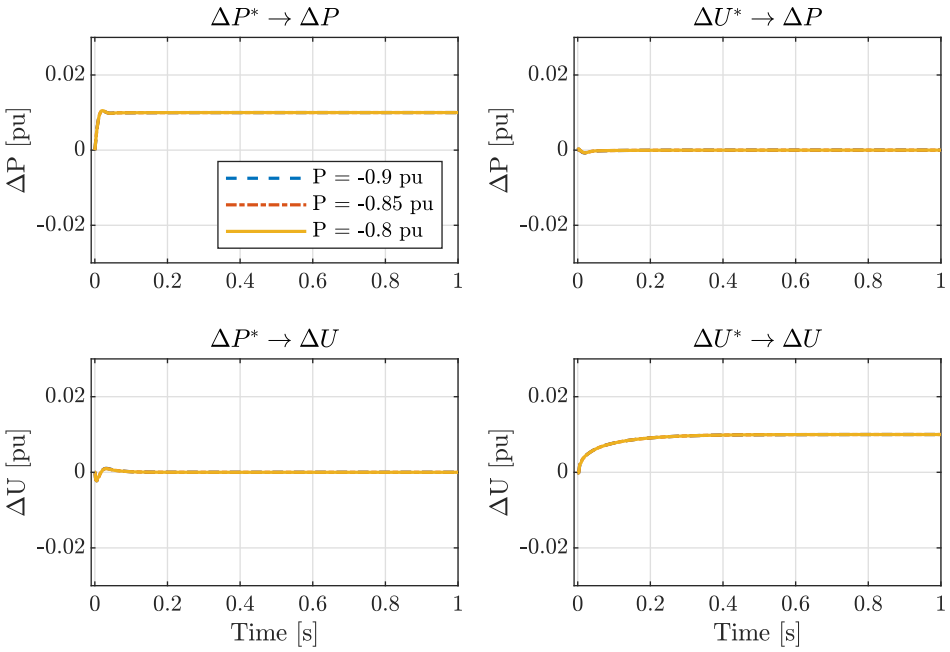


**Figure 4.7:** Step response of the closed loop system with PVD for SCR of 3.

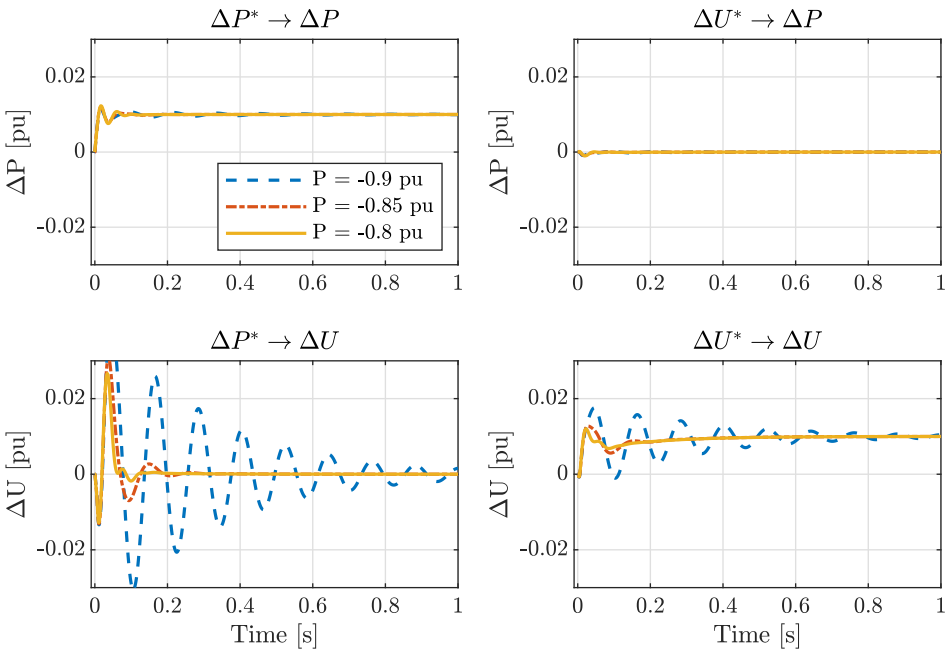


**Figure 4.8:** Step response of the closed loop system with PVD for SCR of 1.

such that $Z_{estim} = C_{errror} Z_n$.

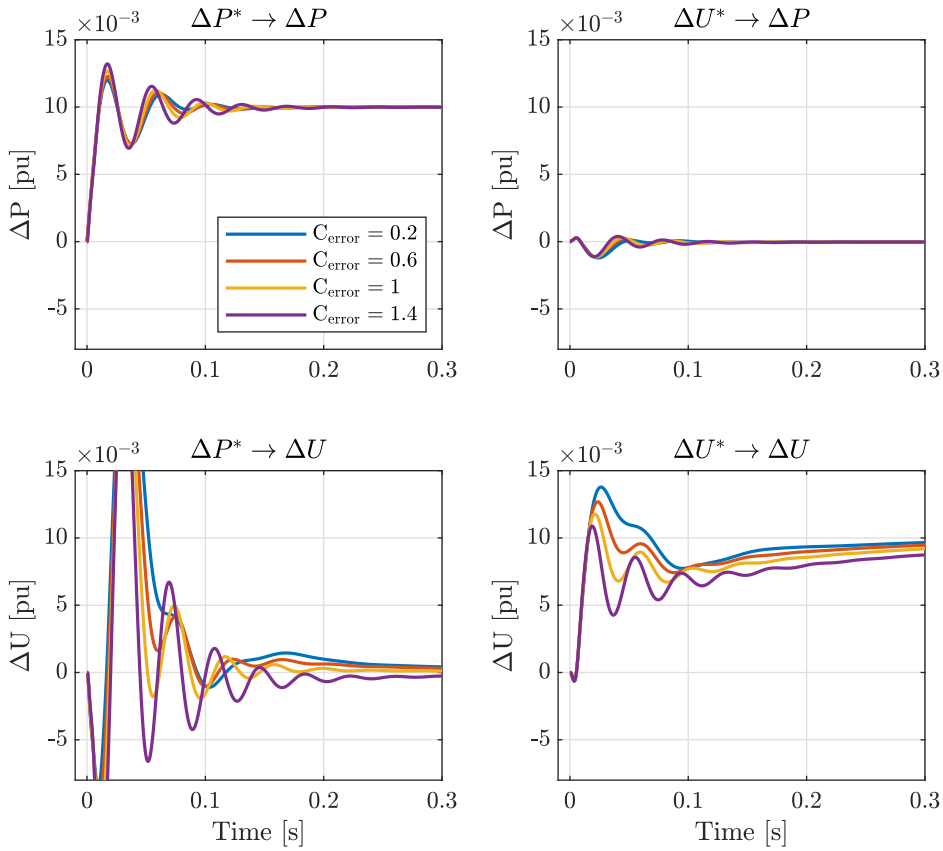


**Figure 4.9:** Step response of the linear closed loop system with PVD and a range of estimation errors.

From this figure, it can be deduced that an under-estimation of the grid impedance appears to have negligible $\Delta P^* \rightarrow \Delta U$ coupling. On the other hand, an over-estimation of the grid impedance results in over-compensation and causes oscillatory behaviour in the voltage, resulting in a longer $\Delta U^* \rightarrow \Delta U$ response. Nonetheless, Fig. 4.9 does suggest sensitivity to over-estimation, with inaccuracies resulting in reduced dynamic performance but not instability.

The next verification undertaken as part of the parametric sensitivity study is the impact of the outer loop gains on stability. In Fig. 4.10, each outer loop gain is multiplied by a gain of 0.8, 1.0, and 1.2. The plot is zoomed to focus on the relevant eigenvalues, and where applicable an arrow is included to show the impact of increasing

the relevant gain.

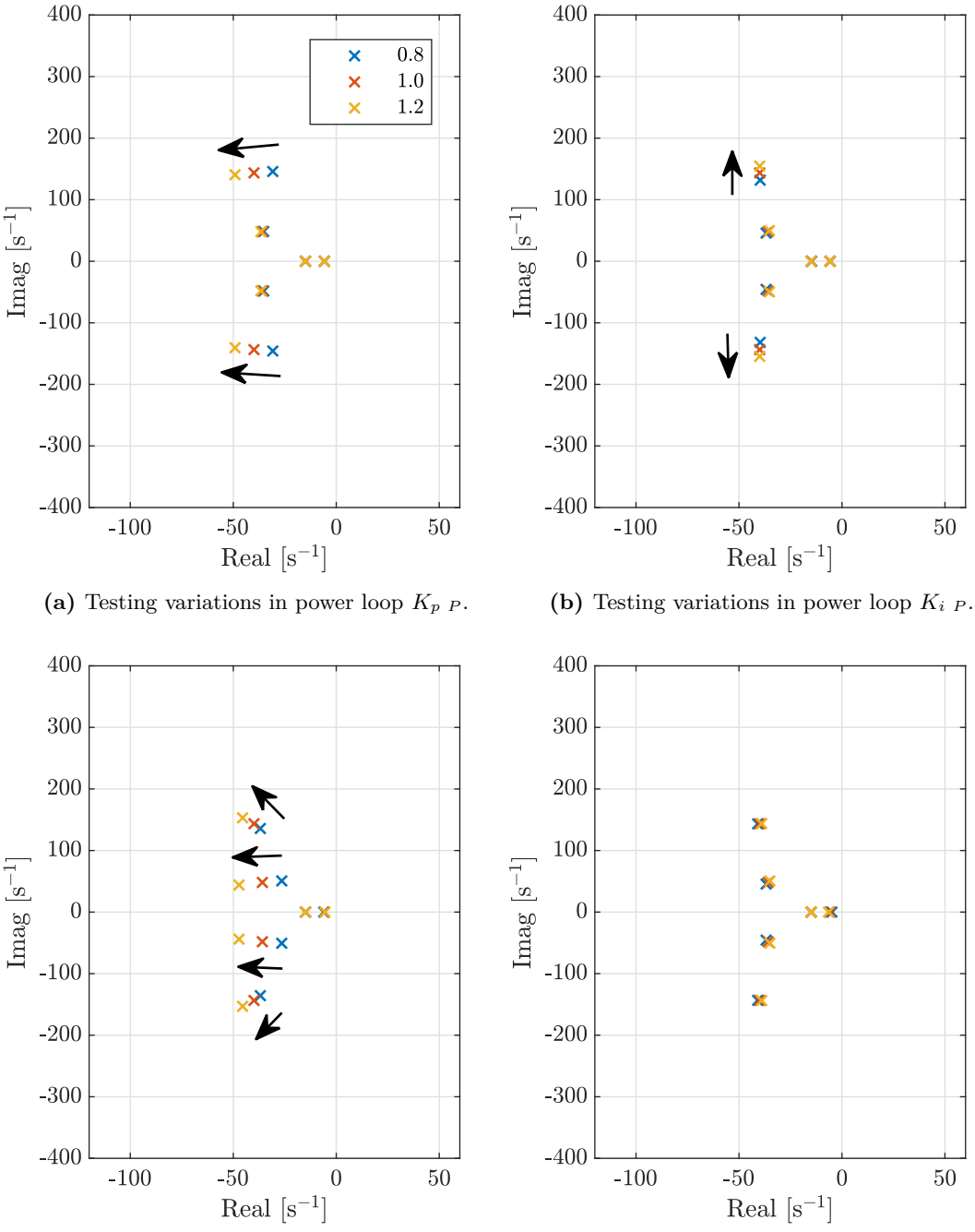


**(a)** Testing variations in power loop $K_{p\ P}$.

**(b)** Testing variations in power loop $K_{i\ P}$.

**(c)** Testing variations in voltage loop $K_{p\ U}$.

**(d)** Testing variations in voltage loop $K_{i\ U}$.

**Figure 4.10:** Eigenvalues of the closed loop system for various outer loop control gains.

It can be determined from Fig. 4.10 that the system small signal stability can cope

with changes to the outer loop gains. While some eigenvalues are shifted as a result of gain modification, none of the control gain amendments affect the critical eigenvalues positioned at [−5.76 0], which remain almost completely stationary across all conditions. Increasing the proportional gain of the power loop shifts some eigenvalues to the left; increasing the integral gain of the power loop makes the system more oscillatory; increasing the proportional gain of the voltage loop makes the system slightly more oscillatory; and increasing the integral gain of the voltage loop has no noticeable impact on the small signal stability.

An alternative presentation of the stability is produced in Fig. 4.11 using bode plots, representing the closed loop transfer functions for power, voltage and the cross couplings. There are numerous interesting outcomes of these plots. For $\Delta P^* \rightarrow \Delta P$, the desire is for a steady gain until the magnitude drops towards the desired cut off frequency. This is only provided with the PVD, as the lack of a PVD produces a dip at approximately 0.8 Hz. This means that the power is better able to respond to the power reference with the PVD in place. For $\Delta U^* \rightarrow \Delta P$ and $\Delta P^* \rightarrow \Delta U$, the objective is for the magnitude to remain as low as possible. Indeed, the bode plots are lower with the PVD. And finally, for $\Delta U^* \rightarrow \Delta U$, the objective for a steady relationship (similar to $\Delta P^* \rightarrow \Delta P$). This is also improved with the PVD.

The final point for Fig. 4.11 is the bandwidth, and for this the focus is on the $P^* \rightarrow \Delta P$ subplot. Without the PVD, the cut-off frequency (at -3 dB) is 39 Hz compared to 46 Hz with the PVD. Thus, in addition to the improved disturbance rejection, the PVD also provides a higher bandwidth.

## 4.4 Transient stability

Similarly to Chapter 2, two transient tests are undertaken: large ramps in power reference, as per Fig. 4.12a, and step changes in SCR from 3 to 1 to 3 (at 0.1 s and 0.6 s, respectively), as per Fig. 4.12b. The impedance information is constant.

In Fig. 4.12, the PVD is successful in maintaining stability when subjected to large power reference ramps and large grid disturbances. The voltage remains within 0.1 pu in Fig. 4.12a, and while the PVD maintains stability during the grid events in Fig.

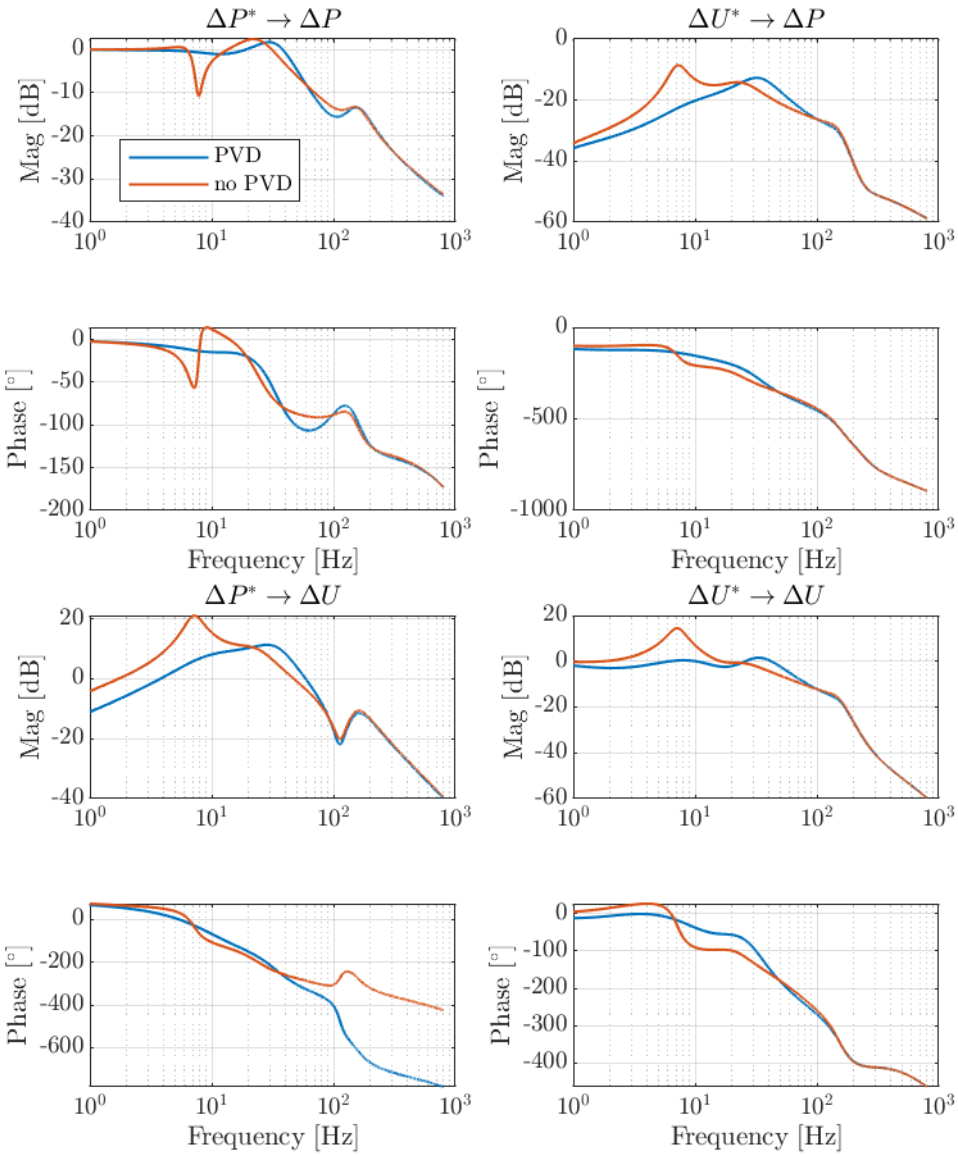


**Figure 4.11:** Bode plot for $P = -0.8$ pu with and without PVD, normalised.

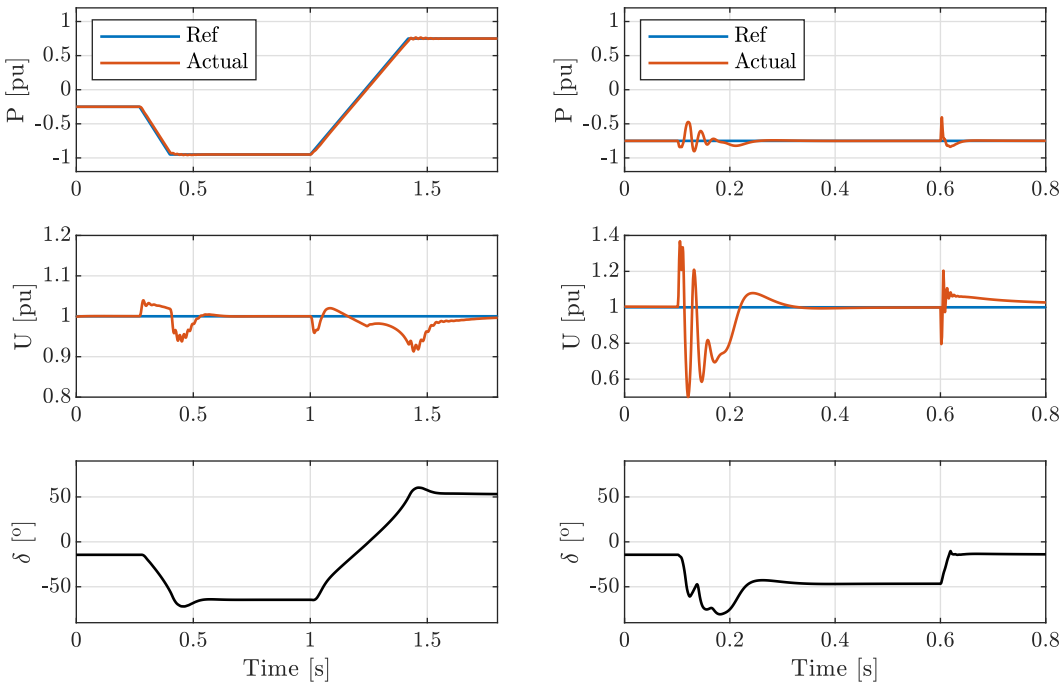


**(a)** Stability in large reference changes. **(b)** Step change in SCR from 3 to 1 to 3.

**Figure 4.12:** Simulation results of the proposed PVD.

4.12b, the oscillations are significant. This is in part due to the impedance estimation being out of date, which is unavoidable given the instantaneous and unpredictable nature of the event.

The final consideration in this section is a side-by-side comparison of employing the PVD versus not employing the PVD, for a modest change in active power reference. The results are presented in Fig. 4.13.

As per Fig. 4.13, the benefits of the PVD are clear; by decoupling the outer loop, disturbances are rejected much more effectively. This results in quicker settling with reduced oscillatory behaviour. The effectiveness of the decoupling is also apparent in the active current plots, showing how $i_{cq}^*$ is a much better reflection of $P^*$, and that $i_{cq}$ matches $i_{cq}^*$ very closely. More importantly, the impact of the feedforward current on the reactive current, and thus on the PCC voltage, is also apparent. The PCC voltage $U$ matches the shape of $i_{cq}^*$ *before* it is combined with the feedforward current, as per the purple trace. This proves that the PVD action of producing $i_{ff}$ effectively decouples the active loop from the reactive loop. With reduced oscillatory behaviour and improved response, it is clear that the PVD is able to improve the dynamic response of the controller to changes in power reference while also improving transient stability.

## 4.5 Experimental results

Using the experimental set-up described in Section 2.4, the PVD is tested experimentally in this section. The parameters used are provided in Appendix A. Small signal studies using the 1 kVA parameters are also included in the thesis, presented in Appendix D.

### 4.5.1 Step change in power in a weak grid with and without PVD

Fig. 4.14 compares the response of the converter to a power reference step change ($-0.4$ to $-0.7$ pu) in a weak grid with a SCR of 1.38 for two different controller implementations: with and without the PVD. The top plot displays the reference and measured power, the second row displays the voltage magnitude, the third row displays

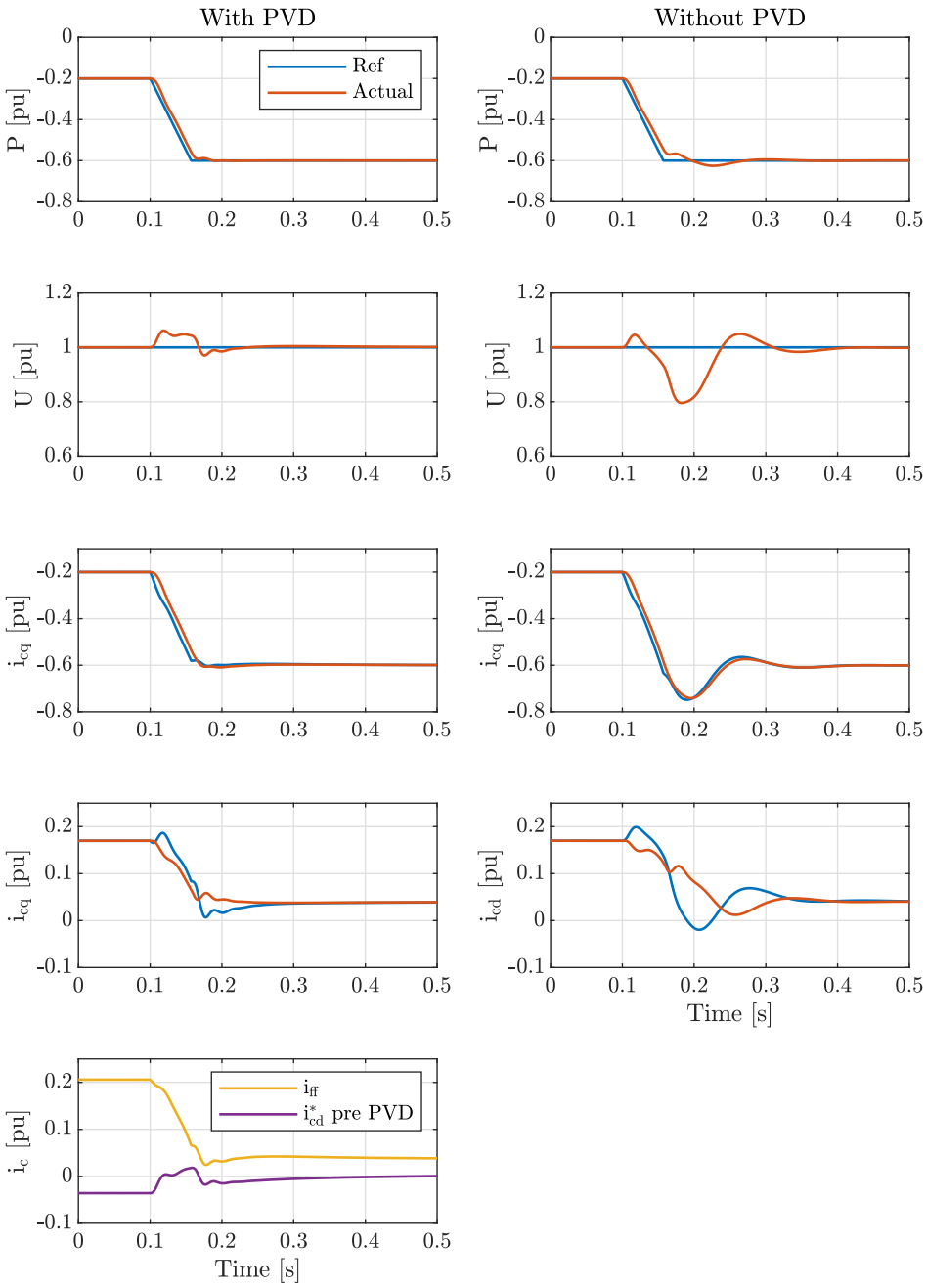


**Figure 4.13:** Effect of PVD on system response and stability.

the current, and the bottom row displays the feedforward branch current.

The VCC implementation that includes the PVD is stable. The power controller action does lead to some reactive current and voltage oscillation. However, the converter is able to meet the power reference and settle. However, without the PVD, the oscillations caused by the power controller action make the converter unstable, with the oscillations growing until instability sets in.

This test illustrates that, in a very weak grid, the performance of the converter is greatly improved with the PVD. The PVD allows for higher power outputs to be achieved and stability to be maintained.

Further, it is possible to extract rise time and settling time information for this step change in power reference. 10 % of the step is reached at 0.207 s and 90 % of the step is reached at 0.247 s, resulting in a rise time of 40 ms. Regarding settling time, a peak value of $-0.75$ pu is reached at 0.308 s, and the system settles by 0.340 s, resulting in a settling time of 32 ms. Both values are within the desired dynamic performance set out in Section 4.1.

### 4.5.2 Step change in power in various SCRs for optimised and not optimised PVD

A well tuned PVD should produce a larger feedforward current in a weak grid than in a strong grid. This is tested and presented in Fig. 4.15 by comparing the converter response to a step change in power (also $-0.4$ to $-0.7$ pu) for various SCRs: the low stiffness grid and the medium stiffness grid.

The same figure also plots the same results but where the PVD tuning is fixed to weak grid parameters.

This test illustrates the importance of good PVD tuning – the PVD is increasingly overcompensating the feedforward current in strong grids and introducing undesirable oscillatory behaviour in the process. However, the figure also illustrates robustness to poor estimations as the converter does not become unstable and eventually settles.

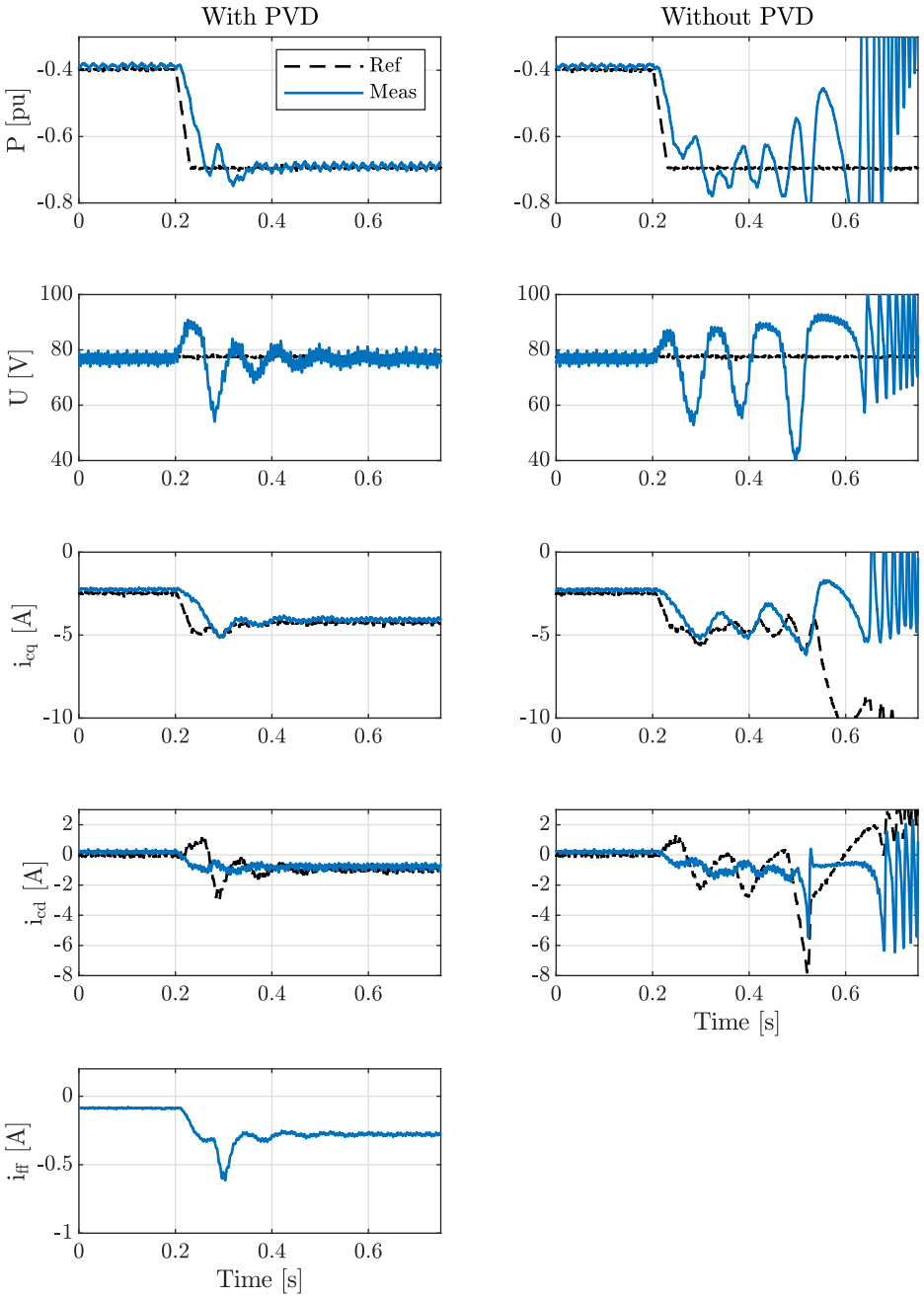


**Figure 4.14:** Step change in power for both VCC with a PVD (left side) and without (right side).

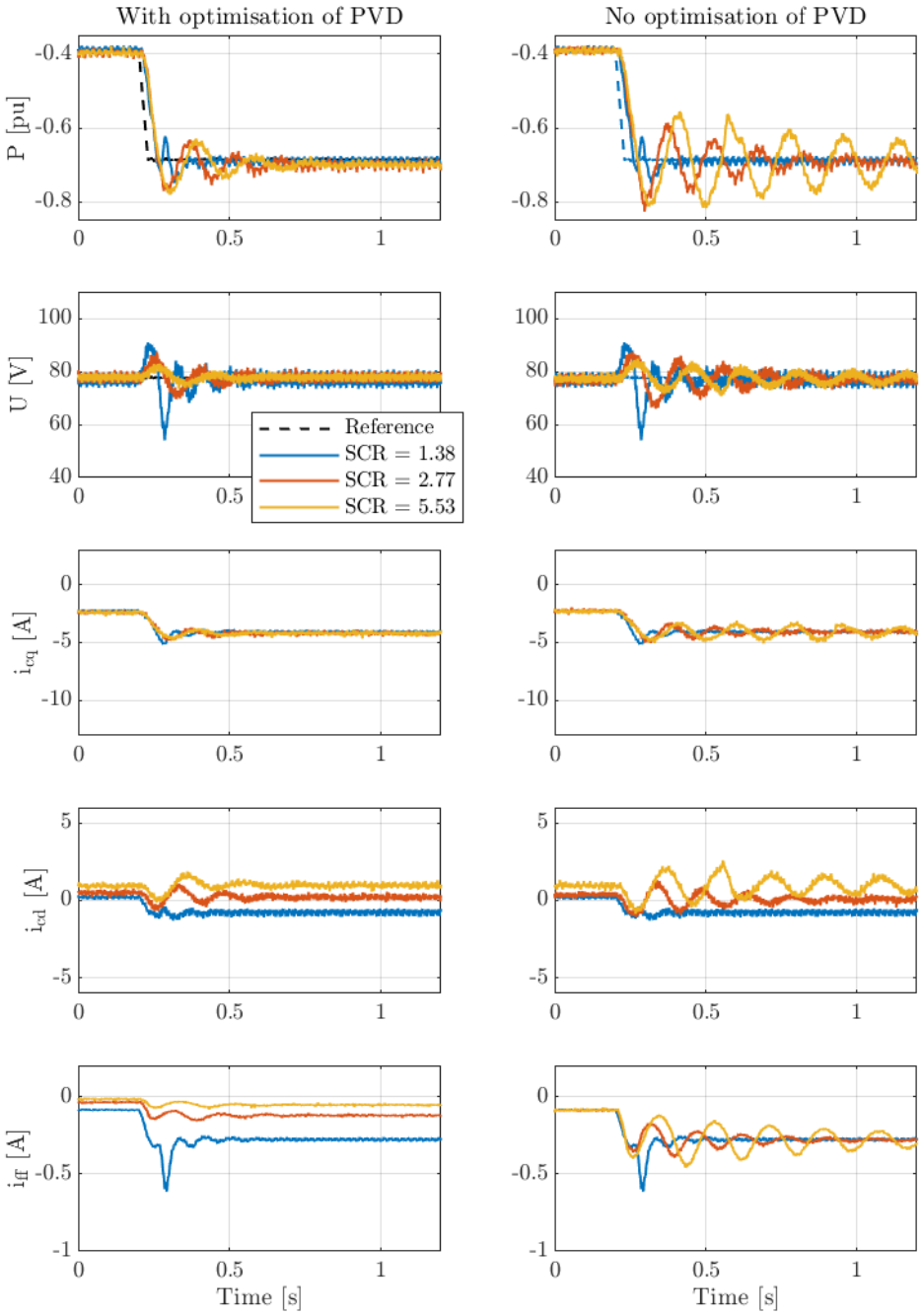


**Figure 4.15:** Step change in power for a variety of SCRs.

### 4.5.3 Step change in grid impedance with and without the PVD

The next test, presented in Fig. 4.16, compares the response of the converter to a grid event (SCR step change from 2.77 to 1.38) both with and without the PVD. For simplicity, the impedance estimation is not currently enabled. The power reference is $-0.67$ pu.

This test illustrates that despite the outdated impedance estimation, the PVD is still capable of compensating for changes in instantaneous power that arises from the change in impedance, and the converter eventually settles. However, with no PVD compensation, the initial voltage oscillations are larger and grow until the converter is unstable.

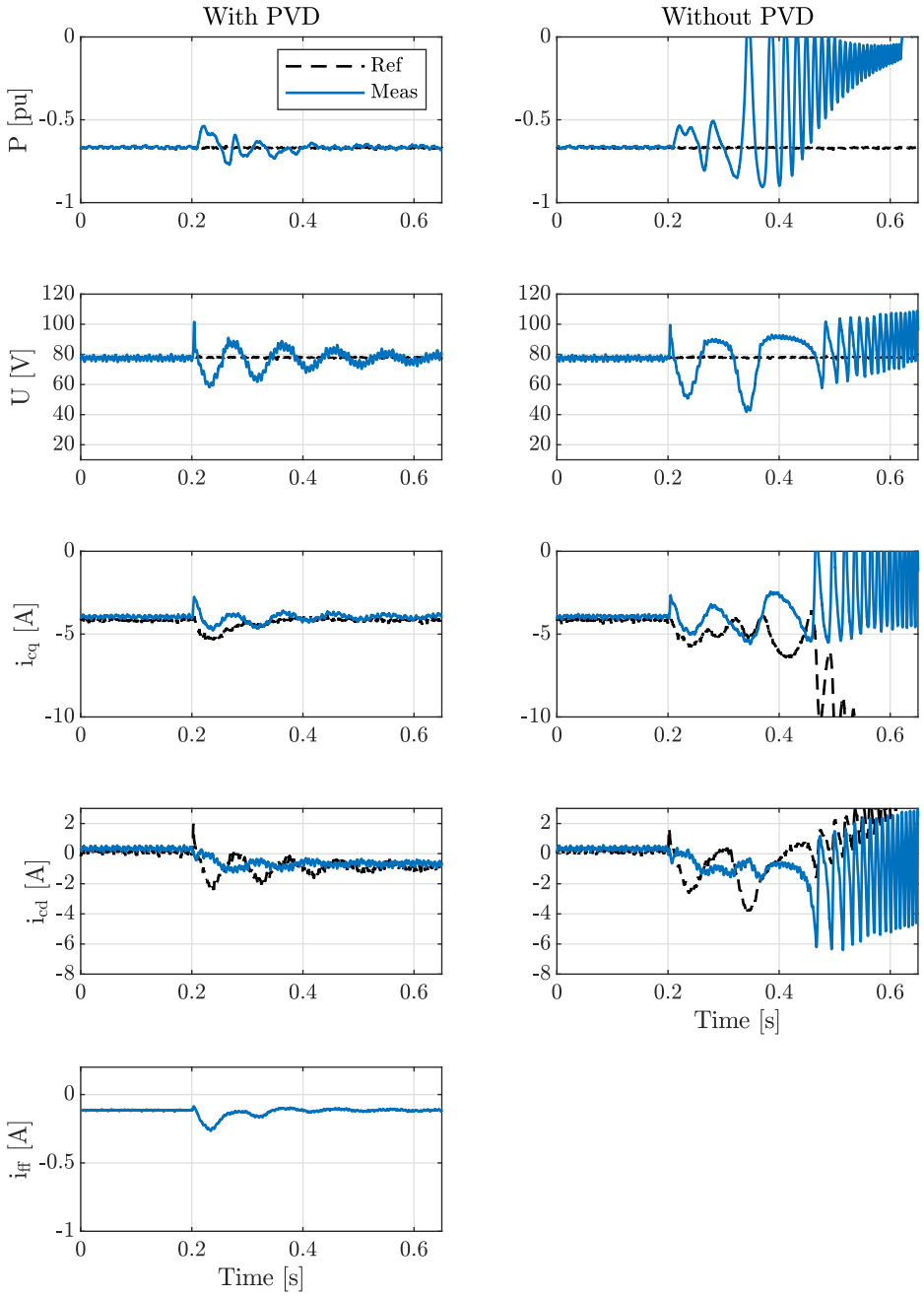


**Figure 4.16:** Step change in SCR (from 2.77 to 1.38) for both VCC with a PVD (left side) and classical VCC without the PVD (right side).

# Chapter 5

# Resilience in Variable Strength Grids

The PVD presented in Chapter 4 improves the steady state and transient stability of VCC, rendering it capable of undertaking large changes in active power transfer in very weak grids. Stability is also maintained during grid events, when injecting modest amounts of active power into the grid.

This chapter takes the modifications to VCC further, proposing an instability detector capable of identifying the onset of instability before voltage collapse occurs. This can occur, for example, when the grid experiences a sudden change in SCR while injecting high amounts of active power into the grid, i.e. the power angle is already high (see Fig. 2.2). The study of such transient events is uncommon in the literature, but given how vulnerable converters are to such events it is an important area of study. The detection of instability onset, manifested by large changes in power angle, is undertaken by monitoring of the average of the local PCC voltage over a 10 ms data window.

The proposed local state machine control is also presented, which combines the PVD, instability detector, and impedance estimation in order to allow for real-time and independent adaptation of the converter to evolving grid conditions. It is the combination of optimisation autonomy and instability detection that results in converter resilience to variable grids. In this chapter, the justifications for autonomous decision making are presented, followed by the state machine diagrams that describe

the implementation of the local state machine control.

## 5.1 Sudden changes in SCR

A major grid event, such as the loss of a transformer or transmission line, would create a sudden change in SCR equivalent to the closing or opening of the contactor in Fig. 2.26. It was demonstrated earlier in Fig. 4.12b that a with the PVD enabled, the converter can successfully withstand the transients caused by a step change in SCR from 3 to 1 and back to 3 while inverting $-0.7$ pu of power into the network without an impedance estimation update. The equivalent Fig. 2.25b without the PVD was unstable when dynamically tuned. The PVD test of Fig. 4.12b is repeated below in Fig. 5.1 at a larger power output of $-0.9$ pu.

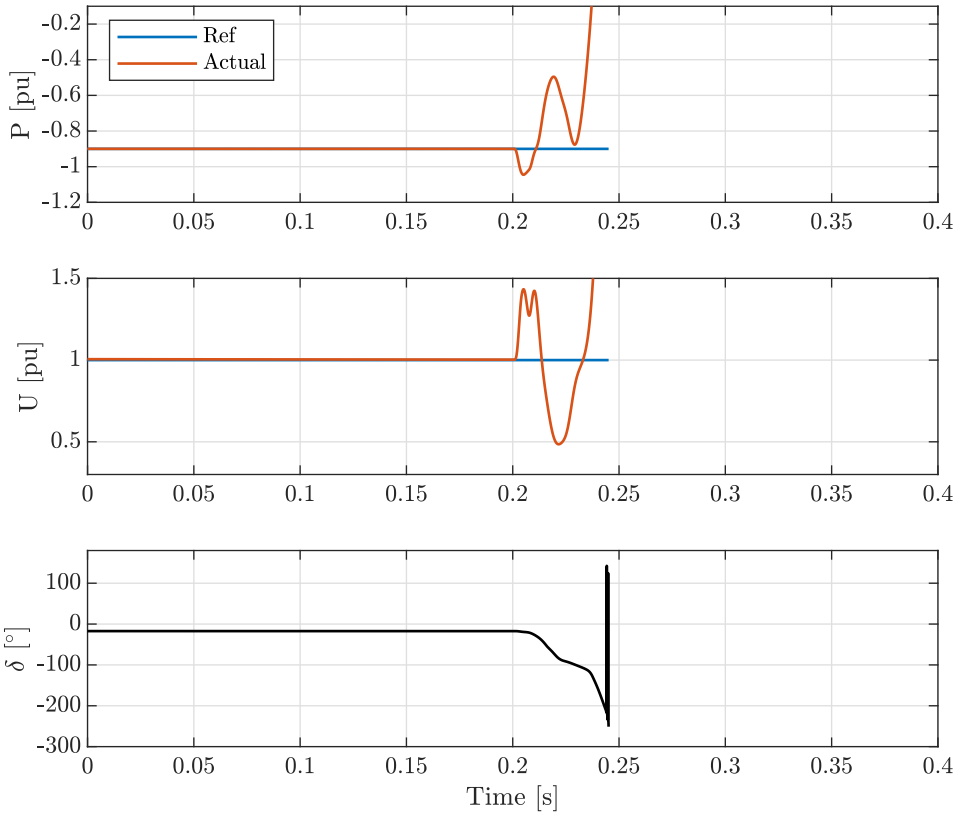


**Figure 5.1:** A sudden SCR step change from 3 to 1, at a power output of $-0.9$ pu, with the PVD enabled.

Fig. 5.1 shows that the increase in power angle $\delta$ due to the grid event leads to instability despite the PVD. With the power angle going beyond $-90°$, the active power no longer responds to the active power controller. The increased coupling between active and PCC voltage, as explained in Section 2.1.1.3, further complicates the situation. With the PVD no longer optimised to the actual grid conditions, it is no longer providing adequate decoupling.

## 5.2 Instability detector

In order to improve resilience, a mechanism is developed to identify grid events that would lead to instability. Given the correlation between instability and the runaway of power angle $\delta$, as per Fig. 5.1, $\delta$ would be the ideal parameter to monitor. However, with only local measurements are available, a substitute for $\delta$ is required – hence instability is determined by monitoring changes in the local power angle instead. With a data window of 10 ms, and a sampling frequency of 5 kHz, the proposed instability detector effectively determines the average power angle by integrating The PLL output frequency over the previous 50 frequency samples. This is presented in the block diagram of Fig. 5.2, where $\omega_{PLL}$ is the output frequency of the PLL, $\theta^c$ is the instantaneous angle, and $\theta_D$ is the same angle but delayed by 0.1 ms. The feedback loop that follows the summation junction is a zero tracking mechanism, where $K_{0tr}$ is a low bandwidth integrator gain. This feedback mechanism is designed slowly draw $\Delta\theta$ back to zero, enabling the use of a logic-based trigger mechanism.

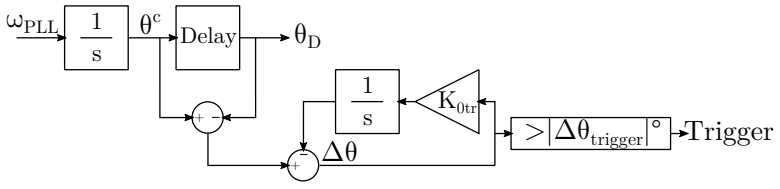


**Figure 5.2:** Block diagram of the instability detector.

### 5.2.1 Responding to instability onset by reducing active power

Once $\Delta\theta > |\Delta\theta_{trigger}|$, the risk of instability is very high. As the immediate objective is to prevent a collapse of the power angle $\delta$, a reduction in active power reference is triggered. This is simulated below in Fig. 5.3. Once settled at a lower power value, the controller will attempt to recover to the original power reference without correcting the PVD.

As seen in Fig. 5.3, the impedance event at 0.2 s no longer causes instability thanks to the reduction in power reference. The instability detector successfully identifies the grid event and curtails the magnitude of the power being injected into the grid, and within 10 ms, the electrical system settles. It can be observed that the voltage magnitude, despite the large swing, is not the cause of instability. While undesirable, it is unavoidable in such an extreme grid event where fast controller action is required.

Further, it is observed that upon the attempted power reference recovery at approximately 0.7 s, instability sets in. This is due to the outdated impedance estimation provided to the PVD, thus producing insufficient decoupling action. It is therefore necessary to re-optimise the PVD before recovering the power reference.

### 5.2.2 Re-optimising the PVD after a grid event

To avoid instability upon power reference recovery, the impedance estimator can be triggered during the reduced active power period, allowing for the PVD to obtain an updated impedance estimation and re-optimise to the new grid conditions. This is tested in Fig. 5.4 below where the impedance estimation is produced for the PVD at 0.5 s and 1.5 s given step changes in grid impedance at 0.2 s and 1.2 s.

With the newly introduced estimation process, the converter is able to make a full recovery at 0.9 s (unlike Fig. 5.3). Further, when the SCR jumps back to 3 at 1.2 s, the converter is able to adapt to those circumstances, too. Thus, for very weak grid integration of the PVD, it is also necessary to introduce an instability detector and an impedance estimator.

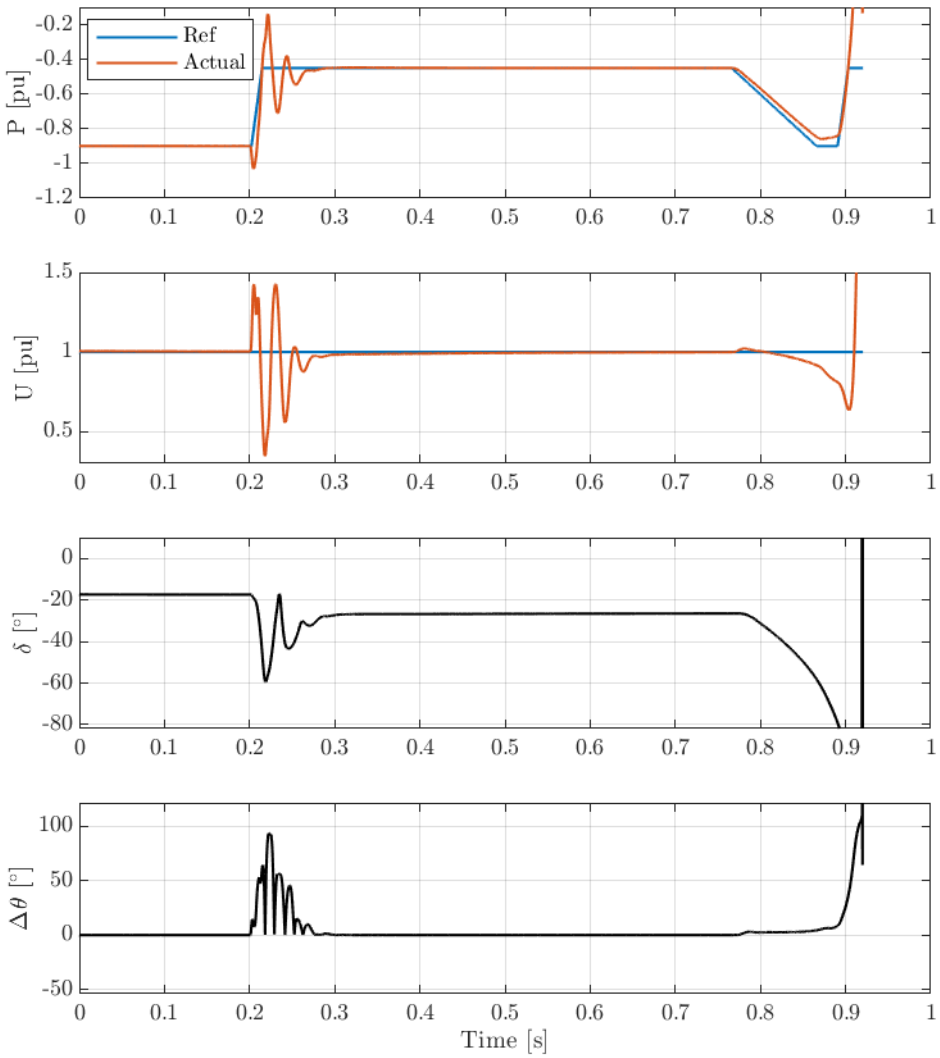


**Figure 5.3:** A sudden SCR step change from 3 to 1, at a power output of −0.9 pu, with the PVD enabled. No updated impedance information.

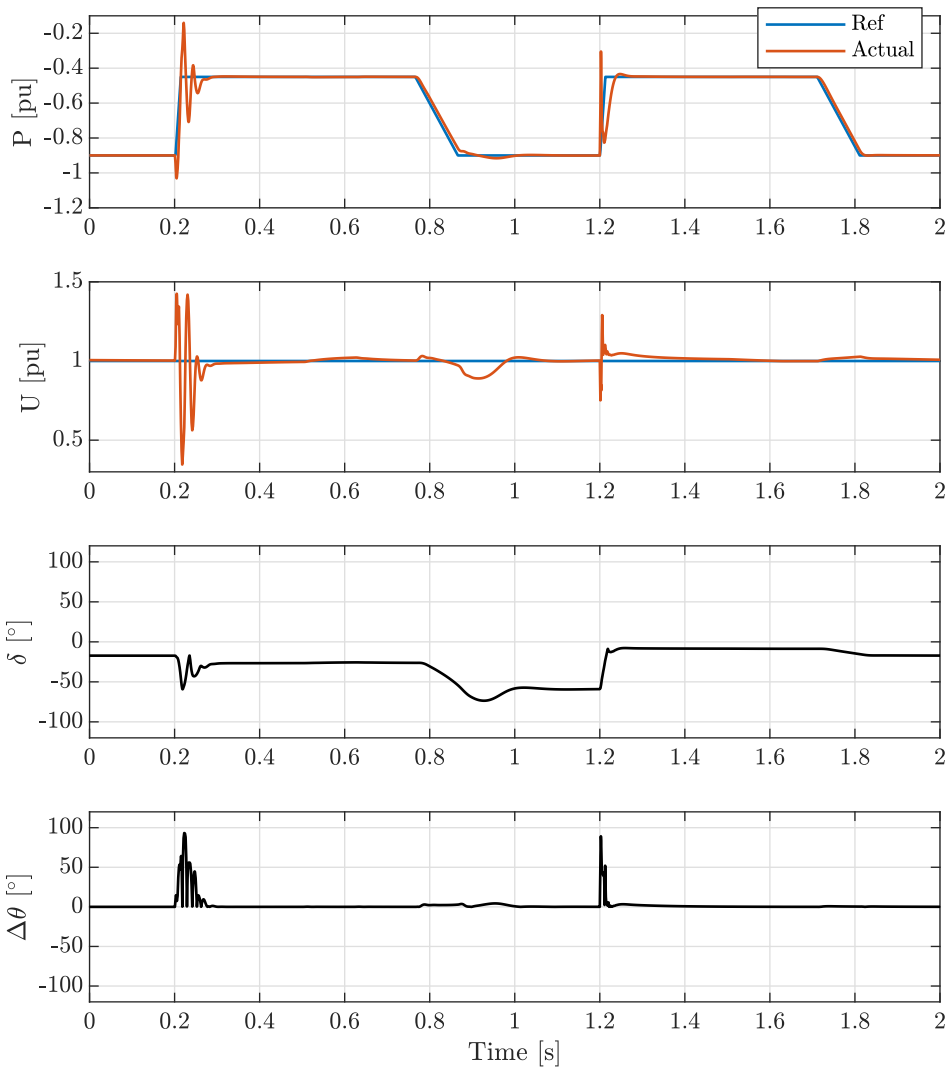


**Figure 5.4:** A sudden SCR step change from 3 to 1 at 0.2 s and 1 to 3 at 1.2 s with a power output of −0.9 pu. The PVD enabled and an impedance estimation is provided to the PVD.

### 5.2.3 Relationship between active power and power angle

The events in Fig. 5.4 can be visualised differently, by assessing the relationship between active power and power angle $\delta$ during the grid event against the backdrop of Fig. 2.2. This is presented in Fig. 5.5, where $\delta$ versus $P$ for both grid events: the step change in SCR from 3 to 1 in Fig. 5.5a, and the step change in SCR from 1 to 3 in Fig. 5.5b.

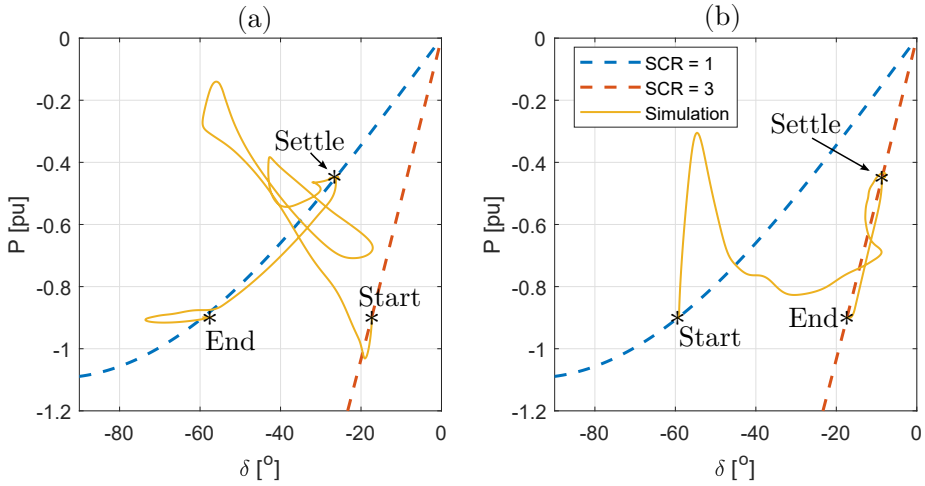


**Figure 5.5:** Alternative presentation of simulation, with (a) the events between 0 s and 1 s, and (b) the events between 1 s and 2 s.

From Fig. 5.5, the disturbance of the grid event is clear in both cases, but especially in Fig. 5.5a where the grid SCR suddenly drops to 1. Despite the active power reference dropping, the oscillations of active power and power angle take time to settle. Fig. 5.5b settles more quickly given the relatively small power angle of the new grid conditions, SCR = 3.

### 5.2.4 Instability detector versus vector shift protection

It is important to differentiate between the instability detector from vector shift protection, as vector shift protection is considered a contributing factor to the 9 August 2019 outage due to its use by smaller generation plants that disconnected during the grid event [30]. It is also no longer accepted as a means of islanding protection for new power parks [205]. Vector shift protection measures the time between zero-crossings of each phase voltage over a fundamental period, and if 5 of the 6 measurements are above

the setting threshold, the relay is tripped [206]. On the other hand, the proposed instability detector determines the average power angle over 50 frequency samples. Thus, it is more robust to noise and detects significant grid events much more quickly.

## 5.3 Local state machine control

Local state machine control is required to coordinate instability monitoring, power reduction, impedance estimation and PVD optimisation. It is presented in state machine notation in Fig. 5.6 and with a control schematic in Fig. 5.7.

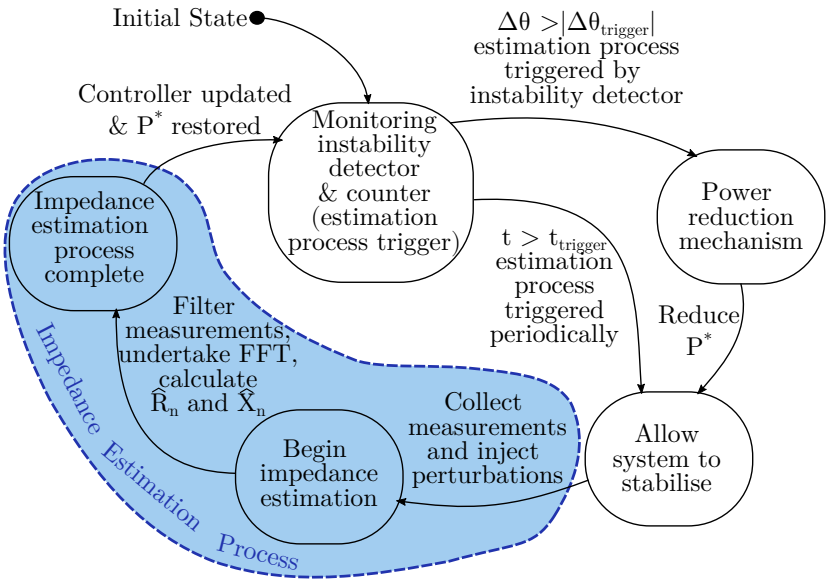


**Figure 5.6:** State machine representation of combined system.

The local state machine control's first task is to determine when to initiate the estimation procedure. This can be triggered in two ways – either by the detection of an instability or periodically with a counter. Periodic triggering of the impedance estimation ensures that the estimation remains up to date when gradual changes in grid impedance occur. In practice, this could be every 15 minutes or more depending on the expected temporal variation of the local grid impedance. In this thesis, this is set at 4 s for validation purposes. When the impedance estimator is triggered via the counter, there is no need for the power reference to be reduced, however it is maintained constant to ensure steady state conditions. Alternatively to the periodic

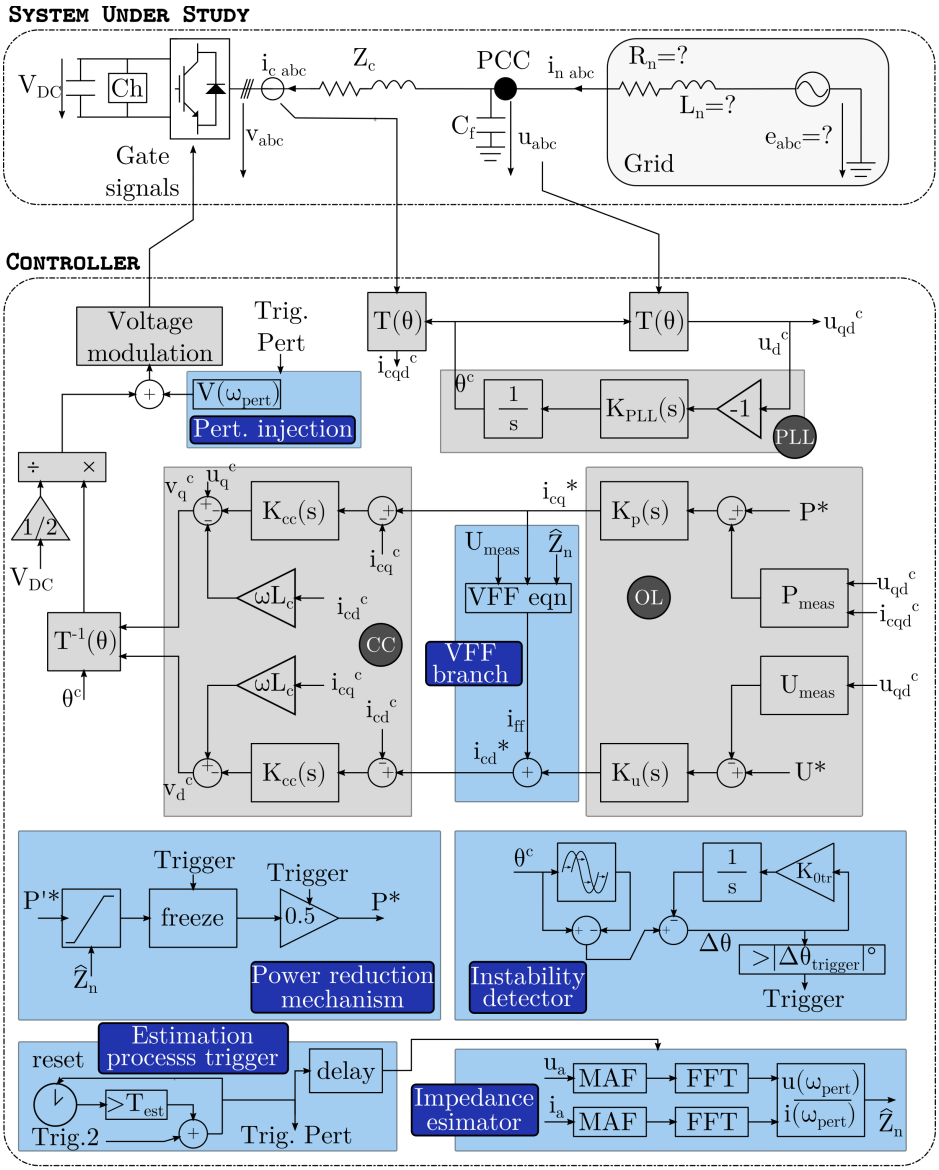


**Figure 5.7:** Proposed controller schematic.

trigger is the instability detector trigger, as presented earlier in Fig. 5.4. In such an event, the impedance estimation can only proceed once the system has settled at a reduced power reference. For the purposes of validation, the instability detection angle is set at $|\Delta\theta_{trigger}| = 20°$ as the optimal sensitivity, determined heuristically. With regards to the power reduction mechanism which is triggered by the instability detector, it is set to 50 % of the active power reference. This is a compromise between ensuring stability versus minimising the impact of reduced generation on the overall grid frequency. While 50 % may seem significant, the power angle will overshoot past 70° if $P = -1$ and the SCR is 1, thus a significant precautionary power reduction is required. It is also important to consider the available hardware, such as a wind turbine chopper's ability to dissipate energy or the ability of a battery system in the DC link to absorb excess energy. Ideally, DC links would have sufficient storage to decouple grid events from wind turbines and also provide additional ancillary services.

## 5.4 Simulation of local state machine control

In order to further illustrate the functionality of the proposed control modifications, the controller is subjected to step changes in grid impedance at various levels of active power transfer over a simulation period of 120 s, presented in Fig. 5.8.

### 5.4.1 Impedance estimator procedure

Fig. 5.9 presents the process of impedance estimation. Once steady state operating conditions are met, the estimator measures the phase A voltage and current, with the measurement periods labelled in the figure. The short duration of the estimation process reduces the risk of varying grid conditions that might affect the accuracy of the estimations.

### 5.4.2 Triggering of the impedance estimator

Fig. 5.10 presents the triggering of the instability detector. The grid SCR changes SCR from 3 to 1 at approx 25.2 s, and the resulting instability onset is detected by

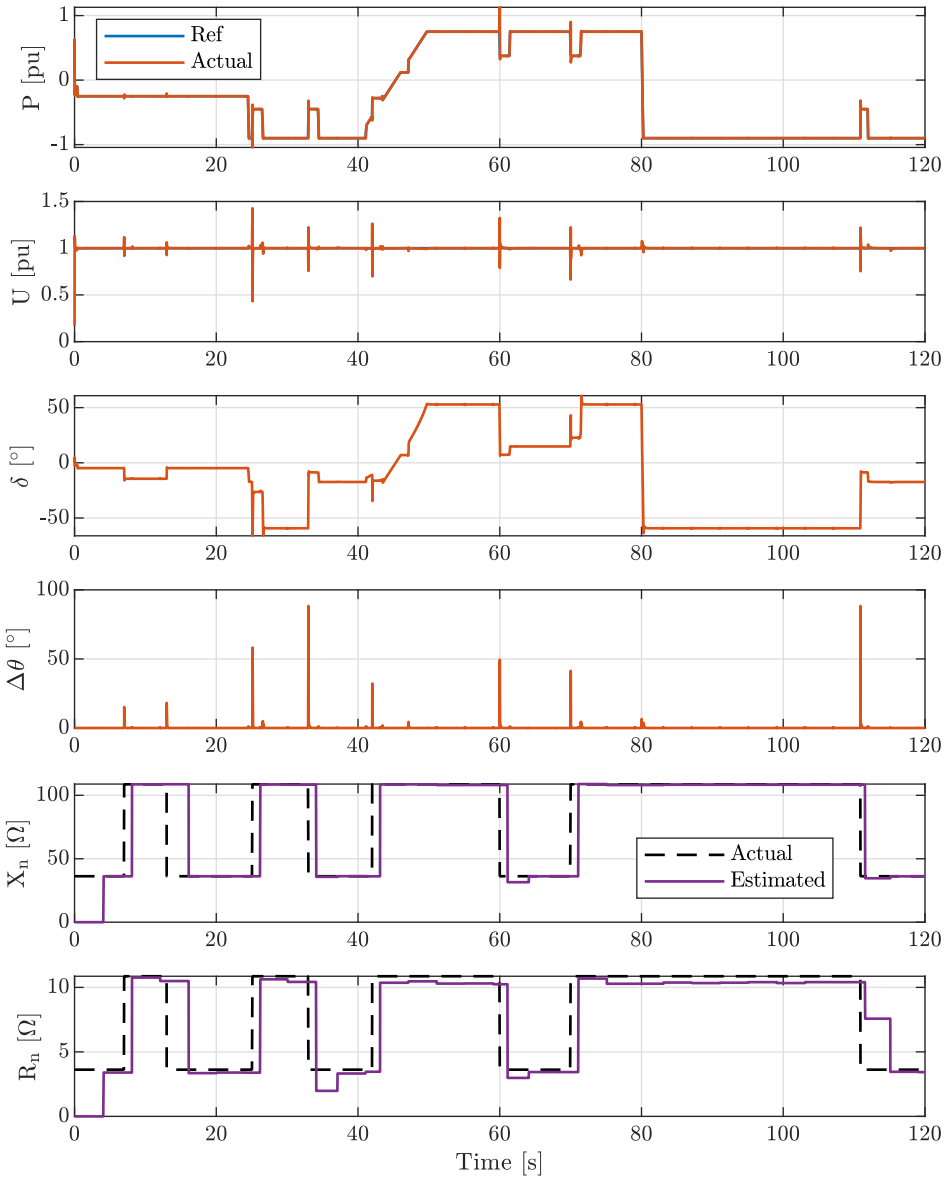


**Figure 5.8:** 120 s simulation.

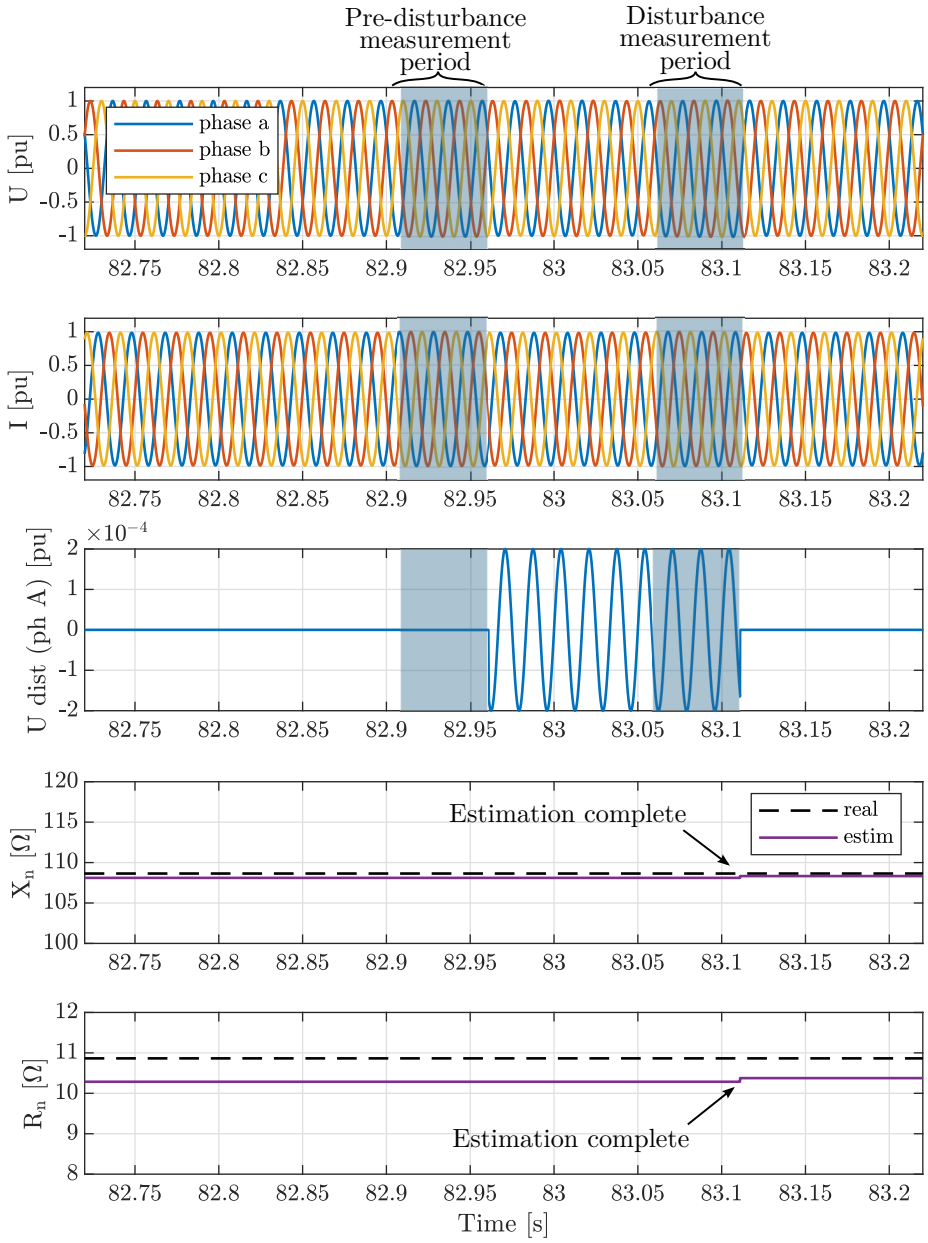


**Figure 5.9:** Annotated procedure for impedance estimation.

the instability detector with the sudden rise in $\Delta\theta$. The active power reference is immediately reduced by the power reduction mechanism, and once settled the impedance estimation process begins. The subsequent impedance estimation is communicated to the PVD and the power reference recovers without any instability despite the very weak grid conditions.

### 5.4.3 Power reference freeze

Fig. 5.11 presents the freezing of the power reference during the impedance estimation, and the subsequent recovery of the reference thereafter. The ramp in power, which begins at 40 s, is delayed due to the periodic triggering of the impedance estimator. Once the estimation is complete, the power reference is recovered. Subsequently, at 42 s, a grid event triggers the instability detector. This results in a power reference reduction and freeze for the duration of the recovery period and the impedance estimation. In this instance the power reference freeze is of a longer duration to allow the system to settle prior to the impedance estimation procedure. Another periodic impedance estimation occurs 4 s later at approximately 46 s.

### 5.4.4 Summary of simulations

In order to improve the integration of VCC in weak grids, it is necessary to introduce a decoupling mechanism, such as the PVD, into the controller. However, the PVD must be tuned adequately to the grid conditions, hence an impedance estimator is necessary. Impedance estimations are periodic, but must also occur when a change in grid parameters is identified. If a significant grid event occurs, there is a risk of voltage collapse. This is prevented by the instability detector, with such grid events identified and the power angle managed by pre-emptively reducing the power reference. This allows the system to settle, the controller to update the grid parameter information via the impedance estimator and for the active power reference to be recovered in a managed way.

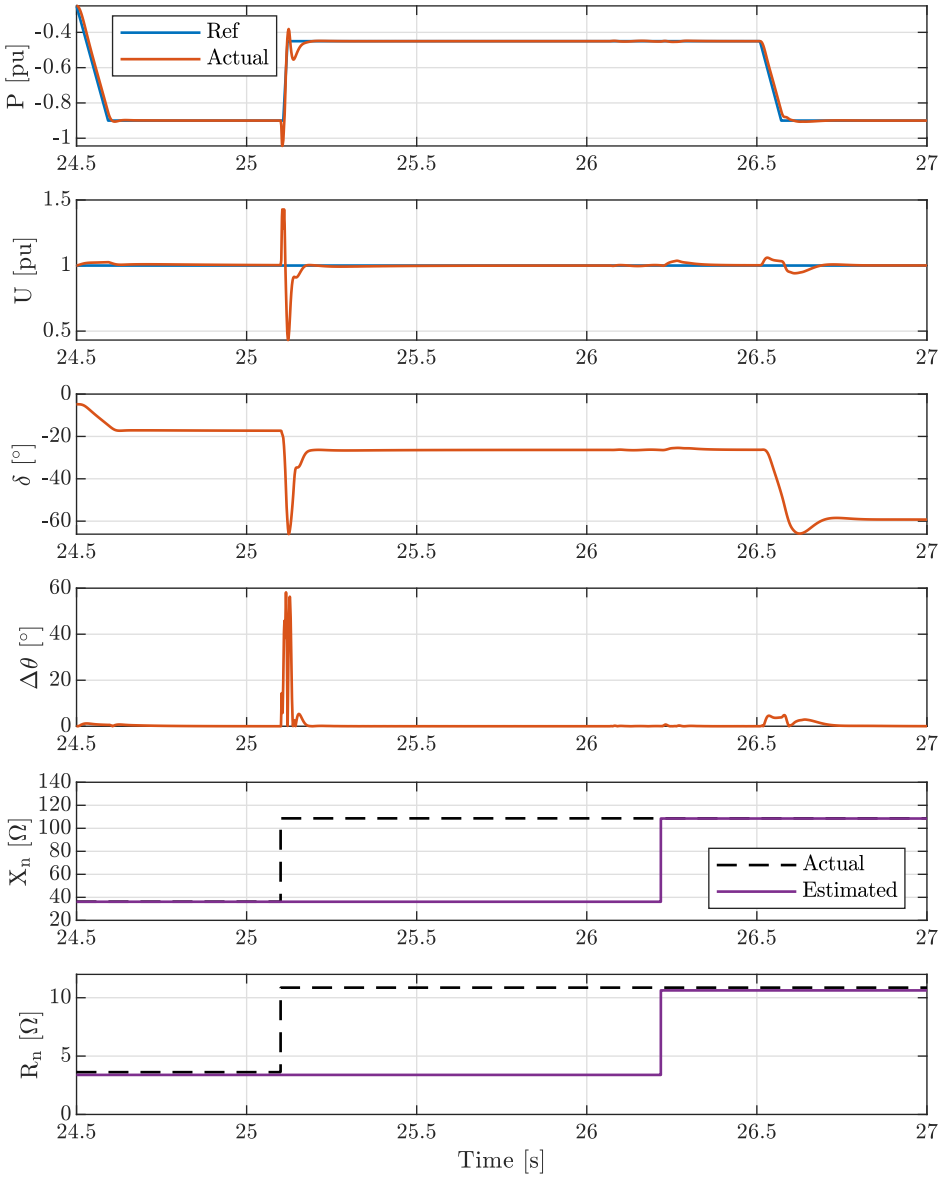


**Figure 5.10:** Annotated procedure for impedance estimation.

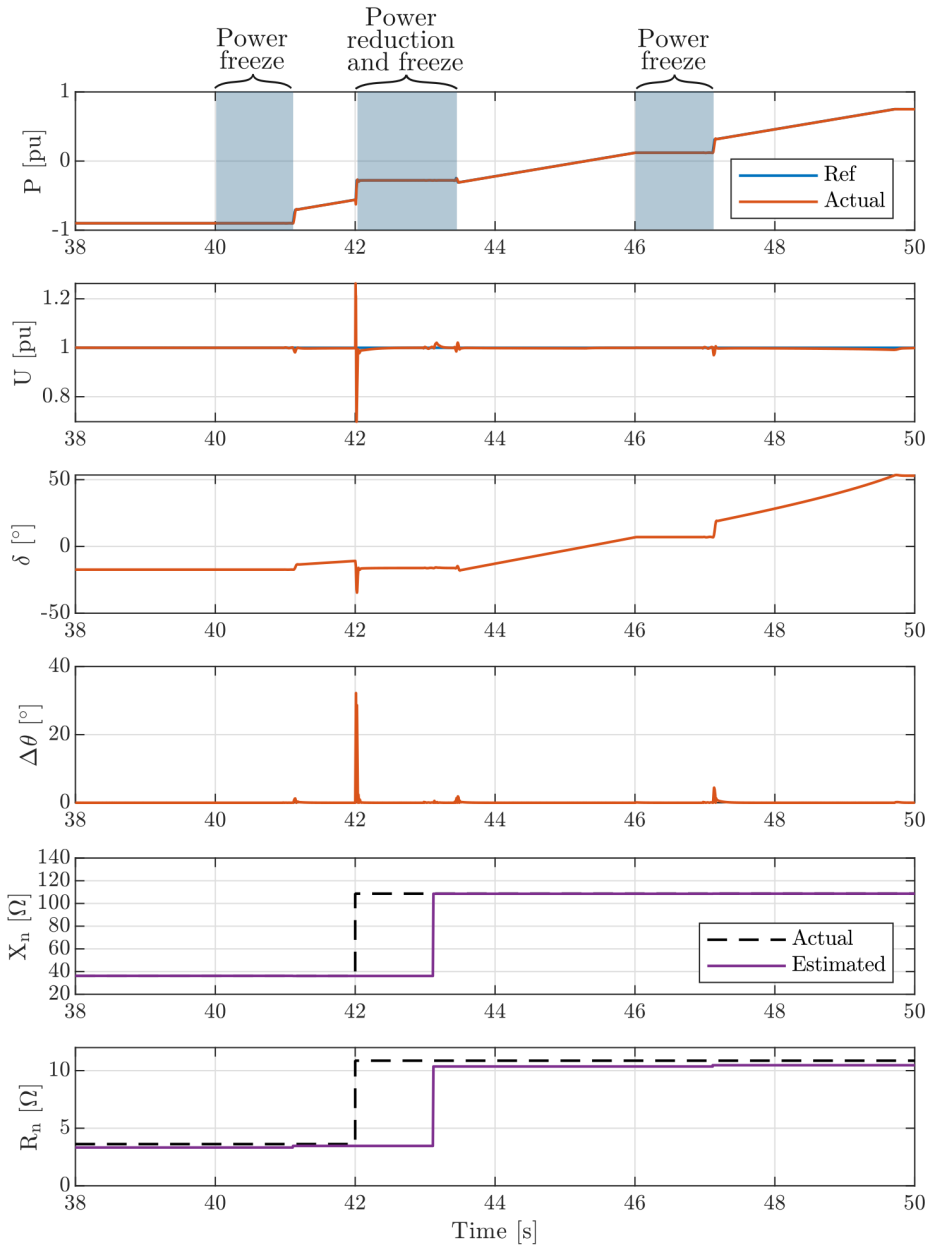


**Figure 5.11:** Annotated procedure for impedance estimation.

## 5.5 Experimental testing of local state machine control

In order to illustrate the principle functions of local state machine control in an experimental setting, the local state machine controller is integrated into the microcontroller of the converter, complete with the PVD, instability detector, power reduction mechanism and impedance estimator. The results, presented in Fig. 5.12, effectively repeat the impedance step change test presented in Fig. 4.16, but at a higher power level, thus producing a larger $\Delta\theta$ triggering the instability detector.

In the experiment, the contactor is disconnected at t = 0.25 s, and the resulting step change in impedance results in an almost immediate trigger of the power reference management control by the instability detector. Without the reduction in power reference, the system would become unstable. In this case, stability is maintained and the converter continues to operate. At approx 1.2 s, the impedance estimation process is complete with the impedance estimation output presented in the bottom two subplots of the figure. About one second later, the power reference is recovered, and the converter returns to normal operation with an updated PVD.

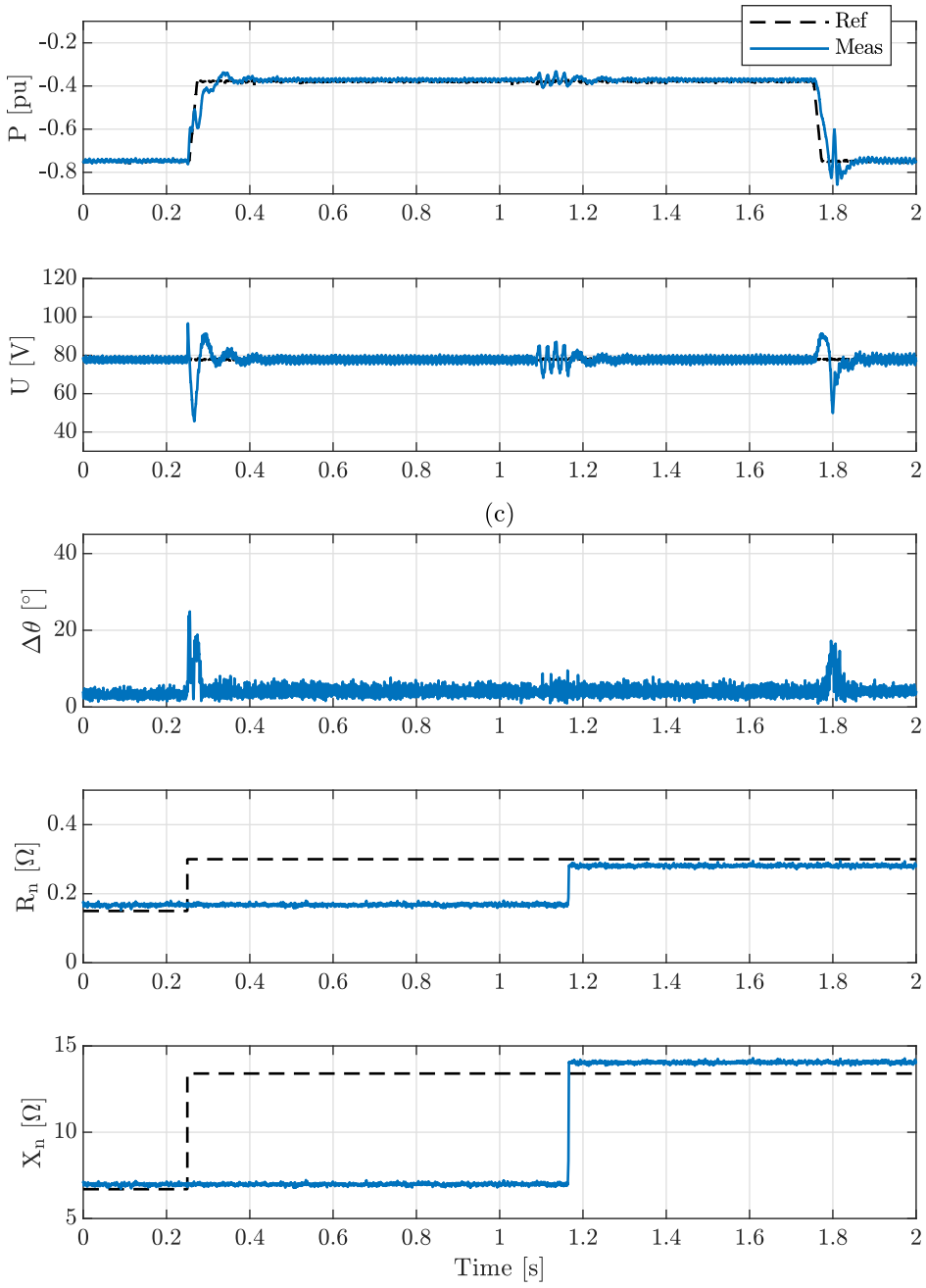


**Figure 5.12:** Step change in SCR for proposed controller with instability detector and impedance estimator enabled.

# Chapter 6

# Resilience in Variable Resonance Grids

As explained in Section 2.1.2, parallel resonances are of increasing concern as the electrical system continues to transition towards low carbon technologies, with an increase in capacitive elements (i.e. subsea AC cables for wind farms or FACT devices) and inductive elements (long overhead transmission lines). The literature also suggests that modelling the grid as a Thévenin equivalent impedance is not sufficient for stability analysis in grids with higher order resonant characteristics. For example, [207] undertakes frequency sweeps of various networks experiencing resonances, producing resistance and reactance plots very similar to those in Fig. 3.20 – 3.23. The instability, according to [207], occurs when the reactance crosses zero, i.e. when the resistance peaks.

The main aim of this chapter, therefore, is to mitigate instability caused by unexpected grid-induced resonances caused by grid-embedded capacitances. This is done by assessing the capabilities of two different control modifications at eliminating resonance issues, specifically outer loop tuning and notch filters. Similarly to Chapter 5, local state machine control is then employed for real-time and independent identification of problematic resonances through the use of wide-spectrum impedance estimation techniques and autonomous mitigation of resonance-induced instability.

## 6.1 Resonant system under study

The electrical system diagram for the resonance studies is presented below in Fig. 6.1.

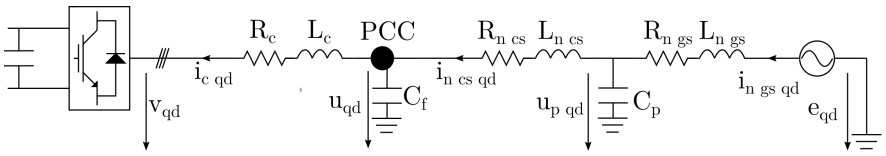


**Figure 6.1:** Diagram of electrical system presented in the *qd*-frame.

The subscript $p$ describes the parallel capacitance and voltage across the capacitor, the subscript $cs$ describes the converter side elements and the subscript $gs$ describes the grid side elements. As a reminder, the parallel capacitance results in two resonances: a parallel resonance, characterised by a peak in impedance magnitude; and a series resonance, characterised by a dip in impedance magnitude. The transfer function of the aggregated impedance as seen from the PCC is as follows

$$Z_n(s) = R_{ncs} + L_{ncs}s + \frac{R_{ngs} + L_{ngs}s}{C_p L_{ngs}s^2 + C_p R_{ngs}s + 1} \tag{6.1}$$

The grid parameters used in this section assume a parallel resonance of 110 Hz, as this is results in instability when the tuning outlined in Appendix A.1.2, as explained in Section 3.5.2.2. This is achieved with $C_p = 18.3\ \mu$F, $R_{ngs} = 3.58\ \Omega$, and $L_{ngs} = 114$ mH. On the converter side, the impedance is assumed to be three times smaller than on the grid side, resulting in $R_{ncs} = 1.81\ \Omega$ and $L_{ncs} = 57.6$ mH. This combination of line impedances and shunt capacitance produces a series resonance of 190 Hz.

## 6.2 Small signal model

All the state space matrices presented in Chapter 2 are applied in this section, except for the new electrical system equations given the new impedances involved. This is defined below in Section 6.2.1. Similar to previous small signal models, the closed loop transfer matrix is produced by combining all the elements of the closed loop system, making $[\Delta P^*\ \Delta U^*]^T$ the system inputs and $[\Delta P\ \Delta U]^T$ the system outputs.

### 6.2.1 Linearised electrical system with parallel resonances

Similar to Section 2.2.2.5, the electrical system state space model is obtained by using KVL across the impedances and KCL at the nodes, resulting in

$$\frac{d}{dt}\begin{bmatrix}\Delta i_{cq}\\ \Delta i_{cd}\\ \Delta u_q\\ \Delta u_d\\ \Delta i_{ncsq}\\ \Delta i_{ncsd}\\ \Delta u_{pq}\\ \Delta u_{qd}\\ \Delta i_{ngsq}\\ \Delta i_{ngsd}\end{bmatrix} = \begin{bmatrix} -\frac{R_c}{L_c} & -\omega & \frac{1}{L_c} & 0 & 0 & 0 & 0 & 0 & 0 & 0\\ \omega & -\frac{R_c}{L_c} & 0 & \frac{1}{L_c} & 0 & 0 & 0 & 0 & 0 & 0\\ -\frac{1}{C_f} & 0 & 0 & -\omega & \frac{1}{C_f} & 0 & 0 & 0 & 0 & 0\\ 0 & -\frac{1}{C_f} & \omega & 0 & 0 & \frac{1}{C_f} & 0 & 0 & 0 & 0\\ 0 & 0 & -\frac{1}{L_{ncs}} & 0 & -\frac{R_{ncs}}{L_{ncs}} & -\omega & \frac{1}{L_{ncs}} & 0 & 0 & 0\\ 0 & 0 & 0 & -\frac{1}{L_{ncs}} & \omega & -\frac{R_{ncs}}{L_{ncs}} & 0 & \frac{1}{L_{ncs}} & 0 & 0\\ 0 & 0 & 0 & 0 & -\frac{1}{C_p} & 0 & 0 & -\omega & \frac{1}{C_p} & 0\\ 0 & 0 & 0 & 0 & 0 & -\frac{1}{C_p} & \omega & 0 & 0 & \frac{1}{C_p}\\ 0 & 0 & 0 & 0 & 0 & 0 & -\frac{1}{L_{ngs}} & 0 & -\frac{R_{ngs}}{L_{ngs}} & -\omega\\ 0 & 0 & 0 & 0 & 0 & 0 & 0 & -\frac{1}{L_{ngs}} & \omega & -\frac{R_{ngs}}{L_{ngs}}\end{bmatrix}\begin{bmatrix}\Delta i_{cq}\\ \Delta i_{cd}\\ \Delta u_q\\ \Delta u_d\\ \Delta i_{ncsq}\\ \Delta i_{ncsd}\\ \Delta u_{pq}\\ \Delta u_{qd}\\ \Delta i_{ngsq}\\ \Delta i_{ngsd}\end{bmatrix}$$
$$+\begin{bmatrix} -\frac{1}{L_c} & 0 & 0 & 0\\ 0 & -\frac{1}{L_c} & 0 & 0\\ 0 & 0 & 0 & 0\\ 0 & 0 & 0 & 0\\ 0 & 0 & 0 & 0\\ 0 & 0 & 0 & 0\\ 0 & 0 & 0 & 0\\ 0 & 0 & 0 & 0\\ 0 & 0 & \frac{1}{L_n} & 0\\ 0 & 0 & 0 & \frac{1}{L_n}\end{bmatrix}\begin{bmatrix}\Delta v_q\\ \Delta v_d\\ \Delta e_q\\ \Delta e_d\end{bmatrix} \tag{6.2}$$

### 6.2.2 Validation of linearised model

By combining (6.2) with the linearised converter model of Section 2.2.2, a complete system is produced. This is validated below in Fig. 6.2, where the strong correlation between time domain and small signal models validates the small signal model.

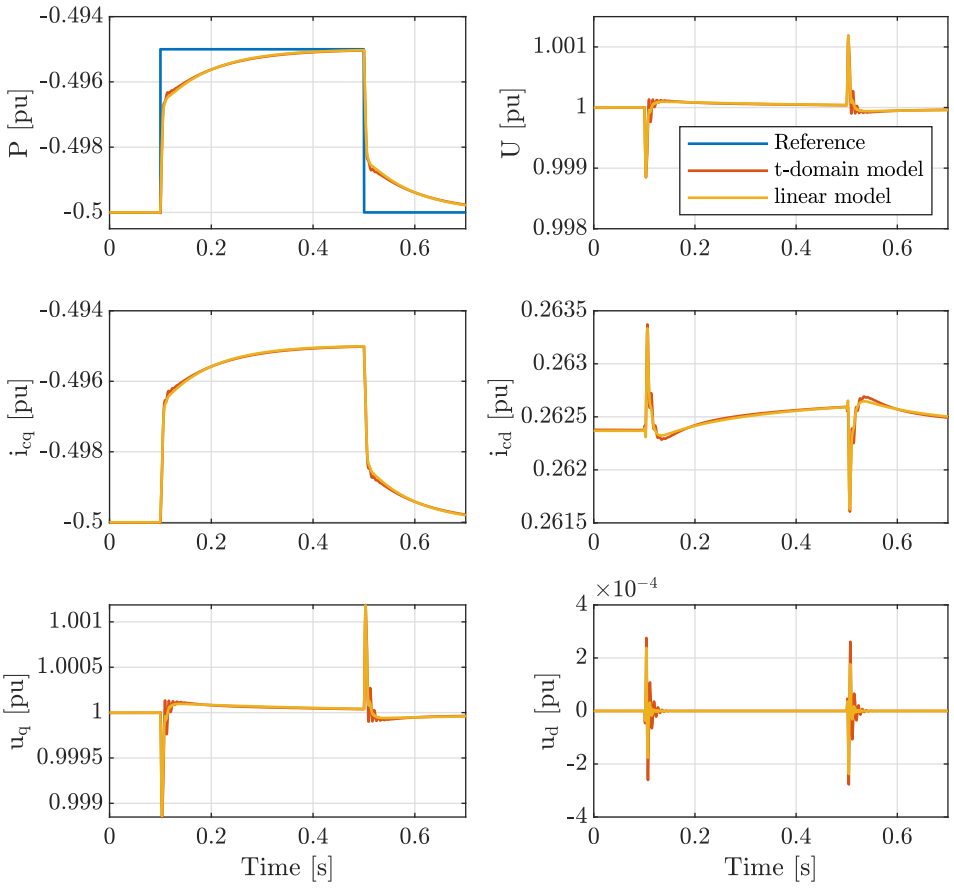


**Figure 6.2:** Validation of small signal model.

### 6.2.3 Analysis of the closed loop transfer matrix

During the study of wideband impedance estimation techniques in Section 3.5.2, system stability was marginal when the resonance frequency was low. At the time, this problem was addressed by re-tuning the outer loop via trial and error. In this chapter, small signal studies are employed to further understand the relationship between outer loop tuning and resonances, in order to optimise the outer loop tuning. Consider the eigenvalues for the closed loop system where $P$ varies from $-1$ to 1 pu, as per Fig. 6.3. The outer loop tuning employed is presented in Appendix A.1.2.1. Inversion is plotted in black and rectification is plotted in red.

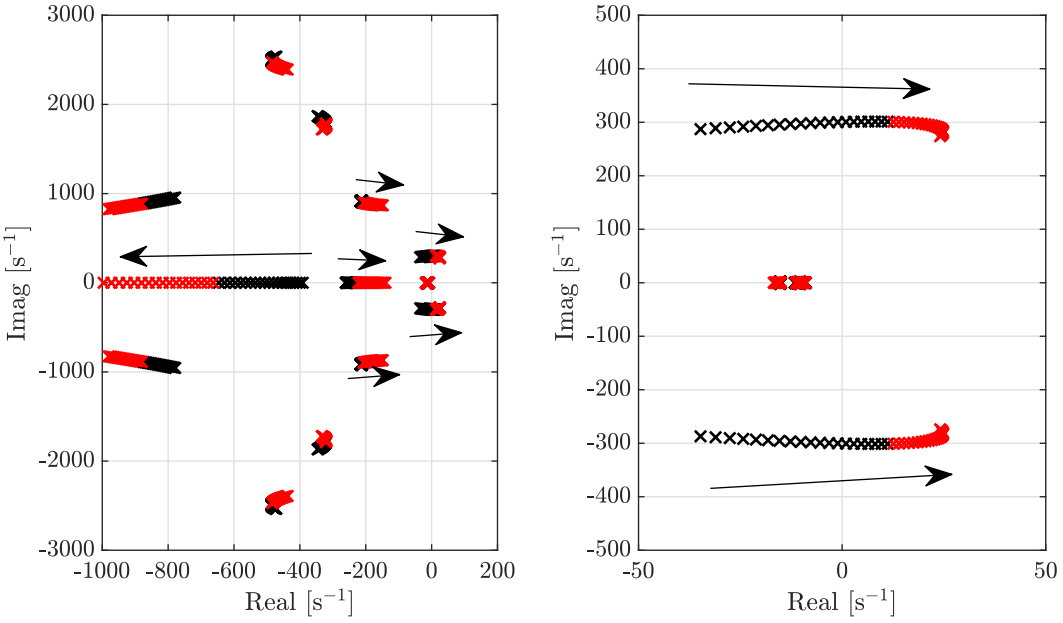


**(a)** Large view. **(b)** Zoomed in.

**Figure 6.3:** Poles of the closed loop system for $P = -1{:}0.05{:}1$.

Fig. 6.3 illustrates that the system is unstable at low values of inversion and all values of rectification, whereas high values of inversion are stable (i.e. $P < -0.4$ pu). This might appear quite different to Fig. 2.22a where a linear grid with a SCR of 3 is stable for all power operating points. However, under closer observation, even the stable system presented in Fig. 2.22a experiences the gradual reduction in damping of some eigenvalues as $P$ increases towards 1 pu. While they do not become unstable,

it does suggest a relationship between active power transfer and damping in linear grids. In this case of Fig. 6.3, the instability occurs for $P \geq -0.4$ pu. The injection of large amounts of active power into the grid, however, provides increased damping and stability is maintained. The underdamping of grid induced resonances is discussed in [120].

### 6.2.4 Analysis of the resonant and equivalent bode plots

To further understand the causes of instability presented in Fig. 6.3, consider the bode plot of Fig. 6.4, where the resonant conditions experienced at $P = 0$ pu are compared to the equivalent linear system with a SCR of 1.71. Although not plotted here, the equivalent system is stable for all power outputs.

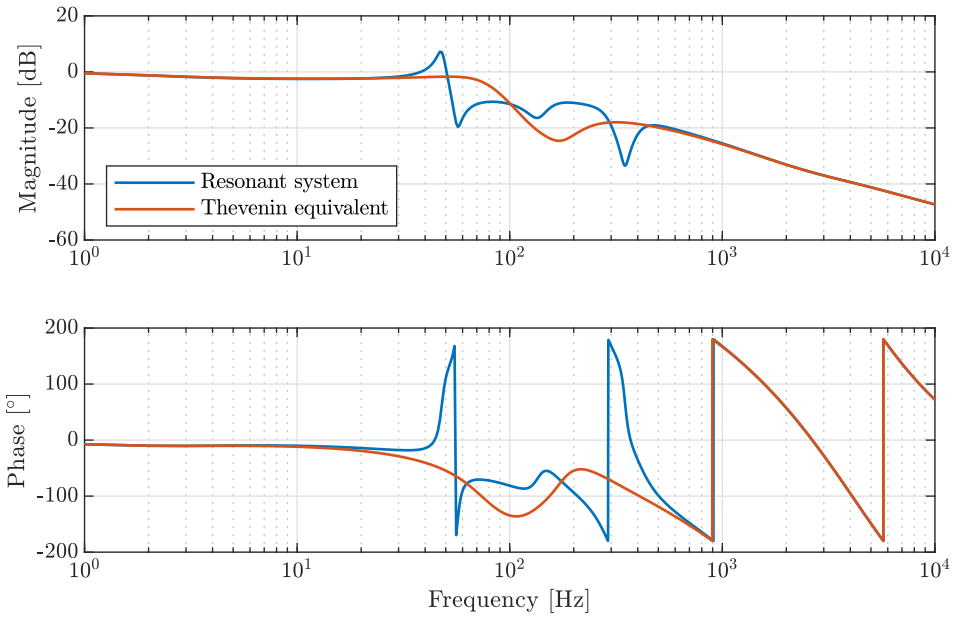


**Figure 6.4:** Bode plots of open loop system $P_{error}$ to $P$ for the resonant grid and the Thévenin equivalent grid, at $P = 0$ pu.

From Fig. 6.4, the impact of both the parallel and series resonances can be seen. The parallel resonance of 110 Hz appears in the converter frame at approx. 50 - 60 Hz, and the secondary parallel resonance, as a result of the PWM filter capacitor, appears in the converter frame at approximately 290 Hz. Outside these resonances, the bode plots are exactly the same.

## 6.3 Resonance mitigation techniques

### 6.3.1 Adapting outer loop tuning

In order to investigate the impact on stability of $K_{p\ P}$, $K_{i\ P}$, $K_{p\ U}$ and $K_{i\ U}$, the eigenvalues for variations in each gain is presented in Fig. 6.5. The system is linearised at $P = 0$ pu, the worst case scenario for RES. For each subplot, one of the gains is multiplied by a constant $C_{gain}$, such that $K_{test} = C_{gain}K_{original}$, where $C_{gain} =$ [0.01 0.05 0.1 0.5 1 1.5 2 3 5 7]. Arrows are included in Fig. 6.5 to show increasing gain direction.

The first observation from Fig. 6.3 is that the integral gains have almost no impact in the overall stability of the system – the proportional gains are much more critical as these have a much greater impact on the position of the poles. The unstable eigenvalues for $K_{p\ P}$ occur for $C_{gain} \geq 0.5$, whereas for $K_{p\ U}$ instability occurs for $C_{gain} \geq 1$. The frequency of the unstable eigenvalues can be extracted from MATLAB, where the unstable eigenvalues of $K_{p\ P}$ occur at a frequency of 45 to 55 Hz in the converter frame (i.e. 95 to 105 Hz in the grid frame); and similarly the unstable eigenvalues of $K_{p\ U}$ occur at a frequency of 47 to 66 Hz in the converter frame (i.e. 97 to 116 Hz in the grid frame). Thus, it can be determined that the cause of the instability is the parallel resonance rather than the series resonance.

To further understand the role of the proportional gains in the system stability, the bode plot magnitudes are presented in Fig. 6.6 and 6.7 for the power and voltage controller, respectively. It can be observed from Fig. 6.6 that with increasing power loop proportional gain, the left hand side plots, where the transfer function input is the power reference, are increasingly steadily. The same can be said for Fig. 6.7, where increases in voltage reference causes a steady increase in the bode magnitudes of relevant (right hand side) plots. Therefore, it can be inferred from these figures is that the proportional gains, by directly lifting the response of the appropriate responses, is amplifying the coupling to the problematic parallel resonance.

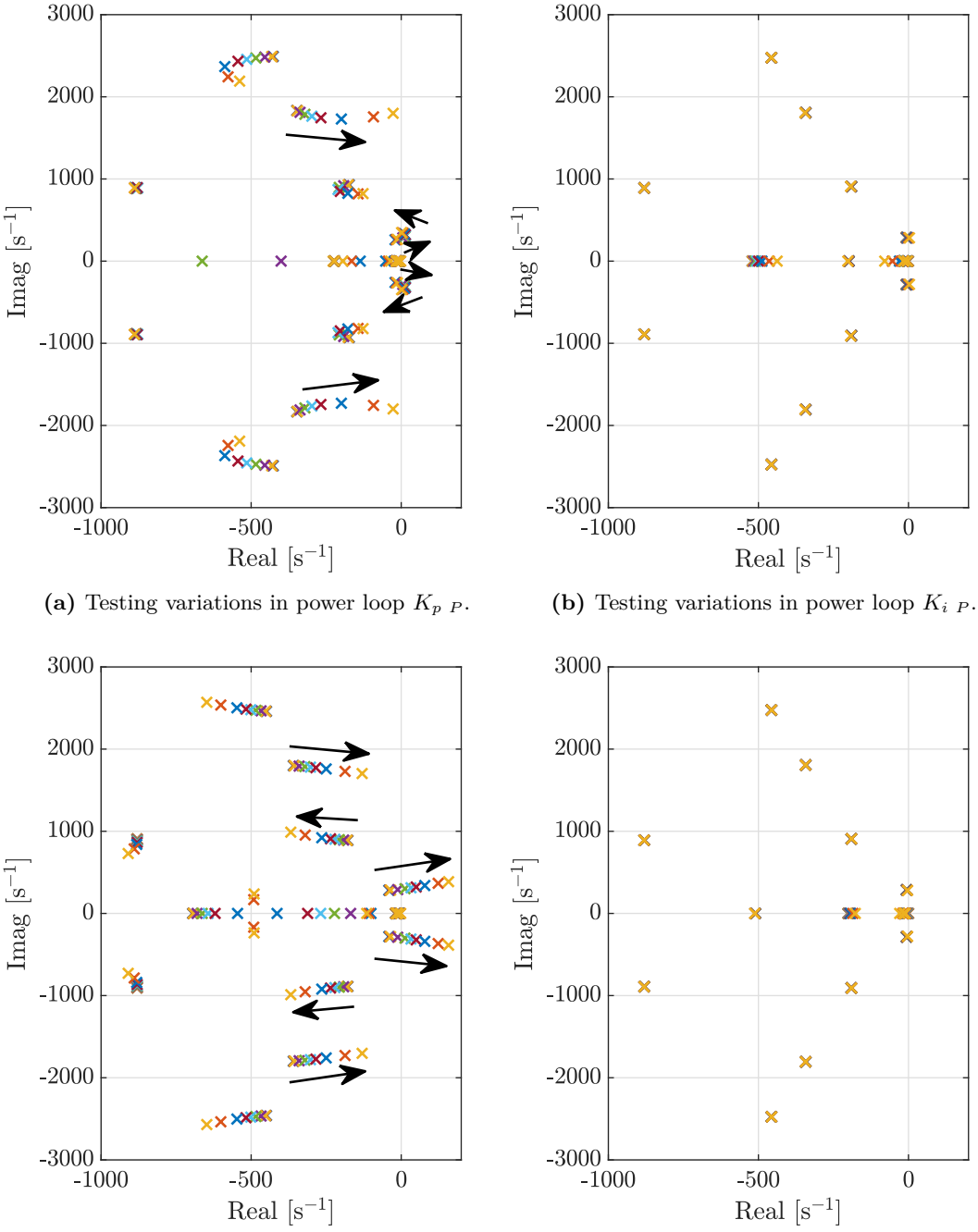


**(a)** Testing variations in power loop $K_{p\ P}$.

**(b)** Testing variations in power loop $K_{i\ P}$.

**(c)** Testing variations in voltage loop $K_{p\ U}$.

**(d)** Testing variations in voltage loop $K_{i\ U}$.

**Figure 6.5:** Eigenvalues of the closed loop system for various outer loop control gains.

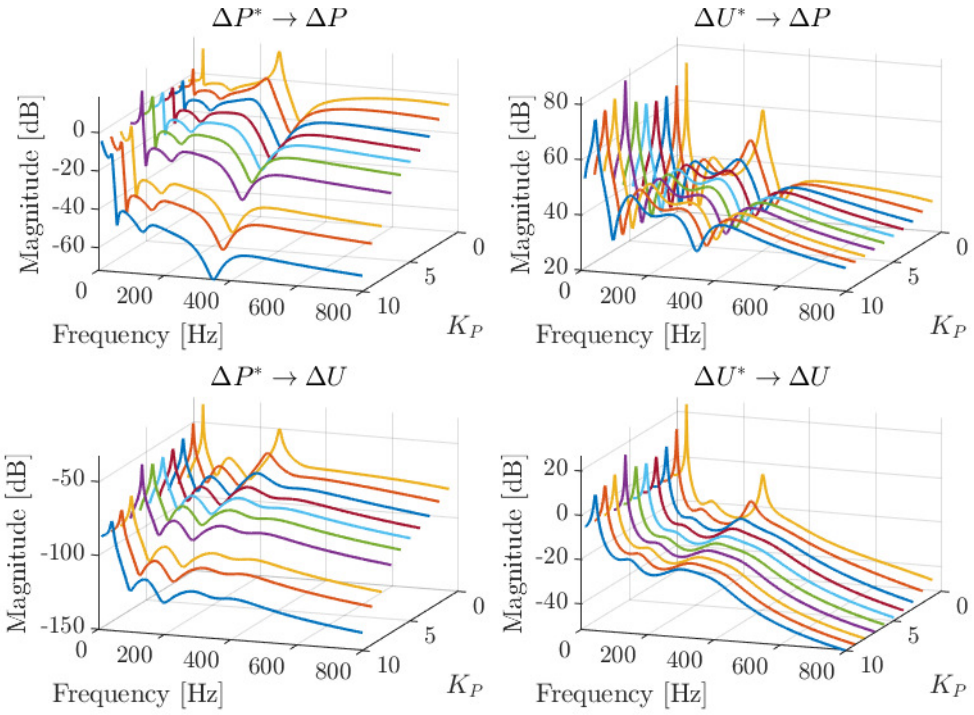


**Figure 6.6:** Bode plots for a range of $K_{p\ P}$.

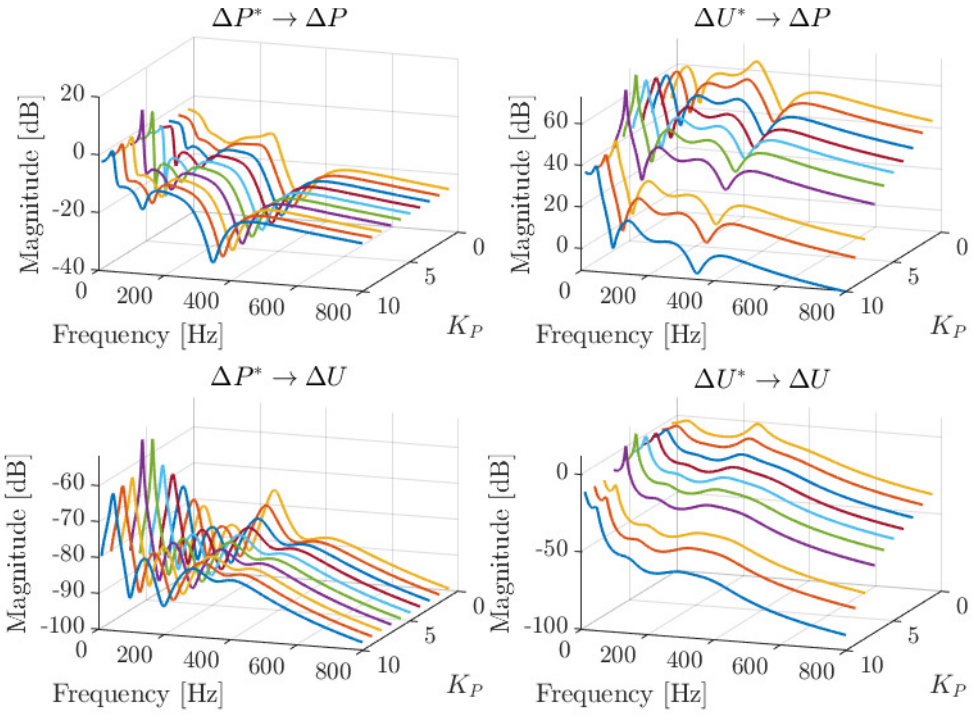


**Figure 6.7:** Bode plots for a range of $K_{p\ U}$.

### 6.3.2 Notch filter

Another possible solution to problematic resonances is the use of notch filters. In [67], the notch is introduced to cover frequencies from 400 Hz to 800 Hz at the input of the current controller.

The notch filter can be described with the following transfer function

$$H_{notch}(s) = \frac{s^2 + \omega_{notch}^2}{s^2 + 2\zeta\omega_{notch}s + \omega_{notch}^2} \tag{6.3}$$

where the damping factor, $\zeta$, is linked to the quality factor $Q$, such that $Q = \frac{1}{2\zeta}$. A total of 12 notch transfer functions are presented in the bode plots of Fig. 6.8, where notch frequencies of 60, 140, 350 and 500 Hz are combined with quality factors 5, 50 and 500.

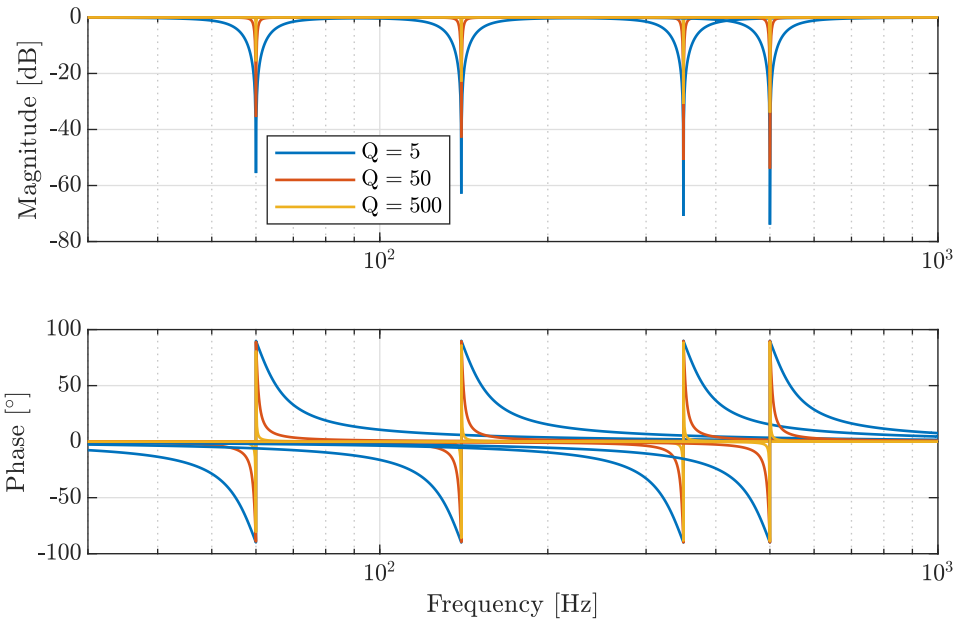


**Figure 6.8:** Bode plots for a range of notch filter quality factors at various notch frequencies: 60, 140, 350 and 500 Hz.

The same notch transfer functions are integrated into the closed loop transfer matrix and the eigenvalues are plotted, as per Fig. 6.9.

From Fig. 6.9, there is only one combination of notch frequency and quality factor

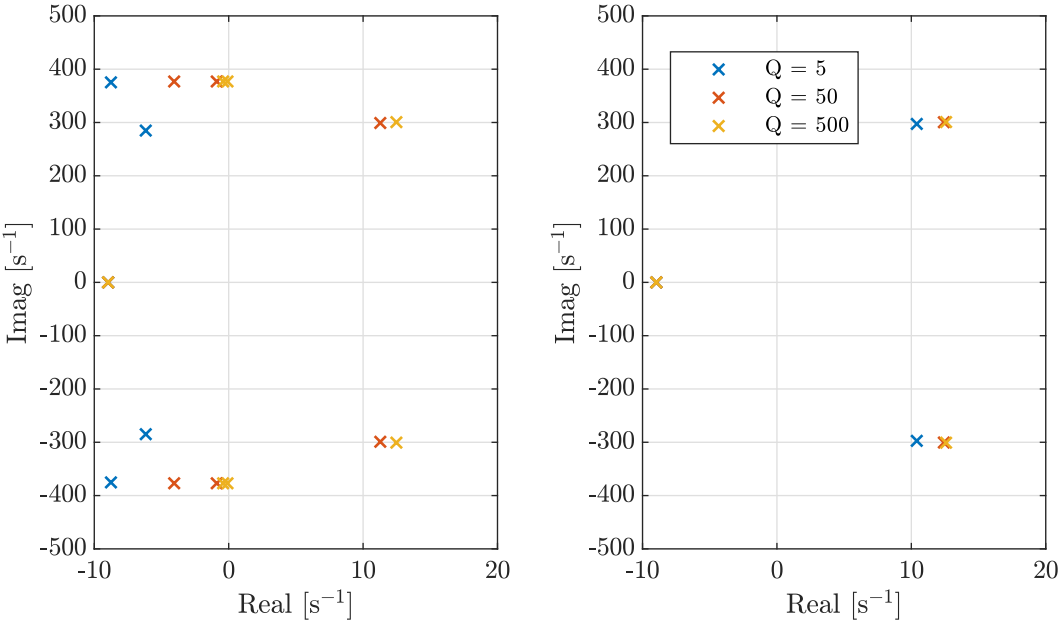


**(a)** $\omega_{notch} = 60$ Hz. **(b)** $\omega_{notch} = 140$ Hz.

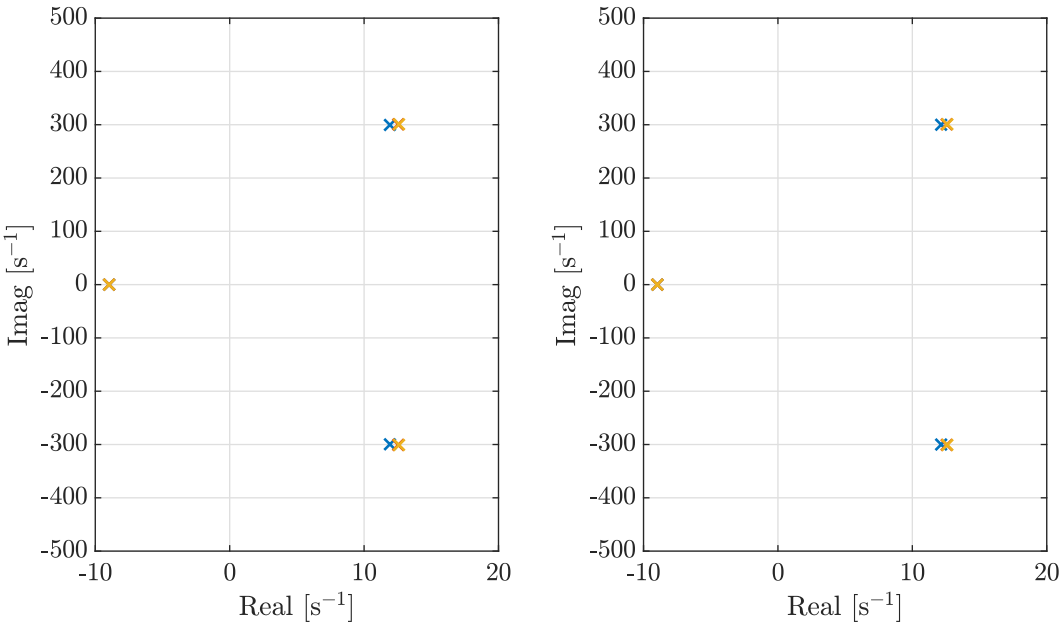


**(c)** $\omega_{notch} = 350$ Hz. **(d)** $\omega_{notch} = 500$ Hz.

**Figure 6.9:** Eigenvalues of the closed loop system for various combinations of quality factor and notch frequency.

that is stable: $\omega_{notch} = 60$ Hz and $Q = 5$. This is further evidence that it is the parallel resonance, and not the series resonance, that causes instability. Further, unlike [67], the application of a large notch (through a large $Q$) does not prevent instability when dealing with low frequency resonances. This is due to the undesired damping of important frequencies required for basic converter functionality.

### 6.3.3 Time domain comparisons

A time domain simulation is used to compare three different controller configurations in the resonant grid scenario:

- The base case (fast controller as per Appendix A.1.2.1).
- The use of a notch frequency of 60 Hz (i.e. 110 Hz in the grid frame), using a quality factor of 5, at the current controller $i^c_{cqd}$ input.
- A reduced outer loop controller where $K_{p\ P}$ and $K_{p\ U}$ in Appendix A.1.2.1 are multiplied by a factor of 0.3 and 0.5, respectively. These values are determined as the largest stable values by the small signal study Fig. 6.5.

The results are presented in Fig. 6.10, where a change in the grid side impedance shifts the resonance from 155 Hz to 110 Hz at 0.1 s, followed by a ramp in power from $-0.8$ pu to $-0.1$ pu. The initial high active power transfer is stable across all controller variations, even when the resonance frequency changes. The fast controller, while well damped at the initial high power output, becomes unstable as the power reference reduces. The notch filter variation of the controller is poorly damped, as per the oscillatory behaviour, but not unstable. The oscillations are due to phase loss in the filtered current measurements at the current controller and eventually fade. The best performing variation in this simulation is the reduced proportional gain controller, producing the expected results given the small signal optimisation. The resonance is well damped without overly affecting the responsiveness of the converter. Further, stability is maintained throughout.

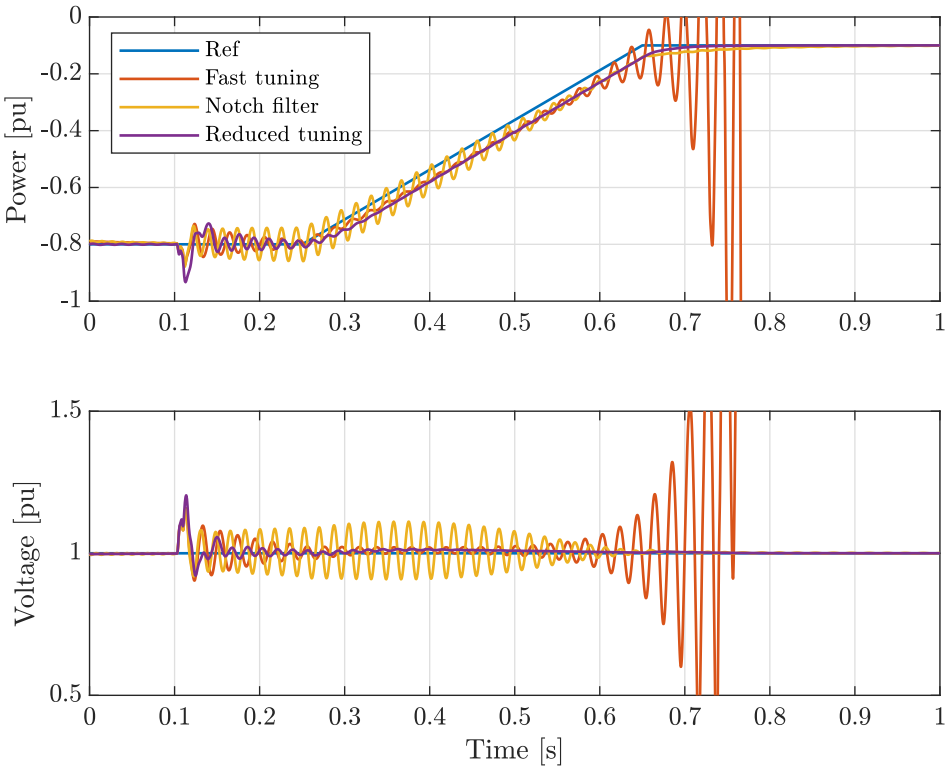


**Figure 6.10:** Time domain plots comparing various control arrangements.

## 6.4 Local state machine control for resonant grids

The task of the local state machine controller is to prevent the onset of instability should a problematic resonance appear. The set of steps proposed are similar to those expressed in Section 5.3, but adapted to suit resonant grids.

### 6.4.1 State machine

The local state machine control can be described using the state machine notation presented in Fig. 6.11, based on the state machine notation from Fig. 5.6.

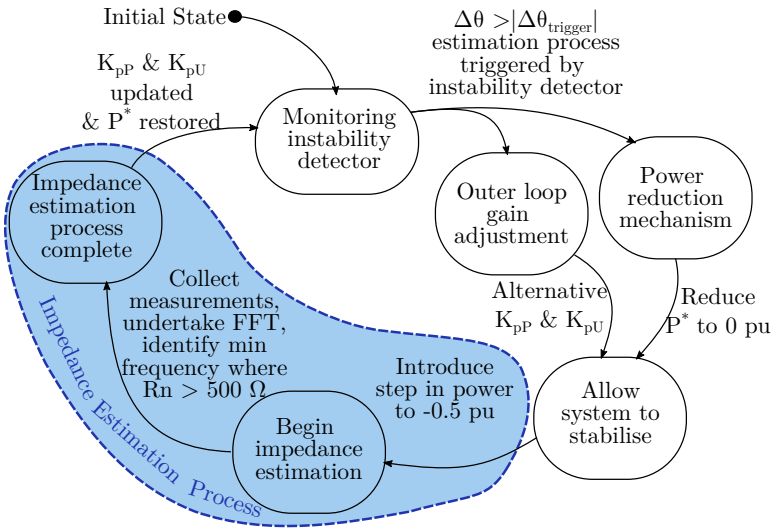


**Figure 6.11:** State machine notation for the local state machine control in resonant grids.

The first step of the local state machine control is to monitor the development of instability with the instability detector presented in Section 5.2. Should the angle $\Delta\theta$ exceed 20°, the risk of instability is mitigated by reducing the proportional gains. To prepare the converter for the impedance estimation process, the power reference is set to zero. A short time later, a step in power reference to $-0.5$ pu is undertaken, and the resultant perturbations allow for resonance identification, as per Section 3.5.2. The frequency of significant resonances determines the set of gains used going forward.

The detection of problematic references is done by using the impedance magnitude, rather than just the resistance or just the reactance. The problematic references are those where the impedance magnitude is greater than 700 Ω.

### 6.4.2 Change in resonance during high active power transfer

The change of resonance frequency at high power transfer levels does not cause instability, but the ensuing changes in power reference will bring the controller into the unstable region. The gentle onset of instability during a ramp in power is presented in Fig. 6.12. This is based on Fig. 6.10 but with the addition of the local state machine control. The original tuning is the fast tuning of Appendix A.1.2.1. The resonance frequency changes at 0.18 s from 155 Hz to 110 Hz.

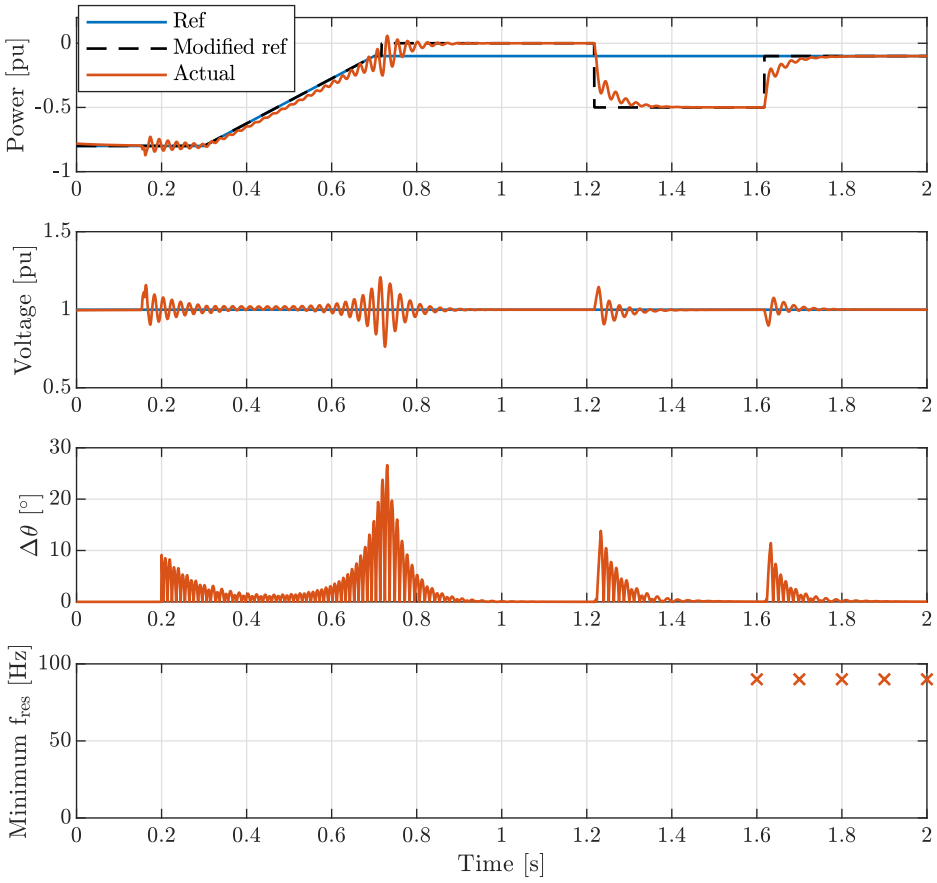


**Figure 6.12:** Testing the local state machine control: resonance change occurs at high $P^*$.

In Fig. 6.12, a gentle build up in oscillations begins at approx. 0.5 s until the instability detector is triggered at approx. 0.7 s. The proportional gains are reduced and the power reference is dropped to zero. The system stabilises and shortly after 1.2 s

a step in power is introduced automatically to $-0.5$ pu for the resonance identification process. Within less than half a second, the frequency of the problematic resonance is identified, the reduced tuning is maintained through the local state machine control logic, and the active power reference is recovered. The determination of the problematic references is presented in the bottom subplot, identified to be 95 Hz.

### 6.4.3 Change in resonance during low active power transfer

Another test is presented in Fig. 6.13, where the change in resonance occurs during low levels of active power transfer at $-0.2$ pu.

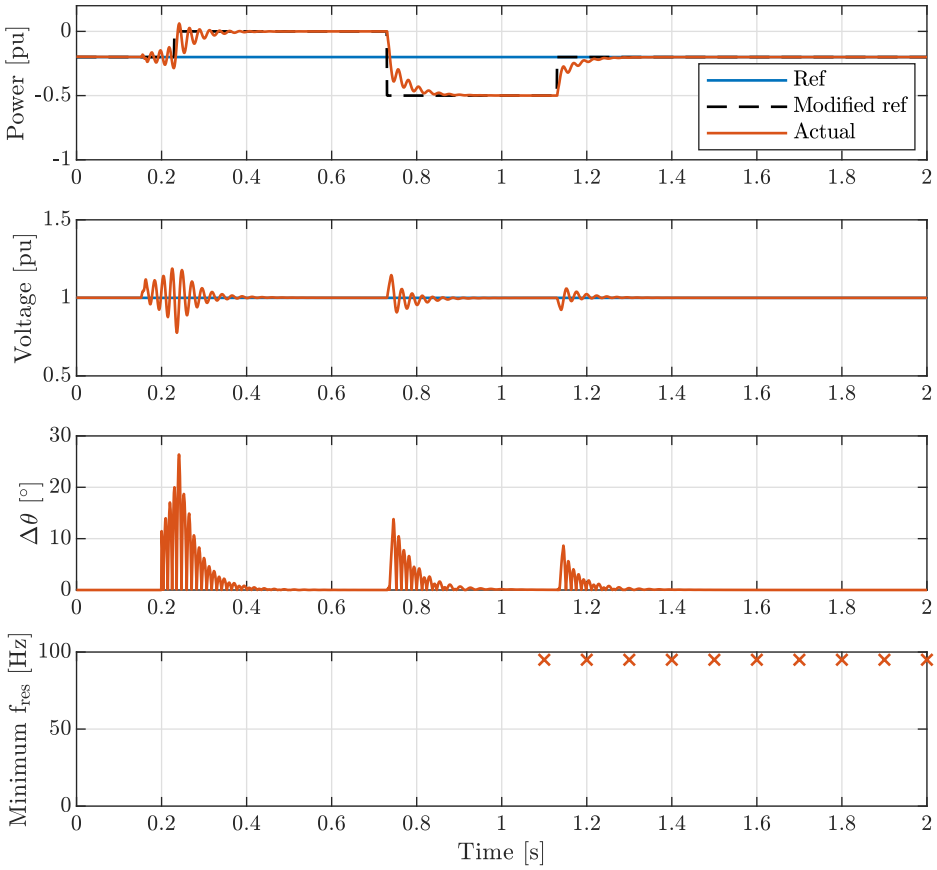


**Figure 6.13:** Testing the local state machine control: resonance change occurs at low $P^*$.

Despite the low power reference, the instability in Fig. 6.13 sets in slowly. This

suggests that instability in resonant grids is not as instantaneous as it is with weak grid instability and voltage angle runaway. The instability mitigation measure, i.e. the change in proportional gains, is effective at reducing the oscillations. The power reference management and the resonance identification process through the impedance estimator allow for autonomous identification of resonances and the maintaining of the reduced outer loop tuning.

# Chapter 7

# Conclusions

In this thesis, the study of converter integration in various challenging grids, namely weak grids and resonant grids, is undertaken. In both instances, impedance estimators provide valuable information about grid parameters, allowing for precise and optimised adaptation to changing grid conditions.

Multiple local impedance estimation techniques are considered, with both passive and active techniques studied. The nonconvergance of the impedance estimation is found for passive techniques operating in stationary grid conditions. Thus, for passive techniques to work, voltage and current values are required for a minimum of two different operating points. This makes it unsuitable for on-demand estimation requirements.

With regards to weak grids, stability issues arise as a result of coupling between active power and voltage. Instead of reducing the controller bandwidth, a more targeted solution is proposed. The PVD, a control modification, is able to reject disturbances caused by the aformentioned coupling, enabling a controller rise time of 40 ms and settling time of 32 ms. The PVD also improves the active power bandwidth of the state space model, from 39 Hz to 46 Hz. To ensure continually optimal performance, an impedance estimator is integrated into the control; and to improve resilience to significant grid events, an instability detector proposed, which automatically reduces the power reference when voltage collapse is imminent. This allows for re-optimisation of the PVD and ensuing recovery of the power reference within less than 2 s.

In the final chapter, the philosophy of stability, dynamic performance and resiliency

through the use of grid impedance estimation is applied to a different problem: resonant grids. Instability onset occurs when undamped resonances become significant. Through the use of root locus analysis, it is shown that the dominant trigger for instability is the outer loop proportional gains. Therefore, when instability onset is detected, these gains are immediately reduced. The power reference is reduced to zero, not for stabilisation, but to prepare the wide-spectrum impedance estimator. Once the estimation process is completed, and any resonant frequencies identified, the outer loop tuning is finalised. The whole process is complete within 1 s.

## 7.1 Future work

From this thesis, future research opportunities have arisen, listed below.

- Combining weak grid and resonant grid adaptations into a single controller. This is challenging because the optimal impedance estimator and instability mitigation measures is different for each scenario.
- Centralising the impedance estimator and communicating local impedance information directly to individual converters without the converters having to undertake the estimation independently. This would allow all converters to optimise to local conditions without having to inject perturbations. While it is unclear how this would work exactly, the combination of network base values and power flow measurements might be sufficient to provide a good indication of local impedances.
- With regards to wide-spectrum impedance estimation, it was found that a grid event that changes the resonance frequency sufficiently excites voltages and currents that a wide-spectrum impedance estimation would accurately determine the new resonant frequency. However, this requires a detection mechanism to trigger the impedance estimator. Future work could identify an appropriate detection mechanism, thus negating the need for an intentionally introduced perturbation.

- Determine how the proposed PVD affects the hardware requirements for wind turbines or wind farm converters.

# Appendix A

# System and control parameters

## A.1 System parameters for simulated 350 MVA system

System parameters below are reproduced from the values used in [44–47].

| Parameters | Value |
|---|---|
| $S_{base}$ | 350 MVA |
| $U_{base}$ | 195 kV (RMS Ph-Ph) |
| $X_n/R_n$ ratio | 10 |
| $R_c$ | 0.01 pu |
| $X_c$ | 0.2 pu |
| $X_f$ | 5.88 pu |

Other system parameters that were not determined by the above mentioned literature.

| Parameters | Value |
|---|---|
| $T_{sampling}$ | 200 $\mu s$ |

### A.1.1 350 MVA weak grid

#### A.1.1.1 Tuning for fast power response

The following tuning is derived to achieve the objectives outlined in 2.2.2.9.1.

| Parameters | Value | Equation |
|---|---|---|
| $\omega_b$ | 500 Hz | N/A |
| $K_{PLLp}$ | 0.028 $rad/(Vs)$ | (2.20) |
| $K_{PLLi}$ | 62.0 $rad/(Vs^2)$ | (2.21) |
| $\tau_{cc}$ | 10 ms | N/A |
| $K_{CCp}$ | 6.92 $V/A$ | (2.31) |
| $K_{CCi}$ | 108.6 $V/(As)$ | (2.32) |
| $K_{Pp}$ | 3.78 $10^{-6}$ $A/W$ | N/A |
| $K_{Pi}$ | 6.75 $10^{-4}$ $A/(Ws)$ | N/A |
| $K_{Up}$ | $-0.007$ $A/V$ | N/A |
| $K_{Ui}$ | $-0.121$ $A/Vs$ | N/A |

An alternative outer loop tuning is utilised in Section 2.3.1.2, optimised for weak grid integration of classical VCC. This results in a slower power loop and a faster voltage loop.

| Parameters | Value | Equation |
|---|---|---|
| $K_{Pp}$ | 2.26 $10^{-6}$ $A/W$ | N/A |
| $K_{Pi}$ | 1.74 $10^{-4}$ $A/(Ws)$ | N/A |
| $K_{Up}$ | $-0.007$ $A/V$ | N/A |
| $K_{Ui}$ | $-0.604$ $A/Vs$ | N/A |

### A.1.2 350 MVA resonant grid

#### A.1.2.1 Tuning for dynamic response in resonant grids

**Table A.1:** Fast OL tuning

| Parameters | Value |
|---|---|
| $K_{Pp}$ | 1.13 $10^{-5}$ A/W |
| $K_{Pi}$ | 1.69 $10^{-4}$ A/(Ws) |
| $K_{Up}$ | $-0.014$ A/V |
| $K_{Ui}$ | $-0.24$ A/(Vs) |

#### A.1.2.2 Tuning for stability in resonant grids

**Table A.2:** Slow OL tuning

| Parameters | Value |
|---|---|
| $K_{P\,p}$ | $0.98\ 10^{-2}$ A/W |
| $K_{P\,i}$ | $7.93\ 10^{-6}$ A/(Ws) |
| $K_{U\,p}$ | $-1.18\ 10^{-4}$ A/V |
| $K_{U\,i}$ | $-0.0845$ A/(Vs) |

## A.2 Tuning of converter for hardware experiments (1 kVA system)

The tuning of the converter used in the laboratory is as follows.

| Parameters | Value | Equation |
|---|---|---|
| $K_{PLLp}$ | 24.2 $rad/(Vs)$ | (2.20) |
| $K_{PLLi}$ | 3.22 $rad/(Vs^2)$ | (2.21) |
| $K_{CCp}$ | 1.12 $V/A$ | (2.31) |
| $K_{CCi}$ | 40 $V/(As)$ | (2.32) |
| $K_{Pp}$ | 0.0048 $A/W$ | N/A |
| $K_{Pi}$ | 0.35 $A/(Ws)$ | N/A |
| $K_{Up}$ | $-0.0048$ $A/V$ | N/A |
| $K_{Ui}$ | $-2$ $A/Vs$ | N/A |

# Appendix B

# Admittance plots

Admittance plots are better suited to identifying series resonances than impedance plots, especially when these plots are linear. These plots are included here, for completeness. Fig. B.1 is the admittance plot for scenario 1, and is equivalent to the impedance plot Fig. 2.8. Similarly, Fig. Fig. B.2 is the admittance plot for scenario 2, and is equivalent to Fig. 2.10.

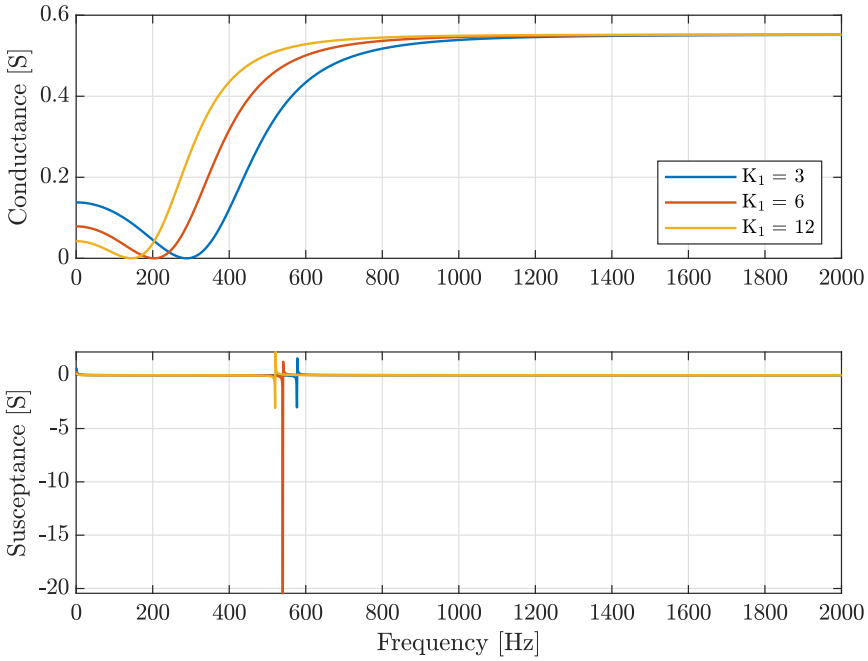


**Figure B.1:** Admittance plots for varying values of grid side impedance.

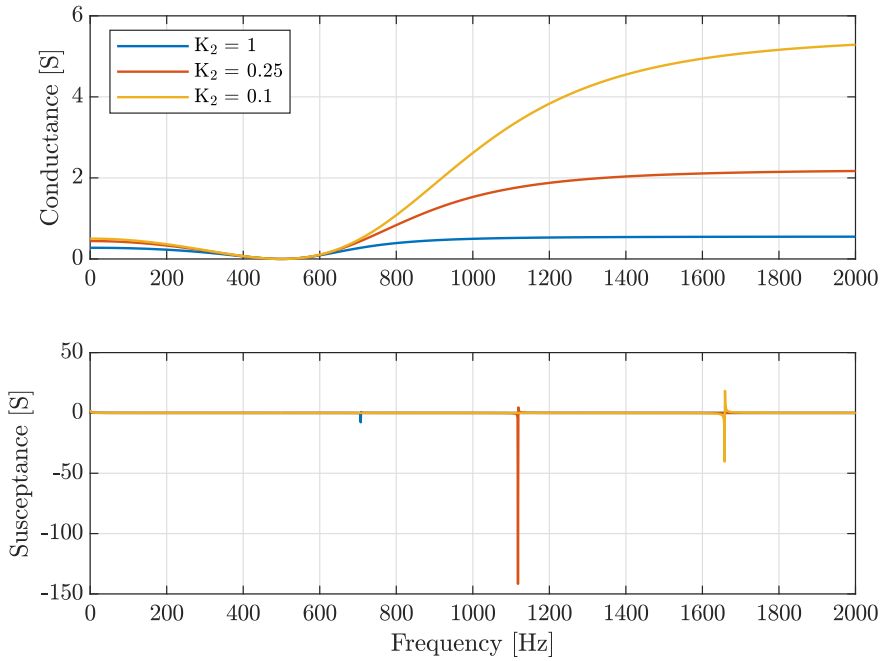


**Figure B.2:** Admittance plots for varying values of converter side impedance.

# Appendix C

# Vector Representation and Transformations

The objective of this Appendix is to demonstrate the equivalent representation of a three phase system as a complex vector. Derivations drawn and adapted from [74, 208].

## C.1 Representation of three phase system as a vector

Consider the following balanced, three phase, instantaneous sinusoidal signals

$$\begin{aligned} f_a(t) &= f \cdot cos(\omega t + \theta_0) \\ f_b(t) &= f \cdot cos(\omega t - \frac{2\pi}{3} + \theta_0) \\ f_c(t) &= f \cdot cos(\omega t + \frac{2\pi}{3} + \theta_0) \end{aligned} \tag{C.1}$$

where $f$ is the amplitude, $\omega$ is the angular velocity of the signal, $\theta_0$ is the initial phase angle (i.e. phase shift) and $t$ is the time. Given that $cos(\omega t) = \frac{1}{2}(e^{+j\omega t} + e^{-j\omega t})$,

$$\begin{aligned} f_a(t) &= f\frac{1}{2}(e^{j\omega t} + e^{-j\omega t}) \\ f_b(t) &= f\frac{1}{2}(e^{j(\omega t - \frac{2\pi}{3})} + e^{-j(\omega t - \frac{2\pi}{3})}) \\ f_c(t) &= f\frac{1}{2}(e^{j(\omega t + \frac{2\pi}{3})} + e^{-j(\omega t + \frac{2\pi}{3})}) \end{aligned} \tag{C.2}$$

For simplicity, the phase shift is negated and the $\alpha$ operator is used to represent $+120°$ rotations [208], such that $e^{j\frac{2\pi}{3}} = \alpha$, and $e^{-j\frac{2\pi}{3}} = \alpha^2$. Thus,

$$\begin{aligned} f_a(t) &= f\frac{1}{2}(e^{j\omega t} + e^{-j\omega t}) \\ f_b(t) &= f\frac{1}{2}(\alpha^2 e^{j\omega t} + \alpha e^{-j\omega t}) \\ f_c(t) &= f\frac{1}{2}(\alpha e^{j\omega t} + \alpha^2 e^{-j\omega t}) \end{aligned} \tag{C.3}$$

Introducing the space phaser, $\overline{f}(t)$ [74],

$$\overline{f}(t) = \frac{2}{3}\left[\, e^{j0} f_a(t) + e^{j\frac{2\pi}{3}} f_b(t) + e^{j\frac{-2\pi}{3}} f_c(t) \,\right] \tag{C.4}$$

Combining (C.3) into (C.4),

$$\overline{f}(t) = \frac{1}{3} f\left[\, (e^{j\omega t} + e^{-j\omega t}) + \alpha(\alpha^2 e^{j\omega t} + \alpha e^{-j\omega t}) + \alpha^2(\alpha e^{j\omega t} + \alpha^2 e^{-j\omega t}) \,\right] \tag{C.5}$$

Simplifying (C.5),

$$\overline{f}(t) = \frac{1}{3} f\left[\, (e^{j\omega t} \cdot (1 + \alpha^3 + \alpha^3) + e^{-j\omega t} \cdot (1 + \alpha + \alpha^2) \,\right] \tag{C.6}$$

Given that $\alpha^3 = 1$ and that $1 + \alpha + \alpha^2 = 0$

$$\overline{f}(t) = f e^{\theta_0} e^{j\omega t} \tag{C.7}$$

With the space vector $\overline{f}(t)$ reduced to a single complex value, it can be represented using two stationary orthogonal components in the $\alpha\beta$-frame.

$$\overline{f} = f_\alpha + jf_\beta \tag{C.8}$$

The stationary $\alpha\beta$-frame can be made to rotate synchronously with the three phase signal by considering the rotation of the three phase system, where the rotation is represented by $e^{j\omega t}$. The convention used in this thesis assigns $q$ as the real component leading the imaginary component $d$ by 90°, such that

$$\overline{f} = (f_q - jf_d)e^{j\omega t} \tag{C.9}$$

## C.2 Clarke Transformation

The Clarke Transformation translates the three phase *abc*-frame to the two phase $\alpha\beta$-frame. Phase $\alpha$ is aligned with the positive real axis of the complex plain, and phase $\beta$ is aligned with the positive imaginary axis of the complex plane, as per Fig. C.1.

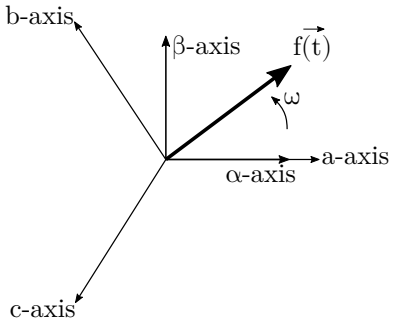


**Figure C.1:** Complex Plane representation of the Clarke Transformation.

The Clarke Transform transforms vector $f_{abc}$ in the *abc*-frame to vector $f_{\alpha\beta}$ in the $\alpha\beta$-frame as per (C.10) below. The zero term included in the transformation allows the inverse transformation to take place; as per (C.11). Unless the *abc* phases are unbalanced, this term will always be zero.

$$\begin{bmatrix} f_\alpha \\ f_\beta \\ f_0 \end{bmatrix} = \frac{2}{3} \begin{bmatrix} 1 & -\frac{1}{2} & -\frac{1}{2} \\ 0 & \sqrt{\frac{3}{2}} & -\sqrt{\frac{3}{2}} \\ \frac{1}{2} & \frac{1}{2} & \frac{1}{2} \end{bmatrix} \begin{bmatrix} f_a \\ f_b \\ f_c \end{bmatrix} \tag{C.10}$$

$$\begin{bmatrix} f_a \\ f_b \\ f_c \end{bmatrix} = \begin{bmatrix} 1 & 0 & 1 \\ -\frac{1}{2} & \sqrt{\frac{3}{2}} & 1 \\ -\frac{1}{2} & -\sqrt{\frac{3}{2}} & 1 \end{bmatrix} \begin{bmatrix} f_\alpha \\ f_\beta \\ f_0 \end{bmatrix} \tag{C.11}$$

Hence, a three-phase *abc*-frame is simplified into two rotating components.

## C.3 DQZ Transformation

The DQZ transformation is achieved by rotating the $\alpha\beta$-frame, synchronising $\alpha$ and $\beta$ to the three phase measurements. This rotating frame was developed by Robert H. Park in 1929 [209]. The generator notation is presented Fig. C.2 and described in (C.12) – (C.13).

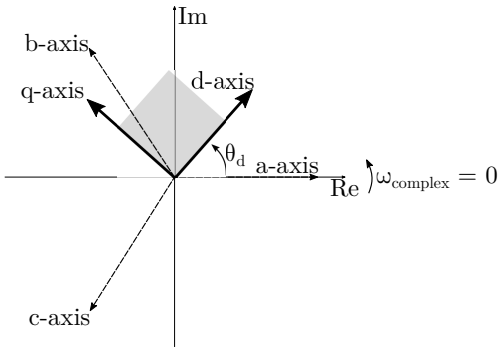


**Figure C.2:** Vectoral representation of the DQZ Transformation in generator notation.

$$\begin{bmatrix} f_d \\ f_q \\ f_0 \end{bmatrix} = \begin{bmatrix} cos(\theta^c) & cos(\theta^c - \frac{2\pi}{3}) & cos(\theta^c + \frac{2\pi}{3}) \\ -sin(\theta^c) & -sin(\theta^c - \frac{2\pi}{3}) & -sin(\theta^c + \frac{2\pi}{3}) \\ \frac{1}{2} & \frac{1}{2} & \frac{1}{2} \end{bmatrix} \begin{bmatrix} f_a \\ f_b \\ f_c \end{bmatrix} \tag{C.12}$$

$$\begin{bmatrix} f_a \\ f_b \\ f_c \end{bmatrix} = \begin{bmatrix} cos(\theta^c) & -sin(\theta^c) & 1 \\ cos(\theta^c - \frac{2\pi}{3}) & -sin(\theta^c - \frac{2\pi}{3}) & 1 \\ cos(\theta^c + \frac{2\pi}{3}) & -sin(\theta^c + \frac{2\pi}{3}) & 1 \end{bmatrix} \begin{bmatrix} f_d \\ f_q \\ f_0 \end{bmatrix} \tag{C.13}$$

There are two motor notations. In this instance the internal voltage is reversed, changing the positive direction of the internal voltage vector, as per Fig. C.3.

Motor notation 1, used in this thesis, is as follows

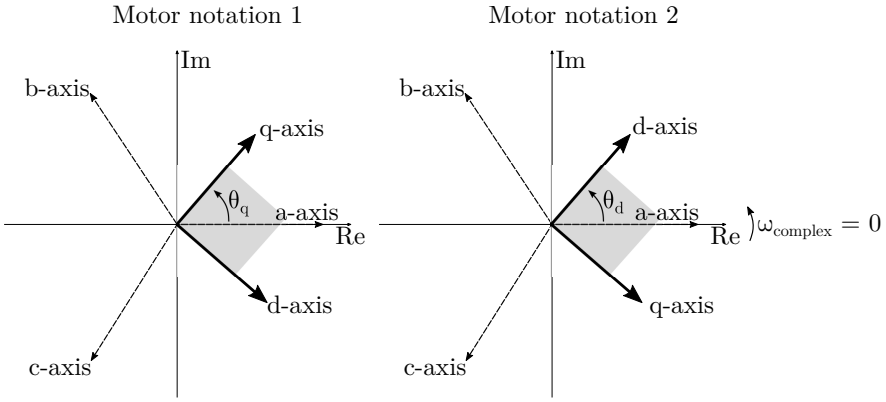


**Figure C.3:** Vectoral representation of the DQZ Transformations in motor notation.

$$\begin{bmatrix} f_q \\ f_d \\ f_0 \end{bmatrix} = \begin{bmatrix} cos(\theta_q) & cos(\theta_q - \frac{2\pi}{3}) & cos(\theta_q + \frac{2\pi}{3}) \\ sin(\theta_q) & sin(\theta_q - \frac{2\pi}{3}) & sin(\theta_q + \frac{2\pi}{3}) \\ \frac{1}{2} & \frac{1}{2} & \frac{1}{2} \end{bmatrix} \begin{bmatrix} f_a \\ f_b \\ f_c \end{bmatrix} \tag{C.14}$$

$$\begin{bmatrix} f_a \\ f_b \\ f_c \end{bmatrix} = \begin{bmatrix} cos(\theta_q) & sin(\theta_q) & 1 \\ cos(\theta_q - \frac{2\pi}{3}) & sin(\theta_q - \frac{2\pi}{3}) & 1 \\ cos(\theta_q + \frac{2\pi}{3}) & sin(\theta_q + \frac{2\pi}{3}) & 1 \end{bmatrix} \begin{bmatrix} f_q \\ f_d \\ f_0 \end{bmatrix} \tag{C.15}$$

As for motor notation 2,

$$\begin{bmatrix} f_d \\ f_q \\ f_0 \end{bmatrix} = \begin{bmatrix} cos(\theta^c) & cos(\theta^c - \frac{2\pi}{3}) & cos(\theta^c + \frac{2\pi}{3}) \\ sin(\theta^c) & sin(\theta^c - \frac{2\pi}{3}) & sin(\theta^c + \frac{2\pi}{3}) \\ \frac{1}{2} & \frac{1}{2} & \frac{1}{2} \end{bmatrix} \begin{bmatrix} f_a \\ f_b \\ f_c \end{bmatrix} \tag{C.16}$$

$$\begin{bmatrix} f_a \\ f_b \\ f_c \end{bmatrix} = \begin{bmatrix} cos(\theta^c) & sin(\theta^c) & 1 \\ cos(\theta^c - \frac{2\pi}{3}) & sin(\theta^c - \frac{2\pi}{3}) & 1 \\ cos(\theta^c + \frac{2\pi}{3}) & sin(\theta^c + \frac{2\pi}{3}) & 1 \end{bmatrix} \begin{bmatrix} f_d \\ f_q \\ f_0 \end{bmatrix} \tag{C.17}$$

# Appendix D

# Small signal study with experimental parameters

This Appendix undertakes the equivalent small signal studies presented in Chapter 4 but with the 1 kVA parameters. The equivalent of Fig. 2.22b (no PVD) and 4.6b (with PVD) is presented in Fig. D.1, for a SCR of 1.38.

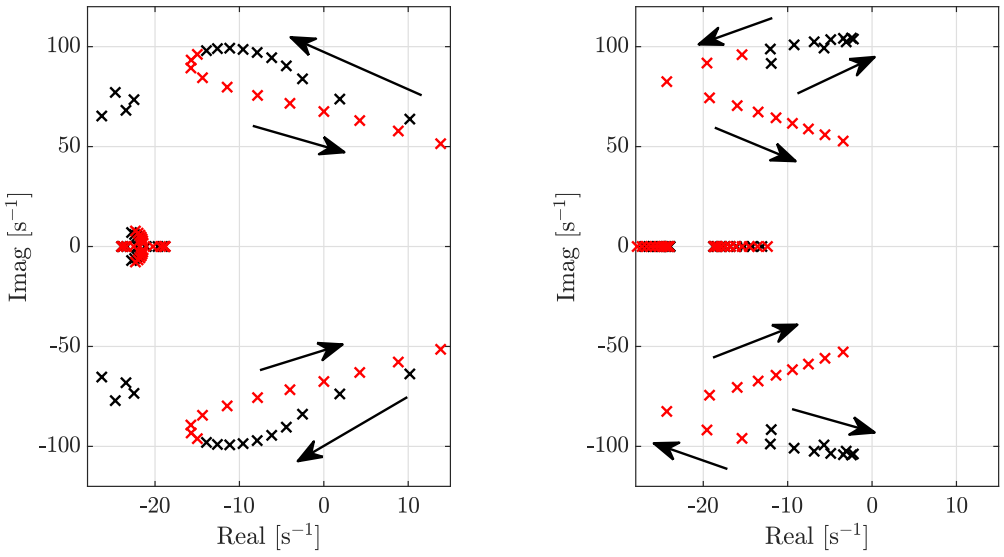


**(a)** Weak grid, no PVD.

**(b)** Weak grid, nwith PVD.

**Figure D.1:** Eigenvalues of the closed loop transfer matrix, the arrow indicates increases in power from $-1$ pu to 1 pu in increments of 0.05.

The small signal model can also be used to determine the rise-time and settling-

time of the closed-loop system in a very weak grid (SCR = 1.38), using the MATLAB *stepinfo* command, resulting in a rise time is 0.016 s and the settling time is 0.29 s. This suggests that the controller is well within the target values as set in Section 4.1 for the experimental parameters.

Fig. 2.23 and 2.24, without PVD, are reproduced with experimental parameters in Fig. D.2 and D.3. The strong grid employs a SCR of 5.53 and the weak grid a SCR of 1.39.

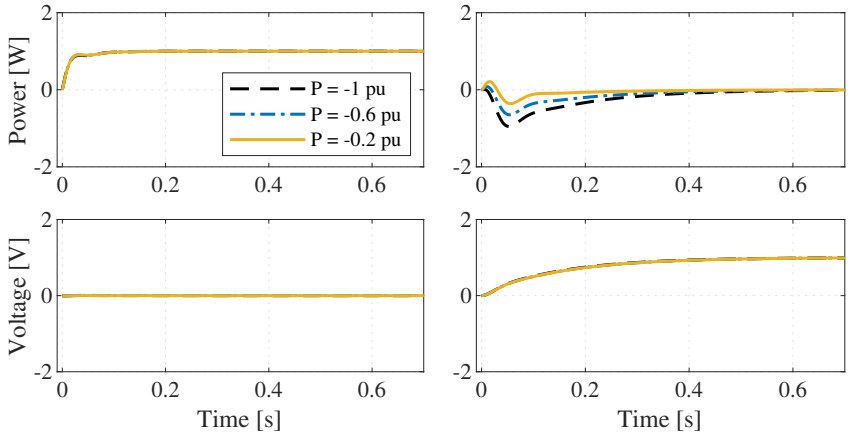


**Figure D.2:** Closed loop step response – without the PVD in a strong grid.

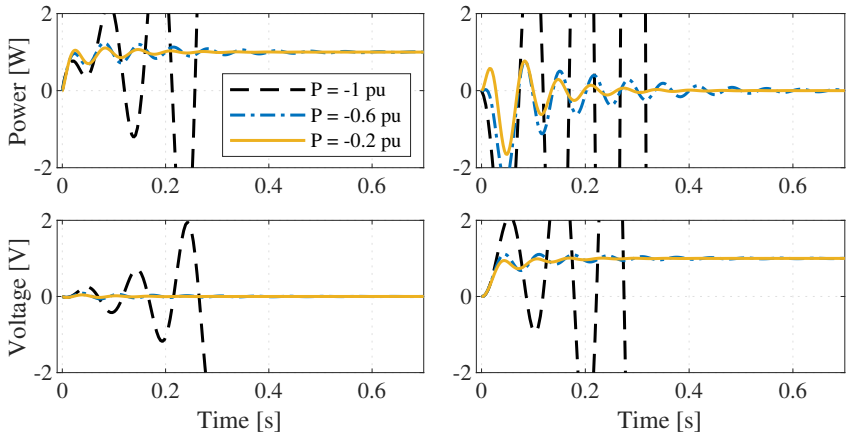


**Figure D.3:** Closed loop step response – without the PVD in a weak grid.

Fig. 4.7 and 4.8, with PVD, are reproduced with experimental parameters in Fig. D.4 and D.5.

The small signal studies with the 1 kVA parameters produce similar results to

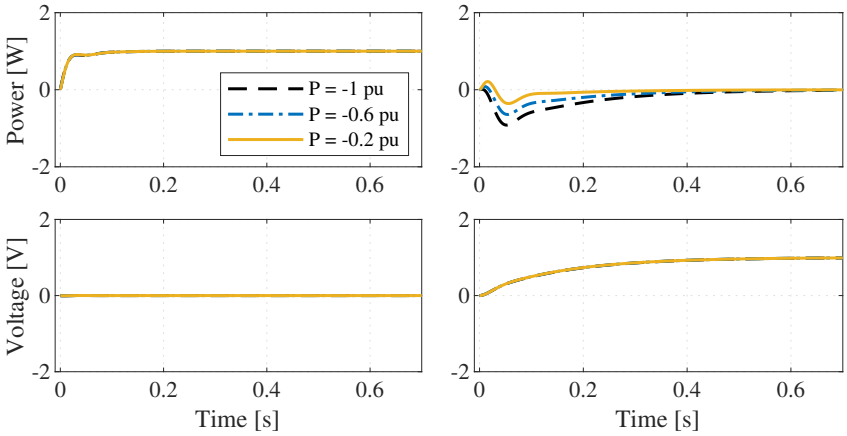


**Figure D.4:** Closed loop step response – with the PVD in a strong grid.

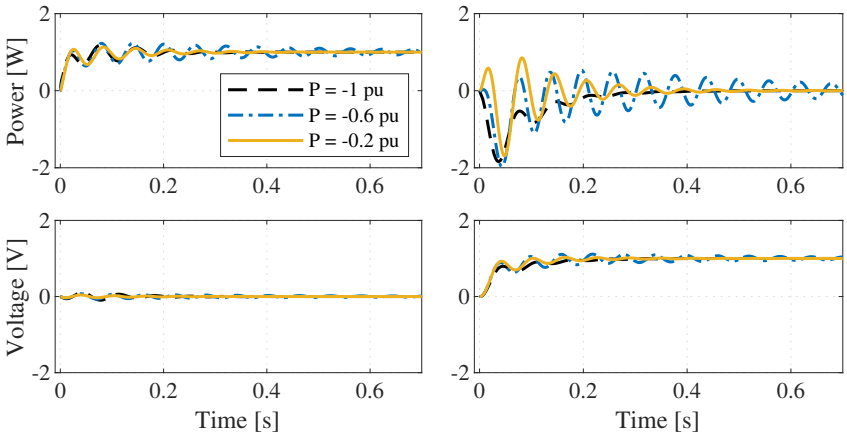


**Figure D.5:** Closed loop step response – with the PVD in a weak grid.

the equivalent studies at 350 MVA. The PVD demonstrates a similar improvement in small signal stability and step response, thus meeting the objectives using both sets of parameters.

# Bibliography

[1] UNFCCC, "Adoption of the Paris Agreement," tech. rep., United Nations, 2015.

[2] A. De and P. Chitkara, "Case Study: Grid and Market Integration of Wind Generation in Tamil Nadu, India," *Renewable Energy Integration: Practical Management of Variability, Uncertainty, and Flexibility in Power Grids*, pp. 125–133, 2014.

[3] S. Fine and K. Kumaraswamy, "Policies for Accommodating Higher Penetration of Variable Energy Resources: US Outlook and Perspectives," *Renewable Energy Integration: Practical Management of Variability, Uncertainty, and Flexibility in Power Grids*, pp. 13–25, 2014.

[4] M. Müller-Mienack, "German Renewable Energy Sources Pathway in the New Century," *Renewable Energy Integration: Practical Management of Variability, Uncertainty, and Flexibility in Power Grids*, pp. 359–365, 2014.

[5] A. Sayigh, D. Milborrow, and J. K. Kaldellis, *The Age of Wind Energy*. Innovative Renewable Energy, Cham: Springer International Publishing, 2020.

[6] ENTSO-E, "High Penetration of Power Electronic Interfaced Power Sources and the Potential Contribution of Grid Forming Converters," tech. rep., 2020.

[7] F. Blaabjerg, M. Liserre, and K. Ma, "Power electronics converters for wind turbine systems," *IEEE Energy Conversion Congress and Exposition: Energy Conversion Innovation for a Clean Energy Future, ECCE 2011, Proceedings*, vol. 48, no. 2, pp. 281–290, 2011.

[8] T. Stehly, P. Beiter, and P. Duffy, "2019 Cost of Wind Energy Review," tech. rep., National Renewable Energy Laboratory, 2019.

[9] J. Hernández-Moro and J. Martínez-Duart, "Analytical model for solar PV and CSP electricity costs: Present LCOE values and their future evolution," *Renewable and Sustainable Energy Reviews*, vol. 20, pp. 119–132, apr 2013.

[10] P. J. Baruah, N. Eyre, M. Qadrdan, M. Chaudry, S. Blainey, J. W. Hall, N. Jenkins, and M. Tran, "Energy system impacts from heat and transport electrification," *Proceedings of the Institution of Civil Engineers - Energy*, vol. 167, pp. 139–151, aug 2014.

[11] B. Widera, "Renewable hydrogen implementations for combined energy storage, transportation and stationary applications," *Thermal Science and Engineering Progress*, vol. 16, p. 100460, may 2020.

[12] J. Flower, "Low-carbon hydrogen supply," Tech. Rep. 645, UK Parliament, 2021.

[13] T. Burton, N. Jenkins, D. Sharpe, and E. Bossanyi, *Wind Energy Handbook*. Chichester, UK: John Wiley & Sons, Ltd, may 2011.

[14] C. Buchhagen, C. Rauscher, A. Menze, and J. Jung, "BorWin1 - First Experiences with harmonic interactions in converter dominated grids," *International ETG Congress 2015; Die Energiewende - Blueprints for the new energy age*, pp. 1–7, 2015.

[15] N. Flourentzou, V. G. Agelidis, and G. D. Demetriades, "VSC-based HVDC power transmission systems: An overview," *IEEE Transactions on Power Electronics*, vol. 24, no. 3, pp. 592–602, 2009.

[16] G. Denis, T. Prevost, M.-S. Debry, F. Xavier, X. Guillaud, and A. Menze, "The Migrate project: the challenges of operating a transmission grid with only inverter-based generation. A grid-forming control improvement with transient current-limiting control," *IET Renewable Power Generation*, vol. 12, pp. 523–529, apr 2018.

[17] U. Tamrakar, D. Shrestha, M. Maharjan, B. P. Bhattarai, T. M. Hansen, and R. Tonkoski, "Virtual inertia: Current trends and future directions," *Applied Sciences (Switzerland)*, vol. 7, no. 7, pp. 1–29, 2017.

[18] M. Asmine, C.-É. Langlois, and N. Aubut, "Inertial response from wind power plants during a frequency disturbance on the Hydro-Quebec system – event analysis and validation," *IET Renewable Power Generation*, vol. 12, pp. 515–522, apr 2018.

[19] M. Di Somma, G. Graditi, E. Heydarian-Forushani, M. Shafie-khah, and P. Siano, "Stochastic optimal scheduling of distributed energy resources with renewables considering economic and environmental aspects," *Renewable Energy*, vol. 116, pp. 272–287, feb 2018.

[20] A. Alanazi and A. Khodaei, "Optimal battery energy storage sizing for reducing wind generation curtailment," in *2017 IEEE Power & Energy Society General Meeting*, pp. 1–5, IEEE, jul 2017.

[21] J. Abe, A. Popoola, E. Ajenifuja, and O. Popoola, "Hydrogen energy, economy and storage: Review and recommendation," *International Journal of Hydrogen Energy*, vol. 44, pp. 15072–15086, jun 2019.

[22] J. Andersson and S. Grönkvist, "Large-scale storage of hydrogen," *International Journal of Hydrogen Energy*, vol. 44, pp. 11901–11919, may 2019.

[23] G. Verbič, S. Mhanna, and A. C. Chapman, "Energizing Demand Side Participation," in *Pathways to a Smarter Power System*, pp. 115–181, Elsevier, 2019.

[24] J. Z. Zhou, H. Ding, S. Fan, Y. Zhang, and A. M. Gole, "Impact of Short-Circuit Ratio and Phase-Locked-Loop Parameters on the Small-Signal Behavior of a VSC-HVDC Converter," *IEEE Transactions on Power Delivery*, vol. 29, pp. 2287–2296, oct 2014.

[25] A. Egea-Alvarez, O. Gomis-Bellmunt, F. Hassan, and C. Barker, "Capability curves of a VSC-HVDC connected to a weak AC grid considering stability and

power limits," in *11th IET International Conference on AC and DC Power Transmission*, pp. 053 (5 .)–053 (5 .), Institution of Engineering and Technology, 2015.

[26] K. Schaber, F. Steinke, P. Mühlich, and T. Hamacher, "Parametric study of variable renewable energy integration in Europe: Advantages and costs of transmission grid extensions," *Energy Policy*, vol. 42, pp. 498–508, 2012.

[27] S. Sumathi, L. Ashok Kumar, and P. Surekha, *Solar PV and Wind Energy Conversion Systems*. Green Energy and Technology, Cham: Springer International Publishing, 2015.

[28] N. P. W. Strachan and D. Jovcic, "Stability of a Variable-Speed Permanent Magnet Wind Generator With Weak AC Grids," *IEEE Transactions on Power Delivery*, vol. 25, pp. 2779–2788, oct 2010.

[29] B. Badrzadeh, Z. Emin, S. Goyal, S. Grogan, A. Haddadi, A. Halley, A. Louis, T. Lund, J. Matevosyan, T. Morton, D. Premm, and S. Sproul, "System Strength," *CIGRE SCIENCE & ENGINEERING Power Systems*, vol. 20, no. 13, 2019.

[30] National Grid ESO, "Technical Report on the events of 9 August 2019," *Technical Report*, no. September, pp. 2–38, 2019.

[31] S.-J. S. Tsai and K.-H. Wong, "On-line estimation of thevenin equivalent with varying system states," in *2008 IEEE Power and Energy Society General Meeting - Conversion and Delivery of Electrical Energy in the 21st Century*, pp. 1–7, IEEE, jul 2008.

[32] J. Lavenius, L. Vanfretti, and G. N. Taranto, "Performance assessment of PMU-based estimation Methods of Thevenin Equivalents for real-time voltage stability monitoring," *2015 IEEE 15th International Conference on Environment and Electrical Engineering, EEEIC 2015 - Conference Proceedings*, pp. 1977–1982, 2015.

[33] Y. Gui, X. Wang, and F. Blaabjerg, "Vector Current Control Derived from Direct Power Control for Grid-Connected Inverters," *IEEE Transactions on Power Electronics*, vol. 34, pp. 9224–9235, sep 2019.

[34] S. Grunau and F. W. Fuchs, "Effect of Wind-Energy Power Injection into Weak Grids,"

[35] L. Harnefors, J. Kukkola, M. Routimo, M. Hinkkanen, and X. Wang, "A Universal Controller for Grid-Connected Voltage-Source Converters," *IEEE Journal of Emerging and Selected Topics in Power Electronics*, vol. 6777, no. c, pp. 1–1, 2020.

[36] J. A. Suul, S. D'Arco, P. Rodríguez, and M. Molinas, "Impedance-compensated grid synchronisation for extending the stability range of weak grids with voltage source converters," *IET Generation, Transmission & Distribution*, vol. 10, no. 6, pp. 1315–1326, 2016.

[37] T. Kalitjuka, "Control of Voltage Source Converters for Power System Applications," no. July, pp. 1–69, 2011.

[38] S. Lu, Z. Xu, L. Xiao, W. Jiang, and X. Bie, "Evaluation and Enhancement of Control Strategies for VSC Stations under Weak Grid Strengths," *IEEE Transactions on Power Systems*, vol. 33, no. 2, pp. 1836–1847, 2018.

[39] D. Jovcic and K. Ahmed, *High-Voltage Direct-Current Transmission*. Chichester, UK: John Wiley & Sons, Ltd, jul 2015.

[40] A. Ahlawat and S. Nagarajan, "Laboratory Scale Power Cable Model For Power System Education," in *2020 International Conference for Emerging Technology (INCET)*, pp. 1–5, IEEE, jun 2020.

[41] G. Liu, M. Fan, P. Wang, and M. Zheng, "Study on Reactive Power Compensation Strategies for Long Distance Submarine Cables Considering Electrothermal Coordination," *Journal of Marine Science and Engineering*, vol. 9, p. 90, jan 2021.

[42] R. K. Varma, S. Auddy, and Y. Semsedini, "Mitigation of subsynchronous resonance in a series-compensated wind farm using FACTS controllers," *IEEE Transactions on Power Delivery*, vol. 23, no. 3, pp. 1645–1654, 2008.

[43] J. Enslin and P. Heskes, "Harmonic interaction between a large number of distributed power inverters and the distribution network," in *IEEE 34th Annual Conference on Power Electronics Specialist, 2003. PESC '03.*, vol. 4, pp. 1742–1747, IEEE, 2003.

[44] A. Egea Àlvarez, *Multiterminal HVDC transmissions systems for offshore wind.* PhD thesis, 2014.

[45] L. Zhang, *Modeling and Control of VSC-HVDC Links Connected to Weak AC Systems.* PhD thesis, KTH Royal Institute of Technology, 2010.

[46] A. Egea-Alvarez, S. Fekriasl, F. Hassan, and O. Gomis-Bellmunt, "Advanced Vector Control for Voltage Source Converters Connected to Weak Grids," *IEEE Transactions on Power Systems*, vol. 30, no. 6, pp. 3072–3081, 2015.

[47] G. Wu, "Analysis and design of vector control for VSC-HVDC connected to weak grids," *CSEE Journal of Power and Energy Systems*, 2017.

[48] K. Givaki, D. Chen, and L. Xu, "Current Error Based Compensations for VSC Current Control in Weak Grids for Wind Farm Applications," *IEEE Transactions on Sustainable Energy*, vol. 10, no. 1, pp. 26–35, 2019.

[49] M. Ashabani and Y. A.-R. I. Mohamed, "Integrating VSCs to Weak Grids by Nonlinear Power Damping Controller With Self-Synchronization Capability," *IEEE Transactions on Power Systems*, vol. 29, pp. 805–814, mar 2014.

[50] IEEE, *IEEE Guide for Planning DC Links Terminating at AC Locations Having Low Short-Circuit Capacities.* IEEE, 1997.

[51] National Grid Electricity Transmission plc, "The Grid Code," Tech. Rep. 5, 2017.

[52] J. Khazaei, P. Idowu, A. Asrari, A. B. Shafaye, and L. Piyasinghe, "Review of HVDC control in weak AC grids," *Electric Power Systems Research*, vol. 162, no. February, pp. 194–206, 2018.

[53] H. Alenius, T. Messo, T. Reinikka, and T. Roinila, "Aggregated Modeling and Power Hardware-in-the-Loop Emulation of Grid Impedance," *2018 IEEE Energy Conversion Congress and Exposition, ECCE 2018*, pp. 4179–4186, 2018.

[54] S. Achilles, A. Isaacs, J. MacDowell, and C. Smith, "Integrating Inverter-Based Resources into Low Short Circuit Strength Systems Reliability Guideline," tech. rep., North American Electric Reliability Corportation, jun 2017.

[55] J. Ballance and S. Goldberg, "Subsynchronous Resonance in Series Compensated Transmission Lines," *IEEE Transactions on Power Apparatus and Systems*, vol. PAS-92, pp. 1649–1658, sep 1973.

[56] X. Xie, X. Zhang, H. Liu, H. Liu, Y. Li, and C. Zhang, "Characteristic Analysis of Subsynchronous Resonance in Practical Wind Farms Connected to Series-Compensated Transmissions," *IEEE Transactions on Energy Conversion*, vol. 32, no. 3, pp. 1117–1126, 2017.

[57] L. Kilgore, L. Elliott, and E. Taylor, "The Prediction and Control of Self-Excited Oscillations Due to Series Capacitors in Power Systems," *IEEE Transactions on Power Apparatus and Systems*, vol. PAS-90, pp. 1305–1311, may 1971.

[58] F. Bizzarri, A. Brambilla, and F. Milano, "Simplified Model to Study the Induction Generator Effect of the Subsynchronous Resonance Phenomenon," *IEEE Transactions on Energy Conversion*, vol. 33, pp. 889–892, jun 2018.

[59] NERC, "Lesson Learned Sub-Synchronous Interaction between Series-Compensated Transmission Lines and Generation," tech. rep., 2009.

[60] V. Virulkar and G. Gotmare, "Sub-synchronous resonance in series compensated wind farm: A review," *Renewable and Sustainable Energy Reviews*, vol. 55, pp. 1010–1029, mar 2016.

[61] L. Harnefors, "Analysis of subsynchronous torsional interaction with power electronic converters," *IEEE Transactions on Power Systems*, vol. 22, no. 1, pp. 305–313, 2007.

[62] M. Janaki, N. Prabhu, R. Thirumalaivasan, and D. P. Kothari, "Mitigation of SSR by subsynchronous current injection with VSC HVDC," *International Journal of Electrical Power and Energy Systems*, vol. 57, pp. 287–297, 2014.

[63] M. I. Chehardeh, H. Lesani, M. K. Zadeh, and E. M. Siavashi, "An optimal control strategy to alleviate subsynchronous resonance in VSC-HVDC systems," *PEITS 2009 - 2009 2nd Conference on Power Electronics and Intelligent Transportation System*, vol. 1, pp. 250–255, 2009.

[64] T. Joseph, C. E. Ugalde-Loo, S. Balasubramaniam, and J. Liang, "Real-time estimation and damping of SSR in a VSC-HVDC connected series-compensated system," *IEEE Transactions on Power Systems*, vol. 33, no. 6, pp. 7052–7063, 2018.

[65] K. Md Hasan, K. Rauma, A. Luna, J. I. Candela, and P. Rodriguez, "Harmonic Resonance Study for Wind Power Plant," *Renewable Energy and Power Quality Journal*, vol. 1, pp. 1507–1512, apr 2012.

[66] M. Bradt, B. Badrzadeh, E. Camm, D. Mueller, J. Schoene, T. Siebert, T. Smith, M. Starke, and R. Walling, "Harmonics and resonance issues in wind power plants," in *PES T&D 2012*, pp. 1–8, IEEE, may 2012.

[67] P. Brogan, "The stability of multiple, high power, active front end voltage sourced converters when connected to wind farm collector systems," *EPE Wind Energy Chapter Symposium 2010*, pp. 1–6, 2010.

[68] Z. Staroszczyk, "A Method for Real-Time, Wide-Band Identification of the Source Impedance in Power Systems," *IEEE Transactions on Instrumentation and Measurement*, vol. 54, pp. 377–385, feb 2005.

[69] M. Bollen, S. Mousavi-Gargari, and S. Bahramirad, "Harmonic resonances due to transmission-system cables," *Renewable Energy and Power Quality Journal*, vol. 1, pp. 712–716, apr 2014.

[70] A. H. Senta and M. D. Solanki, "Analysis of Sub Synchronous Resonance," in *2019 IEEE International Conference on Intelligent Techniques in Control, Optimization and Signal Processing (INCOS)*, pp. 1–6, IEEE, apr 2019.

[71] G. Li, Y. Chen, A. Luo, Z. He, H. Wang, Z. Zhu, W. Wu, and L. Zhou, "Analysis and Mitigation of Subsynchronous Resonance in Series-Compensated Grid-Connected System Controlled by a Virtual Synchronous Generator," *IEEE Transactions on Power Electronics*, vol. 35, no. 10, pp. 11096–11107, 2020.

[72] F. A. Rahman al Jowder and B. T. Ooi, "VSC-HVDC station with SSSC characteristics," *IEEE Transactions on Power Electronics*, vol. 19, no. 4, pp. 1053–1059, 2004.

[73] B. Bose, "The past, present, and future of power electronics [Guest Introduction]," *IEEE Industrial Electronics Magazine*, vol. 3, pp. 7–11, 14, jun 2009.

[74] A. Yazdani and I. Reza, *Voltage source converter in power system.* John Wiley & Sons, Inc., 2010.

[75] M. Chaudhary, S. M. Brahma, and S. J. Ranade, "Interpreting the short circuit behavior of type 4 wind turbine generator," *Proceedings of the IEEE Power Engineering Society Transmission and Distribution Conference*, pp. 14–18, 2014.

[76] M. Barnes, D. S. Vilchis-Rodriguez, X. Pei, R. Shuttleworth, O. Cwikowski, and A. C. Smith, "HVDC Circuit Breakers-A Review," *IEEE Access*, vol. 8, pp. 211829–211848, 2020.

[77] S. K. Chung, "A phase tracking system for three phase utility interface inverters," *IEEE Transactions on Power Electronics*, vol. 15, no. 3, pp. 431–438, 2000.

[78] Guan-Chyun Hsieh and J. Hung, "Phase-locked loop techniques. A survey," *IEEE Transactions on Industrial Electronics*, vol. 43, pp. 609–615, dec 1996.

[79] C. Bajracharya, M. Molinas, J. A. Suul, and T. M. Undeland, "Understanding of tuning techniques of converter controllers for VSC-HVDC," *Proceedings of the Nordic Workshop on Power and Industrial Electronics (NORPIE/2008)*, pp. 1–8, 2008.

[80] L. Harnefors and H. P. Nee, "Model-based current control of ac machines using the internal model control method," *IEEE Transactions on Industry Applications*, vol. 34, no. 1, pp. 133–141, 1998.

[81] Shuhui Li, T. A. Haskew, and Ling Xu, "Control of HVDC Light System Using Conventional and Direct Current Vector Control Approaches," *IEEE Transactions on Power Electronics*, vol. 25, pp. 3106–3118, dec 2010.

[82] J. He and Y. W. Li, "Generalized closed-loop control schemes with embedded virtual impedances for voltage source converters with LC or LCL filters," *IEEE Transactions on Power Electronics*, vol. 27, no. 4, pp. 1850–1861, 2012.

[83] K. Sharifabadi, L. Harnefors, H.-P. Nee, S. Norrga, and R. Teodorescu, *Design, Control and Application of Modular Multilevel Converters for HVDC Transmission Systems*. No. Mmc, Chichester, UK: John Wiley & Sons, Ltd, oct 2016.

[84] R. Peña-Alzola, M. Liserre, F. Blaabjerg, R. Sebastían, J. Dannehl, and F. W. Fuchs, "Analysis of the passive damping losses in lcl-filter-based grid converters," *IEEE Transactions on Power Electronics*, vol. 28, no. 6, pp. 2642–2646, 2013.

[85] P. Kundur, *Power System Stability and Control*. McGraw-Hill, 1993.

[86] J. F. Silva and S. F. Pinto, *35. Advanced control of switching power converters*. 2011.

[87] K. Hangos, J. Bokor, and G. Szederkényiio, *Analysis and control of nonlinear process systems*, vol. 42. 2006.

[88] J. F. Morris, K. H. Ahmed, and A. Egea-Alvarez, "Analysis of Controller Bandwidth Interactions for Vector-Controlled VSC Connected to Very Weak AC

Grids," *IEEE Journal of Emerging and Selected Topics in Power Electronics*, vol. 6777, no. c, pp. 1–1, 2020.

[89] M. F. M. Arani and Y. A. R. I. Mohamed, "Analysis and Performance Enhancement of Vector-Controlled VSC in HVDC Links Connected to Very Weak Grids," *IEEE Transactions on Power Systems*, vol. 32, no. 1, pp. 684–693, 2017.

[90] P. Gahinet and P. Apkarian, "Structured H synthesis in MATLAB," *IFAC Proceedings Volumes (IFAC-PapersOnline)*, vol. 44, no. 1 PART 1, pp. 1435–1440, 2011.

[91] O. Anaya-Lara, D. Campos-Gaona, E. Moreno-Goytia, and G. Adam, *Offshore Wind Energy Generation*. 2014.

[92] M. Rashed, M. Sumner, A. Ghanem, M. A. Elsayes, and I. I. Mansy, "Grid impedance estimation for islanding detection and adaptive control of converters," *IET Power Electronics*, vol. 10, no. 11, pp. 1279–1288, 2017.

[93] K. Givaki, D. Chen, L. Xu, and Y. Xu, "An Alternative Current-Error Based Control for VSC Integration to Weak Grid," in *2018 IEEE Power & Energy Society General Meeting (PESGM)*, pp. 1–5, IEEE, aug 2018.

[94] K. M. Alawasa, Y. A. R. I. Mohamed, and W. Xu, "Active mitigation of subsynchronous interactions between PWM voltage-source converters and power networks," *IEEE Transactions on Power Electronics*, vol. 29, no. 1, pp. 121–134, 2014.

[95] J. Fang, X. Li, H. Li, and Y. Tang, "Stability Improvement for Three-Phase Grid-Connected Converters Through Impedance Reshaping in Quadrature-Axis," *IEEE Transactions on Power Electronics*, vol. 33, pp. 8365–8375, oct 2018.

[96] A. J. Agbemuko, J. L. Dominguez-Garcia, O. Gomis-Bellmunt, and L. Harnefors, "Passivity-based analysis and performance enhancement of a vector controlled VSC connected to a weak AC grid," *IEEE Transactions on Power Delivery*, vol. 36, no. 1, pp. 156–167, 2021.

[97] J. Fang, J. Yu, Y. Zhang, and S. M. Goetz, "An Estimation-Based Solution to Weak-Grid-Induced Small-Signal Stability Problems of Power Converters," *IEEE Journal of Emerging and Selected Topics in Power Electronics*, vol. 9, pp. 4558–4572, aug 2021.

[98] G. Wu, "Analysis and design of vector control for VSC-HVDC connected to weak grids," *CSEE Journal of Power and Energy Systems*, 2017.

[99] X. Zhang, M. Li, and D. Xu, "PCC Voltage Perturbation Path Analysis and Compensation for Grid-Connected Voltage-Source Converter under Weak Grid," *IEEE Transactions on Industrial Electronics*, vol. 68, no. 12, pp. 12331–12339, 2021.

[100] H. Khazraj, F. Faria Da Silva, and C. L. Bak, "An improved current controller to ensure the robust performance of grid-connected converters under weak grid Conditions," *EEEIC 2016 - International Conference on Environment and Electrical Engineering*, 2016.

[101] M. Cespedes and J. Sun, "Adaptive Control of Grid-Connected Inverters Based on Online Grid Impedance Measurements," *IEEE Transactions on Sustainable Energy*, vol. 5, pp. 516–523, apr 2014.

[102] M. Li, X. Zhang, Z. Guo, J. Wang, Y. Wang, F. Li, and W. Zhao, "The Control Strategy for the Grid-Connected Inverter through Impedance Reshaping in q-Axis and its Stability Analysis under a Weak Grid," *IEEE Journal of Emerging and Selected Topics in Power Electronics*, vol. 9, no. 3, pp. 3229–3242, 2021.

[103] Ö. Göksu, R. Teodorescu, C. L. Bak, F. Iov, and P. C. Kjær, "Instability of wind turbine converters during current injection to low voltage grid faults and PLL frequency based stability solution," *IEEE Transactions on Power Systems*, vol. 29, no. 4, pp. 1683–1691, 2014.

[104] Q. C. Zhong and G. Weiss, "Synchronverters: Inverters that mimic synchronous generators," *IEEE Transactions on Industrial Electronics*, vol. 58, no. 4, pp. 1259–1267, 2011.

[105] Q. C. Zhong, "Virtual Synchronous Machines: A unified interface for grid integration," *IEEE Power Electronics Magazine*, vol. 3, no. 4, pp. 18–27, 2016.

[106] P. Brogan, T. Knueppel, D. Elliott, and N. Goldenbaum, "Experience of Grid Forming Power Converter Control," *17th International Wind Integration Workshop*, no. October, 2018.

[107] S. D'Arco and J. A. Suul, "Virtual synchronous machines - Classification of implementations and analysis of equivalence to droop controllers for microgrids," in *2013 IEEE Grenoble Conference*, pp. 1–7, IEEE, jun 2013.

[108] Song Ruihua, Zheng Chao, Li Ruomei, and Zhou Xiaoxin, "VSCs based HVDC and its control strategy," in *2005 IEEE/PES Transmission and Distribution Conference and Exposition: Asia and Pacific*, pp. 1–6, IEEE, 2005.

[109] M. Davari and Y. A. R. I. Mohamed, "Robust Vector Control of a Very Weak-Grid-Connected Voltage-Source Converter Considering the Phase-Locked Loop Dynamics," *IEEE Transactions on Power Electronics*, vol. 32, no. 2, pp. 977–994, 2017.

[110] A. A. Abdelrahim, M. Smailes, K. Ahmed, P. Mckeever, and A. Egea-alvarez, "Modified grid forming converter controller with fault ride through capability without PLL or current loop," *18th Wind Integration Workshop*, no. October, pp. 1–8, 2019.

[111] R. Ierna, J. Zhu, H. Urdal, A. J. Roscoe, and C. D. Booth, "Effects of VSM Converter Control on Penetration Limits of Non-Synchronous Generation in the GB Power System," in *15th Wind Integration Workshop*, 2016.

[112] A. D. Giles, *A study of small signal stability in power systems with converters*. PhD thesis, University of Strathclyde, 2018.

[113] J. F. Morris, K. H. Ahmed, and A. Egea, "Standardized Assessment Framework for Design and Operation of Weak AC Grid-Connected VSC Controllers," *IEEE Access*, vol. 9, pp. 95282–95293, 2021.

[114] A. Johnson and N. Tleis, "The Development of Grid Code Requirements for New and Renewable Forms of Generation in Great Britain," *Wind Engineering*, vol. 29, pp. 201–215, may 2005.

[115] M. Ciobotaru, R. Teodorescu, and F. Blaabjerg, "On-line grid impedance estimation based on harmonic injection for grid-connected PV inverter," *IEEE International Symposium on Industrial Electronics*, no. i, pp. 2437–2442, 2007.

[116] T. Roinila, M. Vilkko, and J. Sun, "Broadband methods for online grid impedance measurement," *2013 IEEE Energy Conversion Congress and Exposition, ECCE 2013*, pp. 3003–3010, 2013.

[117] R. Luhtala, T. Roinila, and T. Messo, "Implementation of Real-Time Impedance-Based Stability Assessment of Grid-Connected Systems Using MIMO-Identification Techniques," *IEEE Transactions on Industry Applications*, vol. 54, no. 5, pp. 5054–5063, 2018.

[118] B. Alinezhad and H. Kazemi Karegar, "On-Line Thévenin Impedance Estimation Based on PMU Data and Phase Drift Correction," *IEEE Transactions on Smart Grid*, vol. 9, pp. 1033–1042, mar 2018.

[119] N. Mohammed, M. Ciobotaru, and G. Town, "Online parametric estimation of grid impedance under unbalanced grid conditions," *Energies*, vol. 12, no. 24, 2019.

[120] J. Sun, G. Wang, X. Du, and H. Wang, "A Theory for Harmonics Created by Resonance in Converter-Grid Systems," *IEEE Transactions on Power Electronics*, vol. 34, pp. 3025–3029, apr 2019.

[121] A. O. Akinrinde, A. Swanson, and R. Tiako, "Investigation and analysis of temporary overvoltages caused by filter banks at onshore wind farm substation," *International Journal of Renewable Energy Research*, vol. 7, no. 2, pp. 770–777, 2017.

[122] M. H. Samimi, I. Ahmadi-Joneidi, A. Majzoobi, and S. Golshannavaz, "Appropriate selection of shunt compensation reactor in parallel transmission lines: A

case study," *International Journal of Electrical Power & Energy Systems*, vol. 96, pp. 163–173, mar 2018.

[123] H. Yin, M. Sahni, N. Karnik, and H. K. Nia, "Root cause analysis for harmonic resonance tripping in wind power plants: An ERCOT case study," in *2017 IEEE Power & Energy Society General Meeting*, vol. 2018-Janua, pp. 1–5, IEEE, jul 2017.

[124] R. Peña-Alzola, M. Liserre, F. Blaabjerg, M. Ordonez, and Y. Yang, "LCL-filter design for robust active damping in grid-connected converters," *IEEE Transactions on Industrial Informatics*, vol. 10, no. 4, pp. 2192–2203, 2014.

[125] X. Chen, C. Y. Gong, H. Z. Wang, and L. Cheng, "Stability analysis of LCL-type grid-connected inverter in weak grid systems," *2012 International Conference on Renewable Energy Research and Applications, ICRERA 2012*, pp. 1–6, 2012.

[126] H. Goh, M. Armstrong, and B. Zahawi, "Adaptive control technique for suppression of resonance in grid-connected PV inverters," *IET Power Electronics*, vol. 12, pp. 1479–1486, may 2019.

[127] C. Zou, H. Rao, S. Xu, Y. Li, W. Li, J. Chen, X. Zhao, Y. Yang, and B. Lei, "Analysis of Resonance Between a VSC-HVDC Converter and the AC Grid," *IEEE Transactions on Power Electronics*, vol. 33, pp. 10157–10168, dec 2018.

[128] A. de Oliveira, J. de Oliveira, J. Resende, and M. Miskulin, "Practical approaches for AC system harmonic impedance measurements," *IEEE Transactions on Power Delivery*, vol. 6, no. 4, pp. 1721–1726, 1991.

[129] M. Nagpal, W. Xu, and J. Sawada, "Harmonic impedance measurement using three-phase transients," *IEEE Transactions on Power Delivery*, vol. 13, no. 1, pp. 272–277, 1998.

[130] A. Robert, T. Deflandre, E. Gunther, R. Bergeron, A. Emanuel, A. Ferrante, G. Finlay, R. Gretsch, A. Guarini, J. Gutierrez Iglesias, D. Hartmann, M. Lahtinen, R. Marshall, K. Oonishi, C. Pincella, S. Poulsen, P. Ribeiro,

M. Samotyj, K. Sand, J. Smid, P. Wright, and Y. Zhelesko, "Guide for assessing the network harmonic impedance," *CIRED*, vol. 1997, no. 438, pp. 3/1–310, 1997.

[131] R. Redi, P. Tenti, and J. D. Van Wyk, "Power electronics' polluting effects," *IEEE Spectrum*, vol. 34, no. 5, pp. 32–39, 1997.

[132] M. Tsukamoto, S. Ogawa, Y. Natsuda, Y. Minowa, and S. Nishimura, "Advanced technology to identify harmonics characteristics and results of measuring," in *Ninth International Conference on Harmonics and Quality of Power. Proceedings (Cat. No.00EX441)*, vol. 1, pp. 341–346, IEEE, 2000.

[133] Z. Staroszczyk, "Accuracy problems in on-line one-phase distribution/load system identification task," in *Proceedings of IEEE International Symposium on Industrial Electronics*, vol. 1, pp. 354–357, IEEE, 1996.

[134] Z. Staroszczyk, "Problems in real-time wide band identification of power systems," in *IMTC/98 Conference Proceedings. IEEE Instrumentation and Measurement Technology Conference.*, vol. 2, pp. 779 – 784, 1998.

[135] M. Liserre, F. Blaabjerg, and R. Teodorescu, "Grid impedance detection via excitation of LCL-filter resonance," in *Fourtieth IAS Annual Meeting. Conference Record of the 2005 Industry Applications Conference, 2005.*, vol. 2, pp. 910–916, IEEE, 2005.

[136] M. Liserre, F. Blaabjerg, and R. Teodorescu, "Grid Impedance Estimation via Excitation of LCL-Filter Resonance," *IEEE Transactions on Industry Applications*, vol. 43, no. 5, pp. 1401–1407, 2007.

[137] S. C. Paiva, R. L. d. A. Ribeiro, D. K. Alves, F. B. Costa, and T. d. O. A. Rocha, "A wavelet-based hybrid islanding detection system applied for distributed generators interconnected to AC microgrids," *International Journal of Electrical Power & Energy Systems*, vol. 121, p. 106032, oct 2020.

[138] A. V. Timbus, R. Teodorescu, F. Blaabjerg, and U. Borup, "Online grid measurement and ENS detection for PV inverter running on highly inductive grid," *IEEE Power Electronics Letters*, vol. 2, no. 3, pp. 77–82, 2004.

[139] L. Asiminoaei, A. Asiminoaei, R. Teodorescu, F. Blaabjerg, U. Borup, L. Asiminoaei, R. Teodorescu, F. Blaabjerg, and U. Borup, "Implementation and Test of an Online Embedded Grid Impedance Estimation Technique for PV Inverters," *Industrial Electronics, IEEE Transactions on*, vol. 52, no. 4, pp. 1136–1144, 2005.

[140] L. Asiminoaei, R. Teodorescu, F. Blaabjerg, and U. Borup, "A digital controlled PV-inverter with grid impedance estimation for ENS detection," *IEEE Transactions on Power Electronics*, vol. 20, no. 6, pp. 1480–1490, 2005.

[141] S. Cobreces, E. Bueno, D. Pizarro, F. Rodriguez, and F. Huerta, "Grid Impedance Monitoring System for Distributed Power Generation Electronic Interfaces," *IEEE Transactions on Instrumentation and Measurement*, vol. 58, pp. 3112–3121, sep 2009.

[142] A. Massoud, K. Ahmed, S. Finney, and B. Williams, "Harmonic distortion-based island detection technique for inverter-based distributed generation," *IET Renewable Power Generation*, vol. 3, no. 4, p. 493, 2009.

[143] BSI-Standards-Publication, "Utility-interconnected photovoltaic inverters — Test procedure of islanding prevention measures BS EN 62116:2014," tech. rep., 2014.

[144] D. Sivadas and K. Vasudevan, "An Active Islanding Detection Strategy With Zero Nondetection Zone for Operation in Single and Multiple Inverter Mode Using GPS Synchronized Pattern," *IEEE Transactions on Industrial Electronics*, vol. 67, pp. 5554–5564, jul 2020.

[145] T. Roinila and T. Messo, "Online Grid-Impedance Measurement Using Ternary-Sequence Injection," *IEEE Transactions on Industry Applications*, vol. 54, no. 5, pp. 5097–5103, 2018.

[146] X. Zhang, D. Xia, Z. Fu, G. Wang, and D. Xu, "An Improved Feedforward Control Method Considering PLL Dynamics to Improve Weak Grid Stability of Grid-Connected Inverters," *IEEE Transactions on Industry Applications*, vol. 54, no. 5, pp. 5143–5151, 2018.

[147] Y. Wang, B. Ren, and Q. C. Zhong, "Robust Power Flow Control of Grid-Connected Inverters," *IEEE Transactions on Industrial Electronics*, vol. 63, no. 11, pp. 6887–6897, 2016.

[148] IEC, "IEC/IEEE 60255-118-1 – Measuring relays and protection equipment – Part 118-1: Synchrophasor for power systems – Measurements," tech. rep., 2018.

[149] J. Ma, P. Zhang, H. J. Fu, B. Bo, and Z. Y. Dong, "Application of phasor measurement unit on locating disturbance source for low-frequency oscillation," *IEEE Transactions on Smart Grid*, vol. 1, no. 3, pp. 340–346, 2010.

[150] Y. Guo, K. Li, Z. Yang, J. Deng, and D. M. Laverty, "A novel radial basis function neural network principal component analysis scheme for PMU-based wide-area power system monitoring," *Electric Power Systems Research*, vol. 127, no. June, pp. 197–205, 2015.

[151] P. Dehghanian, B. Wang, and M. Tasdighi, *New Protection Schemes in Smarter Power Grids With Higher Penetration of Renewable Energy Systems*. Elsevier Ltd., 2019.

[152] R. Matica, V. Kirincic, S. Skok, and A. Marusic, "Transmission line impedance estimation based on PMU measurements," *IEEE EuroCon 2013*, no. July, pp. 1438–1444, 2013.

[153] H. Zhou, X. Zhao, D. Shi, H. Zhao, and C. Jing, "Calculating sequence impedances of transmission line using PMU measurements," *IEEE Power and Energy Society General Meeting*, vol. 2015-Septe, pp. 1–5, 2015.

[154] J. Yang, W. Li, T. Chen, W. Xu, and M. Wu, "Online estimation and application of power grid impedance matrices based on synchronised phasor measurements,"

*IET Generation, Transmission and Distribution*, vol. 4, no. 9, pp. 1052–1059, 2010.

[155] S. Corsi and G. N. Taranto, "A real-time voltage instability identification algorithm based on local phasor measurements," *IEEE Transactions on Power Systems*, vol. 23, no. 3, pp. 1271–1279, 2008.

[156] T. An, S. Zhou, J. Yu, W. Lu, and Y. Zhang, "Research on Illed-Conditioned Equations in Tracking Thevenin Equivalent Parameters with Local Measurements," in *2006 International Conference on Power System Technology*, no. 1, pp. 1–4, IEEE, oct 2006.

[157] G. Fusco, A. Losi, and M. Russo, "Constrained least squares methods for parameter tracking of power system steady-state equivalent circuits," *IEEE Transactions on Power Delivery*, vol. 15, no. 3, pp. 1073–1080, 2000.

[158] S. M. Abdelkader and D. J. Morrow, "Online Tracking of Thévenin Equivalent Parameters Using PMU Measurements," *IEEE Transactions on Power Systems*, vol. 27, pp. 975–983, may 2012.

[159] R. Isermann and M. Münchhof, *Identification of Dynamic Systems*. Berlin, Heidelberg: Springer Berlin Heidelberg, 2011.

[160] D. Serfontein, J. Rens, G. Botha, and J. Desmet, "Continuous harmonic impedance assessment using online measurements," *2015 IEEE International Workshop on Applied Measurements for Power Systems (AMPS)*, pp. 1–6, 2015.

[161] D. Serfontein, J. Rens, G. Botha, and J. Desmet, "Continuous Event-Based Harmonic Impedance Assessment Using Online Measurements," *IEEE Transactions on Instrumentation and Measurement*, vol. 65, pp. 2214–2220, oct 2016.

[162] Herong Gu, X. Guo, Deyu Wang, and W. Wu, "Real-time grid impedance estimation technique for grid-connected power converters," in *2012 IEEE International Symposium on Industrial Electronics*, pp. 1621–1626, IEEE, may 2012.

[163] D. Perez-Estevez and J. Doval-Gandoy, "Grid Impedance Identification Using the VSC Switching Ripple," in *2019 IEEE Energy Conversion Congress and Exposition (ECCE)*, pp. 1506–1513, IEEE, sep 2019.

[164] B. L. Eidson, D. L. Geiger, and M. Halpin, "Equivalent power system impedance estimation using voltage and current measurements," *2014 Clemson University Power Systems Conference, PSC 2014*, pp. 1–6, 2014.

[165] G. Welch, G. Bishop, and C. Hill, "An Introduction to the Kalman Filter," pp. 1–16, 1997.

[166] N. Hoffmann and F. W. Fuchs, "Minimal invasive equivalent grid impedance estimation in inductive-resistive power networks using extended kalman filter," *IEEE Transactions on Power Electronics*, vol. 29, no. 2, pp. 631–641, 2014.

[167] J. Ye, Z. Zhang, A. Shen, J. Xu, and F. Wu, "Kalman filter based grid impedance estimating for harmonic order scheduling method of active power filter with output LCL filter," *2016 International Symposium on Power Electronics, Electrical Drives, Automation and Motion, SPEEDAM 2016*, pp. 359–364, 2016.

[168] J. Rhode, A. Kelley, and M. Baran, "Complete characterization of utilization-voltage power system impedance using wideband measurement," *IEEE Transactions on Industry Applications*, vol. 33, no. 6, pp. 1472–1479, 1997.

[169] L. Capponi, I. Fernández, and D. Roggo, "Comparison of measurement methods of grid impedance for Narrow Band-PLC up to 500 kHz," *2018 IEEE 9th International Workshop on Applied Measurements for Power Systems (AMPS)*, pp. 1–6, 2018.

[170] M. Harris, A. Kelley, J. Rhode, and M. Baran, "Instrumentation for measurement of line impedance," in *Proceedings of 1994 IEEE Applied Power Electronics Conference and Exposition - ASPEC'94*, pp. 887–893, IEEE, 1994.

[171] D. Roggo, D. Furrer, and L. Merendaz, "On-line 2 to 150 kHz grid impedance meter," in *22nd International Conference and Exhibition on Electricity Distri-*

*bution (CIRED 2013)*, no. June, pp. 1417–1417, Institution of Engineering and Technology, 2013.

[172] A. Rygg and M. Molinas, "Real-time stability analysis of power electronic systems," *2016 IEEE 17th Workshop on Control and Modeling for Power Electronics, COMPEL 2016*, 2016.

[173] Y. A. Familiant, J. Huang, K. A. Corzine, and M. Belkhayat, "New Techniques for Measuring Impedance Characteristics of Three-Phase AC Power Systems," *IEEE Transactions on Power Electronics*, vol. 24, pp. 1802–1810, jul 2009.

[174] G. Francis, R. Burgos, D. Boroyevich, F. Wang, and K. Karimi, "An algorithm and implementation system for measuring impedance in the D-Q domain," *IEEE Energy Conversion Congress and Exposition: Energy Conversion Innovation for a Clean Energy Future, ECCE 2011, Proceedings*, pp. 3221–3228, 2011.

[175] M. Sumner, B. Palethorpe, and D. Thomas, "Impedance Measurement for Improved Power Quality—Part 1: The Measurement Technique," *IEEE Transactions on Power Delivery*, vol. 19, pp. 1442–1448, jul 2004.

[176] R. Parthiban, T. Nivetha, and B. Umamaheswari, "Harmonic injection technique-based grid impedance estimation for an LCL-filtered grid connected inverter - an investigation," *International Journal of Power Electronics*, vol. 10, no. 1/2, p. 155, 2019.

[177] J. Kukkola, M. Routimo, and M. Hinkkanen, "Real-Time Grid Impedance Estimation Using a Converter," *2019 IEEE Energy Conversion Congress and Exposition, ECCE 2019*, pp. 6005–6012, 2019.

[178] D. K. Alves, R. L. Ribeiro, F. B. Costa, and T. O. A. Rocha, "Real-time wavelet-based grid impedance estimation method," *IEEE Transactions on Industrial Electronics*, vol. 66, no. 10, pp. 8263–8265, 2019.

[179] A. V. Timbus, P. Rodriguez, R. Teodorescu, and M. Ciobotaru, "Line impedance estimation using active and reactive power variations," *PESC Record - IEEE Annual Power Electronics Specialists Conference*, pp. 1273–1279, 2007.

[180] J. H. Suarez, H. M. C. Gomes, L. S. Santana, A. J. Sguarezi Filho, L. L. O. Carralero, and F. F. Costa, "An Improved Impedance Estimation Method Based on Power Variations in Grid-Connected Inverters," in *2019 IEEE 15th Brazilian Power Electronics Conference and 5th IEEE Southern Power Electronics Conference (COBEP/SPEC)*, pp. 1–6, IEEE, dec 2019.

[181] M. Ciobotaru, R. Teodorescu, P. Rodriguez, A. Timbus, and F. Blaabjerg, "Online grid impedance estimation for single-phase grid-connected systems using PQ variations," *PESC Record - IEEE Annual Power Electronics Specialists Conference*, no. 1, pp. 2306–2312, 2007.

[182] S. Cobreces, F. Huerta, D. Pizarro, F. J. Rodrguez, and E. J. Bueno, "Three-phase power system parametric identification based on complex-space recursive least squares," in *2007 IEEE International Symposium on Intelligent Signal Processing*, pp. 1–6, IEEE, 2007.

[183] J. Fang, H. Deng, and S. Goetz, "Grid Impedance Estimation through Grid-Forming Power Converters," *IEEE Transactions on Power Electronics*, vol. 8993, no. c, pp. 1–1, 2020.

[184] R. Fantino, C. A. Busada, and J. A. Solsona, "Grid Impedance Estimation by Measuring Only the Current Injected to the Grid by a VSI with LCL Filter," *IEEE Transactions on Industrial Electronics*, vol. 0046, no. c, pp. 1–1, 2020.

[185] L. Czarnecki and Z. Staroszczyk, "On-line measurement of equivalent parameters for harmonic frequencies of a power distribution system and load," *IEEE Transactions on Instrumentation and Measurement*, vol. 45, pp. 467–472, apr 1996.

[186] B. Palethorpe, M. Sumner, and D. W. P. Thomas, "System impedance measurement for use with active filter control," *Proc. of Power Electronics and Variable Speed Drives*, no. 475, pp. 24–28, 2000.

[187] Z. Staroszczyk and A. Josko, "Real-time Power System Linear Model Identification: Instrumentation and Algorithms," *Instrumentation and Measurement Technology Conference*, no. 1, pp. 897–901, 2000.

[188] M. M. AlyanNezhadi, H. Hassanpour, and F. Zare, "Grid-impedance estimation in high-frequency range with a single signal injection using time–frequency distribution," *IET Science, Measurement and Technology*, vol. 13, no. 7, pp. 1009–1018, 2019.

[189] M. Cespedes and J. Sun, "Online grid impedance identification for adaptive control of grid-connected inverters," *2012 IEEE Energy Conversion Congress and Exposition, ECCE 2012*, pp. 914–921, 2012.

[190] P. Garcia, M. Sumner, A. Navarro-Rodriguez, J. M. Guerrero, and J. Garcia, "Observer-Based Pulsed Signal Injection for Grid Impedance Estimation in Three-Phase Systems," *IEEE Transactions on Industrial Electronics*, vol. 65, pp. 7888–7899, oct 2018.

[191] X. Chen, Y. Zhang, S. Wang, J. Chen, and C. Gong, "Impedance-Phased Dynamic Control Method for Grid-Connected Inverters in a Weak Grid," *IEEE Transactions on Power Electronics*, vol. 32, pp. 274–283, jan 2017.

[192] M. Sumner, B. Palethorpe, D. W. Thomas, P. Zanchetta, and M. C. Di Piazza, "A technique for power supply harmonic impedance estimation using a controlled voltage disturbance," *IEEE Transactions on Power Electronics*, vol. 17, no. 2, pp. 207–215, 2002.

[193] M. Sumner, D. W. Thomas, A. Abusorrah, and P. Zanchetta, "Power system impedance estimation for improved active filter control, using continuous wavelet transforms," *Proceedings of the IEEE Power Engineering Society Transmission and Distribution Conference*, pp. 653–658, 2006.

[194] K. G. Firouzjah, A. Sheikholeslami, and M. Khaleghi, "A New Harmonic Detection Method for Shunt Active Filter Based on Wavelet Transform," *Journal of Applied Sciences*, vol. 4, no. 11, pp. 1561–1568, 2008.

[195] M. Sifuzzaman, M. R. Islam, and M. Z. Ali, "Application of Wavelet Transform and its Advantages Compared to Fourier Transform," *Journal of Physical Sciences*, vol. 13, pp. 121–134, 2009.

[196] M. Sumner, A. Abusorrah, D. Thomas, and P. Zanchetta, "Real time parameter estimation for power quality control and intelligent protection of grid-connected power electronic converters," *IEEE Transactions on Smart Grid*, vol. 5, no. 4, pp. 1602–1607, 2014.

[197] N. Mohammed, M. Ciobotaru, and G. Town, "Performance Evaluation of Wideband Binary Identification of Grid Impedance Using Grid-connected Inverters," in *2019 21st European Conference on Power Electronics and Applications (EPE '19 ECCE Europe)*, pp. P.1–P.10, IEEE, sep 2019.

[198] A. Riccobono, E. Liegmann, A. Monti, F. Castelli Dezza, J. Siegers, and E. Santi, "Online wideband identification of three-phase AC power grid impedances using an existing grid-tied power electronic inverter," *2016 IEEE 17th Workshop on Control and Modeling for Power Electronics, COMPEL 2016*, vol. 00, no. c, pp. 1–8, 2016.

[199] S. Neshvad, S. Chatzinotas, and J. Sachau, "Wideband Identification of Power Network Parameters Using Pseudo-Random Binary Sequences on Power Inverters," *IEEE Transactions on Smart Grid*, vol. 6, no. 5, pp. 2293–2301, 2015.

[200] D. Martin, I. Nam, J. Siegers, and E. Santi, "Wide bandwidth three-phase impedance identification using existing power electronics inverter," *Conference Proceedings - IEEE Applied Power Electronics Conference and Exposition - APEC*, no. 2, pp. 334–341, 2013.

[201] T. Roinila, M. Vilkko, and Jian Sun, "Online Grid Impedance Measurement Using Discrete-Interval Binary Sequence Injection," *IEEE Journal of Emerging and Selected Topics in Power Electronics*, vol. 2, pp. 985–993, dec 2014.

[202] T. Roinila, T. Messo, and E. Santi, "MIMO-identification techniques for rapid impedance-based stability assessment of three-phase systems in DQ Domain," *IEEE Transactions on Power Electronics*, vol. 33, no. 5, pp. 4015–4022, 2018.

[203] M. Esparza, J. Segundo, C. Gurrola-Corral, N. Visairo-Cruz, E. Barcenas, and E. Barocio, "Parameter Estimation of a Grid-Connected VSC Using the Extended Harmonic Domain," *IEEE Transactions on Industrial Electronics*, vol. 66, pp. 6044–6054, aug 2019.

[204] D. Martin, E. Santi, and A. Barkley, "Wide bandwidth system identification of AC system impedances by applying pertubations to an existing converter," *IEEE Energy Conversion Congress and Exposition: Energy Conversion Innovation for a Clean Energy Future, ECCE 2011, Proceedings*, pp. 2549–2556, 2011.

[205] National Grid ESO, "Guidance Notes for Power Park Modules," Tech. Rep. 4, 2019.

[206] R. Bugdał, A. Dyśko, G. M. Burt, and J. R. Mcdonald, "Performance analysis of the ROCOF and Vector Shift methods using a dynamic protection modelling approach," in *15th International Conference on Power System Protection*, pp. 139–144, 2006.

[207] B. Hoseinzadeh, C. L. Bak, and F. Blaabjerg, "Impact of grid impedance variations on harmonic emission of grid-connected inverters," in *2017 IEEE Manchester PowerTech*, pp. 1–5, IEEE, jun 2017.

[208] N. Zorbas, "Derivation of Induction Motor Equivalent Circuit Using Space-Phasor Concepts," *IEEE Transactions on Education*, vol. E-30, no. 2, pp. 90–97, 1987.

[209] R. H. Park, "Two-Reaction Theory of Synchronous Machines: Generalized Method of Analysis-Part I," *Transactions of the American Institute of Electrical Engineers*, vol. 48, no. 3, pp. 716–727, 1929.

Bibliography